RÉPUBLIQUE ALGÉRIENNE DÉMOCRATIQUE ET POPULAIRE

Ministère de l'Enseignement Supérieur et de la Recherche Scientifique

Université Hadj Lakhdar - BATNA 1

Faculté des Sciences de la Matière

Département de Physique

THÈSE

Présentée en vue de l'obtention du

Diplôme de Doctorat

par :

TOUATI Abdellah

Thème :

La théorie de jauge non-commutative et la gravité quantique

Domaine:	Sciences de la Matière
Filière:	Physique
Spécialité:	Physique théorique

Soutenue le : 23/05/2024

Devant le jury :

Président :	Delenda Yazid	Pr	Université de Batna 1
Rapporteur :	Zaiem Slimane	Pr	Université de Batna 1
Examinateurs :	Aouachria Mekki	Pr	Université de Batna 1
	Boubaa Dris	MCA	Université de Khenchela
	Aissaoui Habib	Pr	Université de Constantine 1
Invité :	Zamoum Redouane	MCA	Université de Bouira

People's Democratic Republic of Algeria
Ministry of Higher Education and Scientific Research

Hadj Lakhdar University - BATNA 1
Faculty of Matter Sciences
Department of Physics

THESIS

Submitted in fulfillment of the requirement
for the degree of Doctorate

By:
ABDELLAH Touati

Title:

Non-commutative gauge theory and quantum gravity

Domain: Matter Sciences
Branch: Physics
Option: Theoretical Physics

Defended on: 23/05/2024

In front of the jury:

Chair:	Yazid Delenda	Pr	University of Batna 1
Supervisor:	Slimane Zaiem	Pr	University of Batna 1
Examiners:	Mekki Aouachria	Pr	University of Batna 1
	Dris Boubaa	MCA	University of Khenchela
	Habib Aissaoui	Pr	University of Constantine 1
Invited:	Redouane Zamoum	MCA	University of Bouira

Non-Commutative Gauge Theory and Quantum Gravity, © May 2024

Author:
Abdellah Touati

Supervisors:
Prof. Slimane Zaim

Institute:
Batna 1 University, Batna, Algeria

CONTENTS

List of Figures . . . vi

List of Tables . . . xiii

Abstract . . . xv

Declaration of Authorship . . . xvii

Acknowledgments . . . xix

Publications . . . xxi

Seminars and Conferences . . . xxiii

Acronyms . . . xxv

Introduction . . . 1

1 OVERVIEW OF GENERAL RELATIVITY . . . 7
  1.1 Einstein gravity . . . 8
    1.1.1 Generalization of the Special Relativity Principle . . . 8
    1.1.2 The non-Euclidean geometry of spacetime . . . 8
    1.1.3 Equivalence principle . . . 9
    1.1.4 The stress-energy-momentum tensor . . . 9
    1.1.5 Einstein equation . . . 10
  1.2 Schwarzschild solution . . . 12
    1.2.1 Classical test of general relativity . . . 12
  1.3 Black hole thermodynamics and Hawking radiation . . . 21
  1.4 Gauge theory of gravity . . . 22

2 NON-COMMUTATIVE GAUGE THEORY OF GRAVITY . . . 27
  2.1 Motivation of the non-commutative in physics . . . 28
  2.2 Non-commutative framework and gauge theory . . . 29
    2.2.1 Weyl Transformation . . . 29
    2.2.2 Moyal product ($*-$star product) . . . 30
    2.2.3 Seiberg-Witten map . . . 32
  2.3 Deformed gauge gravity . . . 33
    2.3.1 Application to the Schwarzschild black hole . . . 35

3 GEOMETRICAL PROPERTIES OF BLACK HOLES IN NON-COMMUTATIVE GAUGE THEORY . . . 37
3.1 NC stationary black hole in gauge theory of gravity . . . 37
3.2 Non-commutative Schwarzschild black hole . . . 42
3.2.1 Singularity and event horizon . . . 43
3.2.2 Collapse of matter . . . 45
3.3 Non-commutative Reissner–Nordström black hole . . . 47
3.3.1 Singularity and event horizon . . . 49

4 MOTION IN THE NON-COMMUTATIVE SPACE-TIME . . . 53
4.1 Non-commutative Schwarzschild spacetime . . . 54
4.2 Time-like geodesic equation in the NC Schwarzschild spacetime . . . 56
4.2.1 Radial motion of massive particles . . . 56
4.2.2 Circular motion of massive particles . . . 59
4.2.3 Stability condition and Lyapunov exponent . . . 61
4.2.4 NC effect on the orbital motion . . . 69
4.3 Null geodesic equation in the NC Schwarzschild spacetime . . . 71
4.3.1 Radial motion of massless particles . . . 72
4.3.2 Circular motion of massless particles . . . 74
4.3.3 Stability condition and photon sphere . . . 75
4.3.4 Lyapunov exponents . . . 76
4.3.5 Black hole shadow . . . 79
4.4 Non-commutative Reissner-Nordström spacetime . . . 81
4.5 Time-like geodesic motion of neutral particle around a NC RN black hole . . . 83
4.5.1 Circular orbit and stability condition . . . 83
4.5.2 NC effect on the orbital motion . . . 87
4.6 Time-like geodesic equation of charged particle around a RN black hole . . . 89
4.6.1 NC effect on the circular orbits of charged particles . . . 93
4.7 Constraint on the NC parameter Θ from some astrophysical systems . . . 95
4.7.1 Gravitational periastron advance in NC spacetime . . . 95
4.7.2 Gravitational red-shift . . . 101
4.7.3 Gravitational deflection of light . . . 103
4.7.4 Gravitational time delay (Shapiro effect) . . . 104
4.7.5 Results and discussion . . . 106

5 THERMODYNAMICS PROPRIETIES OF THE DEFORMED BLACK HOLE . . . 109
5.1 Classical black hole thermodynamics in NC spacetime . . . 110
5.1.1 Mass, temperature, and entropy of the NC Schwarzschild black hole . 110
5.1.2 Heat capacity and phase transition . . . 116
5.1.3 Helmholtz free energy and black hole stability . . . 119
5.1.4 The black hole pressure and Hawking-Page-like phase transition . . . 121
5.1.5 Modified first law of the BH thermodynamics . . . 126
5.2 NC BH in the grand canonical ensemble . . . 127

5.2.1 Similarity between non-commutativity and the electric charge of a black hole . . . 130
5.2.2 State equation . . . 131
5.2.3 Phase transition and free energy . . . 135
5.3 Black hole phase transition and isothermal cavity . . . 140
5.3.1 Local temperature and energy . . . 141
5.3.2 Local heat capacity and phase transition . . . 142
5.4 Quantum tunneling in NC spacetime . . . 146
5.4.1 NC correction to the Hawking temperature . . . 149
5.4.2 Logarithmic corrections to the entropy in NC spacetime . . . 150
5.4.3 Correlations . . . 152
5.4.4 NC correction to the density number of particles emitted . . . 154
5.4.5 Bekenstein entropy loss and number of particles emitted . . . 155
5.5 Black hole evaporation process in NC spacetime . . . 158
5.5.1 Luminosity of NC SBH radiation . . . 158
5.5.2 Energy emission rate . . . 159
5.5.3 NC effect on the black hole Lifetime . . . 160

Conclusions . . . 165

APPENDICES . . . 169

A SPHERICAL SYMMETRIC METRIC IN NC GAUGE THEORY . . . 169
A.1 Spin connection . . . 169
A.2 Curvature tensor . . . 170
A.3 Non-commutative tetrad fields . . . 173

B ENERGY AND ANGULAR MOMENTUM OF THE CIRCULAR ORBIT AROUND NC RN BH . . . 177
B.1 Uncharged massive test particle . . . 177
B.2 Charged massive test particle . . . 178

BIBLIOGRAPHY . . . 181

LIST OF FIGURES

Figure 1.1 Thought experiment of two rockets (principle of equivalence). 10

Figure 1.2 Schematic picture of periastron advance of the orbit. 13

Figure 1.3 Schematic picture of light deflection by the gravitational field. 16

Figure 1.4 Schematic example of emitter and receiver of two signals of light. . . 18

Figure 1.5 Schematic picture of the Shapiro effect. 19

Figure 3.1 Behavior of the NC component $\hat{g}_{00}$ for a stationary observer at spatial infinity in the equatorial plane $\theta = \pi/2$ as a function of r, for different values of Θ. 44

Figure 3.2 A schematic picture of Schwarzschild BH in the NC spacetime. The red solid line represents the commutative Schwarzschild event horizon, the black dotted line represents the NC event horizon, and the blue dashed line represents the static limit surface. With $\Theta = 0.75$, the black disk represents the singularity. 45

Figure 3.3 A schematic picture of the gravitational collapsing matter in the NC spacetime and the formation of NC Schwarzschild BH. 46

Figure 3.4 A schematic picture for the collapsing matter of a star in the NC spacetime and the formation of Schwarzschild BH. 47

Figure 3.5 Behavior of $\hat{g}_{00}$ in the NC RN spacetime. 49

Figure 3.6 Representation of $\hat{g}_{00}$ for the three conditions of $m^2 - Q^2$, for fixed electric charge $Q = 0.5$ for all cases and different masses $m = 0.7, 0.5, 0.3$. 50

Figure 4.1 The behavior of the proper time for a free fall of a massive test particle in the NC Schwarzschild black hole as a function of r, with $m = 1$ and the initial position $r_0 = 8$. 58

Figure 4.2 The behavior of the time coordinate for a free fall of a massive test particle in the NC Schwarzschild black hole as a function of r, with $m = 1$ and the initial position $r_0 = 8$. 59

Figure 4.3 The behavior of the proper/coordinate time for a free fall of a massive test particle in the NC Schwarzschild black hole as a function of r, with $m = 1$ and the initial position $r_0 = 8$. 60

Figure 4.4 The behaviors of the effective potential for a massive particle. **Left panel:** different Θ and fixed: $E = 0.998$, $m = 1$, and $l = 4.2$. **Right panel:** different m and fixed: $E = 0.998$, $\Theta = 0.4$, $l = 4.2$. 60

Figure 4.5 The behaviors of the effective potential for a massive particle. **Left panel:** different E and fixed: $m = 1$, $\Theta = 0.2$, $l = 4.2$. **Right panel:** different l and fixed: $E = 0.998$, $\Theta = 0.2$, $m = 1$. 61

Figure 4.6 The behaviors of the radius of circular orbits for a particle in the NC space-time. Unstable and multiple stable circular orbits as function of Θ and for fixed $l = 4.2$, $E = 0.998$, $m = 1$ in (a), (b), and (c), and as function of l and for fixed $\Theta = 0.2$, $E = 0.998$, $m = 1$ in (d), (e), and (f). 62

Figure 4.7 The condition of stability for circular orbits for different Θ and other fixed parameters: (left panel) $E = 1$, $l_{crit} = 2\sqrt{3}$, and $m = 1$. (right panel) $E = 1$, $l_{crit} = \sqrt{3}$, $m = 0.5$. 63

Figure 4.8 The condition of stability for circular orbits for fixed $E = 1$. (left panel) different m, $l_{crit} = 2\sqrt{3}m$ and fixed $\Theta = 0.2$. (right panel) different Θ and fixed $m = 0.50$ 64

Figure 4.9 Schematic picture of the first and second bounds of stable circular orbits around the NC Schwarzschild BH, where green solid line represents ISCO for the Schwarzschild BH, black dot-dashed lines represent ISCO in external region for the NC Schwarzschild BH, blue dashed line represents the NC event horizon, and the black disk in the center represents the singularity of the NC Schwarzschild BH, and the red dot lines represent the new region of SCO near the NC event horizon. ($E = 1$, $l = 2\sqrt{3}$, $m = 1$, and $\Theta = 0.6$). 65

Figure 4.10 The behavior of energy (left panel) and angular momentum (right panel) of a circular orbit for massive particles in NC spacetime. 65

Figure 4.11 The behavior of the orbital velocity (left panel) and orbital time scale (right panel) for a massive test particle with different values of NC parameters Θ. 67

Figure 4.12 The behavior of the proper time (left panel) and coordinate time (right panel) Lyapunov exponents for a massive particle as a function of circular orbits r_c. 68

Figure 4.13 The behavior of the ratio proper/coordinate time of Lyapunov exponent for a massive particle in NC spacetime. 69

Figure 4.14 Time-like geodesic for a massive test particle $h = 1$ around a NC Schwarzschild black hole, with $\Theta = 0.1, 0.2, 0.3, 0.4$ (left to right) and fixed mass $m = \frac{3}{14}$ and varying other parameters in the plan $\theta = \frac{\pi}{2}$: (rows 1), $l = 1.586$, $E = 0.993$; (rows 2), $l = 0.915$, $E = 0.975$; (rows 3) $l = 0.99$, $E = 0.9828$; (rows 4) $l = 0.915$, $E = 0.975$. 72

Figure 4.15 The behavior of the affine parameter and the coordinate time along the radial null geodesic of a photon in the NC Schwarzschild black hole as function of r. 73

Figure 4.16 The behavior of the effective potential for massless particle with different values of NC parameters Θ and fixed: $E = 0.998$, $m = 1$, $l = 4.2$ (left panel), and with different angular momentum l and fixed $E = 0.998$, $m = 1$, $\Theta = 0.2$ (right panel). 74

Figure 4.17 The behavior of the photon sphere radius in NC spacetime. stable and unstable circular orbits as a function of Θ and for fixed $l = 4.2$, $E = 1$, $m = 1$ (two left panels), as a function of l and for fixed $\Theta = 0.3$, $E = 1$, $m = 1$ (two right panels). 76

Figure 4.18 The schematic picture of the stable/unstable photon sphere around the NC Schwarzschild black hole. 76

Figure 4.19 The behavior of the coordinate time Lyapunov exponent for massless particles as a function of r_c (left panel) and as a function of the NC parameters Θ (right panel). 77

Figure 4.20 The behavior of $\frac{\hat{\lambda}_c^{Null}}{\hat{\Omega}_c^{Null}}$ as a function of r_c. 78

Figure 4.21 The Schwarzschild black hole shadow in the NC spacetime, for different values of NC parameter Θ (left panel) with $m = 1$, and for different values of black hole mass m (right panel) with $\Theta = 0.4$. . . 80

Figure 4.22 The behaviors of the commutative effective potential $\Theta = 0$ for a massive particle as a function of r. **Left panel:** different Q and fixed: $E = 0.998$, $m = 1$, $l = 4.2$. **Right panel:** different l and fixed: $E = 0.998$, $Q = 0.8$, $m = 1$. 83

Figure 4.23 The behaviors of the NC effective potential for a massive particle as a function of r, with different Θ and fixed: $E = 0.998$, $m = 1$, $l = 4.2$. 84

Figure 4.24 The behaviors of the NC effective potential for a massive particle as a function of r. **Left panel:** different Q and fixed: $E = 0.998$, $m = 1$, $l = 4.2$, $\Theta = 0.2$. **Right panel:** different l and fixed: $E = 0.998$, $m = 1$, $Q = 0.5$, $\Theta = 0.2$. 84

Figure 4.25 The behaviors of the radius of circular orbits for a particle in the NC RN spacetime. Unstable and multiple stable circular orbit as function of Θ and for fixed $l = 4.2$, $E = 0.998$, $m = 1$, $Q = 0.5$ in (a), (b) and (c), and as function of Q and for fixed $\Theta = 0.3$, $E = 0.998$, $l = 4.2$, $m = 1$ in (d), (e) and (f). 85

Figure 4.26 The first and second bound of stable circular orbits around the NC RN black hole. 86

Figure 4.27 Radial dependence of the energy E_c^2 (left panel) and the angular momentum l_c^2 (right panel) of a neutral test particle orbiting around an NC RN black hole, for different values of electric charge Q and for fixed NC parameter Θ. 86

Figure 4.28 Radial dependence of the energy E_c^2 (left panel) and the angular momentum l_c^2 (right panel) of a neutral test particle orbiting around an NC RN black hole, for different values of NC parameter Θ and for fixed electric charge Q. 87

Figure 4.29 Time-like geodesic for a massive particle around Schwarzschild black hole $Q = 0$ and RN black hole $Q = 0.2$ with $m = 3/14$, $E = 0.993$, $l = 3.8$, and $\Theta = 0, 0.4$. 88

Figure 4.30 Periodic orbits of neutral massive particle around Schwarzschild and Reissner-Nordeström black hole for fixed mass $m = 3/14$ and energy $E = 0.993$ and varying other parameters l, Q, and Θ. 89

Figure 4.31 The behaviors of the effective potential for charged massive particle as a function of r, for different electric charges of the test particle q and fixed: $E = 0.998$, $m = 1$, $l = 4.2$. 91

Figure 4.32 The behaviors of the radius of circular orbits for a particle in the NC RN spacetime. Unstable and multiple stable circular orbit as a function of q and for fixed $l = 4.2$, $E = 0.998$, $m = 1$, and $Q = 0.5$. . 91

Figure 4.33 Radial dependence of the angular momentum l_c^2 of a charged test particle orbiting around an NC RN black hole for different values of electric charge of test particle q (left panel) and for different values of NC parameter Θ (right panel). 92

Figure 4.34 Radial dependence of the energy E_c^2 of a charged test particle orbiting around an NC RN BH for different values of electric charge of test particle q and a fixed NC parameter Θ. 93

Figure 4.35 Time-like geodesic for charged massive test particle around NC RN black hole $Q = 0.2$ with $m = 3/14$, $E = 0.993$, $l = 3.7$, and $\Theta = 0.4$ for different particle electric charge $q = -0.2, 0.0, 0.2$. 94

Figure 4.36 Periodic orbits of charged massive test particle around NC RN black hole for fixed $m = 3/14$, $E = 0.993$, $\Theta = 0.2$, $Q = 0.1$ and varying other parameters l and q. 95

Figure 4.37 Behaviors of the gravitational periastron advance of Mercury in the NC spacetime. 97

Figure 4.38 Behavior of the gravitational red-shift in NC spacetime. 102

Figure 4.39 Behavior of the gravitational deflection of light in NC spacetime . . 103

Figure 4.40 Behavior of the gravitational time delay in the NC spacetime. 105

Figure 5.1 Behavior of BH mass as a function of r_h. 111

Figure 5.2 Behavior of NC Hawking temperature as a function of the event horizon r_h, with different Θ (left panel) and for different θ (right panel) for the case $a = b = \Theta$. 112

Figure 5.3 Behavior of NC Hawking temperature as a function of the event horizon r_h, with different Θ (left panel) and for different θ (right panel) for the case $a = 0$, $b = \Theta$. 113

Figure 5.4 Behavior of NC temperature distribution as a function of the observation angle θ and NC parameter Θ, for the two cases, $a = b = \Theta$ (left panel) and $a = 0$, $b = \Theta$ (right panel), with $r_h = 0.8$. 114

Figure 5.5 Behavior of NC temperature emitted from the surface horizon of the BH as a function of r_h, for the case $a = 0$, $b = \Theta$. 114

Figure 5.6 Behavior of NC entropy as a function of r_h. 116

Figure 5.7 Behavior of Schwarzschild BH heat capacity as a function of the event horizon r_h, for different values of Θ (left panel) and for different values of θ (right panel). 117

Figure 5.8 Behavior of the global heat capacity as a function of r_h in the case of $a = 0$ end $b = \Theta$. 118

Figure 5.9 Behavior of Helmholtz free energy $\hat{F}$ as a function of r_h in NC spacetime. 119

Figure 5.10 Behavior of Helmholtz free energy $\hat{F}$ as a function of r_h in NC spacetime for different Hawking temperatures $\hat{T}$. 120

Figure 5.11 Behavior of the Helmholtz free energy $\hat{F}$ as a function of the NC Hawking temperature $\hat{T}$. 121

Figure 5.12 Behavior of pressure $\hat{P}$ as a function of r_h. 122

Figure 5.13 Behavior of Gibbs free energy $\hat{G}$ as a function of r_h in NC spacetime, for different values of pressure $\hat{P}$ (left panel) and different Hawking temperature $\hat{T}$ (right panel). 123

Figure 5.14 Behavior of Gibbs free energy $\hat{G}$ as a function of the NC Hawking temperature $\hat{T}$, for different values of NC pressure $\hat{P}$. 124

Figure 5.15 Behavior of Gibbs free energy $\hat{G}$ as a function of NC Hawking temperature $\hat{T}$, for different values of Θ. 125

Figure 5.16 The behaviors of the modified Gibbs $\tilde{G}$ free energy in the grand canonical ensemble as a function of the NC Hawking temperature $\hat{T}$. 129

Figure 5.17 The behaviors of the modified Gibbs free energy in the grand canonical ensemble as a function of the NC Hawking temperature $\hat{T}$ in the presence of pressure. 130

Figure 5.18 Hawking temperature for AdS RN BH compared to NC Schwarzschild BH as a function of the event horizon. 132

Figure 5.19 Hawking temperature for AdS RN BH (left panel) and NC Schwarzschild one (right panel) as a function of the event horizon r_h, with different values of pressure. 133

Figure 5.20 Black hole pressure for AdS RN (left panel) and NC Schwarzschild (right panel) as a function of the event horizon, with different values of temperature. 133

Figure 5.21 The heat capacity behavior of the NC Schwarzschild BH as a function of the event horizon r_h, for different Θ (left panel) and for different $\tilde{p}$ (right panel). 135

Figure 5.22 Behaviors of the new Helmholtz free energy $\tilde{F}$ as a function of r_h in NC spacetime, for different new deformed Hawking temperatures $\tilde{t}$. 137

Figure 5.23 Behaviors of the new Helmholtz free energy $\tilde{F}$ as a function of the new Hawking temperature $\tilde{t}$ in NC spacetime, for different pressure $\tilde{p}$, where $\tilde{p}_c = \frac{1}{72\pi\Theta^2}$. 138

Figure 5.24 $\tilde{p}-\tilde{t}$ phase diagram of the NC Schwarzschild BH. The cyan solid line and green dashed line are the plots of $\tilde{t}_{min}$ and $\tilde{t}_{max}$, respectively, as a function of the pressure $\tilde{p}$. 139
Figure 5.25 The behavior of BH entropy with logarithmic correction as a function of the event horizon r_h. 140
Figure 5.26 The behavior of local temperature as a function of r_h inside a cavity with radius $R = 10$. 141
Figure 5.27 The behavior of local heat capacity as a function of r_h inside a cavity with radius $R = 10$. 143
Figure 5.28 The behavior of Helmholtz free energy as a function of $\hat{T}_{local}$ inside a cavity with radius $R = 10$. 145
Figure 5.29 The behavior of tunneling rate BH as a function of the emitting particle energy ω, with $m = 1$. 148
Figure 5.30 The behavior of tunneling rate as a function of BH mass m, for different values of energy ω (right panel), and for different values of the NC parameter Θ (left panel). 148
Figure 5.31 Behaviors of the tunneling rate distribution as a function of the parameters m, ω, and Θ. (raw1) as a function of ω and Θ at different masses $m = 0.2, 0.5, 1.0$. (raw2) as a function of m and ω at different NC parameters $\Theta = 0.0, 0.2, 0.04$. (raw3) as a function of m and Θ at different frequencies $\omega = 0.05, 0.10, 0.15$. 149
Figure 5.32 The behavior of NC Hawking temperature as a function of r_h (in the case $a = \Theta$ and $b = 0$). 150
Figure 5.33 The behavior of the correlation function as a function of the NC parameter Θ for different ω. 153
Figure 5.34 The behavior of the density number of particles emitted $\hat{n}$ from a NC Schwarzschild BH as a function of particle frequency ω (left panel) with $m = 1$ and different NC parameter Θ. (right panel) The density number of particles emitted $\hat{n}$ as a function of the NC parameter Θ with $m = 1$ and different frequency ω. 154
Figure 5.35 The commutative $\Theta = 0$ behavior of $\hat{n}$ as a function of the BH mass m (left panel), with different frequency ω. (right panel) The density number of particles emitted $\hat{n}$ as a function of the BH mass m in the NC spacetime $\Theta = 0.2$ and different frequency ω. 155
Figure 5.36 The behavior of the Bekenstein entropy loss of the NC Schwarzschild BH per emitted quanta as a function of the BH mass m and for a different NC parameter. 156
Figure 5.37 The behavior of the NC total number of particles emitted by the NC Schwarzschild BH as a function of the BH mass m and for different NC parameter. 158
Figure 5.38 The behaviors of the NC Schwarzschild BH Luminosity $\hat{L}$ as a function of r_h. 159

Figure 5.39 The behaviors of energy emission rate of the NC Schwarzschild BH as a function of frequency ω (left panel) and as a function of r_h (right panel). 160
Figure 5.40 The behaviors of NC evaporation rate as a function of mass m with different values of Θ. 161
Figure 5.41 The behaviors of the NC Schwarzschild BH mass during the evaporation process $\hat{m}$ as a function of BH lifetime t, with initial mass $m_i = 10$. 163
Figure 5.42 A schematic picture of the formation and evaporation process of BH in the NC spacetime. 164

LIST OF TABLES

Table 1.1 Comparison between the experimental observation and the theoretical prediction of GR of the angel deviation of some planet of our solar system, which are: mass of the planet (M), semi-major axis (α), eccentricity (e), orbital period (T), orbital precession in columns 2–6, respectively. The prediction of the orbital precession in general relativity in column 7 . . . 16

Table 4.1 Some numerical values of event horizon r_h^{NC}, unstable circular orbit r_{uns}, and multiple stable circular orbit r_{sta} in the commutative and the NC case with different parameter Θ and fixed $E = 0.998, l = 4.2, m = 1$. . . . 62

Table 4.2 Some numerical solution for the radius condition of the innermost stable circular orbit with different parameters Θ and fixed $E = 1, \quad l_{crit} = 2\sqrt{3}m$, m. (a) $m = 1$, (b) $m = 0.5$, (c) $m = 3/14$. . . . 64

Table 4.3 Some numerical values of unstable r_{uns} and new stable circular orbit r_{sta} of photon sphere in the NC spacetime with different parameter Θ and fixed $E = 0.998$, $l = 4.2$, $m = 1$. . . . 75

Table 4.4 Some numerical values of the critical exponent $\hat{\gamma}^{Null}$ for unstable r_{uns} and new stable circular orbit r_{sta} of photon sphere in the NC spacetime with different parameter Θ with $m = 1$. . . . 79

Table 4.5 Some observable values for different planets of our solar system are: mass of the planet (M), semi-major axis (α), eccentricity (e), orbital period (T), and orbital precession in columns 2–6, respectively. The prediction of the orbital precession in general relativity is in column 7, and in the finale column we give the lower bound for the non-commutative parameter Θ^{Phy}. . . . 99

Table 4.6 Upper bound on the NC parameter Θ^{Phy} for the classical tests of general relativity. . . . 106

Table 5.1 Comparison of some thermodynamic properties between RN BH and NC Schwarzschild BH in the grand canonical ensemble. . . . 131

Table 5.2 Comparison of state equation between AdS RN BH and the NC Schwarzschild BH. . . . 131

Table 5.3 Critical parameter of AdS RN BH and NC Schwarzschild one. . . . 135

Table 5.4 Region, heat capacity, state, and stability of the NC Schwarzschild BH for different branches. . . . 136

Table 5.5 Region, heat capacity, state, and stability of the Schwarzschild BH surrounded by a cavity in NC/Commutative geometry for different branches. . . . 144

Table 5.6 Evaporation time for two possible scenarios of the NC Schwarzschild BH, with different Θ, and remnant mass $\hat{m}_0 = \Theta/2$. 162

Table 5.7 Evaporation time $\hat{t}$ of NC Schwarzschild BH in the scenario of remnant BH with its minimum mass, for different values of Θ 163

ABSTRACT

In this thesis, we study several applications of black hole (BH) physics in the presence of two different deformed metrics. This deformation is implemented by the non-commutative (NC) gauge theory of gravity. The first part of the thesis is devoted to obtain the deformed metric in the presence of non-commutativity for two black holes (BHs), which are the Schwarzschild and Reissener-Nordström (RN) metrics. The use of the NC gauge theory affects the geometry of BH and their properties, such as singularity, static limit surface, and event horizon. The second part is devoted for a detailed investigation of the particle motions around a NC BH. Two cases are studied for each deformed metric. Firstly, we study the motion of both massless and massive test particles in the NC Schwarzschild spacetime for two kinds of motions: free fall and circular motion. For free-fall motion, these two types of particles take an infinite time to reach the NC singularity. Moreover, for the circular motion, the non-commutativity predicts a new stable circular orbit (SCO) near the event horizon, which is not allowed in the commutative case. In the third part of this thesis, we investigate in detail the effect of non-commutativity on the BH evaporation process for different scenarios. In the first one, we study in detail the thermal proprieties of the NC Schwarzschild BH in the context of the classical BH thermodynamics, where we predict four important results, which are a new scenario of BH evaporation, a new fundamental length, and a remnant BH in the final stage. We show then similarity between the NC Schwarzschild BH and the Anti-de-Sitter (AdS) RN one in the grand canonical ensemble. The second scenario is devoted to the investigation of the thermal stability and the phase transition of this BH inside a thermal spherical cavity in the presence of this geometry, in which this NC BH shows a two-coexistence phase transition. In the final scenario, we present a detailed study of the NC effect on Hawking radiation, using the quantum tunneling process for two cases. In the first one, we investigate pure thermal radiation, where we show an equivalence between this approach and the thermodynamical one, and then we show the effect of this geometry on the density number of particles that are emitted from the NC Schwarzschild BH. Secondly, we investigate the non-thermal radiation in the presence of this geometry, and then we check the correlation between two successive particle emissions, in which the non-commutativity doesn't preserve only the correlation in this geometry but also reduces it compared to the commutative case, which allows the information to come out with Hawking radiation. Finally, we show the effect of this geometry on the BH evaporation process.

Keywords: Non-commutative gauge theory, black hole physics, geodesic equation, thermodynamical quantities, Hawking radiation, evaporation process.

STATEMENT OF AUTHORSHIP

I, Abdellah Touati, born February 10, 1995 in Bouira, Algeria, declare that this thesis titled *Non-Commutative Gauge Theory and Quantum Gravity* and the work presented in it are my own. I confirm that this work was done mainly while in candidature for a research degree at Batna 1 University.

Except where reference is made in the text of the thesis, this thesis contains no material published elsewhere or extracted in whole or in part from a thesis accepted for the award of any other degree or diploma. No other person's work has been used without due acknowledgment in the main text of the thesis. This thesis has not been submitted for the award of any degree or diploma in any other tertiary institution.

Abdellah Touati May 23, 2024

ACKNOWLEDGMENTS

First of all, I thank the good Lord, Almighty, for enlightening me on the right path to follow and for giving me the strength and audacity to overcome all difficulties.

During my time here in Batna and in particular at Batna 1 University, I had the honor of meeting a lot of interesting people, many of whom have become friends. To all of you, I hereby say: *Thank You for everything!* However, there are a couple of individuals who deserve special mention.

Firstly, I would like to thank my supervisor **Prof. Slimane Zaim** for agreeing to supervise me and for guiding and advising me throughout this modest work.

I express all my gratitude to **Pr. Yazid Delenda** for agreeing to chair the jury for this dissertation. I also thank **Pr. Mekki Aouachria**, **Pr. Habib Aissaoui**, **Mr. Dris Boubaa** and **Mr. Redouane Zamoum** for agreeing to examine my work.

I would like to thank all the professors of the physics department, in particular **Mr. Soufiane Boukhalfa**, **Mr. Mohamed Ameziane Sadoun**, **Mr. Salim Benaiche**, **Mrs. Nadjma Bouchemla**, **Mrs. Nassima Boulkroune** and **Mr. Mohamed Boudref**, professor in the Mathematics department, for their dedication and support throughout my years of study at the University of Bouira.

I thank my dear parents, who have always been there for me. I also thank my sister, my brother and my dear friend **M. Medjras**. Finally, I thank all my friends in particular **A. Haddad**, **M. Adjrade**, **M.A. Gadja** and **S. Djemaoune**, and all of my dear master students, in particular **H. Ferhi**. Special thanks go to **C. Medjras** and **A. Haddad** for their numerous helpful discussions, comments and encouragement and also for helping me to improve my English, during my PhD.

Furthermore, I would like to thank all the members of the *PRIMA Lab*, in particular **T. Otmane**, **H. Bouaziz**, **A. Boudersa**, **A. Larbi** and **S. Gaid**, **H. Rezki** and **F. Bara**. Also, my college during my PhD **M. Mammeri** and **M. Daif**, without forgetting **K. Aouadj**.

PUBLICATIONS

In particular, some data, ideas, opinions and figures presented in this thesis have previously appeared or may appear shortly after the submission of this thesis as follows:

- Abdellah Touati, Slimane Zaim "**Geodesic equation in non-commutative gauge theory of gravity**", Published in *Chinese Physics C*, ISSN: 1674-1137, DOI: 10.1088/1674-1137/ac75ca
- Abdellah Touati, Slimane Zaim "**The Bound on non-commutative parameter based on gravitational measurements**" published in *Physical Sciences Forum* , Presented at the 2nd Electronic Conference on Universe, 16 February–2 March 2023, ISSN: , DOI: 10.3390/ECU2023-14061
- Abdellah Touati, Slimane Zaim "**Thermodynamic Properties of Schwarzschild Black hole in Non-Commutative Gauge Theory of Gravity**", Published in *Annals of Physics*, ISSN: 0003-4916, DOI: 10.1016/j.aop.2023.169394
- Abdellah Touati, Slimane Zaim "**Quantum tunneling from Schwarzschild black hole in non-commutative gauge theory of gravity.**" Published in *Physics Letters B*, ISSN: 1873-2445, DOI: 10.1016/j.physletb.2023.138335
- Abdellah Touati, Slimane Zaim "**Schwarzschild black hole surrounded by a cavity and phase transition in the non-commutative gauge theory of gravity.**" Published in *Astroparticle Physics*, ISSN: 0927-6505, DOI: 10.1016/j.astropartphys.2024.102988

SEMINARS AND CONFERENCES

- The 2nd Electronic Conference on Universe, 16 February–2 March 2023, MDPI: Basel, Switzerland, DOI: 10.3390/ECU2023-14061.
- The 2nd Workshop on Matter and Radiation, 17-18 Mai 2023, Batna, Algeria.

ACRONYMS

ADM R. Arnowitt; S. Deser; C. W. Misner

AdS Anti-de Sitter

BCH Baker-Campbell-Hausdorff

BH Black hole

dS de Sitter

EUP Extended uncertainty principle

GR General Relativity

GUP Generalized Uncertainty Principle

GW Gravitational Waves

IBH Intermidiat black hole

ISCO Innermost Stable Circular Orbit

LBH Large black hole

LQG Loop Quantum Gravity

MDR Modified Dispersion Relation

NC Non-commutative

QG Quantum Gravity

RG Rainbow Gravity

RN Reissner-Nordeström

SBH Small black hole

SCO Stable Circular Orbit

SgrA* Sagittarius A

ST String Theory

SW Seiberg-Witten

INTRODUCTION

General relativity (GR) theory is one of the foundations of modern physics and one of the major scientific discoveries at the beginning of this century; it describes one of the four fundamental interactions in nature, known by gravity, and this theory provides an excellent relativistic description of this interaction. This theory was proposed for the first time by Albert Einstein in 1915. The success of this theory is due to its direct and indirect prediction of some phenomena, such as the four classical tests of GR [1], which were the prediction of the anomaly in Mercury's orbit (the periastron advance of orbit), the deflection of light around massive objects, the red-shift, and the time delay. More modern predictions, such as the detection of gravitational waves (GW) by the collaboration of the LIGO/Virgo experiment in 2016 [2] and the recent indirect observation of a supermassive BH for the first time in the center of the galaxy $M87$ by the event horizon telescope in 2019 [3].

The BHs are considered the most mysterious bodies in the universe. Unfortunately, nothing can escape its gravity, and that makes direct observation of these objects difficult. The only observation is the indirect one, for example, the motion of the stars around the center of the galaxy, such as the star $S2$ around the supermassive BH Sagittarius A (SgrA*) in the Milky Way galaxy [4–7], where we only observe the effect of their gravitational field on the stars orbits. Also, it is possible to detect these celestial objects through their interaction. For example, a pair of BH can emit gravitational radiation, which is observed as an GW, or detect the radiation emitted from their accretion disk and also their shadow, etc. The first theoretical prediction of the existence of BHs was established by K. Schwarzschild in 1916, which is a vacuum solution of Einstein's equations with static spherical symmetry. After the Schwarzschild solution, several solutions were proposed, such as the Reissner-Nordström (RN) RN, which is also a vacuum solution with a static spherical symmetry, and the more realistic Kerr and Kerr-Newman solutions, which describe a rotating uncharged and charged BH, respectively, etc. In this thesis, we focus only on the Schwarzschild and RN solutions.

The geodesic motion of a test body around a compact object has great importance in astrophysics to understand the physics and geometry of these objects, such as neutron stars, BHs, etc. The motion of different types of particles around a BH reveals a lot to understand their nature [8–32]. Moreover, the classification of stable and unstable orbits is interesting to describe the geometrical properties of spacetime around massive objects. Among the various methods for analyzing the stability of geodesics, the Lyapunov exponents [33] has a great application in this context, in which it is considered a bridge between the non-linear GR and the non-linear dynamics. The Lyapunov exponent measures the average rate of separation between two nearby geodesics in phase space [34–44], where the instability of orbits is expressed by the real Lyapunov exponent, while the marginal stable and the stable ones are expressed by the zero and imaginary Lyapunov exponents, respectively.

Although GR predicts BHs, it fails miserably in explaining or studying the center of these objects, in which a spacetime singularity appears, where the geometry at this point diverges at infinity, and this physical singularity is considered as a quantum object. Add to that the failure of this theory to describe gravity signals at the quantum scale. These issues lead physicists to look beyond the GR theory for solving the above problems and search for a new theory that enables them to describe gravity effect at the quantum level. In this context, quantum gravity (QG) theory is one of the biggest modern problems in physics and one of the largest and most active research areas. At the end of the last century, there were several theories that emerged to solve these issues. Among the most promising theories are string theory (ST) [45, 46], loop quantum gravity (LQG) [47, 48], as well as super-gravity [49–52], without forgetting the semi-classical approach [53]. Unfortunately, none of these theories provide a complete theory of QG, despite their impressive applications and theoretical results, and to this day, none of them has been proved experimentally. We must point out that looking for a theory of QG results from the idea of unifying the four fundamental interactions in one single gauge theory. As we know, the classical theory of GR is not a gauge theory. In this context, the first gauge theory of gravity was proposed by R. Utiyama in 1956 [54], which is constructed by analogy to the gauge models of internal symmetries ($U(1), SU(2)$, ...etc.), where the gauge theory of gravity is based on the spacetime symmetry [55–58]. In 2002, G. Zet et al. [59] published an elegant gauge theory of gravity in the Poincaré group, based on a 4-dimensional spherical Minkowski metric, and the gauge fields in this theory are described by four tetrad fields e_μ^a and six spin-connections ω_μ^{ab}, where these gauge potentials are generated by a point-like particle source of mass m. The solution of the equations raised from this gauge gravity reproduced the Schwarzschild one for a vacuum solution. Then, G. Zet et al. generalized their work to the de-Sitter (dS) $SO(4,1)$ group [60], and the solution for vacuum became the Schwarzschild with cosmological constant solution [60, 61]. In this thesis, we will use this theory as a mathematical background for our calculations.

In the semi-classical approach context, the first mechanism that unifies quantum mechanics and gravity near the event horizon of BH was proposed by S. Hawking in 1975 [53], and it's considered the first bridge to the QG theory, where this discovery changed our idea about the BHs, in which these objects can emit radiation and thus evaporate [53, 62], similarly to black body radiation. This phenomenon is called Hawking radiation. Also these objects are considered a perfect thermodynamical system, and they are subject to the thermodynamic laws [63] in a similar way to the classical one. Later, the BH thermodynamic became a large part of the research area of the BH phenomenology, [62, 64–75],...etc., and that enhanced our comprehension about this relation between quantum mechanics and gravity, and deepened our understanding about BHs, which is the aim of this thesis.

It is worth noting that, after Hawking's original derivation of BH radiation, several approaches were derived to deduce Hawking radiation. Amongst them is the quantum tunneling process with its two methods: the null geodesic method [76] and the Hamilton-Jacobi one [77]. Also, the use of anomaly mechanisms [78–80] near the event horizon provides a way to reproduce Hawking radiation. In this thesis, we will focus on the tunneling process using the null geodesic method, which was initiated by Kraus and Wilczek [81] and developed by Parikh and Wilczek [76, 82, 83]. This approach describes Hawking radiation as a quantum tunneling process within a semi-classical framework. In a variety of BH with static spherical symmetry, this technique has proven to be invaluable for studying Hawking radiation [84–98].

In the semi-classical approach, Hawking demonstrated that the pure thermal spectrum of the Schwarzschild has a temperature, which relates all fundamental constants of physics in one single formula: $T_H = \hbar c^3/(8\pi G k_B M)$. It is clearly evident that this expression has a divergent quantity in the final stage of evaporation, $M \to 0$. Thus, the final stage of Schwarzschild BH evaporation is not clear in the classical theory, and the explanation problem requires a QG theory. In this context, many theories emerged to solve this problem, which studied the effect of some QG models on BH thermodynamics in different scenarios, such as rainbow gravity (RG) [99–104], and quantum deformation effect, which predicts a minimal length (as an example, the generalized uncertainty principle (GUP), the extended uncertainty principle (EUP), etc.) [105–120] in which these models predict a minimal length and are expected to be in the order of the Planck scale, which acts as a natural cutoff to eliminate the divergence behavior. In the second scenario, there is an interest in studying the thermodynamic stability of BH in the presence of boundary conditions, where the BH is surrendered by a isothermal spherical cavity [70, 71], and in the presence of the QG effect on this BH [73, 75, 102–104, 118, 121, 122], to maintain the thermal stability, and the results look promising. In addition to previous models of QG, another model of quantizating gravity has been proposed.

In 1994, Alain Connes presented a new idea in the treatment of space geometry [123], in which he adopted the same concept as quantum mechanics concerning the commutation relations between observables (position, momentum, energy, etc.) and applied it to the spacetime coordinates, which led to the so-called NC geometry. Lately, this theory has become one of the most promising in physics to solve the problems of modern physics concerning the quantization of gravity. The application of this geometry in physics predicts a new minimal length, which is expected to be on the Planck scale. At this scale, the gravity effect is significant, which makes this theory one of the most promising to describe QG. The idea of this geometry is simple, in which the quantization of spacetime leads to quantizing gravity, and that leads to the concept of QG. The QG effects can be considered negligible in low energy limits, but they must be taken into account in the powerful gravitational field of a BH. In the beginning of this century, there has been a lot of interest in the study of the NC geometry in different fields of physics, for example, the standard model of particle physics [124–126], ST [127], quantum Hall effect [128, 129], quantum fields theory [130, 131], and even the GR [119, 132, 133],...etc., which is the aim of this thesis. Recently, there has been interest in studying the geodesic in the presence of non-commutativity [133–144], as well as their effect on the thermodynamic properties of BH and their thermal stability

[132, 145–152], and it's useful with new mechanism as the tunneling process [153–159], which show promising results in solving the issues mentionned above.

This geometry is also mainly motivated by string theory, in which non-commutativity emerges naturally between the endpoints of the open string in a B-field background with D-branes [160]. In the same paper [160], N. Seiberg and E. Witten established a gauge transformation that gives an important correspondence between the NC gauge fields and the ordinary gauge ones and is known by the SW map. The application of this map in gravity was given in [161], in which the author obtained a deformed Einstein's gravity, where that is due to gauging the NC dS $SO(4,1)$ group and contracted to the Poincaré[1] group $ISO(3,1)$, and in this theory the gravitational potentials are given by 10 gauge potentials, four deformed tetrad fields $\hat{e}^a_\mu$, and six deformed spin-connection fields $\hat{\omega}^{ab}_\mu$. Through the use of this theory together with the commutative gauge theory that we mentioned above [60], we obtained an NC gauge theory of gravity, which has shown interest among physicists [149–151, 162–166]. Our thesis will be in this context.

THESIS OUTLINE

This thesis was based on my works [167–173], which are focused on studying various aspects of BH physics in the presence of non-commutativity. We summarize some notable results of these studies. In this thesis, we obtain a deformed metric for Schwarzschild BH and RN in the context of NC gauge theory of gravity. The non-commutativity affects some geometrical properties of these BHs, shifts the singularity at a finite radius, increases the event horizon, and adds a new static limit surface. Then we investigate in detail the geodesic motion of a few types of particles in these metrics, and then we observe a new type of motion near the event horizon, which is not allowed in the commutative case. Also, the massless particles present a new stable photon sphere near the event horizon. Finally, we investigate the thermodynamic properties of NC Schwarzschild BH and their thermal stability in different scenarios, where this geometry presents a new scenario of evaporation, predicts a new fundamental length at the Planck scale, presents a solution to the information paradox, and predicts a remnant BH in the final stage of evaporation.

This thesis is organized as follows:

Chapter 1 , we provide an overview of the fundamental concepts that guided the development of the theory of GR concisely and clearly. Then we present a brief review of the gauge theory of gravity.

Chapter 2 , we provide an overview of the fundamental idea of NC geometry and its motivation in physics. In particular, we present some mathematical tools of geometry, such as the star product and the SW map for the foundation of the NC gauge theory of gravity.

Chapter 3 , we investigate the effect of non-commutativity on the geometry of some BHs metric by computing the NC correction to a general form of spherical symmetric

---

[1] In-homogeneous Lorentz group.

metric. Then, we investigate some geometrical properties of two types of BHs, which are the Schwarzschild BH and RN ones, where we present the effect of this geometry on both singularity and the event horizon.

Chapter 4 , we investigate the motion of different types of particles in the deformed spacetime in the presence of non-commutativity in a different spacetime. In particular, we are interested in two kinds of motion around the deformed BHs, which are the radial and the circular geodesic, where we present the NC correction to each one of them for different types of particles. Also, we discuss the stability of circular orbits. Finally, we examine the four classical experimental tests of GR inspired by the NC geometry to give an estimation for the lower bound on the NC parameter.

Chapter 5 , we investigate in detail the thermodynamic properties of the deformed Schwarzschild BH in the presence of non-commutativity in different scenarios. In particular, we are interested in two approaches to BH thermodynamics in the NC geometry and for different scenarios. First, we use the classical approach to investigate its thermal stability and phase transition in different cases. In the second approach, we study Hawking radiation as a quantum tunneling process of massless particles from BH in the context of NC gauge theory, in which we investigate two scenarios: thermal and non-thermal radiation. Finally, we examine some of the BH phenomenology quantities inspired by the gauge theory of non-commutativity.

In the last chapter , we present our remarks and conclusions.

1

OVERVIEW OF GENERAL RELATIVITY

In this first chapter, we provide an overview of the fundamental concepts that guided the development of the theory of GR concisely and clearly. In particular, the relationship between gravitational interaction, accelerated reference frames, and spacetime geometry will be highlighted. For further mathematical details, we refer the readers to visit some text books [1, 8, 174–179].

This chapter is organized as follows: In Sect. 1.1, we present briefly the basic ideas of the GR theory. In Sect. 1.2, we present some consequences of the Schwarzschild solution, and then we study the four classical tests of GR. In Sect. 1.3, we briefly present the main results of Hawking radiation and summarize the four laws of the BH thermodynamics. In the final Sec. 1.4, we briefly see the basis of gravity in the gauge theory.

1.1 EINSTEIN GRAVITY

In 1905, when A. Einstein published his special theory of relativity, he only dealt with the cases of inertial systems, i.e., systems in motion without acceleration, so this theory only describes some cases of physical phenomena. At that time, the question of the object's acceleration, as much as it bothered him, allowed him to discover a global theory of relativity. At the same time, this new theory allows us to treat all possible cases (whatever the state of the movement), if the theory of general relativity can write all the laws of physics, whatever the system of coordinates. This problem caused Einstein to generalize the principle of special relativity to general relativity.

1.1.1 *Generalization of the Special Relativity Principle*

To wait for a general theory of relativity and to avoid the problem of non-inertia or so-called accelerating frames. In 1907, Einstein generalized the principle of restricted relativity for all reference frames, whatever their state of motion, i.e., an accelerated reference frame compared to the inertial reference frame or a rotating reference frame [180]:

"The laws of physics are the same in all systems of reference regardless of their state of motion."

So all reference frames, whatever their state of motion, are equivalent to writing the laws of physics in the same way.

1.1.2 *The non-Euclidean geometry of spacetime*

The problem of right geodesics in Euclidean space (with a positive signature (+1,+1,+1,+1), masking the essential quality of the free system, which is subject to a law of minimum [180], to avoid it, Einstein thought of a non-Euclidean space-time to describe all the information possible on the free system to its information is contained in their geodesic:

"Any free system is animated by a geodesic movement of space-time."

where each point of this spacetime is labeled by a four-vector $x^\mu \equiv (x^0, x^1, x^2, x^3) = (ct, x, y, z)$.

Einstein used differential geometry to construct the law of geodesics, which generalized Galileo's principle:

"The geodesic equations are straight lines in spacetime (4-space) that correspond to the motion of free particles in 3-space."

$$\frac{d^2x^\mu}{d\lambda^2} + \Gamma^\mu_{\alpha\beta}\frac{dx^\alpha}{d\lambda}\frac{dx^\beta}{d\lambda} = 0 \tag{1.1}$$

where λ is the affine parameter, and the quantities $\Gamma^{\mu}_{\alpha\beta}$ are called the linear connection coefficients or Christoffel symbols of the 2nd kind, defined by:

$$\Gamma^{\mu}_{\alpha\beta} = \frac{1}{2} g^{\mu\rho} \left(\partial_{\alpha} g_{\rho\beta} + \partial_{\beta} g_{\alpha\rho} - \partial_{\rho} g_{\alpha\beta} \right) . \tag{1.2}$$

where $g_{\mu\nu}$ is the metric tensor. The problem is to determine the non-Euclidean metric $g_{\mu\nu}$ to solve the geodesic equations. To solve this problem, Einstein used Riemannian geometry to construct his famous gravitational field equation; instead, Minkowski spacetime was replaced by pseudo-Riemannian spacetime, in which the habitual notion of "distance" was replaced by the notion of the "metric" $g_{\mu\nu}$. The metric $g_{\mu\nu}$ can be defined by the invariant distance between two events, which is called the line element ds^2:

$$ds^2 = g_{\mu\nu} dx^{\mu} dx^{\nu} \tag{1.3}$$

In the flat spacetime as an example, the components of $g_{\mu\nu}$ are given by the Minkowski metric $g_{\mu\nu} = \eta_{\mu\nu} = (-1, 1, 1, 1)$, and in the curved spacetime, the metric $g_{\mu\nu}$ is a function of spacetime coordinates x^{μ} and describes all geometrical properties of spacetime.

1.1.3 *Equivalence principle*

The principle of equivalence was published by A. Einstein [176]:

> *"In a freely falling (non-rotating) laboratory occupying a small region of spacetime, the laws of physics are those of special relativity."*

Moreover, Einstein made a revolutionary proposal when he proposed the equivalence between the gravity mass and the inertial mass ($m_g = m_i$), in which locally the acceleration is equivalent to a gravitational field ($\overrightarrow{a} \equiv \overrightarrow{g}$) [180]:

> *"At least locally, a field of gravitational forces is equivalent to the inertial force field that would create the acceleration of the reference system, suitably accelerated by relation to the Galilean frames of reference."*

Einstein inspired this relation of equivalence by a thought experiment of two rockets, one motionless on earth and the other in space with accelerated motion.

1.1.4 *The stress-energy-momentum tensor*

The distribution of matter and energy in space-time can be expressed as an energy-momentum tensor; in its most simple form, it can describe a perfect fluid, or a fluid is said to be a perfect fluid if there is no transport of heat or viscosity; moreover, isotropic fluids, which are defined by an energy-momentum tensor $T^{\mu\nu}$ with the following components [176]:

T^{00}: energy density.

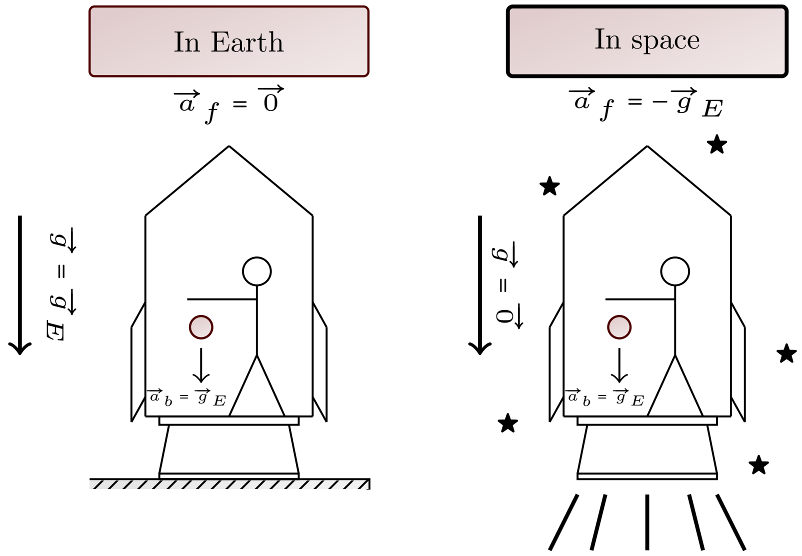

Figure 1.1: Thought experiment of two rockets (principle of equivalence).

T^{0i}: the energy flow divided by c in direction i.

T^{i0}: the momentum density multiplied by c in the direction i.

T^{ij}: the flow of the i component of the pulse in the j direction.

In a rest frame, the tensor components $T^{\mu\nu}$ of a perfect fluid[1], are a function of the energy density ρ and the pressure p with the four-vector perfect fluid velocity u^{μ}, so T is written:

$$T^{\mu\nu} = \begin{pmatrix} \rho c^2 & 0 & 0 & 0 \\ 0 & p & 0 & 0 \\ 0 & 0 & p & 0 \\ 0 & 0 & 0 & p \end{pmatrix} \tag{1.4}$$

The general case of the energy-momentum tensor in any coordinate system is given by:

$$T^{\mu\nu} = (\rho + \frac{p}{c^2})u^{\mu}u^{\nu} - pg^{\mu\nu}. \tag{1.5}$$

This tensor satisfies the following conservation equation:

$$\partial_{\mu}T^{\mu\nu} = 0 \tag{1.6}$$

1.1.5 *Einstein equation*

The famous idea of A. Einstein on the nature of space-time and its pseudo-Riemannian geometry allowed him to find the relationship between curvature and the presence of matter, at which matter can influence the geometry of space-time and likewise geometry can influence the motion of matter. This relationship revolutionized our vision of the classical

---

[1] i.e. in the absence of any dissipative transport phenomena, for example, heat, diffusion, and viscosity

theory of gravity (Newtonian gravity), which allowed him to make a relativistic description of gravitation [176]:

> *"Gravity should no longer be regarded as a force in the conventional sense but rather as a manifestation of the curvature of spacetime, this curvature being induced by the presence of matter."*

So space-time is sensitive to the presence of matter or energy. This geometry (non-Euclidean) allows the test particles that are subjected to inertial forces to be considered free test particles; on the other hand, in Euclidean geometry, the particles subjected to Newton's gravitational force are not free, and their movement is accelerated relative to the inertial reference [180]. In pseudo-Riemannian geometry, the tensor that characterizes the propriety of the curved spacetime is a tensor of rank $(1,3)$ and is the so-called Riemannian tensor $R^{\mu}_{\nu\lambda\rho}$ [181]. This tensor vanishes only in flat spacetime, as the Minkowski one, and is defined as a nonlinear combination of the Christoffel symbol $\Gamma^{\mu}_{\nu\lambda}$ and its derivative. Moreover, the general tensor that describes the geometrical properties of spacetime is defined by a linear combination of the curvature tensor and the metric and is written as follows [176]:

$$G_{\mu\nu} = R_{\mu\nu} + \frac{1}{2} g_{\mu\nu} R \tag{1.7}$$

where $G_{\mu\nu}$ is called Einstein's tensor, $R_{\mu\nu} = R^{\eta}_{\mu\eta\nu}$, and R denotes the tensor and the scalar of Ricci, respectively. The only equation that describes gravitational field dynamics is Einstein's equation in GR, in which he coupled the geometry to energy and matter by his famous equation [176]:

$$G_{\mu\nu} = \frac{8\pi G}{c^4} T_{\mu\nu} \tag{1.8}$$

where the constants G and c are Newton's gravitational constant and the speed of light constant, respectively, and $T^{\;muv}$, which describes the physical containment of matter and energy (the perfect fluid), is defined by the relation (1.5). The solution of the above equation allows us to obtain all the information on the geometry of spacetime in the metric tensor $g_{\mu\nu}$. We can clearly see that the left term of this equation writes the geometric information and tells us how spacetime is curved, while the right term writes the distribution of matter (the perfect fluid). We note that the Ricci tensor trace is proportional to the energy-momentum tensor trace[2], so we have:

$$R = -8\pi G T \tag{1.9}$$

In the vacuum case, i.e., there is no matter and no energy, $T^{\mu\nu} = 0$, so the curvature scalar is zero, $R = 0$, then Einstein's equation comes down to a simple one:

$$R_{\mu\nu} = 0 \tag{1.10}$$

To determine the metric $g_{\mu\nu}$, it is necessary to solve Einstein's equation in vacuum (1.10) or in the presence of matter (1.8) according to the case studied.

---

[2] Defined as follows: $T = g_{\mu\nu} T^{\mu\nu}$.

1.2 SCHWARZSCHILD SOLUTION

In December 1915, a few weeks after Einstein's publication of his gravitational field equation (1.8), a German astrophysicist called Karl Schwarzschild published the first free solution of Einstein's equations (1.10). This solution was called the Schwarzschild metric. Schwarzschild solution is a particular solution of Einstein's equations, since he considered the case of the gravitational field source outside[3], or he has considered a static (i.e., time-independent) metric with spherical symmetry, and the only variable is r. The Schwarzschild solution is written [1, 8, 174, 176, 179]:

$$ds^2 = -\left(1 - \frac{2GM}{c^2 r}\right) c^2 dt^2 + \left(1 - \frac{2GM}{c^2 r}\right)^{-1} dr^2 + r^2 d\Omega^2 \tag{1.11}$$

with $d\Omega^2 = r^2 d\theta^2 + r^2 sin^2\theta d\phi^2$ denoting the solid angle, M describing the mass of the gravitational field source, and G is the Newton constant. This solution describes the space-time metric around a spherical mass, and this metric can be used to study the motion of a planet around the sun. One of the uses of this metric is to find the Keplerian equations of motion in first approximation to the geodesic equation (1.1) of Schwarzschild spacetime (1.11); moreover, the Schwarzschild equations describe well the periastron advances of the planets and some secondary phenomena inaccessible to the approximate theory of Newtonian gravitation.

One of the other phenomena described by the Schwarzschild metric are BHs, where the singularity problem begins. The Schwarzschild metric is valid from infinity to the surface of the spherical object of mass M, and the vacuum equations no longer apply at the boundary of this surface. This surface is defined by a singularity of the Schwarzschild coordinates at $r_s = \frac{2GM}{c^2}$, at its radius called the Schwarzschild radius, and this surface is also called the event horizon. When a massive object of mass M and radius r contracts sufficiently so that its radius tends towards the Schwarzschild radius $r \to r_s$, this object becomes a Schwarzschild BH due to the gravitation of itself. BH will become intense, and all other nearby objects will fall on this surface (the event horizon). Nothing can escape from this surface, not even light.

1.2.1 *Classical test of general relativity*

In 1915, Albert Einstein, when he published his theory of general relativity, proposed three classical tests for his theory, which provide success to general relativity for the prediction with good accuracy to the experimental test. The first three classical tests are considered the first signs of the validity of his theory, which were the periastron advance of the Mercury orbit, the deflection of light, and the red-shift [182]. Later in 1964, the fourth classical test of general relativity was discovered and observed by I. Shapiro [183], which is so-called the time delay, and became another successful test of general relativity.

---

[3] i.e., au $T_{\mu\nu} = 0$

In which we present the first four successful classical tests of general relativity, which are based on the Schwarzschild geometry (1.11).

1.2.1.1 *Periastron Advance of Mercury*

Let us consider the motion of the Mercury planet around the Sun's as a massive particle in Schwarzschild geometry.

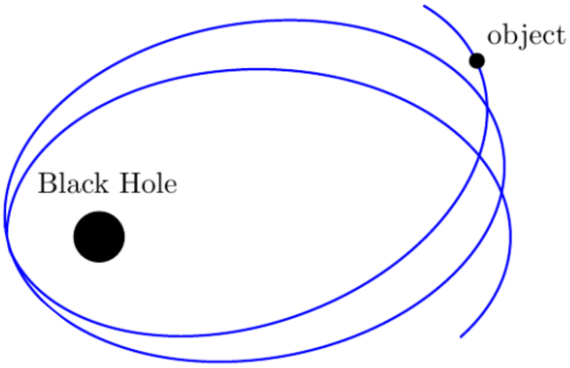

Figure 1.2: Schematic picture of periastron advance of the orbit.

The geodesic equation that describes this system can be obtained using (1.1) together with (1.2), or using the Lagrangian of the massive particle in curved spacetime. For a simple case, we would consider the motion of the test particle only in the equatorial plane $\theta = \frac{\pi}{2}$ with the initial condition $\dot{\theta} = 0$. The lagrangian in this case is given by

$$\begin{aligned} 2L &= g_{\mu\nu}\dot{x}^{\mu}\dot{x}^{\nu}, \\ &= -\left(1-\frac{2m}{r}\right)c^2\dot{t}^2 + \left(1-\frac{2m}{r}\right)^{-1}\dot{r}^2 + r^2\dot{\phi}^2. \end{aligned} \tag{1.12}$$

where the dot denotes the derivative with respect to the affine parameter, τ, along the geodesic, and $m = \frac{GM}{c^2}$. The extract of the constant of motion can be obtained using the following Euler-Lagrange equation:

$$\frac{d}{ds}\left(\frac{\partial L}{\partial \dot{x}^{\mu}}\right) - \frac{\partial L}{\partial x^{\mu}} = 0. \tag{1.13}$$

and use the fact that L is independent of t and ϕ, we obtain two conserved quantities.

$$\begin{aligned} \frac{d}{ds}\left(\frac{\partial L}{\partial \dot{t}^{\mu}}\right) &= \frac{d}{ds}\left(-\left(1-\frac{2m}{r}\right)\dot{t}\right) = 0. \\ \left(1-\frac{2m}{r}\right)\dot{t} &= cnst = E, \end{aligned} \tag{1.14}$$

and for ϕ,

$$\frac{d}{ds}\left(\frac{\partial L}{\partial \dot{\phi}^{\mu}}\right) = \frac{d}{ds}\left(r^2\dot{\phi}\right) = 0.$$

$$r^2\dot{\phi} = cnst = l, \tag{1.15}$$

where E and l are denoted, respectively, as the energy and the orbital momentum per unit mass. In a similar way, we use the Euler-Lagrange equation to obtain the second-order equation for r, but the obtained equation provides a challenge to solve; it is better to deal with the first-order one in (1.12), which is the sample to solve it. For that, using the two above conserved quantities together with (1.12) for a massive particle, we get

$$\begin{aligned}
-c^2 &= -\left(1-\frac{2m}{r}\right)c^2\dot{t}^2 + \left(1-\frac{2m}{r}\right)^{-1}\dot{r}^2 + r^2\dot{\phi}^2, \\
&= -\left(1-\frac{2m}{r}\right)c^2\left(\frac{E}{(1-\frac{2m}{r})}\right)^2 + \left(1-\frac{2m}{r}\right)^{-1}\dot{r}^2 + r^2\left(\frac{l}{r^2}\right)^2, \\
&= -\frac{c^2E^2}{(1-\frac{2m}{r})} + \left(1-\frac{2m}{r}\right)^{-1}\dot{r}^2 + \frac{l^2}{r^2},
\end{aligned} \tag{1.16}$$

rearrange our equation, we find the first-order equation for r.

$$\left(\frac{dr}{d\tau}\right)^2 = c^2E^2 - \left(1-\frac{2m}{r}\right)\left(\frac{l^2}{r^2}+c^2\right). \tag{1.17}$$

In order to obtain the orbital motion equation of the test massive particle, we need to write the above equation as a function of ϕ, and that can be done by using the conserved quantity of the angular momentum (1.15) to write $r = r(\phi)$.

$$\frac{dr}{d\tau} = \frac{dr}{d\phi}\frac{d\phi}{d\tau} = \frac{l}{r^2}\frac{dr}{d\phi}. \tag{1.18}$$

Let us define a new variable, $u = 1/r$. The above equation became

$$\frac{l}{r^2}\frac{dr}{d\phi} = -l\frac{du}{d\phi}. \tag{1.19}$$

By setting the above relation into the Eq. (1.17), we obtain

$$\left(\frac{du}{d\phi}\right)^2 = \frac{c^2(E^2-1)}{l^2} + \frac{2m}{l^2}u - u^2 + 2mu^3. \tag{1.20}$$

Writing the above equation in the second derivative form with respect to ϕ, we find

$$\frac{d^2u}{d\phi^2} = \frac{m}{l^2} - u + 3mu^2. \tag{1.21}$$

This equation is called the geodesic equation in Schwarzschild spacetime. As we see, the first two terms in the right hand of the geodesic equation correspond to the Newtonian case, and the third one, $3mu^2$, corresponds to the relativistic correction to test particle motion. The solution to this equation without the relativistic corrections, $3mu^2$,

$$u_0(\phi) = \frac{m}{l^2}(1 + e\,cos\phi) \tag{1.22}$$

where e is the eccentricity of the orbit, and this solution represents the zero-order solution to the relativistic equation (1.21). The general solution to the geodesic equation in Schwarzschild spacetime can be obtained by considering the relativistic correction term as a first-order perturbation in the Newton equation.

$$u(\phi) = u_0(\phi) + u_1(\phi) \tag{1.23}$$

where $u_1(\phi)$ is considered as a particular solution, which can be obtained by submitting the general solution (1.23) into the geodesic equation (1.21) and solving it for the first order of $u_1(\phi)$. Therefore, the general solution can be expressed as follows:

$$u(\phi) = \frac{m}{l^2}\left(1 + e\ cos\left(\phi(1 - \frac{3m^2}{l^2})\right)\right). \tag{1.24}$$

and hypothetically, the quantity $\frac{3m^2}{l^2} \ll 1$ is small. Both the solution of the Newtonian case and the Schwarzschild solution represent the elliptic orbit of a massive test particle, and the difference can be found in the orbits themselves, in which the Newton solution represents a closed orbit with a 2π period, while the Schwarzschild solution provides a non-closed orbit with a $2\pi/(1 - \frac{3m^2}{l^2})$ period, which means the period in the Schwarzschild solution is longer compared to the Newtonian case. As we mentioned above, the period in Schwarzschild spacetime is shifted from the Newtonian case by a factor of $\frac{3m^2}{l^2}$ (in the leading order of the period $2\pi/(1 - \frac{3m^2}{l^2})$). Let us now derive the deviation angle of the orbit in Schwarzschild spacetime.

$$\Delta\phi = \frac{2\pi}{1 - \frac{3m^2}{l^2}} - 2\pi \approx \frac{6\pi m^2}{l^2} \tag{1.25}$$

where angular momentum satisfied the following relation for an elliptic orbit: $l^2 = ma(1 - e^2)$. By setting this relation into the above one, we obtain the angel deviation of the planet orbiting around a massive static object (Schwarzschild spacetime) [176].

$$\Delta\phi = \frac{6\pi G\, M}{c^2\, a(1 - e^2)}. \tag{1.26}$$

As an application to the angle deviation, we use experimental data of some planet's from our solar system [184–186] and compare it to the prediction results using the above equation (1.26), which is summarized in the following table:

It is clear that the prediction results from this theory are in agreement with the observation, which has high accuracy, for the different planets in our solar system.

1.2.1.2 *Deflection of light*

The deflection of light is one of the three first successful experimental tests of general relativity, as predicted by Einstein. In this phenomenon, the light passing near a massive object is deflected from its original path (see Fig. 1.3).

Table 1.1: Comparison between the experimental observation and the theoretical prediction of GR of the angel deviation of some planet of our solar system, which are: mass of the planet (M), semi-major axis (α), eccentricity (e), orbital period (T), orbital precession in columns 2–6, respectively. The prediction of the orbital precession in general relativity in column 7

Planet	Mass	α	e	T	$\Delta\phi_{obs}$	$\Delta\phi_{GR}$
	$(10^{24}Kg)$	(AU)		$(\frac{rev}{centry})$	$(\frac{arc-sec}{centry})$	$(\frac{arc-sec}{centry})$
Mercury	$0,3301$	0.39	0.206	415.203	42.9800 ± 0.0020	42.9805
Venus	$4,8675$	0.72	0.007	162.574	8.6247 ± 0.0005	8.6283
Earth	$5,9724$	1.00	0.017	100	3.8387 ± 0.0004	3.8399
Mars	6.44171	1.52	0.093	53.175	1.3565 ± 0.0004	1.3514
Jupiter	1898.19	5.20	0.048	8.431	0.0700 ± 0.0040	0.0623
Saturn	568.34	9.54	0.056	3.396	0.0140 ± 0.0020	0.0137

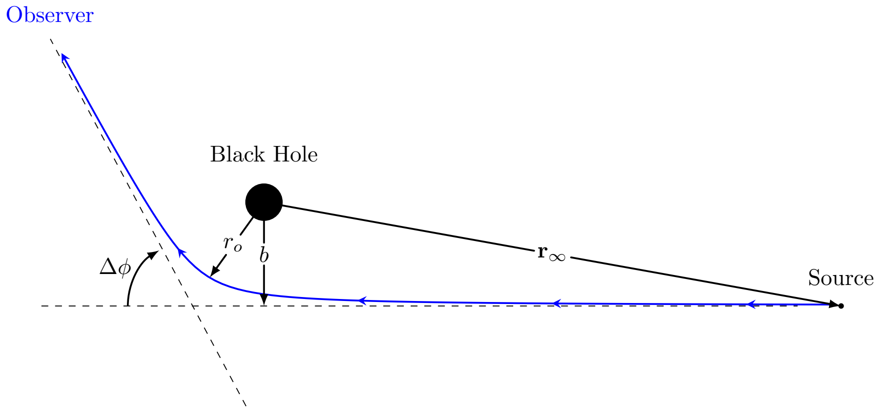

Figure 1.3: Schematic picture of light deflection by the gravitational field.

Considering now a photon approaching a compact object from infinity r_∞ (see Fig. 1.3), at this distance the spacetime is described by the Minkowski metric, and the motion of photons is expected to be a straight line passing near the massive object at distance b (called the impact parameter). However, this is not the simple case as in Minkowski spacetime; in Schwarzschild spacetime, the phat of the photon near a massive object is deflected with angle $\Delta\phi$, which is determined in a similar way as above. In the case of the photons, we use the same Lagrangian expression (1.12) with $2L = 0$, and together with the two conserved quantities (1.14)-(1.15), we obtain

$$\left(\frac{dr}{d\tau}\right)^2 = c^2E^2 - \frac{l^2}{r^2}\left(1 - \frac{2m}{r}\right). \tag{1.27}$$

Using the relation (1.18) to write the orbital equation $r(\phi)$ as a function of ϕ, we find

$$\left(\frac{dr}{d\phi}\right)^2 = \frac{r^4}{l^2}c^2E^2 - r^2\left(1 - \frac{2m}{r}\right). \tag{1.28}$$

Considering that this type of particle at a distance of r_0 from the massive object is in a circular orbit, for which $\dot{r}_0 = 0$, we can extract the energy condition of this particle from the equation (1.27).

$$E^2 = \frac{l^2}{c^2 r_0^2}\left(1 - \frac{2m}{r_0}\right). \tag{1.29}$$

substituting this relation into (1.28), with some algebra, we obtain the general solution to Eq. (1.28)

$$\phi(r) - \phi_\infty = \int_r^\infty \frac{dr}{r\left(1 - \frac{2m}{r}\right)^{1/2}} \left[\frac{r^2}{r_0^2}\frac{\left(1 - \frac{2m}{r_0}\right)}{\left(1 - \frac{2m}{r}\right)} - 1\right]^{-1/2} \tag{1.30}$$

It is practical to expand this expression in the first order on m before integrating; after some algebra, we find

$$\phi(r) - \phi_\infty = \frac{2m}{r_0} + \frac{\pi}{2} - \frac{m(r_0 + 2r)\sqrt{\frac{r_0^2}{r^2} - 1}}{r(r_0 + r)} - tan^{-1}\left(\sqrt{\frac{r_0^2}{r^2} - 1}\right) + ..., \tag{1.31}$$

The deflection angle of the light closing on the massive object can be evaluated as follows: [187]

$$\begin{aligned}\Delta\phi = 2|\phi(r_0) - \phi_\infty| - \pi &= \frac{4m}{r_0}, \\ &= \frac{4G\,M}{c^2\,r_0}.\end{aligned} \tag{1.32}$$

The above formula allows us to predict the angle of deflection of the light path close to any massive object. For example, if a light passes close to the Sun, its path is deflected by angle $\Delta\phi \approx 1.749''$, compared to the experimental results observed by Eddington in the 1919 Sun eclipse, which give two values [181]: $\Delta\phi \approx 1.98 + 0.16''$ and $\Delta\phi \approx 1.61 + 0.4''$. As we see the theoretical prediction, it's in agreement with the observation, and that is considered another success test for the GR.

1.2.1.3 *Einstein effect*

The third experimental test of GR was described for the first time by Einstein in 1907 before he published his full theory of relativity, which is known as the Einstein effect[4] or more generally, the gravitational red-shift. This phenomenon is one of the four success classical tests of GR, in which the light moving away from a gravitating field created by a massive object loses some of its energy, and this loss of energy corresponds to an increase in the wavelength λ (a decrease in frequency).

This shift in the spectral of light due to gravity can be determined using a simple example of two fixed observers, emitter r_E and receiver r_R in Schwarzschild spacetime.

---

[4] This effect is similar to the Doppler effect in flat space.

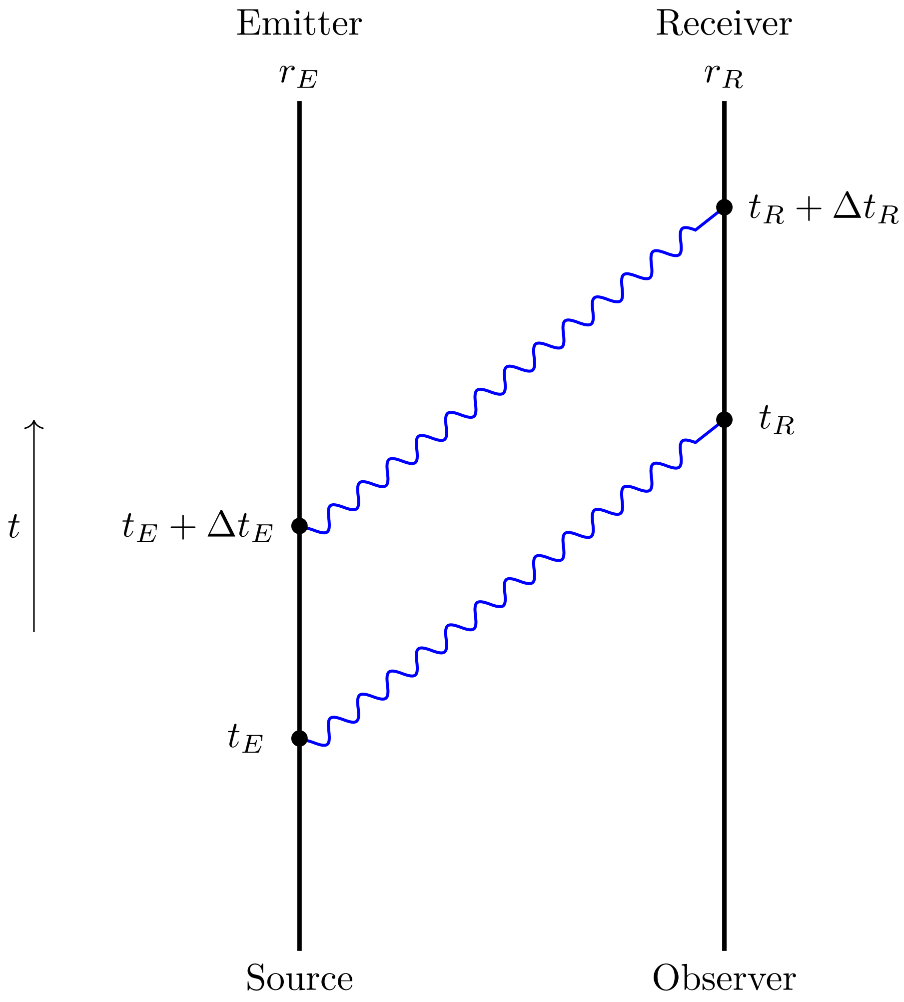

Figure 1.4: Schematic example of emitter and receiver of two signals of light.

Let us now suppose that the emitter observer r_E sends two luminous signals successively and separated by an interval of proper time $\Delta\tau_E$ measured by the observer r_E, and there are received by the observer r_R in interval $\Delta\tau_R$ (see Fig. 1.4). The traveling of the light between r_E and r_R is described by the null-geodesic, and the two luminous signals travel in the same spatial path at two different coordinate times for emission at the time t_E and $t_E + \Delta t_E$ and reception at the time t_R and $t_E + \Delta t_R$, which means the two signals take the same coordinate time to travel from r_E to r_R, and that suggests the following equality: $\Delta t_E = \Delta t_R$.

The relation between the proper time measured by the two fixed observers ($dr = d\theta = d\phi = 0$) and the coordinate time in Schwarzschild spacetime can be obtained from the metric (1.11) in the following formula:

$$ds^2 \equiv -c^2 d\tau^2 = -\left(1 - \frac{2m}{r}\right) c^2 dt^2, \tag{1.33}$$

which gives us the following two relationships:

$$\Delta t_E = \left(1 - \frac{2m}{r_E}\right)^{-1/2} \Delta\tau_E, \quad \Delta t_R = \left(1 - \frac{2m}{r_E}\right)^{-1/2} \Delta\tau_R, \tag{1.34}$$

With the equality $\Delta t_E = \Delta t_R$, we get

$$\frac{\Delta\tau_R}{\Delta\tau_E} = \sqrt{\frac{1 - \frac{2m}{r_R}}{1 - \frac{2m}{r_E}}} \tag{1.35}$$

Using the definition of the frequency $\nu = \frac{2\pi}{T}$, with $\Delta\tau$ representing the period of the signal in this case, the above expression became

$$\frac{\nu_R}{\nu_E} = \sqrt{\frac{1 - \frac{2m}{r_E}}{1 - \frac{2m}{r_R}}}, \tag{1.36}$$

According to this relationship, we can now define the red-shift expression by:

$$z = \sqrt{\frac{1 - \frac{2m}{r_R}}{1 - \frac{2m}{r_E}}} - 1. \tag{1.37}$$

1.2.1.4 *Shapiro effect*

In 1964, the fourth successful classical test of GR was discovered and observed by I. Shapiro [183]. Shapiro and the Lincoln Laboratory team made measurements of the time needed for the radar signals to travel to the inner planets and reflect back to Earth [181]. In this phenomenon, the radar signals passing near a massive object (such as the Sun) take slightly longer to travel to the inner planets (such as Venus) and longer to return to the Earth than they would if the Sun were not present, and that is known as gravitational time delay and also the Shapiro effect.

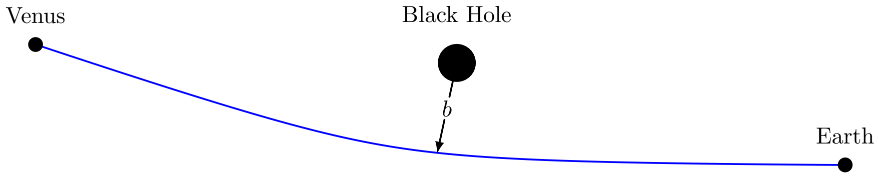

Figure 1.5: Schematic picture of the Shapiro effect.

Supposing now that a radar signal travels from the Earth $r = r_E$ to Venus $r = r_V$ passes near the sun, the geodesic equation corresponding to this system is given by (1.27). Now we want to write this equation as a function of coordinate time t, $r \equiv r(t)$.

$$\frac{dr}{d\tau} = \frac{dr}{dt}\frac{dt}{d\tau} = \frac{E}{(1 - \frac{2m}{r})}\frac{dr}{dt}. \tag{1.38}$$

substituting this into the equation (1.27), we get

$$\left(\frac{dr}{dt}\right)^2 = c^2(1-\frac{2m}{r})^2 - \frac{l^2(1-\frac{2m}{r})^3}{E^2r^2}. \tag{1.39}$$

For the closest point passing by the light near the sun, $r = r_0$; at this point, $\dot{r}_0 = 0$, so the above equation gives us

$$\frac{l^2}{E^2} = \frac{c^2r_0^2}{(1-\frac{2m}{r_0})}, \tag{1.40}$$

substituting this condition inside the Eq. (1.39), we find

$$\frac{dr}{dt} = c(1-\frac{2m}{r})\left(1-\frac{r_0^2(1-\frac{2m}{r})}{r^2(1-\frac{2m}{r_0})}\right)^{1/2}. \tag{1.41}$$

The integral to the above equation gives us the coordinate time.

$$\begin{aligned} t(r,r_0) &= \int_{r_0}^{r} \frac{1}{c(1-\frac{2m}{r'})}\left(1-\frac{r_0^2(1-\frac{2m}{r'})}{r'^2(1-\frac{2m}{r_0})}\right)^{-1/2} dr', \\ &= \frac{\sqrt{r^2-r_0^2}}{c} + \frac{2m}{c}\, ln\left(\frac{r+\sqrt{r^2-r_0^2}}{r_0}\right) + \frac{m}{c}\left(\frac{r-r_0}{r+r_0}\right)^{1/2}. \end{aligned} \tag{1.42}$$

For the example illustrated in Fig. 1.5, the necessary time for a radar signal traveling in a straight line from Earth to Venus and reflected is given by

$$\Delta t = 2\left[t(r_E,b) + t(r_V,b) - \frac{\sqrt{r_E - r_0}}{c} - \frac{\sqrt{r_V - r_0}}{c}\right] \tag{1.43}$$

If we take into consideration the distance at our solar system level (see Fig. 1.5), we have $r_E \gg r_0$ and $r_V \gg r_0$. At this limit, our above equation became

$$\Delta t \approx \frac{4GM}{c^3}\left(ln\left(\frac{4r_E\, r_V}{r_0^2}\right)+1\right), \tag{1.44}$$

The above expression describes the time delay of a radar signal passing near the Sun, in the case of the Venus planet on the opposite side of the Sun from the Earth (see Fig. 1.5). For the numerical application, we get

$$\Delta t \approx 252\mu s. \tag{1.45}$$

For more detail in the experiment (Fig. 1.5), see Refs. [179, 188].

1.3 BLACK HOLE THERMODYNAMICS AND HAWKING RADIATION

In the classical picture, a BH is a physical object with a strong gravitational field in which nothing can escape from its gravity, not even light (as we see in the above Sec. 1.2), and that led the scientists to consider that the BHs are the darkest objects in the universe. Unfortunately, that is not the case. In 1975, Stephen Hawking published the most important theoretical paper [53], in which he discovered the first mechanism that unified quantum mechanics with gravity, where he applied the techniques of quantum field theory in curved spacetime near the event horizon of BHs, and that led him to find amazing results, for which the BHs are note so dark as we expected, in a same way as the blackbody can radiate, also the BH can emit a spectrum of particles and thus evaporate, and recently this phenomenon is known as "Hawking radiation". Moreover, in the same paper, Hawking demonstrated that the BHs emit radiation with a temperature proportional to their surface gravity κ[5],

$$T_H = \frac{\kappa}{4\pi} = \frac{\hbar c^3}{8\pi G k_B M}. \tag{1.46}$$

where $\hbar$ and k_B are respectively the Planck and the Boltzmann constants. Before this discoverer, precisely in 1973 [189], Bekenstein found a connection between the event horizon area and the BH entropy $S \propto \frac{A_h}{\hbar G}$. A few years later, Hawking fixed the proportionality factor to the Bekenstein entropy, which was given by

$$S = \frac{k_B c^3 A_h}{4\hbar G} = \frac{4\pi k_B G M^2}{\hbar c}. \tag{1.47}$$

The above expression is called the Bekenstein-Hawking entropy of BH. The results found by Hawking and Bekenstein for the BHs are clearly analogous to the ordinary thermodynamics system and thus lead to the emergent of the BH mechanics. After these works [189, 190], Hawking together with Bardeen and Carter [63] formulated the version of thermodynamic laws for BHs in analogy to the laws of classical thermodynamics, which are known as "the four laws of BH mechanics".

1. ***The zeroth law:*** The horizon of a stationary BH has constant surface gravity.

2. ***The first law:*** The first law of BH thermodynamics is given by the change in BH mass.

   $$dM = T_H dS + \phi dQ + \Omega dJ. \tag{1.48}$$

   where ϕ, Q, Ω, and J are the electrostatic potential, electric charge, angular velocity, and angular momentum, respectively.

3. ***The Second Law:*** The area of any BH event horizon cannot decrease $\delta A \geqslant 0$.

4. ***The Third Law:*** It is impossible for any process to reduce the surface gravity of a BH to zero with a finite number of operations.

---

[5] For Schwarzschild BH, the surface gravity is defined as follows: $\kappa = -\frac{1}{2}\frac{\partial g_{00}}{\partial r}\mid_{r=r_h}$,

These four laws become independent tools to study the BH thermodynamics. Therefore, the thermodynamics of BH allowed us a better understanding of the connection between quantum mechanics and gravity, which was considered the first bridge to QG theory.

1.4 GAUGE THEORY OF GRAVITY

The gauge theory of gravity is a model of general relativity in which the gravitation has a dS group $SO(4,1)$ as active symmetry group [191], and the gravitational field is generated by a point-like source of mass m. This model was developed by G. Zet et al. [60, 61], based on the flat manifold, which is the Minkowski spacetime in 4-dimension with spherical coordinates.

As a first step, consider a four-dimensional Minkowski spacetime M_4, in spherical coordinates $x^\mu = (ct, r, \theta, \phi)$, which is our base manifold [60, 61]:

$$ds^2 = -dt^2 + dr^2 + r^2 \left(d\theta^2 + \sin^2\theta d\varphi^2\right). \tag{1.49}$$

The dS group $SO(4,1)$ is 10-dimensional, where in this group the infinitesimal generators are the dS "translations" and the Lorentz transformations, which are denoted respectively by Π_a and $M_{ab} = -M_{ba}$, $a, b = 0, 1, 2, 3$. In general formulation of the gauge theory for the dS group, these generators are denoted by X_A, $A = 1, 2, \ldots, 10$. Which is subject to the general form of the structure equation:

$$[X_A, X_B] = i f^C_{AB} X_C. \tag{1.50}$$

where $f^C_{AB} = -f^C_{BA}$ are the structure constants. In order to write this constant, we use the following notation for the index A:

$$A = \begin{cases} a = 0, 1, 2, 3 \\ [ab] = [01], [02], [03], [12], [13], [23]. \end{cases} \tag{1.51}$$

From this notation, we have $X_a \equiv \Pi_a$ and $X_{[ab]} \equiv M_{ab}$. The constant of the structure f^C_{AB} is given in [60, 61] by:

$$\begin{aligned} f^a_{bc} &= f^{[ab]}_{c[de]} = f^a_{[bc][de]} = 0, \\ f^{[ab]}_{cd} &= 4\lambda^2 \left(\delta^b_c \delta^a_d - \delta^a_c \delta^b_d\right) = -f^{[ab]}_{dc}, \\ f^a_{b[cd]} &= -f^a_{[cd]b} = \frac{1}{2}\left(\eta_{bc}\delta^a_d - \eta_{bd}\delta^a_c\right), \\ f^{[ef]}_{[ab][cd]} &= \frac{1}{4}\left(\eta_{bc}\delta^e_a \delta^f_d - \eta_{ac}\delta^e_b \delta^f_d + \eta_{ad}\delta^e_b \delta^f_c - \eta_{bd}\delta^e_a \delta^f_c\right) - e \longleftrightarrow f, \end{aligned} \tag{1.52}$$

where λ is a real parameter and $\eta_{ab} = diag(-1, 1, 1, 1)$ is the Minkowski metric. It is interesting to note that the contraction $\lambda \to 0$ leads to the contracts of the dS group to the Poincaré group ($ISO(3,1)$ gauge group) [60]. In the dS gauge group, gravity is described by a 10 gauge field denoted by $h^A_\mu(x)$, $A = 1, 2, \ldots, 10$, $\mu = 0, 1, 2, 3$. The strength tensor of the gauge fields of gravity is $F_{\mu\nu} = F^A_{\mu\nu} X_A$, which takes its value in the Lie algebra of the dS group. The components of this tensor are related to the gauge fields h^A_μ by the relation:

$$F^A_{\mu\nu} = \partial_\mu h^A_\nu - \partial_\nu h^A_\mu + f^A_{BC} h^B_\mu h^C_\nu. \tag{1.53}$$

Using the notation above of the index A (1.51), we can group the 10-gauge fields h^A_μ as the four tetrad fields e^a_μ if $A = a$, and the six spin connection $\omega^{ab}_\mu(x) = -\omega^{ba}_\mu(x)$, $[ab] = [01], [02], [03], [12], [13], [23]$ if $A = [ab]$. Then, the corresponding components of the strength tensor can be written in the standard form as the torsion tensor if $A = a$:

$$F^a_{\mu\nu} = \partial_\mu e^a_\nu - \partial_\nu e^a_\mu + \left(\omega^{ab}_\mu e^c_\nu - \omega^{ab}_\nu e^c_\mu\right) \eta_{bc} = T^a_{\mu\nu}, \tag{1.54}$$

and as the curvature tensor if $A = [ab]$:

$$F^{ab}_{\mu\nu} \equiv R^{ab}_{\mu\nu} = \partial_\mu \omega^{ab}_\nu - \partial_\nu \omega^{ab}_\mu + \left(\omega^{ac}_\mu \omega^{db}_\nu - \omega^{ac}_\nu \omega^{db}_\mu\right) \eta_{cd} - 4\lambda^2 \left(e^a_\mu e^b_\nu - e^b_\mu e^a_\nu\right) = R^{ab}_{\mu\nu}, \tag{1.55}$$

The integration of action associated with the gravitational gauge fields $e^a_\mu(x)$ and $\omega^{ab}_\mu(x)$ will be chosen as [60, 61]:

$$S_g = \frac{1}{16\pi G} \int d^4x\, e\, F, \tag{1.56}$$

where $e = \det(e^a_\mu)$ and

$$F = F^{ab}_{\mu\nu}\, e^\mu_a\, e^\nu_b. \tag{1.57}$$

Here, $e^\mu_a(x)$ denotes the inverse of $e^a_\mu(x)$ satisfying the usual properties:

$$e^a_\mu e^\mu_b = \delta^a_b, \qquad e^a_\mu e^\nu_a = \delta^\nu_\mu. \tag{1.58}$$

The field equations for the gravitational potentials $e^a_\mu(x)$ are obtained by imposing the variational principle $\delta_e S = 0$, with respect to $e^a_\mu(x)$, firstly we write:

$$\begin{aligned}
\delta_e(e\,F) &= \left[(\delta_e e)F + e(\delta_e F^{ab}_{\mu\nu}) e^\mu_a e^\nu_b + e F^{ab}_{\mu\nu} \delta_e (e^\mu_a e^\nu_b)\right] \\
&= \left[-e\, F e^a_\mu\, \delta e^\mu_a + e\,(\delta F^{ab}_{\mu\nu})\, e^\mu_a e^\nu_b + e\,(F^{ab}_{\mu\nu} \delta e^\mu_a\, e^\nu_b + \underset{a\leftrightarrow b, \mu\leftrightarrow\nu}{F^{ab}_{\mu\nu}\, e^\mu_a\, \delta e^\nu_b)}\right] \\
&= \left[-e\, F\, e^a_\mu\, \delta e^\mu_a + e\,(\delta F^{ab}_{\mu\nu})\, e^\mu_a e^\nu_b + 2e\, F^{ab}_{\mu\nu} \delta e^\mu_a\, e^\nu_b\right]
\end{aligned} \tag{1.59}$$

The second term in this equation vanishes with the integration, so we get:

$$\delta S_g = \frac{1}{16\pi G} \int d^4x\, e \left[-\, F\, e^a_\mu + 2\, F^{ab}_{\mu\nu}\, e^\nu_b\right] \delta e^\mu_a = 0, \tag{1.60}$$

Then we get the Einstein equation in the vacuum:

$$F^a_\mu - \frac{1}{2} F\, e^a_\mu = 0, \tag{1.61}$$

where F^a_μ is equivalent to the Ricci tensor, which is defined by:

$$F^a_\mu = F^{ab}_{\mu\nu} e^\nu_b, \tag{1.62}$$

For the other gravitational gauge potentials $\omega^{ab}_\mu(x)$ (spin connection), their field equations are equivalent to:

$$F^a_{\mu\nu} = 0. \tag{1.63}$$

We suppose that the gravitational field has spherical symmetry and is created by a point-like source of mass m in our base manifold (1.49). Where the gravitational field is described by a particular form of the spherically symmetric 10-gauge field, which is given by the following ansatz [60, 61, 192]:

$$e^0_\mu = (A, 0, 0, 0)\,, \quad e^1_\mu = \left(0, \frac{1}{A}, 0, 0\right), \quad e^2_\mu = (0, 0, r, 0)\,, \quad e^3_\mu = (0, 0, 0, r\sin\theta)\,, \tag{1.64}$$

and

$$\begin{gathered} \omega^{01}_\mu = (U, 0, 0, 0)\,, \quad \omega^{02}_\mu = \omega^{03}_\mu = 0, \quad \omega^{12}_\mu = (0, 0, A, 0)\,, \\ \omega^{13}_\mu = (0, 0, 0, A\sin\theta)\,, \quad \omega^{23}_\mu = (0, 0, 0, \cos\theta)\,, \end{gathered} \tag{1.65}$$

where A and U are functions only of the 3-dimensional radius r. Using the above expressions (1.54) and (1.55) to compute the components of the tensors $F^a_{\mu\nu}$ and $F^{ab}_{\mu\nu}$. The non-null components of these tensors are:

$$F^0_{01} = -\frac{AA' + U}{A}. \tag{1.66}$$

respectively:

$$\begin{aligned} F^{01}_{10} &= U' + 4\lambda^2, \qquad F^{02}_{20} = A\left(U + 4\lambda^2 r\right), \qquad F^{03}_{30} = A\sin\theta\left(U + 4\lambda^2 r\right), \\ F^{12}_{21} &= \frac{-AA' + 4\lambda^2 r}{A}, \qquad F^{13}_{31} = \frac{\left(-AA' + 4\lambda^2 r\right)\sin\theta}{A}, \\ F^{23}_{32} &= \left(1 - A^2 + 4\lambda^2 r^2\right)\sin\theta, \end{aligned} \tag{1.67}$$

where A' and U' denote the derivatives with respect to the variable r.

Using the definitions (1.57) and (1.62) to compute the equivalent of the Ricci scalar F and Ricci tensor F^a_μ (only the non-null components) in the dS gauge group:

$$F = -2\frac{r^2U' + 2rU - 2rAA' - A^2 + 1}{r^2} - 48\lambda^2. \tag{1.68}$$

and:

$$\begin{aligned} F^0_0 &= -\frac{A(rU' + 2U + 12\lambda^2 r)}{r}, \qquad F^2_2 = -\frac{rU - rAA' + 1 - A^2 + 12\lambda^2 r}{r}, \\ F^1_1 &= -\frac{rU' - 2AA' + 12\lambda^2 r}{rA}, \qquad F^3_3 = -\frac{rU - rAA' + 1 - A^2 + 12\lambda^2 r}{rA} sin\theta, \end{aligned} \tag{1.69}$$

Put all of these in the equation (1.61), and we obtain the following equations for the gauge fields e^a_μ:

$$\begin{aligned} \frac{2AA'}{r} - \frac{1-A^2}{r^2} - 12\lambda^2 &= 0\,, \\ U - AA' + rU' + 12\lambda^2 r &= 0\,, \\ -2AA' + rU' + 12\lambda^2 r &= 0\,. \end{aligned} \tag{1.70}$$

In the null torsion, the field equation of ω^{ab}_μ (1.54) gives us a constraint on the component U. From (1.66) we get:

$$U = -AA', \tag{1.71}$$

Use this constraint, the second and third equations in (1.70) become identical, and these systems of equations reduce to two field equations with one unknown function, $A(r)$:

$$\begin{aligned} -\frac{2AA'}{r} + \frac{1-A^2}{r^2} + 12\lambda^2 &= 0\,, \\ -\frac{2AA'}{r} - U' - 12\lambda^2 &= 0\,. \end{aligned} \tag{1.72}$$

The difference between these two equations is:

$$\frac{1-A^2}{r^2} - U' = 0\,, \tag{1.73}$$

Then, using the constraint (1.71), we can get the differential equation of the function $A^2(r)$, which can be written as:

$$r^2(A^2)'' - 2(A^2) + 2 = 0\,, \tag{1.74}$$

The solution of this equation is:

$$A^2 = 1 + \frac{\alpha}{r} + \beta\, r^2\,, \tag{1.75}$$

where α and β are constants of integration. It is well-known [8, 179] that the constant α is determined at the Newtonian limit by the mass m of the point-like source that creates the gravitational field:

$$\alpha = -2m\,. \tag{1.76}$$

The other constant β was determined by using the effect that the solution (1.75) satisfies the field equation (1.72), then we find $\beta = 4\lambda^2 = -\frac{\Lambda}{3}$, where Λ is the cosmological constant of the model [193], such that the solution finally reads:

$$A^2 = 1 - \frac{2m}{r} - \frac{\Lambda}{3}r^2, \qquad U = -\frac{m}{r^2} + \frac{\Lambda}{3}r. \tag{1.77}$$

If we consider the contraction $\lambda \to 0$, then the dS group becomes the Poincaré group, and the solution (1.77) reduces to the Schwarzschild one.

The final metric $g_{\mu\nu}$ can be obtained using the following relation:

$$g_{\mu\nu} = e^a_\mu e^b_\nu \, \eta_{ab} \,, \tag{1.78}$$

Using the relations (1.64) and (1.77), we get:

$$g_{\mu\nu} = -\left(1 - \frac{2m}{r} - \frac{\Lambda}{3} r^2\right) c^2 \, dt^2 + \left(1 - \frac{2m}{r} - \frac{\Lambda}{3} r^2\right)^{-1} dr^2 + r^2 \, d\theta^2 + r^2 \, sin\theta^2 \, d\phi^2 \,. \tag{1.79}$$

It is clear that this solution represents the dS Schwarzschild BH, and in the Poincaré group limit $\Lambda = 0$, this metric is reduced to the Schwarzschild one (1.11).

2

NON-COMMUTATIVE GAUGE THEORY OF GRAVITY

In this chapter, we provide an overview of the fundamental idea of NC geometry and its motivation in physics. In this overview, we present briefly some mathematical tools of non-commutativity, in particular the star product and the SW map for the foundation of the NC gauge theory of gravity. For more detail in this context, we refer to the readers to some Refs. [130, 160, 178, 194–196].

This chapter is organized as follows: In Sect. 2.1, we present the motivation to use non-commutativity in physics. In Sect. 2.2, we present briefly the basic idea of non-commutativity and their gauge theory by presenting the Weyl transformation, the Moyal product, and the SW map. In the final Sec. 2.3, we present the deformed gauge theory of gravity in the context of the NC resulting from solving the SW map, and then we present an application to the dS Schwarzschild BH.

2.1 MOTIVATION OF THE NON-COMMUTATIVE IN PHYSICS

In the NC geometry, we adopt the same concept as in the quantization of observables in quantum mechanics, where the position changes to the operator one $x_\mu \to \hat{x}_\mu$ and is subject to the commutation relation between the coordinates themselves, which is given by

$$[\hat{x}^\mu, \hat{x}^\nu] = i\hbar\Theta^{\mu\nu}, \tag{2.1}$$

where $\Theta^{\mu\nu} = -\Theta^{\nu\mu}$ is an anti-symmetric matrix with a positive constant parameter Θ. The NC parameter determines the fundamental cell discretization of spacetime much in a similar way as the Planck constant $\hbar$[1] discretizes the phase space, and this constant can define a minimal length. The use of this geometry is motivated by many problems in modern physics. Here we summarize some of the them:

1. **Strong magnetic field in the classical level:** In [197], the author demonstrated that, for a charged test particle e with a small mass moving in a homogeneous constant strong magnetic field B, the classical Poisson bracket between positions is different from zero and it's given by

   $$\{x^\mu, x^\nu\} = \frac{c(B^{-1})^{\mu\nu}}{e}, \tag{2.2}$$

   It is clear that the coordinates of spacetime in this physical problem do not commute in the classical Poisson bracket, which are the coordinates perpendicular to the magnetic field.

2. **Fundamental length:** For any theory of QG,a fundamental length must be predicted at the Planck scale because the effects of gravity at this scale are significant and must be taken into account [198]. As we know in the algebra of the NC spacetime, we have an uncertainty relation between the coordinates of the spacetime themselves, in a similar way to the Heisenberg uncertainty relation in quantum mechanics.

   $$\Delta\hat{x}^\mu \Delta\hat{x}^\nu \geqslant \frac{1}{2}\Theta^{\mu\nu}, \tag{2.3}$$

   and that prevents one from measuring positions with better accuracy than the Planck length.

3. **Remove the divergence:** The presence of the fundamental length and the uncertainty relation between coordinates of spacetime lead to a lower bound for any position measurement, which removes the short-distance divergences in quantum field theory, and that is due to the presence of non-commutativity.

4. **String theory:** In [160], the authors shows that, in the B-field background with D-branes, for the open string, their endpoints become non-commutative.

---

[1] In our calculation we take $\hbar = 1$.

2.2 NON-COMMUTATIVE FRAMEWORK AND GAUGE THEORY

In this section we present briefly the NC spacetime and its algebra, where we present the Weyl transformation and the star product, with the gauge theory of non-commutativity. For more detail we refer the readers to visit some references that take in detail the above points such as [130, 160, 178, 194–196].

2.2.1 *Weyl Transformation*

Let us now consider the algebra of the Schwartz functions $f(x)$ on the 4-dimensional Euclidean spacetime $\mathcal{R}^4$, in which these functions and their all-order derivatives vanish rapidly at infinity in both spaces of positions and momentum [199]. These functions admit a Fourier transform $\tilde{f}(p)$ with it's inverse transformation, given by

$$\tilde{f}(p) = \int d^4x e^{-ip_\mu x^\mu} f(x), \tag{2.4a}$$

$$f(x) = \int \frac{d^4p}{(2\pi)^4} e^{ip_\mu x^\mu} \tilde{f}(p), \tag{2.4b}$$

The Fourier transform function $\tilde{f}(p)$ is also a Schwartz function and it's subject to the same properties we mentioned above.

The Weyl operator for a function f is given by

$$\hat{\mathcal{W}}[f] = \int \frac{d^4p}{(2\pi)^4} \tilde{f}(p) e^{ip_\mu \hat{x}^\mu}, \tag{2.5}$$

It is easy to prove that the Weyl operator is hermitian $\hat{\mathcal{W}}[f]^\dagger = \hat{\mathcal{W}}[f]$ for a real function $f(x)$ [130]. The form of the quantizer operator $\Delta(\hat{x}_i, x_i)$ can be obtained by substituting the function $\tilde{f}(p)$ inside (2.5),

$$\hat{\mathcal{W}}[f] = \int d^4x f(x) \Delta(\hat{x}_i, x_i), \tag{2.6}$$

where $\Delta(\hat{x}_i, x_i)$ is given by

$$\Delta(\hat{x}, x) = \int \frac{d^4p}{(2\pi)^4} e^{ip_\mu \hat{x}^\mu} e^{-ip_\mu x^\mu}, \tag{2.7}$$

It is clear that in the commutative limit $\Theta \to 0$, the operator function $\Delta(\hat{x}, x)$ is reduced to the Dirac distribution $\delta^4(\hat{x} - x)$; injecting this inside Eq. (2.6), we can easily show that $\hat{\mathcal{W}}[f] = f(\hat{x})$, while for $\Theta \neq 0$, we must use the Baker-Campbell-Hausdorff (BCH) formula, which gives us

$$e^{ip_\mu \hat{x}^\mu} e^{ip'_\nu \hat{x}^\nu} = e^{-\frac{i}{2}\Theta^{\mu\nu} p'_\mu p_\nu} e^{i(p+p')_\mu \hat{x}^\mu}. \tag{2.8}$$

Let us now consider the non-hermitian derivative operator $\hat{\partial}_\mu$ in the non-commutative space $\mathcal{R}^4_\Theta$, which satisfies the following commutation relations:

$$\left[\hat{\partial}_\mu, \hat{x}_\nu\right] = \delta_{\mu\nu}, \quad \left[\hat{\partial}_\mu, \hat{\partial}_\nu\right] = 0. \tag{2.9}$$

By using the commutation relations above, it is easy to prove the following commutation relations:

$$\left[\hat{\partial}_\mu, \Delta(\hat{x}, x)\right] = -\partial_\mu \Delta(\hat{x}, x), \tag{2.10a}$$

$$\left[\hat{\partial}_\mu, \hat{\mathcal{W}}[f]\right] = \hat{\mathcal{W}}[\partial_\mu f]. \tag{2.10b}$$

According to the result in Eq. (2.10a), we can compute the translation transformation in spacetime for the operator $\Delta(\hat{x}, x)$. By using the unitary translation operator $e^{\alpha\hat{\partial}_\mu}$, with some algebra, we can show that

$$e^{\alpha^\mu \hat{\partial}_\mu} \Delta(\hat{x}, x) e^{-\alpha^\mu \hat{\partial}_\mu} = \Delta(\hat{x}, x - \alpha) \tag{2.11}$$

This result suggests that, for any trace on the algebra of the Weyl operator, the $Tr\Delta(\hat{x}, x)$ is independent of x, which means $Tr\Delta(\hat{x}, x) = Tr\Delta(\hat{x}, x - \alpha)$. We choose the following normalization factor: $Tr\Delta(\hat{x}, x) = 1/\sqrt{det(2\pi\Theta)}$, where in the phase space, the quantity $\sqrt{det(2\pi\Theta)}$ represents the volume of an elementary cell in the NC spacetime $\mathcal{R}^4_\Theta$. Using this fact, the trace of the Weyl operator given by Eq. (2.6) is given by the following integral:

$$\sqrt{det(2\pi\Theta)}Tr\hat{\mathcal{W}}[f] = \int d^4x f(x), \tag{2.12}$$

We use the anti-symmetric property of the NC matrix Θ to show that the operators $\Delta(\hat{x}, x)$ for any x from the commutative spacetime $\mathcal{R}^4$ form an orthogonal relation, given by

$$\sqrt{det(2\pi\Theta)}Tr\left(\Delta(\hat{x}, x)\Delta(\hat{x}, y)\right) = \delta^4(x - y), \tag{2.13}$$

By using this formula, we can easily prove the following trace,

$$\sqrt{det(2\pi\Theta)}Tr\left(\hat{\mathcal{W}}[f]\Delta(\hat{x}, x)\right) = f(x), \tag{2.14}$$

It is evident from this that the Weyl map Δ does, in fact, give a one-to-one correspondence between operators and fields.

2.2.2 *Moyal product ($*-$star product)*

In the NC spacetime, the coordinates of spacetime x_μ become operators $\hat{x}_\mu$ (by applying Weyl operator (2.5)) to satisfy the commutation relation (2.1), and that leads to the deformation in the habitual algebra of the commutative case. In this context, the ordinary product is not held in this deformed geometry; for that reason, the ordinary product is replaced by a new product, which is called the Groenewold-Moyal-Weyl product. In order to find the proper definition of the deformed product in this algebra, we use the fact that the product of the two Weyl operators $\hat{\mathcal{W}}[f]$ and $\hat{\mathcal{W}}[g]$ corresponds to the Weyl operator of the new function $\hat{\mathcal{W}}[h]$, and we need to find $h(x)$ as a function of $f(x)$ and $g(x)$. For that, we begin by defining the generalization form of the orthogonal relation given in Eq. (2.13),

$$\sqrt{det(2\pi\Theta)}Tr\left(\Delta(\hat{x},x)\Delta(\hat{x},y)\Delta(\hat{x},z)\right) = \delta^4(x-y), \tag{2.15}$$

$$\hat{\mathcal{W}}[f]\hat{\mathcal{W}}[g] = \int\int \frac{d^4p}{(2\pi)^4}\frac{d^4k}{(2\pi)^4}\tilde{f}(p)\tilde{g}(k)e^{ip_\mu\hat{x}^\mu}e^{ik_\nu\hat{x}^\nu} \tag{2.16}$$

Using the BCH formula given by Eq. (2.8), we find

$$\begin{aligned}
\hat{\mathcal{W}}[f]\hat{\mathcal{W}}[g] &= \int\int \frac{d^4p}{(2\pi)^4}\frac{d^4k}{(2\pi)^4}\tilde{f}(p)\tilde{g}(k)e^{-\frac{i}{2}\Theta^{\mu\nu}p_\mu k_\nu}e^{i(p+k)_\mu\hat{x}^\mu}, \\
&= \int\int \frac{d^4p}{(2\pi)^4}\frac{d^4k}{(2\pi)^4}\tilde{f}(p)\tilde{g}(q-p)e^{-\frac{i}{2}\Theta^{\mu\nu}p_\mu q_\nu}e^{iq_\mu\hat{x}^\mu}, \\
&= \int \frac{d^4q}{(2\pi)^4}\tilde{h}(q)e^{iq_\mu\hat{x}^\mu} = \hat{\mathcal{W}}[h],
\end{aligned} \tag{2.17}$$

where we use this change $q = p + k$ and the fact that $\Theta^{\mu\nu} = -\Theta^{\nu\mu}$ is an anti-symmetric tensor. It is clear that, in the limit of the commutative spacetime, the function $\tilde{h}(p)$ is defined by the ordinary product $\tilde{h}(p) \propto (\tilde{f}.\tilde{g})(p)$, while in the NC case this product is deformed and is replaced by a new notation called star product $\tilde{h}(p) \propto \widetilde{(f * g)}(p)$, so the Eq. (2.17) becomes [130]:

$$\hat{\mathcal{W}}[f]\hat{\mathcal{W}}[g] = \hat{\mathcal{W}}[f * g], \tag{2.18}$$

According to our previous result (2.14), we can define the function $(f * g)(x)$ by using the inverse transform of the Weyl operator to the above Eq. (2.18), is given by [196]

$$\sqrt{det(2\pi\Theta)}Tr\left(\hat{\mathcal{W}}[f * g]\Delta(\hat{x},x)\right) = (f * g)(x). \tag{2.19}$$

where the function $(f * g)(x)$ is the Fourier inverse transformation of the function $\tilde{h}(q)$ given in Eq. (2.17), which is given by [200, 201]

$$\begin{aligned}
(f * g)(x) &= f(x)e^{\frac{i}{2}\overleftarrow{\partial}_\mu\Theta^{\mu\nu}\overrightarrow{\partial}_\nu}g(x), \\
&= f(x)g(x) + \sum_{n=1}^{\infty}\left(\frac{i}{2}\right)^n\frac{1}{n!}\Theta^{\mu_1\nu_1}...\Theta^{\mu_n\nu_n}\partial_{\mu_1}...\partial_{\mu_n}f(x)\partial_{\nu_1}...\partial_{\nu_n}g(x).
\end{aligned} \tag{2.20}$$

The above expression is the Groenewold-Moyal-Weyl product or star product in the NC spacetime $\mathcal{R}^4_\Theta$, and it is clear that for $\Theta = 0$ we recover the habitual expression of the product in the commutative spacetime. Also, we can write the above expression in the second order in Θ.

$$(f * g)(x) = f(x)g(x) + \frac{i}{2}\Theta^{\mu\nu}\partial_{\mu}f(x)\partial_{\nu}g(x) - \frac{1}{8}\Theta^{\mu\nu}\Theta^{\rho\eta}\partial_{\mu}\partial_{\rho}f(x)\partial_{\nu}\partial_{\eta}g(x) + \mathcal{O}(\Theta^{3}). \tag{2.21}$$

In the remaining calculations in this thesis, we use only the second order in Θ of the star product.

2.2.3 *Seiberg-Witten map*

In one of the significant theoretical papers [160], N. Seiberg and E. Witten demonstrated that there is a gauge transformation that gives an important correspondence between the ordinary gauge fields and the NC gauge ones. This transformation is called the SW map and it's given by [160].

$$\hat{A}(A,\Theta) + \hat{\delta}_{\hat{\lambda}}\hat{A}(A,\Theta) = \hat{A}(A + \delta_{\lambda}A,\Theta), \tag{2.22}$$

where $\hat{\delta}_{\hat{\lambda}}$ and δ_{λ} denote the infinitesimal variations under the NC and commutative gauge transformation, while for the quantities $\hat{A}(A)$, $\hat{\lambda}(\lambda, A)$ are denoted respectively the NC gauge field and NC gauge parameter, while A and λ represent the commutative gauge field and the commutative gauge parameter, respectively.

$$\delta_{\lambda}A_{\mu} = \partial_{\mu}\lambda + i\left[\lambda, A_{\mu}\right] \equiv D_{\mu}\lambda, \tag{2.23a}$$

$$\hat{\delta}_{\hat{\lambda}}\hat{A}(A,\Theta) = \partial_{\mu}\hat{\lambda} + i\left[\hat{\lambda}, \hat{A}(A,\Theta)\right]_{*} \equiv \hat{D}_{\mu}\hat{\lambda}. \tag{2.23b}$$

where $*$ denotes the star product and it's given by Eq. (2.20). According to the SW map, the NC gauge field and gauge parameter are a function of the commutative ones, and that allows us to write the NC gauge fields as a power series in the NC parameter Θ.

$$\hat{\lambda} = \lambda + \lambda^{(1)} + \lambda^{(2)} + ... + \lambda^{(n)} + ..., \tag{2.24a}$$

$$\hat{A}_{\mu} = A_{\mu} + A_{\mu}^{(1)} + A_{\mu}^{(2)} + ... + A_{\mu}^{(n)} + ..., \tag{2.24b}$$

$$\hat{F}_{\mu\nu} = F_{\mu\nu} + F_{\mu\nu}^{(1)} + F_{\mu\nu}^{(2)} + ... + F_{\mu\nu}^{(n)} + ... \tag{2.24c}$$

where ($\hat{F}_{\mu\nu} = \partial_{\mu}\hat{A}_{\nu} - \partial_{\nu}\hat{A}_{\mu}$-i$\left[\hat{A}_{\mu}, \hat{A}_{\nu}\right]_{*}$) is the NC field strength of the NC gauge field $\hat{A}_{\mu}$. The first-order solution to the Eq. (2.22) for the gauge fields is given in the original paper [160] by:

$$\lambda^{(1)} = \frac{1}{4}\Theta^{kl}\left\{A_{k}, \partial_{l}\lambda\right\}, \tag{2.25a}$$

$$A_{\mu}^{(1)} = \frac{1}{4}\Theta^{kl}\left\{A_{k}, (\partial_{l}A_{\mu} + F_{l\mu})\right\}, \tag{2.25b}$$

$$F_{\mu\nu}^{(1)} = \frac{1}{4}\Theta^{kl}(2\left\{F_{\mu k}, F_{l\nu}\right\} - \left\{A_{k}, (D_{l}F_{\mu\nu} + \partial_{l}F_{\mu\nu})\right\}). \tag{2.25c}$$

It is worthy to note that the above solutions are not unique; we can add more terms of homogeneous solutions with an arbitrary coefficient. The second-order solutions are given in Ref. [194]. In order to write the second-order solution as a function of the first-order one, are given in Ref.[195]

$$\lambda^{(2)} = -\frac{1}{8}\Theta^{\mu\nu}\left(\left\{A_\mu^{(1)}, \partial_\nu\lambda\right\} + \left\{A_\mu, \partial_\nu\lambda^{(1)}\right\}\right) - \frac{i}{16}\Theta^{kl}\Theta^{\mu\nu}\left[\partial_k A_\mu, \partial_l\partial_\nu\lambda\right], \tag{2.26a}$$

$$\begin{aligned} A_\mu^{(2)} &= -\frac{1}{8}\Theta^{\rho\nu}\left(\left\{A_\rho^{(1)}, (\partial_\nu A_\mu + F_{\nu\mu})\right\} + \left\{A_\rho, (\partial_\nu A_\mu^{(1)} + F_{\nu\mu}^{(1)})\right\}\right) \\ &\quad - \frac{i}{16}\Theta^{\rho\nu}\Theta^{\alpha\beta}\left[\partial_\alpha A_\rho, \partial_\beta(\partial_\nu A_\mu + F_{\nu\mu})\right], \end{aligned} \tag{2.26b}$$

$$\begin{aligned} F_{\mu\nu}^{(2)} &= -\frac{1}{8}\Theta^{\rho\eta}\left(\left\{A_\rho, \partial_\eta F_{\mu\nu}^{(1)} + (D_\eta F_{\mu\nu})^{(1)}\right\} + \left\{A_\rho^{(1)}, (\partial_\eta F_{\mu\nu} + D_\eta F_{\mu\nu})^{(1)}\right\} - 2\left\{F_{\mu\rho}, F_{\nu\eta}^{(1)}\right\}\right. \\ &\quad \left. -2\left\{F_{\mu\rho}^{(1)}, F_{\nu\eta}\right\}\right) - \frac{i}{16}\Theta^{\rho\eta}\Theta^{\alpha\beta}\left(\left[\partial_\alpha A_\rho, \partial_\beta(\partial_\eta F_{\mu\nu} + D_\eta F_{\mu\nu})\right] - 2\left[\partial_\alpha F_{\mu\rho}, \partial_\beta F_{\nu\eta}\right]\right). \end{aligned} \tag{2.26c}$$

For a solution in high order, we refer the readers to Ref. [195].

2.3 DEFORMED GAUGE GRAVITY

As we see in the previous chapter Sec. 1.4, the gravitational gauge fields in the gauge theory of gravity are described by the tetrads e_μ^a and the spin connection $\omega_\mu^{ab} = -\omega_\mu^{ba}$ fields in the commutative dS group $SO(4,1)$, while for the NC dS gauge symmetry, the deformed gauge fields are denoted by $\hat{e}_\mu^a(x,\Theta)$ and $\hat{\omega}_\mu^{ab}(x,\Theta)$. According to the previous section, the deformed gauge field can be obtained using the commutative ones by the use of the SW map. For that, the Eq. (2.22) for the spin connection can be written as follows [161]

$$\hat{\omega}_\mu^{ab}(\omega,\Theta) + \delta_{\hat{\lambda}}\hat{\omega}_\mu^{ab}(\omega,\Theta) = \hat{\omega}_\mu^{ab}(\omega + \delta_\lambda\omega,\Theta) \tag{2.27}$$

The solution of this equation can be obtained in series of power in Θ up to the second order,

$$\hat{\omega}_\mu^{ab}(x) = \omega_\mu^{ab} + \Theta^{\nu\rho}\omega_{\mu\nu\rho}^{ab}(x) + \Theta^{\nu\rho}\Theta^{\lambda\tau}\omega_{\mu\nu\rho\lambda\tau}^{ab}(x) + \mathcal{O}(\Theta^3). \tag{2.28}$$

where the components $\omega_{\mu\nu\rho}^{ab}(x)$ and $\omega_{\mu\nu\rho\lambda\tau}^{ab}(x)$ are given by

$$\omega_{\mu\nu\rho}^{ab}(x) = \frac{1}{4}\ \{\omega_\nu,\ \partial_\rho\omega_\mu + F_{\rho\mu}\}^{ab}, \tag{2.29}$$

$$\begin{aligned} \omega_{\mu\nu\rho\lambda\tau}^{ab}(x) &= \frac{1}{32}\ \Big(-\{\omega_\lambda, \partial_\tau\{\omega_\nu, \partial_\rho\omega_\mu + F_{\rho\mu}\}\} + 2\{\omega_\lambda, \{F_{\tau\nu}, F_{\mu\rho}\}\} \\ &\quad - \{\omega_\lambda, \{\omega_\nu, D_\rho F_{\tau\mu} + \partial_\rho F_{\tau\mu}\}\} - \{\{\omega_\nu, \partial_\rho\omega_\lambda + F_{\rho\lambda}\}, (\partial_\tau\omega_\mu + F_{\tau\mu})\} \\ &\quad + 2\left[\partial_\nu\omega_\lambda, \partial_\rho\left(\partial_\tau\omega_\mu + F_{\tau\mu}\right)\right]\Big)^{ab}, \end{aligned} \tag{2.30}$$

In a similar way, the SW map for the deformed tetrad fields $\hat{e}_\mu^a(x,\Theta)$ is given by:

$$\hat{e}_\mu^a(e,\Theta) + \delta_{\hat{\lambda}}\hat{e}_\mu^a(e,\Theta) = \hat{e}_\mu^a(e + \delta_\lambda e,\Theta) \tag{2.31}$$

The solution to the above equation is obtain as a series in the power of Θ up to the second-order [161]:

$$\hat{e}^a_\mu(x,\Theta) = e^a_\mu(x) - i\Theta^{\nu\rho}e^a_{\mu\nu\rho}(x) + \Theta^{\nu\rho}\Theta^{\lambda\tau}e^a_{\mu\nu\rho\lambda\tau}(x) + \mathcal{O}(\Theta^3) \tag{2.32}$$

where:

$$\begin{aligned} e^a_{\mu\nu\rho} &= \frac{1}{4}[\omega^{ac}_\nu\partial_\rho e^d_\mu + (\partial_\rho\omega^{ac}_\mu + F^{ac}_{\rho\mu})e^d_\nu]\eta_{cd} && (2.33)\\ e^a_{\mu\nu\rho\lambda\tau} &= \frac{1}{32}\Big[2\{F_{\tau\nu},F_{\mu\rho}\}^{ab}e^c_\lambda - \omega^{ab}_\lambda(D_\rho F^{cd}_{\tau\mu} + \partial_\rho F^{cd}_{\tau\mu})e^m_\nu\eta_{dm} \\ &\quad -\{\omega_\nu,(D_\rho F_{\tau\nu} + \partial_\rho F_{\tau\nu})\}^{ab}e^c_\lambda - \partial_\tau\{\omega_\nu,(\partial_\rho\omega_\mu + F_{\rho\mu})\}^{ab}e^c_\lambda \\ &\quad -\omega^{ab}_\lambda\left(\omega^{cd}_\nu\partial_\rho e^m_\mu + \left(\partial_\rho\omega^{cd}_\mu + F^{cd}_{\rho\mu}\right)e^m_\nu\right)\eta_{dm} + 2\partial_\nu\omega^{ab}_\lambda\partial_\rho\partial_\tau e^c_\lambda \\ &\quad -2\partial_\rho\left(\partial_\tau\omega^{ab}_\mu + F^{ab}_{\tau\mu}\right)\partial_\nu e^c_\lambda - \{\omega_\nu,(\partial_\rho\omega_\lambda + F_{\rho\lambda})\}^{ab}\partial_\tau e^c_\mu \\ &\quad -\left(\partial_\tau\omega_\mu + F_{\tau\mu}\right)\left(\omega^{cd}_\nu\partial_\rho e^m_\lambda + \left((\partial_\rho\omega_\lambda + F_{\rho\lambda})\right)e^m_\nu\right)\eta_{dm}\Big]\eta_{cb} && (2.34) \end{aligned}$$

and

$$\{\alpha,\beta\}^{ab} = \left(\alpha^{ac}\beta^{db} + \beta^{ac}\alpha^{db}\right)\eta_{cd}, \quad [\alpha,\beta]^{ab} = \left(\alpha^{ac}\beta^{db} - \beta^{ac}\alpha^{db}\right)\eta_{cd} \tag{2.35}$$

$$D_\mu F^{ab}_{\rho\sigma} = \partial_\mu F^{ab}_{\rho\sigma} + \left(\omega^{ac}_\mu F^{db}_{\rho\sigma} + \omega^{bc}_\mu F^{da}_{\rho\sigma}\right)\eta_{cd} \tag{2.36}$$

The complex conjugate $\hat{e}^{a\dagger}_\mu(x,\Theta)$ of the deformed tetrad fields is obtained from the hermitian conjugate of the relation (2.32):

$$\hat{e}^{a\dagger}_\mu(x,\Theta) = e^a_\mu(x) + i\Theta^{\nu\rho}e^a_{\mu\nu\rho}(x) + \Theta^{\nu\rho}\Theta^{\lambda\tau}e^a_{\mu\nu\rho\lambda\tau}(x) + \mathcal{O}(\Theta^3) \tag{2.37}$$

Where the $*$-inverse of $\hat{e}^a_\mu$ is denoted by $\hat{e}^\mu_a$:

$$\hat{e}^\mu_a(x,\Theta) = e^\mu_a(x) - i\Theta^{\nu\rho}e^\mu_{a\nu\rho}(x) + \Theta^{\nu\rho}\Theta^{\lambda\tau}e^\mu_{a\nu\rho\lambda\tau}(x) + \mathcal{O}(\Theta^3) \tag{2.38}$$

Where $e^\mu_{a\nu\rho}$ and $e^\mu_{a\nu\rho\lambda\tau}$ can be computed using ($\hat{e}^\mu_a * \hat{e}^a_\mu = \delta^b_a$):

$$\begin{aligned} e^\mu_{a\nu\rho} &= -e^\alpha_a\, e^b_{\alpha\nu\rho}\, e^\mu_b + \frac{1}{2}\partial_\nu e^\alpha_a\partial_\rho e^b_\alpha\, e^\mu_b, && (2.39)\\ e^\mu_{a\nu\rho\lambda\tau} &= -e^\alpha_a\, e^b_{\alpha\nu\rho\lambda\tau}\, e^\mu_b + -e^a_{\alpha\nu\rho}\, e^b_{\alpha\lambda\tau}\, e^\mu_b + \frac{1}{4}\partial_\nu\partial_\lambda e^\alpha_a\,\partial_\nu\partial_\lambda e^b_\alpha\, e^\mu_b \\ &\quad -\frac{1}{2}(\partial_\nu e^\alpha_a\,\partial_\rho e^b_{\alpha\lambda\tau}\, e^\mu_b + \partial_\nu e^\alpha_{a\lambda\tau}\,\partial_\rho e^b_\alpha\, e^\mu_b) && (2.40) \end{aligned}$$

The NC Riemann tensor can also be expanded in powers of Θ:

$$\hat{F}^{ab}_{\mu\nu} = F^{ab}_{\mu\nu} + i\Theta^{\rho\tau}F^{ab}_{\mu\nu\rho\tau} + \Theta^{\rho\tau}\Theta^{\kappa\sigma}F^{ab}_{\mu\nu\rho\tau\kappa\sigma} + O(\Theta^3)\,, \tag{2.41}$$

where

$$F^{ab}_{\mu\nu\rho\tau} = \partial_\mu\omega^{ab}_{\nu\rho\tau} + (\omega^{ac}_\mu\omega^{db}_{\nu\rho\tau} + \omega^{ac}_{\mu\rho\tau} + \omega^{db}_\nu - \frac{1}{2}\partial_\rho\omega^{ac}_\mu\partial_\tau\omega^{db}_\nu)\eta_{cd} - (\mu \leftrightarrow \nu) \tag{2.42}$$

and

$$F^{ab}_{\mu\nu\rho\tau\kappa\sigma} = \partial_\mu \omega^{ab}_{\nu\rho\tau\kappa\sigma} + (\omega^{ac}_{\mu}\omega^{db}_{\nu\rho\tau\kappa\sigma} + \omega^{ac}_{\mu\rho\tau\kappa\sigma} + \omega^{db}_{\nu} - \omega^{ac}_{\mu\rho\tau}\omega^{db}_{\nu\kappa\sigma} - \frac{1}{4}\partial_\rho\partial_\kappa\omega^{ac}_{\mu}\partial_\tau\partial_\sigma\omega^{db}_{\nu})\eta_{cd}$$
$$- (\mu \leftrightarrow \nu)\,, \tag{2.43}$$

where $\omega^{ab}_{\mu\nu\rho}$ and $\omega^{ab}_{\mu\nu\rho\lambda\tau}$ are given by (2.30) and (2.30)

Now we can compute the NC scalar curvature $\hat{F}$ using the NC curvature tensor $\hat{F}^{ab}_{\mu\nu}$ and the deformed tetrad fields $\hat{e}^{a}_{\mu}$, which are given by:

$$\hat{F} = \hat{e}^{\mu}_{a} * \hat{F}^{ab}_{\mu\nu} * \hat{e}^{\nu}_{b}, \tag{2.44}$$

The general expression of the scalar curvature, expanded in power of Θ, is:

$$\hat{F} = F + \Theta^{\rho\tau}\Theta^{\kappa\sigma}(e^{\mu}_{a}F^{ab}_{\mu\nu\rho\tau\kappa\sigma}e^{\nu}_{b} + e^{\mu}_{a\rho\tau\kappa\sigma}F^{ab}_{\mu\nu}e^{\nu}_{b} + e^{\mu}_{a}F^{ab}_{\mu\nu}e^{\nu}_{b\rho\tau\kappa\sigma} - e^{\mu}_{a\rho\tau}F^{ab}_{\mu\nu}e^{\nu}_{b\kappa\sigma}$$
$$- e^{\mu}_{a\rho\tau}F^{ab}_{\mu\nu\kappa\sigma}e^{\nu}_{b} - e^{\mu}_{a}F^{ab}_{\mu\nu\rho\tau}e^{\nu}_{b\kappa\sigma}) + O(\Theta^4)\,. \tag{2.45}$$

where F is a commutative scalar curvature and the components $e^{\mu}_{b\kappa\sigma}$, $e^{\mu}_{b\rho\tau\kappa\sigma}$, $F^{ab}_{\mu\nu\rho\tau}$ and $F^{ab}_{\mu\nu\rho\tau\kappa\sigma}$ are given by (2.39), (2.40), (2.42) and (2.43), respectively.

2.3.1 *Application to the Schwarzschild black hole*

The deformed Schwarzschild dS metric can be determined using the same ansatz (1.64) and (1.65). Firstly, we need to obtain the corresponding components of the deformed tetrad fields $\hat{e}^{a}_{\mu}(x,\Theta)$ and their complex conjugated $\hat{e}^{a\,+}_{\mu}(x,\Theta)$ given by the Eqs. (2.33) and (2.37). Taking only space-space noncommutativity, $\Theta_{0i} = 0$ (due to the known problem of unitarity), we choose the coordinate system so that the parameters $\Theta^{\mu\nu}$ are given as:

$$\Theta^{\mu\nu} = \begin{pmatrix} 0 & 0 & 0 & 0 \\ 0 & 0 & \Theta & 0 \\ 0 & -\Theta & 0 & 0 \\ 0 & 0 & 0 & 0 \end{pmatrix}, \quad \mu,\nu = 0,1,2,3. \tag{2.46}$$

The non-zero components of the tetrad fields $\hat{e}^{a}_{\mu}(x,\Theta)$ are:

$$\begin{aligned}
\hat{e}^{1}_{1} &= \frac{1}{A} + \frac{A''}{8}\Theta^2 + O(\Theta^3), \\
\hat{e}^{1}_{2} &= -\frac{i}{4}\left(A + 2\,r\,A'\right)\,\Theta + O(\Theta^3), \\
\hat{e}^{2}_{2} &= r + \frac{1}{32}\left(7A\,A' + 12\,r\,A'^2 + 12\,r\,A\,A''\right)\,\Theta^2 + O(\Theta^3), \\
\hat{e}^{3}_{3} &= r\sin\theta - \frac{i}{4}(\cos\theta)\,\Theta + \frac{1}{8}\left(2r\,A'^2 + rAA'' + 2AA' - \frac{A'}{A}\right)(\sin\theta)\,\Theta^2 + O(\Theta^3), \\
\hat{e}^{0}_{0} &= A + \frac{1}{8}\left(2\,r\,A'^3 + 5\,r\,A\,A'\,A'' + r\,A^2\,A''' + 2\,A\,A'^2 + A^2\,A''\right)\,\Theta^2 + O(\Theta^3)\,,
\end{aligned} \tag{2.47}$$

where A', A'', A''' are the first, second, and third derivatives of $A(r)$,with respect to r coordinate, with A^2 given in (1.77).

In the NC spacetime, the ordinary relation of the metric (1.78) is written by the formula given in Ref. [162].

$$\hat{g}_{\mu\nu}(x,\Theta) = \frac{1}{2}\left[\hat{e}^{a}_{\mu} * \hat{e}^{b\dagger}_{\nu} + \hat{e}^{a}_{\nu} * \hat{e}^{b\dagger}_{\mu}\right]\eta_{ab} \tag{2.48}$$

Then,we use this new definition, (2.48), to obtain the following: non-null components of the real deformed metric $\hat{g}_{\mu\nu}\,(x,\Theta)$ up to the second order:

$$\begin{aligned} \hat{g}_{00}\,(x,\Theta) &= -\frac{1}{4}\left(2\,r\,A\,A'^{3} + r\,A^{3}\,A''' + A^{3}\,A'' + 2\,A^{2}\,A'^{2} + 5\,r\,A^{2}\,A'\,A''\right)\Theta^{2} \\ &\quad - A^{2} + O(\Theta^{4}), \qquad (2.49a) \\ \hat{g}_{11}\,(x,\Theta) &= \frac{1}{A^{2}} + \frac{1}{4}\,\frac{A''}{A}\,\Theta^{2} + O(\Theta^{4}), \qquad (2.49b) \\ \hat{g}_{22}\,(x,\Theta) &= r^{2} + \frac{1}{16}\left(A^{2} + 11\,r\,A\,A' + 16\,r^{2}\,A'^{2} + 12\,r^{2}A\,A''\right)\Theta^{2} + O(\Theta^{4}), \qquad (2.49c) \\ \hat{g}_{33}\,(x,\Theta) &= +\frac{1}{16}\left[4\left(2\,r\,A\,A' - r\frac{A'}{A} + r^{2}\,A\,A'' + 2\,r^{2}\,A'^{2}\right)\sin^{2}\,\theta + \cos^{2}\theta + 4\right]\Theta^{2} \\ &\quad + r^{2}\,\sin^{2}\,\theta + O(\Theta^{4}). \qquad (2.49d) \end{aligned}$$

For $\Theta \to 0$, we obtain the commutative type-Schwarzschild metric solution with .

It is worth to note that, the expressions for the NC corrections to the deformed tetrad fields and NC metric elements are the same as the ones obtained in [149, 150, 162] except for the element $\hat{g}_{33}$, where we found a new term $(\frac{1}{4}\Theta^{2})$.

Now, if we insert $A^{2} = 1 - \frac{2m}{r}$ into eqs. (2.49a)-(2.49d), we obtain the deformed Schwarzschild metric with corrections up to the second-order in Θ. The non-zero metric components are:

$$\begin{aligned} \hat{g}_{00} &= -\left(1 - \frac{2m}{r}\right) - \left(\frac{m(4r - 11m)}{4r^{4}}\right)\Theta^{2}\,. \qquad (2.50a) \\ \hat{g}_{11} &= \left(1 - \frac{2m}{r}\right)^{-1} + \left(\frac{m^{2}(2r - 3m)}{4r^{2}(2m - r)^{2}}\right)\Theta^{2}\,, \qquad (2.50b) \\ \hat{g}_{22} &= r^{2} + \left(\frac{34m^{2} - 17mr + r^{2}}{16r(r - 2m)}\right)\Theta^{2}\,, \qquad (2.50c) \\ \hat{g}_{33} &= r^{2}\sin^{2}\,\theta + \left(\frac{\cos^{2}\theta(-4m^{2} + 2mr + r^{2}) + 4(m^{2} - 3mr + r^{2})}{16r(r - 2m)}\right)\Theta^{2}\,. \qquad (2.50d) \end{aligned}$$

This deformed Schwarzschild metric was obtained for the first time in Ref. [162] (except the $\hat{g}_{33}$), and in the limit $\Theta \to 0$, the commutative solution is recovered (1.11).

3

GEOMETRICAL PROPERTIES OF BLACK HOLES IN NON-COMMUTATIVE GAUGE THEORY

In this present chapter, we investigate the effect of non-commutativity in the geometry of some BHs metric by computing the NC correction to a general form of spherical symmetric metric by using the SW maps and star product between the tetrad field. In this study, we investigate some geometrical properties of two types of BHs in the presence of this geometry, which are the Schwarzschild BH [167] and the RN one, where we present the effect of this geometry on both singularity and the event horizon.

This chapter is organized as follows: In Sect. 3.1, we present a NC correction to a general form of a spherical symmetric metric using a SW maps and star product between a non-diagonal form of tetrad fields. In Sect. 3.2, we present the deformed metric of Schwarzschild in the context of the NC gauge theory of gravity. Then we discussed some geometrical properties of NC Schwarzschild BH and their formation by the collapsing matter in this geometry. In final Sects. 3.3, we show the new consequence of the non-commutativity on the geometrical properties of the NC RN BH.

3.1 NC STATIONARY BLACK HOLE IN GAUGE THEORY OF GRAVITY

In the last section of the previous chapter, we see the construction of the NC metric in gauge theory using a Schwarzschild type metric with a diagonal ansatz of tetrad field (1.64). However, in this chapter, we construct a more general form of the NC metric in which we use a non-diagonal tetrad field, a general type of static metric, and spherical symmetry. For that, we take the following metric:

$$ds^2 = -A^2(r)dt^2 + B^2(r)dr^2 + r^2(d\theta^2 + \sin^2\theta d\phi^2) \tag{3.1}$$

where $A(r)$ and $B(r)$ are functions related only to the radius r, and for the tetrad fields we choose a general form of non-diagonal, which satisfied the relation (1.78), and is written as follows:

$$e^a_\mu = \begin{bmatrix} A(r) & 0 & 0 & 0 \\ 0 & B(r)\sin\theta\cos\phi & r\cos\theta\cos\phi & -r\sin\theta\sin\phi \\ 0 & B(r)\sin\theta\sin\phi & r\cos\theta\sin\phi & r\sin\theta\cos\phi \\ 0 & B(r)\cos\theta & -r\sin\theta & 0 \end{bmatrix} \tag{3.2}$$

We note that this form of tetrad field can be used for a stationary observer at spatial infinity [137].

The non-zero component of the spin connection for these tetrad fields is given by (see Appendix. A):

$$\begin{aligned}
\omega^{01}_{\mu} &= \left(\frac{A'(r)}{B(r)}\sin\theta\cos\phi, 0, 0, 0\right), \omega^{02}_{\mu} = \left(\frac{A'(r)}{B(r)}\sin\theta\sin\phi, 0, 0, 0\right),\\
\omega^{03}_{\mu} &= \left(\frac{A'(r)}{B(r)}\cos\theta, 0, 0, 0\right), \omega^{12}_{\mu} = \left(0, 0, 0, [1-\frac{1}{B(r)}]\sin^2\theta\right),\\
\omega^{13}_{\mu} &= \left(0, 0, -[1-\frac{1}{B(r)}]\cos\phi, [1-\frac{1}{B(r)}]\sin\theta\cos\theta\sin\phi\right),\\
\omega^{23}_{\mu} &= \left(0, 0, -[1-\frac{1}{B(r)}]\sin\phi, -[1-\frac{1}{B(r)}]\sin\theta\cos\theta\cos\phi\right). \qquad (3.3)
\end{aligned}$$

Using the relations (1.55) in the limit of $\lambda \to 0$, to compute the non-null components of the curvature tensor $F^{ab}_{\mu\nu}$ (see Appendix. A):

$$\begin{aligned}
F^{01}_{01} &= -\left[\frac{A''(r)}{B(r)} - \frac{A'(r)B'(r)}{B^2(r)}\right]\sin\theta\cos\phi, \quad F^{01}_{02} = -\frac{A'(r)}{B^2(r)}\cos\theta\cos\phi,\\
F^{01}_{03} &= \frac{A'(r)}{B^2(r)}\sin\theta\sin\phi, \quad F^{02}_{01} = -\left[\frac{A''(r)}{B(r)} - \frac{A'(r)B'(r)}{B^2(r)}\right]\sin\theta\sin\phi,\\
F^{02}_{02} &= -\frac{A'(r)}{B^2(r)}\cos\theta\sin\phi, \quad F^{02}_{03} = -\frac{A'(r)}{B^2(r)}\sin\theta\cos\phi, \quad F^{03}_{02} = \frac{A'(r)}{B^2(r)}\sin\theta,\\
F^{03}_{01} &= -\left[\frac{A''(r)}{B(r)} - \frac{A'(r)B'(r)}{B^2(r)}\right]\cos\theta, \quad F^{12}_{23} = \left[1 - \frac{1}{B^2(r)}\right]\sin\theta\cos\theta,\\
F^{12}_{13} &= \frac{B'(r)}{B^2(r)}\sin^2\theta, \quad F^{13}_{12} = -\frac{B'(r)}{B^2(r)}\cos\phi, \quad F^{13}_{13} = \frac{B'(r)}{B^2(r)}\sin\theta\cos\theta\sin\phi,\\
F^{13}_{23} &= -\left[1 - \frac{1}{B^2(r)}\right]\sin^2\theta\sin\phi, \quad F^{23}_{13} = -\frac{B'(r)}{B^2(r)}\sin\theta\cos\theta\cos\phi,\\
F^{23}_{12} &= -\frac{B'(r)}{B^2(r)}\sin\phi, \quad F^{23}_{23} = \left[1 - \frac{1}{B^2(r)}\right]\sin^2\theta\cos\phi. \qquad (3.4)
\end{aligned}$$

where $A'(r)$, $B'(r)$, and $A''(r)$ denote the derivatives of first- and second-order with respect to the r-coordinate.

In this case, we took only space-space non-commutativity, $\Theta_{0i} = 0$, and the best choice of metric for the NC parameter $\Theta^{\mu\nu}$ in this case is $r - \phi$ and $r - \theta$:

$$\Theta^{\mu\nu} = \begin{pmatrix} 0 & 0 & 0 & 0 \\ 0 & 0 & a & b \\ 0 & -a & 0 & 0 \\ 0 & -b & 0 & 0 \end{pmatrix}, \qquad \mu, \nu = 0, 1, 2, 3 \qquad (3.5)$$

where $a = b = \Theta$ for a sample case of the same deformation in all directions, and this notation a, b is useful if we duel with special cases as $r - \theta$ ($a = \Theta$, $b = 0$), $r - \phi$ ($a = 0$, $b = \Theta$), or for the general case $r - \theta$, $r - \phi$. The non-null components of the deformed gauge fields $\hat{e}^a_\mu$ can be written in the second-order on the NC parameter as follows (see Appendix. A):

$$\begin{aligned}
\hat{e}^0_0 = A(r) &+ \frac{(a^2+b^2\sin^2\theta)}{32B^4(r)}\{16rA'(r)B'^2(r)-4B(r)(4rB'(r)A''(r)+A'(r)(2B'(r)\\
&+rB''(r)))+B^3(r)(A'(r)B'(r)+4A''(r))+B^2(r)(-3A'(r)B'(r)+4(A''(r)\\
&+rA'''(r)))\}+\mathcal{O}(a^3,b^3,ab^2,a^2b)\,,
\end{aligned}\tag{3.6a}$$

$$\begin{aligned}
\hat{e}^1_1 = B(r)\sin\theta\cos\phi &+ \frac{iB'(r)}{4}(b\sin\theta\sin\phi-a\cos\theta\cos\phi)+\frac{b^2\sin\theta}{64B^3(r)}\{8(2B'(r)\\
&-B(r)B''(r))\sin^2\theta+B^3(r)B''(r)(3+\cos2\theta)+B(r)(B'^2(r)-B(r)B''(r))(1+3\\
&\times\cos2\theta)\}\cos\phi+\frac{a^2\sin\theta}{32B^3(r)}\{(8-B(r))B'^2(r)+B(r)B''(r)(-4+B(r)\ +B^2(r))\}\\
&\times\cos\phi+\frac{ab\cos\theta}{8B^2(r)}\{B'^2(r)+B(r)B''(r)(-1+B(r))\}\sin\phi+\mathcal{O}(a^3,b^3,ab^2,a^2b)\,,
\end{aligned}\tag{3.6b}$$

$$\begin{aligned}
\hat{e}^2_1 = B(r)\sin\theta\sin\phi &- \frac{iB'(r)}{4}(a\cos\theta\sin\phi+b\sin\theta\cos\phi)+\frac{a^2\sin\theta}{32B^3(r)}\{(B(r)-8)\\
&\times B'(r)^2+(B(r)^2+B(r)-4)B(r)B''(r)\}\sin\phi+\frac{b^2\sin\theta}{64B(r)^3}\{(B(r)(1+3cos2\theta)\\
&+16\sin^2\theta)B'(r)^2+B(r)B''(r)(B(r)^2(3+cos2\theta)-B(r)(1+3cos2\theta)-8\sin^2\theta)\}\\
&\times\sin\phi+\frac{ab\cos\theta}{8B(r)^3}\{B(r)^2B''(r)-B(r)B'(r)-B(r)^3B''(r)\}\cos\phi\\
&+\mathcal{O}(a^3,b^3,ab^2,a^2b)\,,
\end{aligned}\tag{3.6c}$$

$$\begin{aligned}
\hat{e}^3_1 = B(r)\cos\theta &+ \frac{B'(r)\sin\theta}{4}a+\frac{a^2\cos\theta}{32B(r)^3}\{(8-B(r))B'(r)^2+B(r)B''(r)(-4+(B(r)\\
&+1)B(r))\}-\frac{b^2\sin^2\theta}{32B(r)^3}\{B'(r)^2(-8+3B(r))+B(r)B''(r)(4-3B(r)+B(r)^2)\}\\
&\times\cos\theta+\mathcal{O}(a^3,b^3,ab^2,a^2b)\,,
\end{aligned}\tag{3.6d}$$

$$\begin{aligned}
\hat{e}^1_2 = r\cos\theta\cos\phi &- \frac{ib}{4}[B(r)-1]\cos\theta\sin\phi+\frac{ia}{4B(r)^2}\left[B(r)^2-B(r)+2rB'(r)\right]\sin\theta\\
&\times\cos\phi+\frac{a^2\cos\theta}{32B(r)^4}\{2B(r)^3B'(r)+36rB'(r)^2+B(r)^2(3B'(r)+8rB''(r))-(7B'(r)\\
&+16rB'(r)^2+12rB''(r))B(r)\}\cos\phi-\frac{ab\sin\theta}{32B(r)^4}\{B(r)^3B'(r)+20rB'(r)^2+8rB(r)^2\\
&\times B''(r)+B(r)(B'(r)-16rB'(r)^2-8rB''(r))\}\sin\phi+\frac{b^2\cos\theta}{32B(r)^4}\Big\{B(r)^4B'(r)(-3\\
&+cos2\theta)-\frac{B(r)^3}{2}B'(r)(-9+5cos2\theta)+\sin^2\theta\,\big[16rB'(r)^2-B(r)^2(B'(r)-4rB''(r))\\
&-4B(r)(2B'(r)+2rB'(r)^2+rB''(r))\big]\Big\}\cos\phi+\mathcal{O}(a^3,b^3,ab^2,a^2b)\,,
\end{aligned}\tag{3.6e}$$

$$\begin{aligned}
\hat{e}^2_2 = r\cos\theta\sin\phi &- \frac{ib\cos\theta}{4}[B(r)-1]\cos\phi+\frac{ia\sin\theta}{4B(r)^2}\left[B(r)^2-B(r)+2rB'(r)\right]\sin\phi\\
&+\frac{a^2\cos\theta}{32B(r)^4}\{2B(r)^3B'(r)+36rB'(r)^2+B(r)^2(3B'(r)+8rB''(r))-B(r)(7B'(r)\\
&+16rB'(r)^2+12rB''(r))\}\sin\phi+\frac{ab\sin\theta}{32B(r)^4}\{B(r)^3B'(r)+20rB'(r)^2+8rB(r)^2B''(r)
\end{aligned}$$

$$
\begin{aligned}
&+B(r)(B'(r)-16rB'(r)^2-8rB''(r))\big\}\cos\phi+\frac{b^2\cos\theta}{32B(r)^4}\Big\{B(r)^4B'(r)(-3+cos2\theta)-\frac{1}{2}\\
&\times B(r)^3B'(r)(-9+5cos2\theta)+\sin^2\theta\left[16rB'(r)^2-B(r)^2(B'(r)-4rB''(r))-4(2B'(r)\right.\\
&\left.+2rB'(r)^2+rB''(r))B(r)\right]\big\}\sin\phi+\mathcal{O}(a^3,b^3,ab^2,a^2b)\,, \qquad (3.6f)
\end{aligned}
$$

$$
\begin{aligned}
\hat{e}^3_2 &= -r\sin\theta+\frac{ia\cos\theta}{4B(r)^2}(2rB'(r)+B(r)^2-B(r))-\frac{a^2\sin\theta}{32B^4(r)}\big\{2B(r)^3B'(r)+36rB'(r)^2\\
&+B(r)^2(3B'(r)+8rB''(r))-B(r)(7B'(r)+16rB'(r)^2+12rB''(r))\big\}+\frac{b^2\sin\theta}{64B(r)^4}\big\{B'(r)\\
&\times B(r)^3(-1+5\cos 2\theta)-16rB(r)B'(r)^2\cos^2\theta+\sin^2\theta\Big[16B(r)B'(r)+4B(r)^4B'(r)\\
&-32rB'(r)^2+8rB(r)B''(r)\Big]+B(r)^2((5-\cos 2\theta)B'(r)+8rB''(r)\cos^2\theta)\big\}\\
&+\mathcal{O}(a^3,b^3,ab^2,a^2b)\,, \qquad (3.6g)
\end{aligned}
$$

$$
\begin{aligned}
\hat{e}^1_3 &= -r\sin\theta\sin\phi-\frac{ia}{4}(-1+B(r))\cos\theta-\frac{ib\sin\theta\cos\phi}{4B(r)^2}\big\{B(r)^3\cos^2\theta-B(r)^2+(B(r)\\
&-2rB'(r))\sin^2\theta\big\}\sin\phi+\frac{a^2\sin\theta}{32B^4(r)}\big\{B(r)^2B'(r)(3-5B(r)+4B(r)^2)-16rB'(r)^2\\
&+4B(r)(2B'(r)+rB''(r))\big\}\sin\phi-\frac{ab\cos\theta}{32B(r)^4}\Big\{B'(r)(4B(r)^4\cos 2\theta-\frac{1}{2}B(r)^3(-11\\
&+19\cos 2\theta))-\sin^2\theta\left[18B(r)^2B'(r)+20rB'(r)^2+B(r)(B'(r)-8rB''(r))\right]\big\}\cos\phi\\
&+\frac{b^2\sin\theta}{32B(r)^4}\Big\{-2B(r)^3B'(r)+2B(r)^4B'(r)\cos^2\theta+\sin^2\theta\left[-37rB'(r)-B(r)^2(3B'(r)\right.\\
&\left.+8rB''(r))+B(r)(7B'(r)+16rB'(r)^2+12rB''(r))\right]\big\}\sin\phi+\mathcal{O}(a^3,b^3,ab^2,a^2b)\,, \qquad (3.6h)
\end{aligned}
$$

$$
\begin{aligned}
\hat{e}^2_3 &= r\sin\theta\cos\phi+\frac{ia}{4}(-1+B(r))\cos\theta\cos\phi-\frac{ib\sin\theta}{4B(r)^2}\big\{-B(r)^2+B(r)^3\cos^2\theta+(B(r)\\
&-2rB'(r))\sin^2\theta\big\}\sin\phi-\frac{a^2\sin\theta}{32B^4(r)}\big\{B(r)^2B'(r)(3-5B(r)+4B(r)^2)-16rB'(r)^2\\
&+4B(r)(2B'(r)+rB''(r))\big\}\cos\phi-\frac{ab\cos\theta}{32B(r)^4}\Big\{B'(r)(4B(r)^4\cos 2\theta-\frac{1}{2}B(r)^3(-11\\
&+19\cos 2\theta))-\sin^2\theta\left[18B(r)^2B'(r)+20rB'(r)^2+B(r)(B'(r)-8rB''(r))\right]\big\}\sin\phi\\
&+\frac{b^2\sin\theta}{32B(r)^4}\Big\{-2B(r)^3B'(r)+2B(r)^4B'(r)\cos^2\theta+\sin^2\theta\left[-37rB'(r)-B(r)^2(3B'(r)\right.\\
&\left.+8rB''(r))+B(r)(7B'(r)+16rB'(r)^2+12rB''(r))\right]\big\}\cos\phi+\mathcal{O}(a^3,b^3,ab^2,a^2b)\,, \qquad (3.6i)
\end{aligned}
$$

$$
\begin{aligned}
\hat{e}^3_3 &= \frac{ib\sin^2\theta\cos\theta}{4B(r)^2}\left[(-B(r)+B(r)^3+2rB'(r))\right]+\frac{ab\sin\theta}{64B(r)^4}\big\{\sin^2\theta\left[-2B(r)B'(r)\right.\\
&\left.-40rB'(r)^2+16rB(r)B''(r)\right]+B(r)\left[18B(r)B'(r)-19B(r)^2B'(r)+8B(r)^3B'(r)\right]\\
&\times\cos 2\theta+B(r)(6B(r)B'(r)-13B(r)^2B'(r)+32rB'(r)^2-16rB(r)B''(r))\big\}\\
&+\mathcal{O}(a^3,b^3,ab^2,a^2b)\,. \qquad (3.6j)
\end{aligned}
$$

In the commutative limit $a=b=0$, we recover the commutative tetrad fields given by eq. (3.2)

By using the definition (2.48), we obtain the non-zero components of the NC metric $\hat{g}_{\mu\nu}$ up to the second-order in Θ (see Annex. A).

$$\begin{aligned}
-\hat{g}_{00} = {}& A^2(r) + \frac{A(r)}{16B(r)^4}\Big\{16rA'(r)B'^2(r) + B^3(r)(A'(r)B'(r) + 4A''(r)) - 4B(r)(4rB'(r)A''(r) \\
& + A'(r)(2B'(r) + B''(r))) + B^2(r)(-3A'(r)B'(r) + 4(A''(r) + rA'''(r)))\Big\}\,(a^2 + b^2\sin^2(\theta)) \\
& + \mathcal{O}(a^4, b^4, a^2b^2, ..),
\end{aligned} \tag{3.7a}$$

$$\begin{aligned}
\hat{g}_{11} = {}& B^2(r) + \frac{(a^2 + b^2\sin^2(\theta))}{16B^2(r)}\Big\{8B'^2(r) + 9B^3(r)B''(r) + B^2(r)(9B'^2(r) + B''(r)) - B(r)(B'^2(r) \\
& + 4B''(r))\Big\} + \mathcal{O}(a^4, b^4, a^2b^2, ..),
\end{aligned} \tag{3.7b}$$

$$\begin{aligned}
\hat{g}_{12} = {}& -\frac{\sin(2\theta)b^2}{32B^2(r)}\Big\{6B^3(r)B'(r) + 3rB'^2(r) - B(r)(B'(r) + rB''(r)) - B^2(r)(11B'(r) + 5rB''(r))\Big\} \\
& + \mathcal{O}(a^4, b^4, a^2b^2, ..)\,,
\end{aligned} \tag{3.7c}$$

$$\begin{aligned}
\hat{g}_{22} = {}& r^2 + \frac{b^2}{32B^4(r)}\Big\{9B^4(r) + (2B^6(r) - 12B^5(r))cos^2\theta + 9B^4(r)cos2\theta + rB^3(r)B'(r)(5 - cos2\theta) \\
& - 4rB^4(r)B'(r)(2 + cos2\theta) + \Big[-6rB^2(r)B'(r) + 32r^2B'^2(r) - 8rB(r)(2B'(r) + rB''(r))\Big]\sin^2\theta\Big\} \\
& + \frac{a^2}{16B^4(r)}\Big\{9B^4(r) + 40r^2B'^2(r) + 2B^3(r)(-3 + rB'(r)) - rB(r)(11B'(r) + 32rB'^2(r) \\
& + 12rB''(r)) + B^2(r)(1 + 27rB'(r) + 16r^2B''(r))\Big\} + \mathcal{O}(a^4, b^4, a^2b^2, ..)\,,
\end{aligned} \tag{3.7d}$$

$$\begin{aligned}
\hat{g}_{33} = {}& r^2\sin^2(\theta) + \frac{a^2}{32B^4(r)}\Big\{2B^6(r)cos^2\theta + 2B^5(r)(-3 + cos2\theta) + B^4(r)(9 + cos2\theta - 8rB'(r)) \\
& + \Big[10rB^3(r)B'(r) - 6rB^2(r)B'(r) + 32r^2B'^2(r) - 8rB(r)(2B'(r) + rB''(r))\Big]\sin^2\theta\Big\} \\
& + \frac{b^2\sin^2\theta}{16B^4(r)}\Big\{9B^4(r) + 2rB^3(r)B'(r) + (B^6(r) - 6B^5(r) - 6rB^4(r))cos^2\theta + \sin^2\theta\Big[40r^2B'^2(r) \\
& - 6B^3(r) + rB(r)(11B'(r) + 32rB'^2(r) + 12rB''(r)) + B^2(r)(1 + 27rB'(r) + 16r^2B''(r))\Big]\Big\} \\
& + \mathcal{O}(a^4, b^4, a^2b^2, ..)\,.
\end{aligned} \tag{3.7e}$$

It is clearly that, in the commutative limit when $a = b = 0$, we recover the usual metric (3.1), and for the case $a = \Theta$, $b = 0$ or in the equatorial plane $\theta = \frac{\pi}{2}$ we can obtain a diagonal form of the NC metric. As we see above, the NC metric has a non-diagonal form, and its line element is written as follows:

$$d\hat{s}^2 = -\hat{g}_{00}dt^2 + \hat{g}_{11}dr^2 + 2\hat{g}_{12}drd\theta + \hat{g}_{22}d\theta^2 + \hat{g}_{33}d\phi^2\,. \tag{3.8}$$

Note that the NC spacetime metric (3.8) is static but not spherically symmetric due to the presence of the cross product term $drd\theta$, compared to the commutative metric (3.1), which is static and spherically symmetric. Moreover, that is due to the presence of a coupling between r and θ induced by non-commutativity in the plane of rotation, which disappears when the non-commutativity goes to zero ($a = b = 0$).

In our choice of NC tensor $\Theta^{\mu\nu}$, the rotational invariance is broken but the translational invariance remains; for more detail, see Ref. [202]. The broken rotational invariance occurs in the (r, θ) plane in spherical coordinates. Thus, the metric is non-diagonal in the presence of non-commutativity, leading to only one non-zero off-diagonal term, $\hat{g}_{12}$. We note that we have chosen non-commutativity between just a couple of two coordinates $r-\theta$ and $r-\phi$, while for the case between the angle coordinates $\theta-\phi$ provide a problem in the dimension in NC parameter, which is different from the previous cases, and this problem can be solved by using a normalization constant to keep a homogeneous dimension of Θ in all possibility.

3.2 NON-COMMUTATIVE SCHWARZSCHILD BLACK HOLE

The deformed Schwarzschild BH can be obtained by inserting the Schwarzschild potential, $A(r) = B^{-1}(r) = \left(1-\frac{2m}{r}\right)^{\frac{1}{2}}$, into the above components of the deformed metric $\hat{g}_{\mu\nu}$, and that gives us

$$-\hat{g}_{00} = \left(1-\frac{2m}{r}\right) + \left\{\frac{m\left(88m^2+mr\left(-77+15\sqrt{1-\frac{2m}{r}}\right)-8r^2\left(-2+\sqrt{1-\frac{2m}{r}}\right)\right)}{16r^4(-2m+r)}\right\}(a^2$$

$$+ b^2\sin^2(\theta)) + \mathcal{O}(a^3,b^3,ab^2a^2b), \tag{3.9a}$$

$$\hat{g}_{11} = \left(1-\frac{2m}{r}\right)^{-1} + \left\{\frac{m\left(12m^2+mr\left(-14+\sqrt{1-\frac{2m}{r}}\right)-r^2\left(5+\sqrt{1-\frac{2m}{r}}\right)\right)}{8r^2(r-2m)^3}\right\}(a^2$$

$$+ b^2\sin^2(\theta)) + \mathcal{O}(a^3,b^3,ab^2a^2b), \tag{3.9b}$$

$$\hat{g}_{12} = -b^2\left\{\frac{m\left(-4m^2+r^2\left(\sqrt{1-\frac{2m}{r}}-7\right)+mr\left(16-17\sqrt{1-\frac{2m}{r}}\right)\right)}{32r(2m-r)^3}\right\}\sin(2\theta)$$

$$+ \mathcal{O}(a^3,b^3,ab^2a^2b), \tag{3.9c}$$

$$\hat{g}_{22} = r^2 + \left\{\frac{m^2r\left(50-6\sqrt{1-\frac{2m}{r}}\right)+mr^2\left(-43+23\sqrt{1-\frac{2m}{r}}\right)+2r^3\left(5-3\sqrt{1-\frac{2m}{r}}\right)}{32r(r-2m)^2}\right.$$

$$+\frac{-8m^3+\cos 2\theta\left[8m^3+6m^2r\left(5+\sqrt{1-\frac{2m}{r}}\right)+mr^2\left(-37+13\sqrt{1-\frac{2m}{r}}\right)+2r^3\,(5\right.}{32r(r-2m)^2}$$

$$\left.+\frac{\left.-3\sqrt{1-\frac{2m}{r}}\right)\right]}{32r(r-2m)^2}\right\}b^2 - \left\{\frac{68m^3+18m^r\left(-6+\sqrt{1-\frac{2m}{r}}\right)+mr^2\left(57-29\sqrt{1-\frac{2m}{r}}\right)}{16r(r-2m)^2}\right.$$

$$\left.+\frac{2r^3\left(-5+3\sqrt{1-\frac{2m}{r}}\right)}{16r(r-2m)^2}\right\}a^2 + \mathcal{O}(a^3,b^3,ab^2a^2b) \tag{3.9d}$$

$$\hat{g}_{33} = r^2\sin^2\theta + \left\{\frac{-8m^3+m^2r\left(50-6\sqrt{1-\frac{2m}{r}}\right)+mr^2\left(-43+23\sqrt{1-\frac{2m}{r}}\right)+2r^3\,(5}{32r(r-2m)^2}\right.$$

$$\begin{aligned}
&+\frac{-3\sqrt{1-\frac{2m}{r}}\Big)+(r-2m)\left[4m^2+3mr\left(-1+\sqrt{1-\frac{2m}{r}}\right)-2r^2\left(\sqrt{1-\frac{2m}{r}}\right)\right]\cos 2\theta}{32r(r-2m)^2}\Bigg\}a^2\\
&+\Bigg\{\frac{2m^2r\left(74-9\sqrt{1-\frac{2m}{r}}\right)-68m^3+mr^2\left(-97+47\sqrt{1-\frac{2m}{r}}\right)+4r^3\left(5-3\sqrt{1-\frac{2m}{r}}\right)}{32r(r-2m)^2}\\
&+\frac{\left[2m^2r\left(-34+9\sqrt{1-\frac{2m}{r}}\right)+68m^3+mr^2\left(17-11\sqrt{1-\frac{2m}{r}}\right)\right]\cos 2\theta}{32r(r-2m)^2}\Bigg\}b^2\sin^2\theta\\
&+\mathcal{O}(a^3,b^3,ab^2a^2b)
\end{aligned}\tag{3.9e}$$

It is clear that all components of the non-zero NC metric $\hat{g}_{\mu\nu}$ acquire a singularity at $r = 2m$ in the NC correction terms, as well as in the component $\hat{g}_{00}$, where that is in contrast to that given in Ref. [162], because it is a consequence of using a general form of the tetrad field (3.2). As we motioned above, the commutative Schwarzschild metric can be obtained by setting $a = b = 0$, and the diagonal form can be obtained in different ways, for $a = \Theta$, $b = 0$, or in the equatorial plane $\theta = \pi/2$ for the two cases $a = b = \Theta$ and $a = 0$, $b = \Theta$.

3.2.1 *Singularity and event horizon*

As we know, the Schwarzschild BH is apparently two types of singularity, which are the coordinate singularity at $r \equiv r_h = 2m$ (called the event horizon of Schwarzschild BH) and the physical one at $r = 0$, where this one is the only true singularity. In which follow, we analyze these two singularities in the NC framework.

The physical singularity occurs when the NC line element (3.8) goes to infinity at this point $r = r^{NC}_{singularity}$, and that can be due to the analysis of the profile of $\hat{g}_{00}$.

As we see in Fig. 3.1, new behavior of $\hat{g}_{\mu\nu}$ are shown in this theory. Whereas now the non-commutativity of spacetime shifted the singularity of the Schwarzschild BH at $r = 0$ to the finite radius $r^{NC}_{singularity} = 2m$. This result is not available in the diagonal form of the tetrad in the NC gauge theory, as Refs. [149, 162], or in the other additional theory of non-commutativity, see Refs. [138, 139, 203–205]. However, this result is similar to one obtained in the quantum-corrected BH theory as Refs. [206–208], but is observed just in a particular case for $\alpha = r_h = 2m$, where a represents a minimal distance expected to be on the order of the Planck length, l_p. This result is not a natural one because we need to fix the parameter, a, for a particular value in order to observe the same result as in Fig. 3.1. Contrary to our case, in which the singularity of origin is shifted naturally from the quantum structure of spacetime itself, when we impose the NC property of the geometry on spacetime without the need to impose any particular value on the NC parameter, Θ. Then, we conclude that the NC geometry spreads the singularity at the origin of the Schwarzschild BH over a two-dimensional sphere of the Schwarzschild radius $r^{NC}_{singularity} = 2m$ as in the quantum-corrected BH and increases the radius of the event horizon.

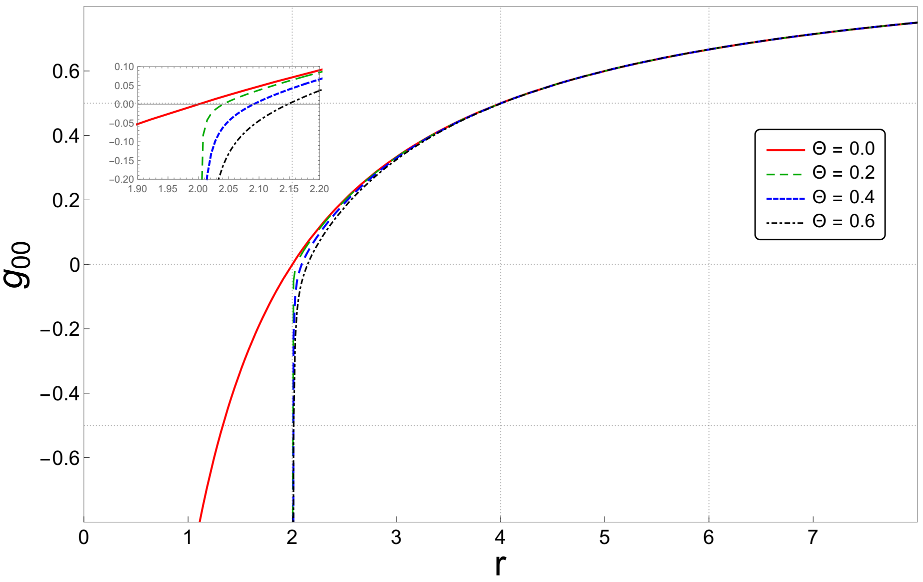

Figure 3.1: Behavior of the NC component $\hat{g}_{00}$ for a stationary observer at spatial infinity in the equatorial plane $\theta = \pi/2$ as a function of r, for different values of Θ.

To investigate the event horizon in the NC spacetime, we cheek the killing vectors in this geometry, where we have two killing vectors in the NC spacetime, which are respectively the time translation and the azimuthal killing vectors, because our deformed line element (3.8) is independent of t and φ. Then we obtain two surfaces in the NC spacetime (3.8): a static limit surface and event horizons. Firstly, the static limit surface is obtained by solving $\hat{g}_{00} = 0$, for which we find

$$r_{sls}^{\mathrm{NC}} = r_h \left[1 + \left(\frac{4\sqrt{5}+1}{32\sqrt{5}} \right) \frac{\sqrt{a^2 + b^2 \sin^2\theta}}{r_h} + \left(\frac{10+\sqrt{5}}{128} \right) \frac{(a^2 + b^2 sin^2\theta)}{r_h^2} \right], \tag{3.10}$$

The spacetime (3.8) has a coordinate singularity at $\frac{1}{\hat{g}_{11}(r_h^{NC})} = 0$, which corresponds to the NC event horizon.

$$r_h^{NC} = r_h \left[1 + \frac{3}{8} \left(\frac{(a^2 + b^2 \sin^2\theta)}{r_h^2} \right) \right]. \tag{3.11}$$

The NC event horizon has three parameters: r_h, Θ (a, b are related to Θ), and the observation angle θ, while in the commutative spacetime there is only one parameter m. The limit surface and event horizon obtained in the NC case are in the general case and can be defined in four scenarios of geometry. For each value of a and b, we have a particular choice of NC matrix (3.5). The dependence between the event horizon and the observational angle is a natural result related to the deformation of the spherical symmetry of the BH, and that is due to the rotation created by non-commutativity in coordinate space. The radius of the event horizon increases with Θ as well as with the angle θ, and when θ takes the value $\pi/2$, we find the upper bound of the radius of the event horizon. However, when θ takes the values 0 or π, we find the lower bound of the event horizon (this observation is available for cases 3 and 4; see Fig. 3.2). The dependence of the NC event horizon on the observational angle is limited only to the condition of $b \neq 0$, and that corresponds to the choice of $r - \phi$ in the NC matrix (see case 3 in Fig. 3.2). This confirms that the NC parameter Θ plays the role of angular momentum induced by the rotation of the BH due to the non-commutativity of coordinates.

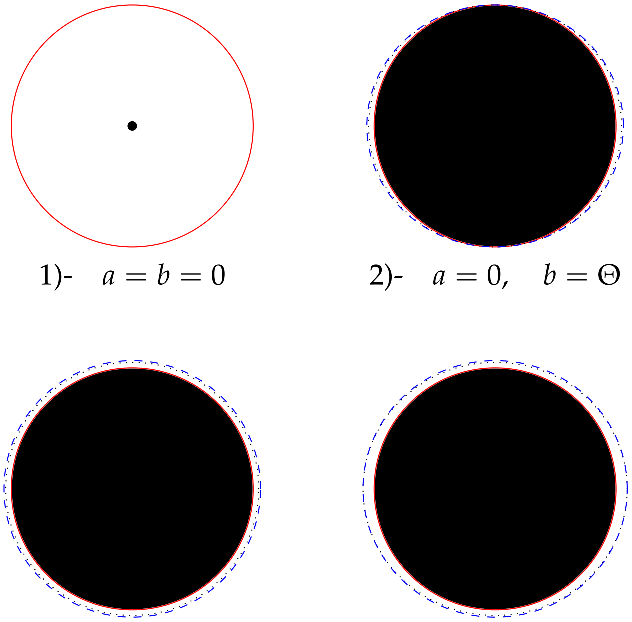

1)- $a = b = 0$ 2)- $a = 0, \quad b = \Theta$

3)- $a = \Theta, \quad b = 0$ 4)- $a = b = \Theta$

Figure 3.2: A schematic picture of Schwarzschild BH in the NC spacetime. The red solid line represents the commutative Schwarzschild event horizon, the black dotted line represents the NC event horizon, and the blue dashed line represents the static limit surface. With $\Theta = 0.75$, the black disk represents the singularity.

3.2.2 *Collapse of matter*

In astrophysics, the BHs are considered the most mysterious celestial objects; unfortunately, these objects can't be observed directly, and only their gravitational effects can be observed, such as the gravitational wave [2], the motion of stars around the galactic center [4–7, 209, 210], etc. However, raising the curtain on the process of the formation of these objects leads us to better understand the physics of BHs. The gravitational collapse of matter is the most popular mechanism to produce a BH, which is considered the final stage of a star's life.

Stars are considered huge nuclear reactors in the universe, like, for example, the sun in our solar system. These objects can survive their own gravity because of the pressure created by their nuclear reaction. This pressure is generated by the energy created by the nuclear fusion inside the star, in which the light nuclei, such as hydrogen, are burned into heavy ones, such as helium atoms. When it consumes all its hydrogen fuel, it begins to use the heavy nuclei as energy, which leads to a decrease in the emission energy that generates the pressure, and the star begins to cool and collapse under its proper gravity. At this point, the star has three scenarios for collapse depending on its own mass, and it is resumed as follow [176]

- $M < 1.4 M_\odot$: The star with this mass collapse to a stable white dwarf.

- $1.4M_{\odot} \leqslant M < 3M_{\odot}$: The white dwarf is unstable[1] in this range of mass and continue collapsing to form a stable neutron star.
- $M \geqslant \; 3M_{\odot}$: The neutron star is unstable[2] in this range of mass and continue collapsing to form a BH.

In this section, we are only interested in the third scenario, concerning the formation of BH. Moreover, the Schwarzschild BH is formed when a star with spherical symmetry and a mass of $M = 3M_{\odot}$ is collapsing under its own strong gravitational fields. In this scenario, this mass is collapsing into one single point, $r = 0$, and this point is called a singularity of Schwarzschild BH. This BH now is defined by its trapped surface (event horizon) and the singularity $r_s = 0$, and that is in the commutative case, as we see in the left panel of Fig. 3.3.

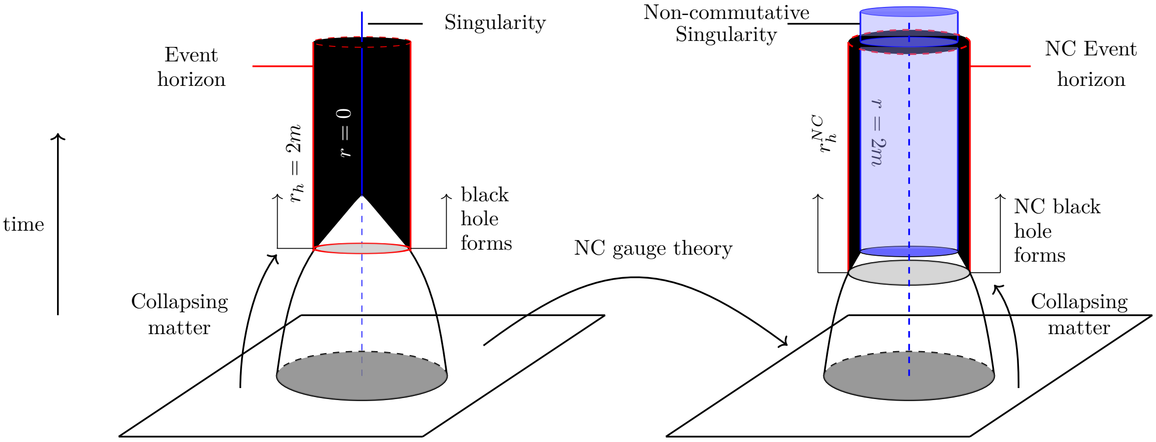

Figure 3.3: A schematic picture of the gravitational collapsing matter in the NC spacetime and the formation of NC Schwarzschild BH.

As we see, when the mass of a star collapsing to a radius $r_h = 2m$ under its own gravity (with respect to the condition on its mass), we obtain an BH and continue to collapse until collapsing into a zero radius $r = 0$ (see Fig. 3.3). At this point, we have a Schwarzschild BH in the commutative spacetime. Unfortunately, this is not the case in the presence of non-commutativity. In this geometry, when a star with a mass of M^{NC}[3], it collapsing to a size of r_h^{NC} (representing the NC event horizon given by Eq. (3.11)), at this moment a NC Schwarzschild BH is formed. Also, the matter continues collapsing to a new singularity at a radius of $r^{NC}_{singularity} = 2m$. In this case, the non-commutativity prevents the star from collapsing mass into a point $r = 0$, in which the singularity is shifted to a two-dimensional sphere with a radius of $r^{NC}_{singularity} = 2m$, and that is represented in the right panel of Fig. 3.3 and Fig. 3.4.

---

[1] The limit $M = 1.4M_{\odot}$ is called the Chandrasekhar limit.

[2] This $M = 3M_{\odot}$ called the Oppenheimer-Volkoff limit.

[3] This mass is the limit mass of the Oppenheimer-Volkoff limit to obtain an acsBH after collapsing matter, in the presence of non-commutativity

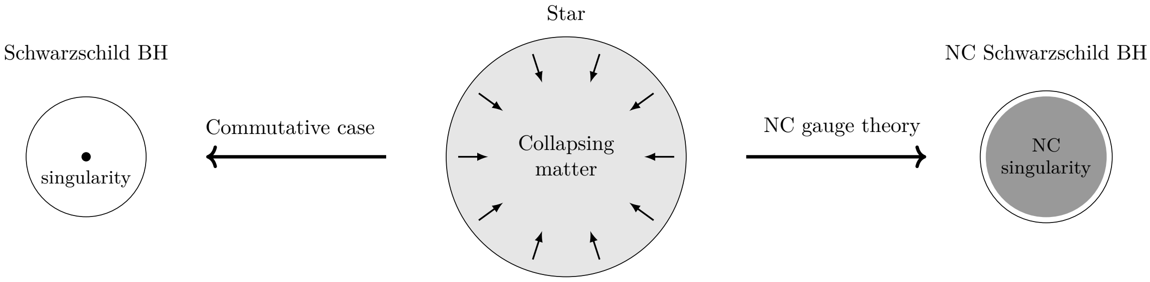

Figure 3.4: A schematic picture for the collapsing matter of a star in the NC spacetime and the formation of Schwarzschild BH.

3.3 NON-COMMUTATIVE REISSNER–NORDSTRÖM BLACK HOLE

In this case, the deformed Reissner-Nordström (RN) BH is obtained by inserting the RN potential $A(r) = \left(1 - \frac{2m}{r} + \frac{Q^2}{r^2}\right)^{\frac{1}{2}}$, into the deformed metric in Sec. 3.1,

$$
\begin{aligned}
-\hat{g}_{00} = {} & \left(1 - \frac{2m}{r} + \frac{Q^2}{r^2}\right) + \Bigg\{ \frac{2Q^2r^2\left(-15m\left(-7+\sqrt{1-\frac{2m}{r}+\frac{Q^2}{r^2}}\right) - 56Q^6 - 284Q^2r^2m^2\right)}{32r^6(Q^2-2mr+r^2)} \\
& + \frac{mr^3\left(88m^2 - 8r^2\left(-2+\sqrt{1-\frac{2m}{r}+\frac{Q^2}{r^2}}\right) + mr\left(-77+15\sqrt{1-\frac{2m}{r}+\frac{Q^2}{r^2}}\right)\right)}{32r^6(Q^2-2mr+r^2)} \\
& + \frac{12Q^2r^4\left(-3+\sqrt{1-\frac{2m}{r}+\frac{Q^2}{r^2}}\right)}{32r^6(Q^2-2mr+r^2)} \Bigg\} (a^2 + b^2\sin^2\theta) + \mathcal{O}(a^3, b^3, ab^2a^2b)
\end{aligned}
\tag{3.12a}
$$

$$
\begin{aligned}
\hat{g}_{11} = {} & \left(1 - \frac{2m}{r} + \frac{Q^2}{r^2}\right)^{-1} + \Bigg\{ \frac{(Q^2-mr)^2\left(8Q^2 - r\left(16m + r\left(-17+\sqrt{1-\frac{2m}{r}+\frac{Q^2}{r^2}}\right)\right)\right)}{16r^2(Q^2-2mr+r^2)^3} \\
& + \frac{r\left(-m^2r - 3Q^2r + 2m\left(Q^2+r^2\right)\right)\left(-4Q^2 + r\left(8m + r\left(5+\sqrt{1-\frac{2m}{r}+\frac{Q^2}{r^2}}\right)\right)\right)}{16r^2(Q^2-2mr+r^2)^3} \Bigg\} \\
& \times (a^2 + b^2\sin^2\theta) + \mathcal{O}(a^3, b^3, a^2b, ab^2)
\end{aligned}
\tag{3.12b}
$$

$$
\begin{aligned}
\hat{g}_{12} = {} & -\Bigg\{ \frac{2Q^6 - Q^4r\left(9m - r\left(10 - 11\sqrt{1-\frac{2m}{r}+\frac{Q^2}{r^2}}\right)\right) + m^2r^4\left(16 - 17\sqrt{1-\frac{2m}{r}+\frac{Q^2}{r^2}}\right)}{32r(Q^2-2mr+r^2)^2} \\
& + \frac{-mr^3\left(4m^2 + r^2\left(7 - \sqrt{1-\frac{2m}{r}+\frac{Q^2}{r^2}}\right)\right) + Q^2r^2\left(12m^2 + 4r^2\left(2+\sqrt{1-\frac{2m}{r}+\frac{Q^2}{r^2}}\right)\right)}{32r(Q^2-2mr+r^2)^2} \\
& - \frac{mQ^2r^3\left(28 - 23\sqrt{1-\frac{2m}{r}+\frac{Q^2}{r^2}}\right)}{32r(Q^2-2mr+r^2)^2} \Bigg\} b^2 \sin 2\theta,
\end{aligned}
\tag{3.12c}
$$

$$
\begin{aligned}
\hat{g}_{22} = r^2 + \Bigg\{ & \frac{Q^4 r \bigg(-135m + r\bigg(68 - 11\sqrt{1-\frac{2m}{r}+\frac{Q^2}{r^2}}\bigg)\bigg) + r^3 \bigg(2r^3\bigg(5 - 3\sqrt{1-\frac{2m}{r}+\frac{Q^2}{r^2}}\bigg)}{16r^2(Q^2-2mr+r^2)^2} \\
& + \frac{-68m^3 + 18m^2 r\bigg(6 - \sqrt{1-\frac{2m}{r}+\frac{Q^2}{r^2}}\bigg) - mr^2\bigg(57 - 29\sqrt{1-\frac{2m}{r}+\frac{Q^2}{r^2}}\bigg)\bigg) + 184m^2Q^2r^2}{16r^2(Q^2-2mr+r^2)^2} \\
& + \frac{Q^2r^2\bigg(3r^2\bigg(16 - 11\sqrt{1-\frac{2m}{r}+\frac{Q^2}{r^2}}\bigg) - mr\bigg(188 - 39\sqrt{1-\frac{2m}{r}+\frac{Q^2}{r^2}}\bigg)\bigg) + 30Q^6}{16r^2(Q^2-2mr+r^2)} \Bigg\} a^2 \\
+ \Bigg\{ & \frac{14Q^4 + Q^2 r\bigg(23r - 51m + 9m\sqrt{1-\frac{2m}{r}+\frac{Q^2}{r^2}} - 17r\sqrt{1-\frac{2m}{r}+\frac{Q^2}{r^2}}\bigg) + 46m^2r^2 + 9r^4}{32(Q^2-2mr+r^2)^2} \\
& + \frac{-mr^3\bigg(41 - 23\sqrt{1-\frac{2m}{r}+\frac{Q^2}{r^2}}\bigg) + (13mr^3 - 7Q^2r^2 - 9mQ^2r)\sqrt{1-\frac{2m}{r}+\frac{Q^2}{r^2}}\cos 2\theta}{32(Q^2-2mr+r^2)^2} \\
& + \frac{\bigg[8Q^4 + Q^2r(19r-33m) + r^2\bigg(34m^2 - 39mr + r^2\bigg(11 - 12\sqrt{1-\frac{2m}{r}+\frac{Q^2}{r^2}}\bigg)\bigg)\bigg]\cos^2\theta}{16r^2(Q^2-2mr+r^2)^2} \\
& + \frac{\bigg[3Q^2r^2(3r^2+5mr-24m^2) - 16Q^6 + 2q^4 r\bigg(32m - r\bigg(8 - 3\sqrt{1-\frac{2m}{r}+\frac{Q^2}{r^2}}\bigg)\bigg) + 16m^3r^3}{16r^2(Q^2-2mr+r^2)^2} \\
& + \frac{r^3\bigg(9r^3 - 35mr^2 + 2m^2r\bigg(13 + 6\sqrt{1-\frac{2m}{r}+\frac{Q^2}{r^2}}\bigg)\bigg)\bigg]\sin^2\theta}{16r^2(Q^2-2mr+r^2)^2} \Bigg\} b^2 + \mathcal{O}(a^3, b^3, a^2b, ab^2)
\end{aligned} \tag{3.12d}
$$

$$
\begin{aligned}
\hat{g}_{33} = r^2\sin^2\theta + \Bigg\{ & \frac{(11Q^2 + 9r^2 - 20mr)(Q^2-2mr+r^2) + \bigg[r\bigg(r - 6(r-3m)\sqrt{1-\frac{2m}{r}+\frac{Q^2}{r^2}}\bigg)}{16(Q^2-2mr+r^2)^2} \\
& + \frac{-2mr + Q^2\bigg(1 \; -12\sqrt{1-\frac{2m}{r}+\frac{Q^2}{r^2}}\bigg)\bigg] r^2\cos^2\theta + \bigg[r^6\bigg(1 - 6\sqrt{1-\frac{2m}{r}+\frac{Q^2}{r^2}}\bigg) + 30Q^6}{16(Q^2-2mr+r^2)^2} \\
& + \frac{+r^3\bigg(-68m^3 + 2m^2r\bigg(34 - 9\sqrt{1-\frac{2m}{r}+\frac{Q^2}{r^2}}\bigg) + mr^2\bigg(-19 + 29\sqrt{1-\frac{2m}{r}+\frac{Q^2}{r^2}}\bigg)\bigg)}{16r^2(Q^2-2mr+r^2)^2} \\
& + \frac{qr^2\bigg(184m^2 + r^2\bigg(28 - 33\sqrt{1-\frac{2m}{r}+\frac{Q^2}{r^2}}\bigg) + mr\bigg(-146 + 39\sqrt{1-\frac{2m}{r}+\frac{Q^2}{r^2}}\bigg)\bigg)}{16r^2(Q^2-2mr+r^2)^2} \\
& + \frac{+Q^4r\bigg(-135m + r\bigg(57 - 11\sqrt{1-\frac{2m}{r}+\frac{Q^2}{r^2}}\bigg)\bigg)\bigg]\sin^2\theta}{16r^2(Q^2-2mr+r^2)^2} \Bigg\} b^2\sin^2\theta \\
- \Bigg\{ & \frac{(Q^2-2mr+r^2)\bigg[r^2\bigg(3mr\bigg(-1 + \sqrt{1-\frac{2m}{r}+\frac{Q^2}{r^2}}\bigg) \; -2r^2\bigg(1 + \sqrt{1-\frac{2m}{r}+\frac{Q^2}{r^2}}\bigg)}{32r^2(Q^2-2mr+r^2)^2} \\
& + \frac{+4m^2)\; 8Q^4 + Q^2r\bigg(-16m + r\bigg(8 - 3\sqrt{1-\frac{2m}{r}+\frac{Q^2}{r^2}}\bigg)\bigg)\bigg]\cos 2\theta - 8Q^6 + 8m^3r^3}{32r^2(Q^22-2mr+r^2)^2}
\end{aligned}
$$

$$
\begin{aligned}
&+\frac{Q^4 r \Bigg(32m + r \Bigg(-26 + 3\sqrt{1-\frac{2m}{r}+\frac{Q^2}{r^2}}\Bigg)\Bigg) + r^3 \Bigg(mr^2 \Bigg(43 - 23\sqrt{1-\frac{2m}{r}+\frac{Q^2}{r^2}}\Bigg)}{32r^2(Q^2-2mr+r^2)^2} \\
&+\frac{-2m^2 r \Bigg(25 - 3\sqrt{1-\frac{2m}{r}+\frac{Q^2}{r^2}}\Bigg) - 2r^3 \Bigg(5 - 3\sqrt{1-\frac{2m}{r}+\frac{Q^2}{r^2}}\Bigg)\Bigg) + Q^2 r^2 \big(-36m^2}{32r^2(Q^2-2mr+r^2)^2} \\
&+\left.\frac{+mr \Bigg(75 - 9\sqrt{1-\frac{2m}{r}+\frac{Q^2}{r^2}}\Bigg) - r^2 \Bigg(28 - 17\sqrt{1-\frac{2m}{r}+\frac{Q^2}{r^2}}\Bigg)\Bigg)}{32r^2(Q^2-2mr+r^2)^2}\right\} a^2 \\
&+ \mathcal{O}(a^3, b^3, a^2 b, ab^2) \qquad (3.12e)
\end{aligned}
$$

where Q is the electric charge of the BH. For the case when $Q = 0$, this deformed metric reduces to the deformed Schwarzschild solution in the previous Sec. 3.2. Also the commutative RN solution is recover when we set $\Theta = 0$ [8].

3.3.1 *Singularity and event horizon*

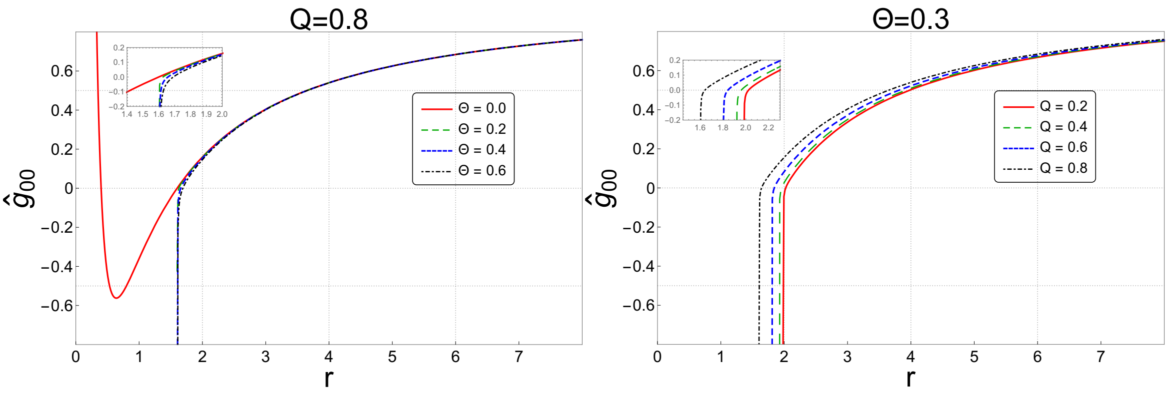

Figure 3.5: Behavior of $\hat{g}_{00}$ in the NC RN spacetime.

The behaviors of the deformed $\hat{g}_{00}$ component as a function of r for different Θ with Q constant (left panel) and for different Q with Θ constant are shown in Fig. 3.5. As we see, in the NC spacetime there is no problem anymore of two horizons as in the commutative RN BH, where in this geometry we have only one static limit surface for a charged BH and the non-commutativity increases its radius r_{sls}^{NC}. It is worth noting that the NC RN BH has a physical singularity at the finite radius $r_+ = m + \sqrt{m^2 - Q^2}$ in the NC spacetime in a similar way to the NC Schwarzschild BH (see Sec. 3.2), where in this case we have a new degree of freedom, which is the electric charge Q. In addition, the NC geometry removes the Cauchy horizon of the commutative RN solution at $r_- = m - \sqrt{m^2 - Q^2}$, and the only existing coordinate singularity is the NC static limit surface $r_{sls}^{NC} > r_+ = m + \sqrt{m^2 - Q^2}$. In the left panel, for a fixed electric charge Q and we increase in the NC parameter Θ, the radius of the static limit surface increases, while in the right panel, for a fixed Θ and we increase in Q, this radius decreases (the same behavior for the commutative case), so the role of the NC parameter in the RN spacetime is the same as in the Schwarzschild one (see Sec. 3.2).

The corresponding static limit surface and event horizon in the NC RN spacetime can be obtained by solving $\hat{g}_{00} = 0$ and $1/\hat{g}_{11} = 0$.

$$r_{sls}^{NC} = r_h + \left(\frac{15d + \sqrt{ds}}{128d}\right)\sqrt{\left(a^2 + b^2 \sin^2\theta\right)} + \left(\frac{8d + \sqrt{ds}}{16}\right)\frac{\left(a^2 + b^2 \sin^2\theta\right)}{r_h} \tag{3.13}$$

where

$$\begin{aligned} s &= \left(\frac{m^2 - Q^2 + m\sqrt{m^2 - Q^2}}{(m + \sqrt{m^2 - Q^2})^2}\right) \\ d &= \left(\frac{80m^5 - 172m^3Q^2 + 93mQ^4 + 80m^4\sqrt{m^2 - Q^2} - 132m^2Q^2\sqrt{m^2 - Q^2} + 37Q^4\sqrt{m^2 - Q^2}}{64\sqrt{m^2 - Q^2}(m + \sqrt{m^2 - Q^2})^4}\right) \end{aligned}$$

and the NC event horizon

$$r_h^{NC} = r_h + p\left(\frac{y + f\sqrt{\frac{2m}{r_h}}}{32r_h^7}\right)\left(a^2 + b^2 \sin^2\theta\right), \tag{3.14}$$

with

$$\begin{aligned} p &= \frac{1}{m}\left(\frac{(m + \sqrt{m^2 - Q^2})^3}{2(m^2 - Q^2) + 2m\sqrt{m^2 - Q^2}}\right), \\ f &= 32m^6 - 60m^4q^2 + 31m^2q^4 - 3q^6 + (32m^5 - 44m^3q^2 + 13mq^4)\sqrt{m^2 - Q^2}, \\ y &= 160m^6 - 664m^4Q^2 + 534m^2Q^4 - 72Q^6 + (150m^5 - 584m^3q^2 + 262mq^4)\sqrt{m^2 - Q^2}. \end{aligned} \tag{3.15}$$

where $r_h = r_+ = m + \sqrt{m^2 - Q^2}$ is the commutative event horizon of the RN BH when $a = b = 0$, while for $Q = 0$ we find the NC Schwarzschild static limit surface and event horizon (3.10) and (3.11) respectively.

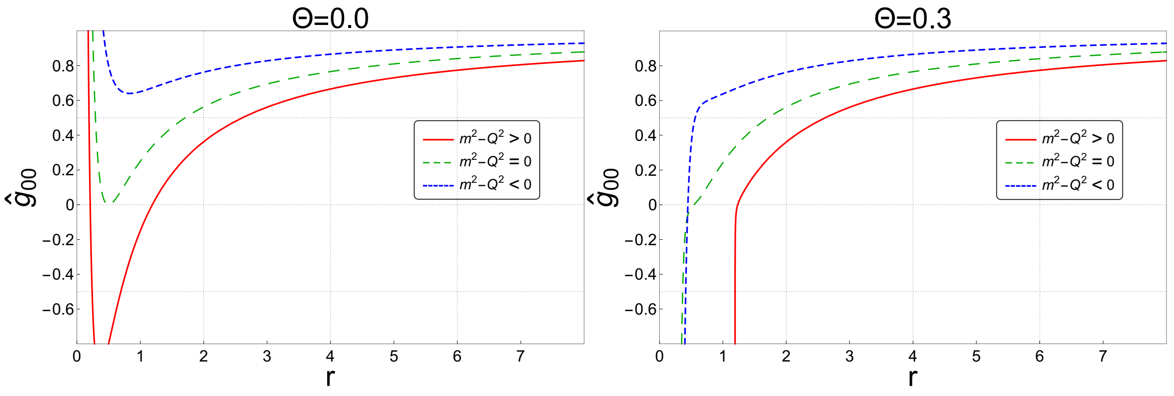

Figure 3.6: Representation of $\hat{g}_{00}$ for the three conditions of $m^2 - Q^2$, for fixed electric charge $Q = 0.5$ for all cases and different masses $m = 0.7, 0.5, 0.3$.

As we knew in the commutative spacetime, the RN BH has three conditions on the quantity $m^2 - Q^2$ [8, 211, 212]. Furthermore, the types of BH can be determined by these conditions: for $m^2 - Q^2 > 0$, we have an BH with two horizons; for $m^2 = Q^2$, we have an extremal BH; and for $m^2 < Q^2$, we have a non-BH (Fig. 3.6 right panel). But in the NC geometry, we always have a BH with a singularity at the finite radius r_+ and one event horizon, whatever the sign of the quantity $m^2 - Q^2$ (Fig. 3.6 left panel). This means non-commutativity corrected this condition when it was not respected and removed the Cauchy horizon.

4

MOTION IN THE NON-COMMUTATIVE SPACE-TIME

In this present chapter, we investigate the motion of different types of particles in the deformed spacetime in the presence of non-commutativity in a different framework than in the previous chapter (see Chap. 3). We are interested in two kinds of motion around the deformed black holes, which are the radial and the circular geodesic [167, 168], where we present the NC correction to each one of them for different types of particles in different deformed spacetime. Also, we present the discussion of the stability of circular orbits for both massive and massless particles, together with charged and uncharged ones. Finally, we examine the four classical experimental tests of GR inspired by the NC geometry to give an estimation for the lower bound on the NC parameter [167, 169].

This chapter is organized as follows: In Sect. 4.1, we present the NC corrections to the radial equation of motion for an arbitrary static metric with spherical symmetry, and we also obtain the NC effective potentials up to the second-order in Θ for a particle in the NC Schwarzschild spacetime. In Sect. 4.2, we study two types of motion for a massive test particle in NC Schwarzschild spacetime, and we check the stability of the circular orbitals by using the Lyapunov exponent. In Sect. 4.3, we present a detailed analysis of the motion of a massless particle in this deformed spacetime, and we investigate the effect of the non-commutativity on the BH shadow. In Sects. 4.4, we present the NC correction to the effective particle in the NC RN spacetime. In Sects. 4.5 and 4.6, we analyze the motion of a charged or uncharged massive test particle in this geometry. In Sect. 4.7, we present the constraint of the NC parameter using the four classical tests of GR.

4.1 NON-COMMUTATIVE SCHWARZSCHILD SPACETIME

The structure of NC spacetime (3.8) in the equatorial plan $\frac{\pi}{2}$ can be written as follows:

$$ds^2 = \hat{g}_{00}(r,\Theta)c^2dt^2 + \hat{g}_{11}(r,\Theta)dr^2 + \hat{g}_{33}(r,\Theta)d\phi^2 \tag{4.1}$$

where the components $\hat{g}_{\mu\nu}$ of the deformed metric (Sec. 3.2) in the case for $a = 0$ and $b = \Theta$ are given by

$$-\hat{g}_{00} = \left(1 - \frac{2m}{r}\right) + \left\{ \frac{m\left(88m^2 + mr\left(-77 + 15\sqrt{1-\frac{2m}{r}}\right) + 8r^2\left(2 - \sqrt{1-\frac{2m}{r}}\right)\right)}{16r^4(-2m+r)} \right\}\Theta^2 \tag{4.2a}$$

$$\hat{g}_{11} = \left(1 - \frac{2m}{r}\right)^{-1} - \left\{ \frac{m\left(12m^2 + mr\left(-14 + \sqrt{1-\frac{2m}{r}}\right) - r^2\left(5 + \sqrt{1-\frac{2m}{r}}\right)\right)}{8r^2(-2m+r)^3} \right\}\Theta^2 \tag{4.2b}$$

$$\hat{g}_{22} = r^2 + \left\{ \frac{m\left(m\left(10 - 6\sqrt{1-\frac{2m}{r}}\right) - \frac{8m^2}{r} + r\left(-3 + 5\sqrt{1-\frac{2m}{r}}\right)\right)}{16(-2m+r)^2} \right\}\Theta^2 \tag{4.2c}$$

$$\hat{g}_{33} = r^2 + \left\{ \frac{5}{8} - \frac{3}{8}\sqrt{1 - \frac{2m}{r}} + \frac{m\left(-17 + \frac{5}{\sqrt{1-\frac{2m}{r}}}\right)}{16r} + \frac{m^2\sqrt{1-\frac{2m}{r}}}{(-2m+r)^2} \right\}\Theta^2 \tag{4.2d}$$

In which follow we use this deformed metric as background for studying the geodesic motion in the equatorial plan of Schwarzschild spacetime.

The motion of a test particle in the NC spacetime (4.1) can be described by the Lagrangian as in eq. (1.12) with the above deformed metric.

$$2\mathcal{L} = \hat{g}_{tt}(r,\Theta)c^2\dot{t}^2 + \hat{g}_{rr}(r,\Theta)\dot{r}^2 + \hat{g}_{\phi\phi}(r,\Theta)\dot{\phi}^2 \tag{4.3}$$

where the dots represent the derivative with respect to the affine parameter, τ, along the geodesic. As we see, $\mathcal{L}$ is independent of t and ϕ, and that means tow conserved quantities,

$$E_0 = p_t = c^2\hat{g}_{tt}(r,\Theta)\dot{t} \Rightarrow \dot{t} = \frac{E_0}{c^2\hat{g}_{tt}(r,\Theta)} \tag{4.4a}$$

$$l = p_\phi = \hat{g}_{\phi\phi}(r,\Theta)\dot{\phi} \Rightarrow \dot{\phi} = \frac{l}{\hat{g}_{\phi\phi}(r,\Theta)} \tag{4.4b}$$

which are obtained by using the Euler-Lagrange equation (1.13). To obtain the orbital equation, we use the following invariance[1] of $\hat{g}_{\mu\nu}U^\mu U^\nu \equiv -h$, together with conserved quantities (4.4a) and (4.4b), we obtain the explicit radial equation of motion $\dot{r}^2$

$$\dot{r}^2 = -\frac{E_0^2}{c^2\hat{g}_{tt}(r,\Theta)\hat{g}_{rr}(r,\Theta)} - \frac{1}{\hat{g}_{rr}(r,\Theta)}\left(\frac{l^2}{\hat{g}_{\phi\phi}(r,\Theta)} + hc^2\right) \tag{4.5}$$

where we shall consider $h = m_0^2$ for massive particles.

We propose the following decomposition of the NC metric: $\hat{g}_{\mu\nu}$

$$-\hat{g}_{00} = A^2(r) + \Theta^2\alpha(r) + \mathcal{O}(\Theta^4) \tag{4.6a}$$

$$\hat{g}_{11} = B^2(r) + \Theta^2\beta(r) + \mathcal{O}(\Theta^4) \tag{4.6b}$$

$$\hat{g}_{33} = r^2 + \Theta^2\eta(r) + \mathcal{O}(\Theta^4) \tag{4.6c}$$

where $\alpha(r)$, $\beta(r)$, and $\eta(r)$ are a function of r, which can be determined using the deformed metric components (4.2a), 4.2b, and (4.2d). Using the relations (4.6a), (4.6b), and (4.6c), the orbital equation (4.5) becomes

$$\begin{aligned}\dot{r}^2 =& \frac{E^2}{(A^2(r)+\Theta^2\alpha(r))(B^2(r)+\Theta^2\beta(r))} - \frac{\left(\frac{l^2}{(r^2+\Theta^2\eta(r))}+h\right)}{(B^2(r)+\Theta^2\beta(r))},\\ =& \frac{E^2}{A^2(r)B^2(r)\left(1+\Theta^2\frac{(\alpha(r)B^2(r)+\beta(r)A^2(r))}{A^2(r)B^2(r)}\right)} - \frac{\left(\frac{l^2}{r^2\left(1+\Theta^2\frac{\eta(r)}{r^2}\right)}+h\right)}{B^2(r)\left(1+\Theta^2\frac{\beta(r)}{B^2(r)}\right)}.\end{aligned} \tag{4.7}$$

As we knew, the non-commutative correction is just a series in the power of Θ, so the non-commutative terms are so small compared to the commutative terms because it's just a correction. Now, we can use this development $(1+x)^{\pm n} \approx (1 \pm nx)$, so we get

$$\begin{aligned}\dot{r}^2 =& \frac{E^2}{A^2(r)B^2(r)}\left(1-\Theta^2\frac{(\alpha(r)B^2(r)+\beta(r)A^2(r))}{A^2(r)B^2(r)}\right) - \frac{\left(1-\Theta^2\frac{\beta(r)}{B^2(r)}\right)}{B^2(r)}\left(\frac{l^2}{r^2}\left(1-\Theta^2\frac{\eta(r)}{r^2}\right)+h\right),\\ =& \frac{E^2}{A^2(r)B^2(r)} - \Theta^2\frac{E^2\left(\alpha(r)B^2(r)+\beta(r)A^2(r)\right)}{A^4(r)B^4(r)} - \frac{1}{B^2(r)}\left(\frac{l^2}{r^2}+h-\Theta^2\frac{l^2\eta(r)}{r^4}\right)\\ &+\Theta^2\frac{\beta(r)}{B^4(r)}\left(\frac{l^2}{r^2}+h\right)+\mathcal{O}(\Theta^4).\end{aligned} \tag{4.8}$$

By keeping only the lower order in NC parameter Θ, we get

$$\begin{aligned}\dot{r}^2 =& \frac{E^2}{A^2(r)B^2(r)} - \frac{1}{B^2(r)}\left(\frac{l^2}{r^2}+h\right) - \Theta^2\left\{\frac{E^2\left(\alpha(r)B^2(r)+\beta(r)A^2(r)\right)}{A^4(r)B^4(r)} - \frac{l^2\eta(r)}{r^4B^2(r)}\right.\\ &\left.-\frac{\beta(r)}{B^4(r)}\left(\frac{l^2}{r^2}+h\right)\right\}+\mathcal{O}(\Theta^4).\end{aligned} \tag{4.9}$$

---

[1] where $U^\mu = c^{-1}\frac{dx^\mu}{d\tau}$ denote the 4-velocity.

This is the general equation of orbital motion for any metric with spherical symmetry. Now, if we take the case of Schwarzschild-type metrics $(A(r) = B^{-1}(r))$, we get the orbital equation for a deformed Schwarzschild metric.

$$\begin{aligned} \dot{r}^2 =& E^2 - A^2(r)\left(\frac{l^2}{r^2} + h\right) - \Theta^2 \bigg\{ E^2 \left(\frac{\alpha(r)}{A^2(r)} + \beta(r)A^2(r)\right) \\ & -\frac{l^2}{r^4}\eta(r)A^2(r) - \beta(r)A^4(r)\left(\frac{l^2}{r^2} + h\right)\bigg\} + \mathcal{O}(\Theta^4) \end{aligned} \tag{4.10}$$

Using the deformed metric components (4.2a), (4.2b), and (4.2d), this equation can be written as:

$$\dot{r}^2 + V_{eff}(r, \Theta) = 0 \tag{4.11}$$

where:

$$\begin{aligned} V_{eff}(r,\Theta) = & \left(1 - \frac{2m}{r}\right)\left(\frac{l^2}{r^2} + hc^2\right) - E^2 + \Theta^2 \Bigg\{ -\frac{l^2\left(1-\frac{2m}{r}\right)}{r^4} \Bigg(\frac{m\left(-17 + \frac{5}{\sqrt{1-\frac{2m}{r}}}\right)}{16r} \\ & -\frac{3}{8}\sqrt{1 - \frac{2m}{r}} + \frac{5}{8} + \frac{m^2\sqrt{1-\frac{2m}{r}}}{(-2m+r)^2}\Bigg) + E^2 \Bigg(\frac{64m^3 + m^2(-49 + 13\sqrt{1-\frac{2m}{r}})r}{16r^5(1-\frac{2m}{r})^2} \\ & + \frac{2m(13 - 3\sqrt{1-\frac{2m}{r}})r^2}{16r^5(1-\frac{2m}{r})^2}\Bigg) + \left(\frac{l^2}{r^2} + hc^2\right)\Bigg(\frac{m(12m^2 + m(-14 + \sqrt{1-\frac{2m}{r}})r}{8r^5(1-\frac{2m}{r})} \\ & - \frac{(5 + \sqrt{1-\frac{2m}{r}}))r^2}{8r^5(1-\frac{2m}{r})}\Bigg)\Bigg\} + \mathcal{O}(\Theta^4), \end{aligned} \tag{4.12}$$

For $\Theta = 0$, we restore the usual commutative effective potential for the Schwarzschild metric.

$$V_{eff}(r, \Theta = 0) = \left(1 - \frac{2m}{r}\right)\left(\frac{l^2}{r^2} + hc^2\right) - E^2 \tag{4.13}$$

4.2 TIME-LIKE GEODESIC EQUATION IN THE NC SCHWARZSCHILD SPACETIME

In this section, we investigate the effect of non-commutativity in the radial and the circular motion of a massive test particle in the equatorial plane of NC Schwarzschild spacetime.

4.2.1 *Radial motion of massive particles*

In order to investigate the radial motion of a massive test particle around the NC Schwarzschild BH, we must use some conditions on the above effective potential (4.12), in which $l = 0$ and $h = 1$, $c = 1$, and that gives us the following equation of radial motion for a massive test particle in NC spacetime.

$$\begin{aligned}\left(\frac{dr}{d\tau}\right)^2 = E^2 - \left(1-\frac{2m}{r}\right) - \Theta^2 \Bigg\{ E^2 \Bigg(&\frac{64m^3 + m^2(-49 + 13\sqrt{1-\frac{2m}{r}})r}{16r^5(1-\frac{2m}{r})^2} \\ &+ \frac{2m(13 - 3\sqrt{1-\frac{2m}{r}})r^2)}{16r^5(1-\frac{2m}{r})^2}\Bigg) + \Bigg(\frac{m(12m^2 + m(-14+\sqrt{1-\frac{2m}{r}})r}{8r^5(1-\frac{2m}{r})} \\ &+ \frac{-(5+\sqrt{1-\frac{2m}{r}}))r^2}{8r^5(1-\frac{2m}{r})}\Bigg)\Bigg\} + \mathcal{O}(\Theta^4). \qquad (4.14)\end{aligned}$$

It is clear that for $\Theta = 0$, we recover the usual commutative radial equation of a massive test particle in Schwarzschild spacetime [8]. Considering now a free fall of massive test particle in NC Schwarzschild BH, and for the initial condition, the test particle considered in the rest, i.e., $\dot{r} = 0$ and located at $r = r_0$ when $\tau = 0$. In NC spacetime, the proper time of a massive test particle can be computed using the above equation (4.14) with $E = 1$.

$$\begin{aligned}\hat{\tau} = -\int_{r_0}^{r} \Bigg(&\frac{2m}{r'} - \Theta^2 \Bigg\{ \Bigg(\frac{m(64m^2 + m(-49+13\sqrt{1-\frac{2m}{r'}})r' + 2(13-3\sqrt{1-\frac{2m}{r'}})r'^2)}{16r'^5(1-\frac{2m}{r'})^2} \Bigg) \\ &+ \Bigg(\frac{m(12m^2 + m(-14+\sqrt{1-\frac{2m}{r'}})r' - (5+\sqrt{1-\frac{2m}{r'}}))r'^2}{8r'^5(1-\frac{2m}{r'})} \Bigg) \Bigg\} \Bigg)^{-1/2} dr', \qquad (4.15)\end{aligned}$$

At the leading order of Θ, we can obtain

$$\begin{aligned}\hat{\tau} = \frac{2}{3}\sqrt{\frac{r_0^3}{2m}} + \Theta^2 \Bigg\{ &\sqrt{\frac{r_0}{2m}} \left(\frac{32m^2 + 4m(-52 + \sqrt{1-\frac{2m}{r_0}})r_0 + 131r_0^2}{128(2m-r_0)r_0^2} \right) \\ &+ \frac{1}{8m} ArcSin\left(\sqrt{\frac{2m}{r_0}}\right) + \frac{67}{256m} ArcTanh\left(\sqrt{\frac{r_0}{2m}}\right) \Bigg\} - (r_0 \to r). \qquad (4.16)\end{aligned}$$

The usual commutative expression can be recovered when $\Theta = 0$ [176].

In Fig. 4.1, we show the proper time $\hat{\tau}$ behavior for a free fall of a massive test particle into NC Schwarzschild BH. As we observe, the non-commutativity effect on the proper time is located near the event horizon, in which the proper time near the event horizon is increasing with the increases of Θ. In this geometry, the massive test particles take more time to reach the NC event horizon compared to the commutative case and an infinite time to reach the singularity, contrary to the commutative behavior [8], and this effect disappears when we move away from the event horizon.

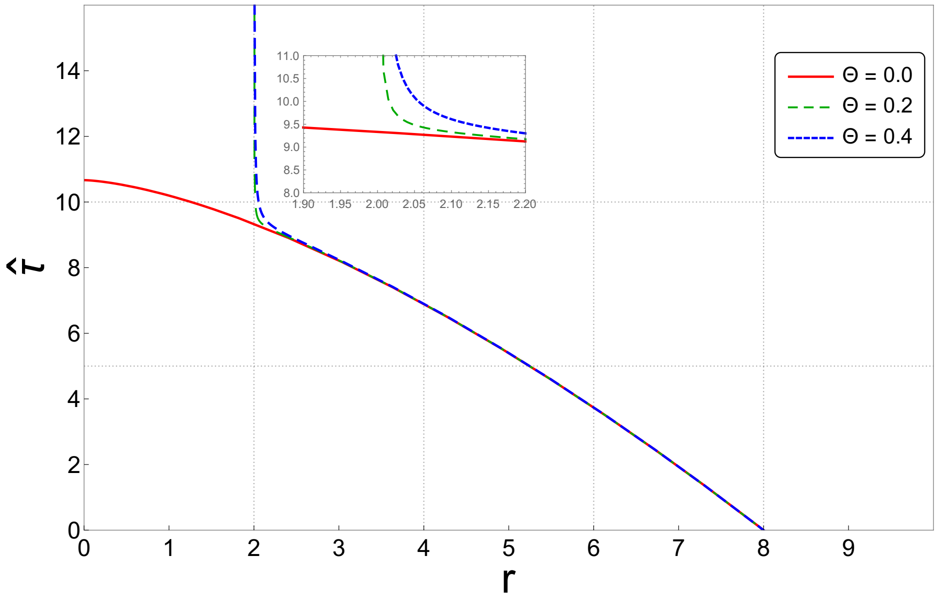

Figure 4.1: The behavior of the proper time for a free fall of a massive test particle in the NC Schwarzschild black hole as a function of r, with $m = 1$ and the initial position $r_0 = 8$.

Now if we use the relations (4.4a) and (4.14) with setting $E = 1$, we can write the coordinate time for a free fall in the NC Schwarzschild BH as follows:

$$\hat{t} = -\int_{r_0}^{r} (\hat{g}_{tt})^{-1} \left(\frac{2m}{r'} - \left\{ \left(\frac{64m^3 + m^2(-49 + 13\sqrt{1 - \frac{2m}{r'}})r' + 2m(13 - 3\sqrt{1 - \frac{2m}{r'}})r'^2}{16r'^5(1 - \frac{2m}{r'})^2} \right) \right.\right.$$
$$\left.\left. + \left(\frac{m(12m^2 + m(-14 + \sqrt{1 - \frac{2m}{r'}})r' - (5 + \sqrt{1 - \frac{2m}{r'}}))r'^2}{8r'^5(1 - \frac{2m}{r'})} \right) \right\} \Theta^2 \right)^{-1/2} dr' \,, \tag{4.17}$$

At the leading order in Θ, the above integral gives us

$$\hat{t} = \frac{2}{3}\sqrt{\frac{r_0^3}{2m}} + 4m\sqrt{\frac{r_0}{2m}} - 4m ArcTanh\left(\sqrt{\frac{r_0}{2m}}\right) + \Theta^2 \left\{ \sqrt{\frac{r_0}{2m}} \left(-\frac{25}{16r_0} \right.\right.$$
$$\left. - \frac{37m}{128(r_0 - 2m)^2} + \frac{15\sqrt{1 - \frac{2m}{r_0}}}{32(r_0 - 2m)^2} - \frac{r_0\sqrt{1 - \frac{2m}{r_0}}}{4(r_0 - 2m)^2} - \frac{61}{512(r_0 - 2m)} \right)$$
$$\left. + \frac{1}{4m} ArcSin\left(\sqrt{\frac{2m}{r_0}}\right) + \frac{605}{1024m} ArcTanh\left(\sqrt{\frac{r_0}{2m}}\right) \right\} - (r_0 \to r). \tag{4.18}$$

The usual commutative expression is recover when $\Theta = 0$ [176].

The coordinate time $\hat{t}$ behavior for a free fall of a massive test particle in the NC Schwarzschild BH is shown in Fig. 4.2. As we see, the non-commutativity effect on the coordinate time is located near the NC event horizon, in which this geometry increases the time coordinate of a massive test particle, and that is a similar behavior to the commutative one [8].

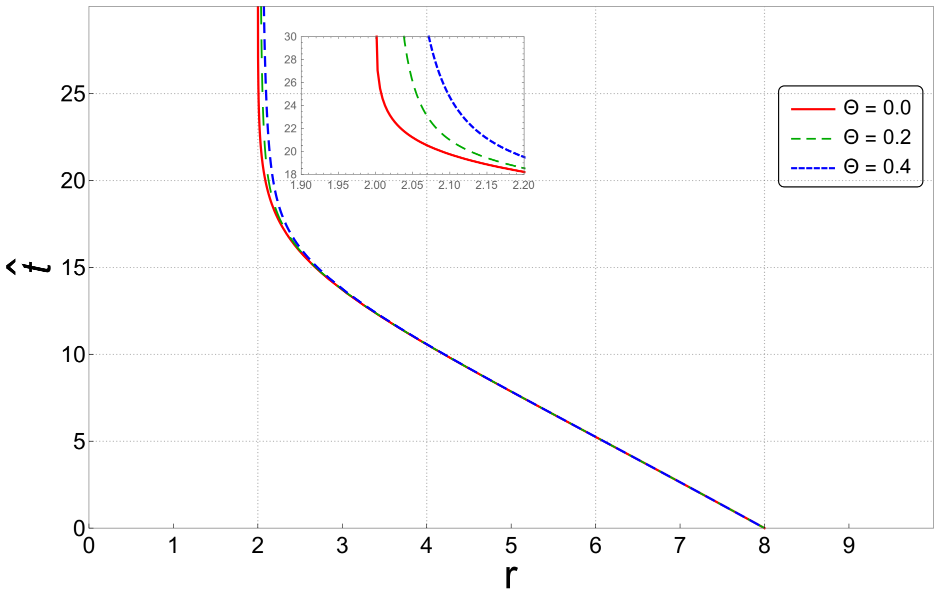

Figure 4.2: The behavior of the time coordinate for a free fall of a massive test particle in the NC Schwarzschild black hole as a function of r, with $m = 1$ and the initial position $r_0 = 8$.

The variation of the proper time $\hat{\tau}$ and the coordinate time $\hat{t}$ of a massive particle falling toward the NC Schwarzschild BH is shown in Fig. 4.3. The massive particles located at r_0 falling toward the NC Schwarzschild black hole take an infinite time with both their own proper time and in the coordinate time to reach the NC singularity and the NC event horizon, respectively, which is contrary to the commutative case for the proper time [8]. In this case, the non-commutativity prevents the massive particles from reaching the singularity in a finit time.

4.2.2 *Circular motion of massive particles*

For studying the orbital motion of a massive test particle around the NC Schwarzschild BH, we analyze the behavior of the effective potential (4.12) with $l \neq 0$ and $h = 1, \quad c = 1$.

The influence of parameters Θ, m, E, and l on the effective potential for a massive test particle is shown in Figs. 4.4 and 4.5. It is clear that, in these figures, all the extremes of the NC effective potential are located outside the NC event horizon for any value of the used parameters. As we can see in the NC geometry, there is a new minimum in the effective potential behavior, and that allowed us to see it as multiple stable circular orbits for a massive test particle. From the left panel in Fig. 4.4, we can see that, when Θ increases, the maximum peak of the curve decreases and shifts a little off the event horizon. We note that the divergence behavior of the effective potential around the NC event horizon is a consequence of the NC geometry, which plays the role of a barrier preventing high-energy particles from falling into the event horizon. In Fig. 4.4 (right panel), the increase in mass shifts the NC effective potential off the event horizon and increases the depth of the potential in NC spacetimes.

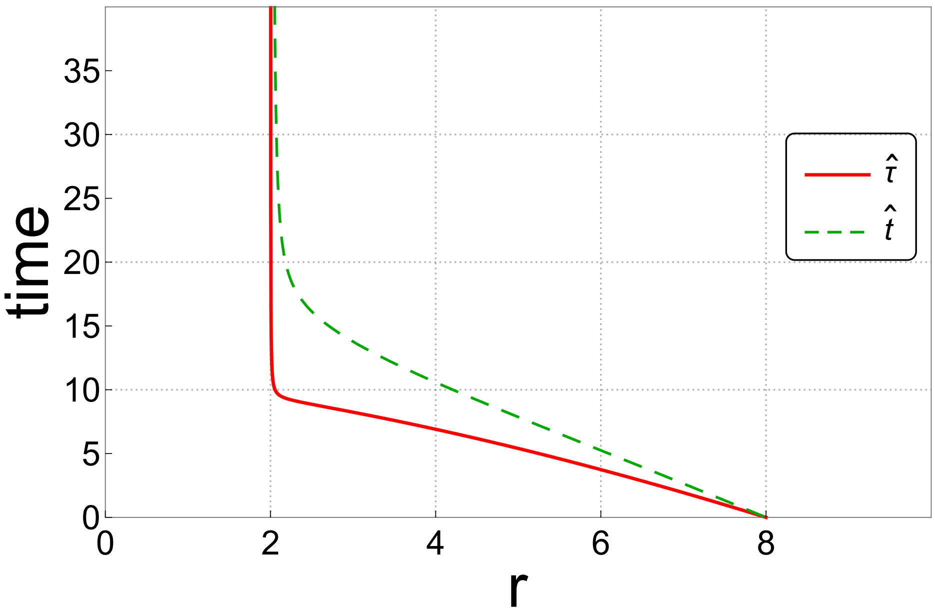

Figure 4.3: The behavior of the proper/coordinate time for a free fall of a massive test particle in the NC Schwarzschild black hole as a function of r, with $m = 1$ and the initial position $r_0 = 8$.

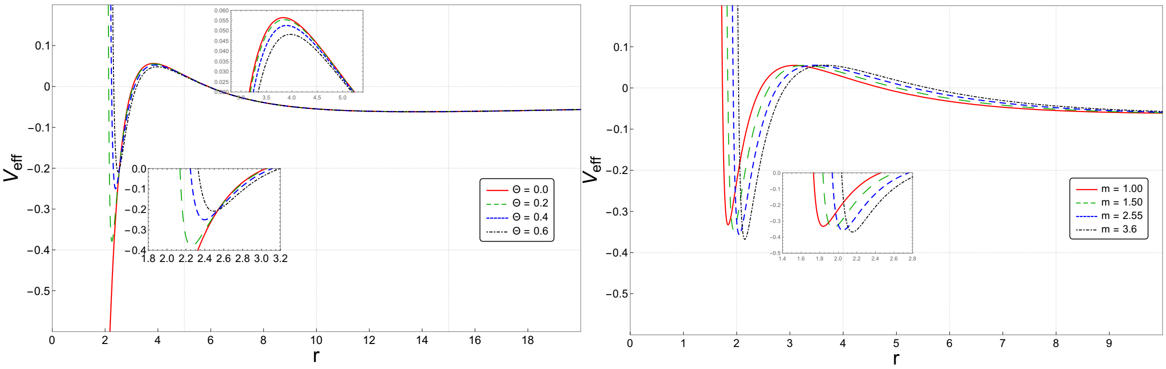

Figure 4.4: The behaviors of the effective potential for a massive particle. **Left panel:** different Θ and fixed: $E = 0.998$, $m = 1$, and $l = 4.2$. **Right panel:** different m and fixed: $E = 0.998$, $\Theta = 0.4$, $l = 4.2$.

As we observe from Fig. 4.5 (left panel), the effective potential depends on the energy of the test particle in the NC spacetime (4.12), in which the increase in energy leads to a decrease in the level of the effective potential and an increase in the depth of the potential well. For low-energy particles, $E \ll 1$, the new minimum of the effective potential disappears, and hence such particles fall into the event horizon of the Schwarzschild BH. While in the right panel (Fig. 4.5), we show the influence of the orbital momentum l on the effective potential, where we found that, in this geometry, there is always a minimum of the effective potential near the event horizon, whatever the value of the orbital momentum; when l increases, the depth of the potential well decreases and shifts towards the event horizon. The other extremes are restored when $l_{crt} > 2\sqrt{3}m$.

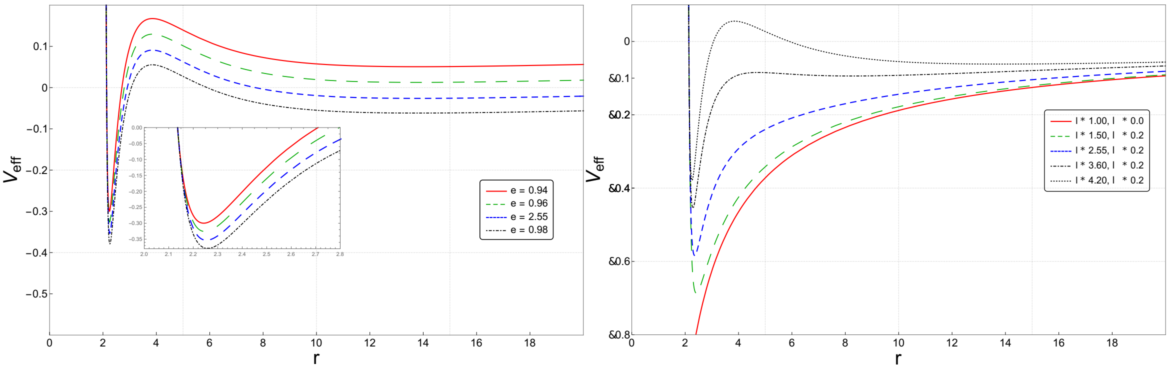

Figure 4.5: The behaviors of the effective potential for a massive particle. **Left panel:** different E and fixed: $m = 1$, $\Theta = 0.2$, $l = 4.2$. **Right panel:** different l and fixed: $E = 0.998$, $\Theta = 0.2$, $m = 1$.

In this scenario, non-commutativity plays a similar role as the potential well near the event horizon, when all matter absorbed by the black hole is compressed into this region before entering the event horizon. This leads to the formation of a new accretion disk near this region with high density and high temperature around the NC BH, which becomes very bright. This is known as "Black Hole Accretion Disk Theory" (see Refs. [213–216]), which is also known in astronomy as "Quasar" (see Ref. [217, 218]).

The new minimum appearing in the behaviors of the effective potential in Figs. 4.4 and 4.5 can be found in other theories such as the Reissner-Nordström BH [219, 220], or the non-singular black hole theory [221, 222], etc. While these theories show a problem in the location of this minimum, which is located inside the event horizon and thus cannot be interpreted as a stable circular orbit, in our work, the NC geometry shifts the new minimum outside of the event horizon, thus giving the possibility of a stable circular orbit near the event horizon. We elaborate on this in the following section.

4.2.3 *Stability condition and Lyapunov exponent*

In what follows, we investigate the orbital motion and their stability in the NC spacetime in order to see how the non-commutativity affects this class of orbits. For that, let us now consider a circular motion ($\dot{r} = 0$), and the corresponding effective potential (4.12) must satisfy the following condition:

$$V_{eff}(r,\Theta) = V^2(r,\Theta) - E^2 = 0, \tag{4.19}$$

and the extreme of the NC effective potential can be obtained by solving the following equation:

$$\frac{dV_{eff}}{dr} = 0, \tag{4.20}$$

The solution to the above equation enables us to obtain stable and unstable orbits.

In NC spacetime, there is always a minimum for the effective potential V_{eff} that appears when $l \geqslant 0$,[2] which corresponds to the Newtonian case. However, the other extremum of V_{eff} exists for a specific condition on the angular momentum, l, namely $l_{crt} > 2\sqrt{3}m$, and it depends on the value of the NC parameter Θ. This is similar to the relativistic case in commutative spacetime. It is clear that the use of the gravitational gauge theory in NC Schwarzschild spacetime using SW map 2.2.3 relates together the Newtonian case and the relativistic case in commutative Schwarzschild geometry.

Table 4.1: Some numerical values of event horizon r_h^{NC}, unstable circular orbit r_{uns}, and multiple stable circular orbit r_{sta} in the commutative and the NC case with different parameter Θ and fixed $E = 0.998, l = 4.2, m = 1$.

Θ	0	0.1	0.15	0.20	0.25	0.30
r_h^{NC}(event horizon)	2	2.00188	2.00422	2.0075	2.01172	2.01688
r_{sta}(internal)	-	2.16349	2.21421	2.25862	2.29837	2.33435
r_{uns}	3.83278	3.83684	3.8419	3.84894	3.85791	3.86876
r_{sta}(external)	13.8072	13.8074	13.8076	13.8078	13.8081	13.8086

The influence of the NC parameter Θ on the event horizon unstable and the multiple stable circular orbits, obtained by the numerical solution to the Eq. (4.20), are shown in Table 4.1. As we see, all types of circular orbits increase with increasing Θ. This behavior can be found in Fig. 4.6.

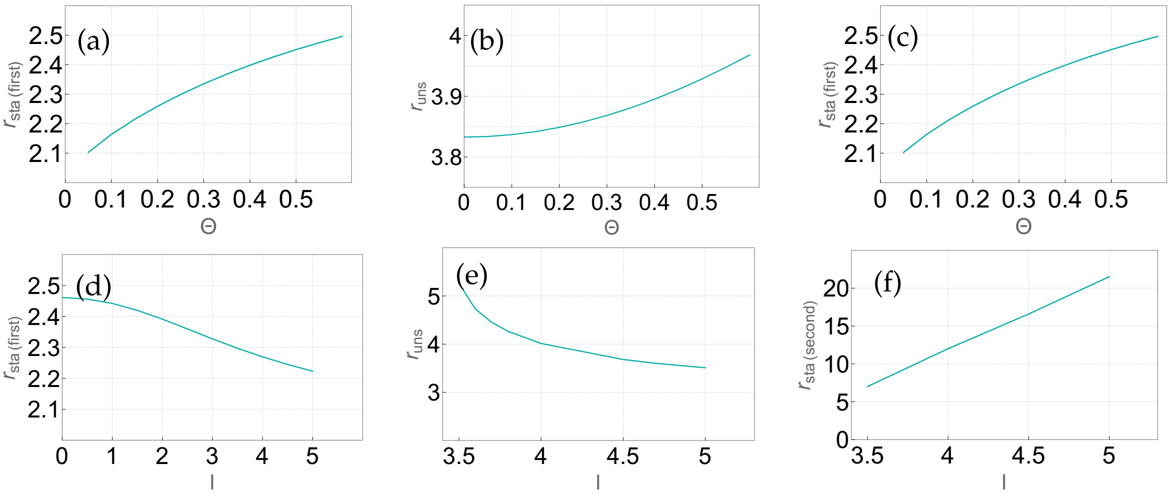

Figure 4.6: The behaviors of the radius of circular orbits for a particle in the NC space-time. Unstable and multiple stable circular orbits as function of Θ and for fixed $l = 4.2$, $E = 0.998$, $m = 1$ in (a), (b), and (c), and as function of l and for fixed $\Theta = 0.2$, $E = 0.998$, $m = 1$ in (d), (e), and (f).

As we see in Fig. 4.6, all the types of radius in (a), (b), and (c) increase as the NC parameter, Θ, increases. Therefore, in NC spacetime, the unstable circular orbital has a greater radius and is increasing as the NC parameter increases, indicating a strong gravitational field. We can also observe that the unstable and internal stable circular orbits

---

[2] When $l = 0$, in this case, the NC parameter plays the role of angular momentum.

decrease when the angular momentum, l, increases, while the external stable circular orbit increases, as shown in (d), (e), and (f).

In astrophysics, studying the motion of test particles around compact objects is due to investigating a specific type of a circular orbit called the innermost stable circular orbit (ISCO), which has great importance in this field and gives us a better understanding of the nature of massive compact objects such as neutron stars, quasars, supermassive black holes, etc. This class of orbits can be obtained from the stability condition given by:

$$\frac{d^2V_{eff}}{dr^2} \geqslant 0 \tag{4.21}$$

The numerical solution of the above condition in the usual commutative case shows that one ISCO at $r^C_{ISCO} \geqslant 6$ in Schwarzschild spacetime with l_{crit}, while in NC spacetime we get two stable circular orbits (SCO) stability orbits (see Fig.4.7), at $r_h \ll r^{NC}_{ISCO} \leqslant 2.46729$ and $r^{NC}_{ISCO} \geqslant 6.00772$, using SW map withe parameter $\Theta = 0.2$, which can see as a multiple SCO separated by unstable region.

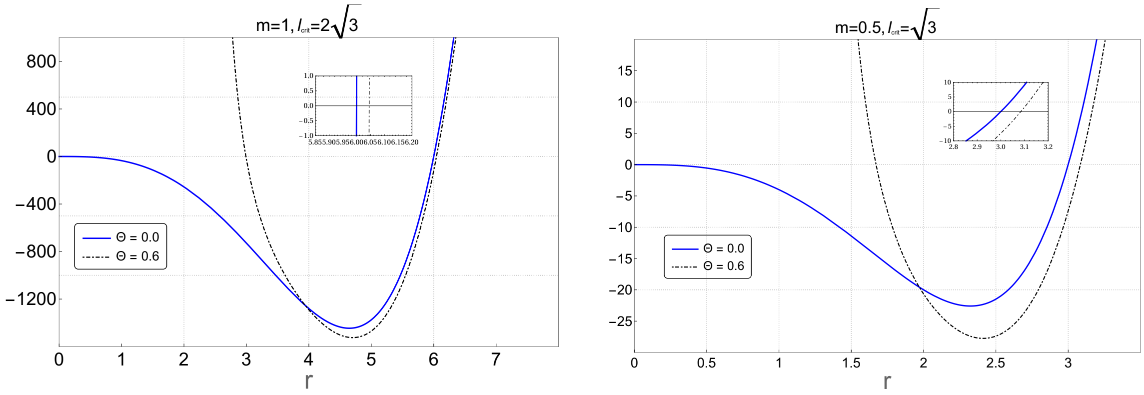

Figure 4.7: The condition of stability for circular orbits for different Θ and other fixed parameters: (left panel) $E = 1$, $l_{crit} = 2\sqrt{3}$, and $m = 1$. (right panel) $E = 1$, $l_{crit} = \sqrt{3}$, $m = 0.5$.

The behavior of the composite conditions equations given in (4.20) and (4.21) is shown in Fig. 4.7, for fixed E and for different values for the parameters l_{crit}, m, and Θ. It is clear that, in the commutative space, $\Theta = 0$, we have just one condition for the ISCO, while the NC spacetime increases this orbit and predicts a new class of SCO near the event horizon of the NC Schwarzschild BH. Another note that can be seen from the figure is that when the mass of the black hole decreases, the NC effect increases, suggesting that the NC correction term is proportional to $(\propto \frac{1}{m})$.

The stability condition behavior of circular orbits is shown in Fig. 4.8, as a function of the mass, m, in the left panel and as a function of the NC parameter, Θ, in the right panel. It is clear that, in the NC spacetime, the effect of the mass (left panel) is similar to the effect of the NC parameter (right panel), in which the increase in one of them leads to an increase in the stability conditions of the two radii. From this behavior in Fig. 4.8 and the interesting result in Ref. [149, 150], the Ricci scalar for the Schwarzschild black hole in the NC spacetime has a non-zero value for $\Theta \neq 0$. Where we see that the NC parameter Θ plays the same role as the mass m, maybe that can be used to explain the dark matter in this universe.

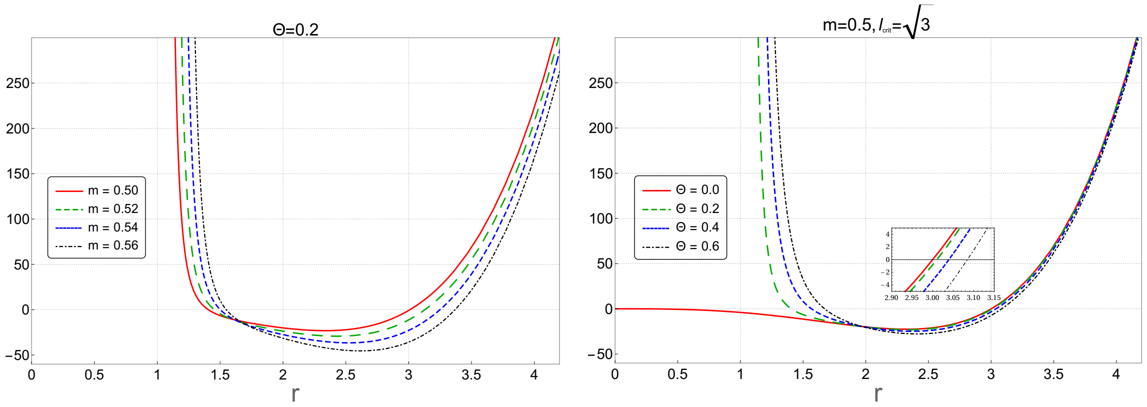

Figure 4.8: The condition of stability for circular orbits for fixed $E = 1$. (left panel) different m, $l_{crit} = 2\sqrt{3}m$ and fixed $\Theta = 0.2$. (right panel) different Θ and fixed $m = 0.50$

Table 4.2: Some numerical solution for the radius condition of the innermost stable circular orbit with different parameters Θ and fixed $E = 1$, $l_{crit} = 2\sqrt{3}m$, m. (a) $m = 1$, (b) $m = 0.5$, (c) $m = 3/14$.

Θ	0	0.10	0.15	0.20	0.25	0.30
$r_{(a)min} \geqslant$	6	6.00127	6.00286	6.00507	6.00792	6.01138
$r_s \ll r_{(a)min} \leqslant$		2.39118	2.48542	2.5655	2.63613	2.69974
$r_{(b)min} \geqslant$	3	3.00254	3.00569	3.01008	3.01566	3.02241
$r_s \ll r_{(b)min} \leqslant$		1.28275	1.34987	1.40569	1.45373	1.49587
$r_{(c)min} \geqslant$	1.28571	1.29157	1.29869	1.3083	1.32011	1.33377
$r_s \ll r_{(b)min} \leqslant$		0.616476	0.657125	0.688445	0.713273	0.733258

In table 4.2, we present some numerical solutions obtained according to the conditions given by Eqs. (4.20) and (4.21). The results in the above table represent the results obtained in Fig. 4.7 and 4.8 (right panel), which represent the effect of Θ in the ISCO radius, where this radius increases with increasing Θ. It is worth noting that the non-commutativity predicts a new class of SCO near the event horizon, which is absent in the usual commutative spacetime.

From the two tables 4.1 and 4.2, we can conclude that the NC space increases the radius of the SCO and allows for the possibility of multiple SCO separated by an unstable region.

For circular orbits, we can compute the energy and the angular momentum of massive particles by using the two stability conditions (4.19) and (4.20).

$$E_c^2 \simeq \frac{(-2m + r_c)^2}{r_c(r_c - 3m)} - \left(\frac{B(r_c) + F(r_c)\sqrt{1 - \frac{2m}{r_c}}}{32(r_c^4(-3m + r_c)^2\sqrt{1 - \frac{2m}{r_c}})} \right) \Theta^2 + \mathcal{O}(\Theta^4), \tag{4.22}$$

$$l_c^2 \simeq \frac{mr_c^2}{r_c - 3m} - \left(\frac{S(r_c) + Q(r_c)\sqrt{1 - \frac{2m}{r_c}}}{32(r_c(-3m + r_c)^2(r_c - 2m)\sqrt{1 - \frac{2m}{r_c}})} \right) \Theta^2 + \mathcal{O}(\Theta^4). \tag{4.23}$$

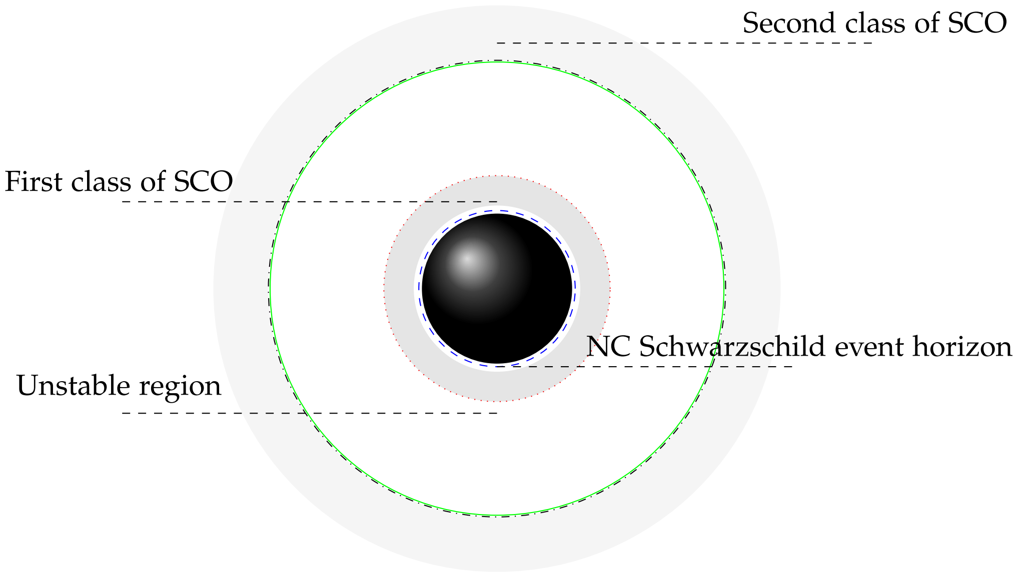

Figure 4.9: Schematic picture of the first and second bounds of stable circular orbits around the NC Schwarzschild BH, where green solid line represents ISCO for the Schwarzschild BH, black dot-dashed lines represent ISCO in external region for the NC Schwarzschild BH, blue dashed line represents the NC event horizon, and the black disk in the center represents the singularity of the NC Schwarzschild BH, and the red dot lines represent the new region of SCO near the NC event horizon. ($E = 1$, $l = 2\sqrt{3}$, $m = 1$, and $\Theta = 0.6$).

where:

$$B(r_c) = -120m^4 + 162m^3 r_c - 71m^2 r_c^2 + 4mr_c^3, \quad F(r_c) = 204m^4 - 174m^3 r_c + 41m^2 r_c^2 - 4mr_c^3, \tag{4.24a}$$

$$S(r_c) = -48m^4 + 126m^3 r_c - 55m^2 r^2, \quad Q(r_c) = -120m^4 + 174m^3 r_c - 75m^2 r_c^2 + 8mr_c^3. \tag{4.24b}$$

The usual expressions for energy and angular momentum of the commutative Schwarzschild BH are recovered when $\Theta = 0$ [176].

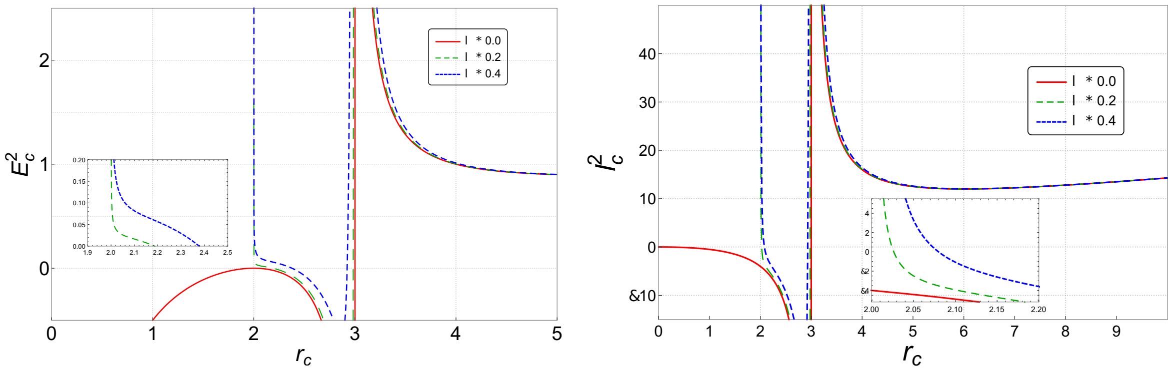

Figure 4.10: The behavior of energy (left panel) and angular momentum (right panel) of a circular orbit for massive particles in NC spacetime.

The variations of the energy E_c^2 (left panel) and angular momentum l_c^2 (right panel) of a circular orbit for massive particles around NC Schwarzschild BH as a function of r_c

are shown in Fig. 4.10. It is clear that in the NC spacetime, the energy E_c^2 of the massive test particle for circular orbit shows a new behavior in the unphysical region ($E_c^2 < 0$) compared to the commutative case (see the left panel), in which the energy turned to positive values ($E_c^2 > 0$) near the event horizon, where that is explained by the new SCO at this region. The effect of non-commutativity on the angular momentum is shown in the right panel, where a new behavior emerges from this geometry and is similar to the energy behavior (see left panel). The angular momentum also has positive values near the event horizon, which corresponds to the new stable circular orbit (see Table. 4.1), and that is not allowed in the commutative case $\Theta = 0$, in which the region near the event horizon is an unphysical region for both energy and angular momentum.

4.2.3.1 *Time period and orbital velocity*

For a massive test particle in circular orbit around a NC Schwarzschild BH, its orbital velocity can be defined as follows: [36, 223]

$$\hat{\Omega}_c = \frac{\dot{\phi}}{\dot{t}}, \tag{4.25}$$

Using Eq. (4.4b) together with (4.22) and (4.23), we obtain the orbital velocity at the second order in the NC parameter Θ as follows:

$$\hat{\Omega}_c = \sqrt{\frac{m}{r_c^3} + \left(\frac{X(r_c) + W(r_c)\sqrt{1 - \frac{2m}{r_c}}}{32 r_c^6 (r_c - 2m)^3} \right) \Theta^2}, \tag{4.26}$$

where

$$X(r_c) = -1272m^5 + 2304m^4 r_c - 1544m^3 r_c^2 + 451m^2 r_c^3 - 48m r_c^4, \tag{4.27a}$$

$$W(r_c) = -192m^4 r + 298m^3 r_c^2 - 137m^2 r_c^3 + 24m r_c^4. \tag{4.27b}$$

The commutative case [36] recovers when $\Theta = 0$.

Lets now consider a massive particle orbiting around a deformed BH. The orbital time or necessary time for a period is defined by [36].

$$\hat{T}_{\hat{\Omega}} = \frac{2\pi}{\hat{\Omega}_c}, \tag{4.28}$$

The orbital velocity (left panel) behavior together with the orbital time scale of coordinate time (right panel) in the NC spacetime as a function of r_c are shown in Fig. 4.11. As we see, in NC spacetime, both orbital velocity (left panel) and orbital time scale (right panel) show a new behavior that appears only near the event horizon r_h^{NC} (in the outside region), and this geometry increases the orbital velocity near the event horizon, and this effect becomes negligible for large orbits. Also for the orbital time scale, the effect of non-commutativity is limited only near the event horizon, in which in this geometry the time

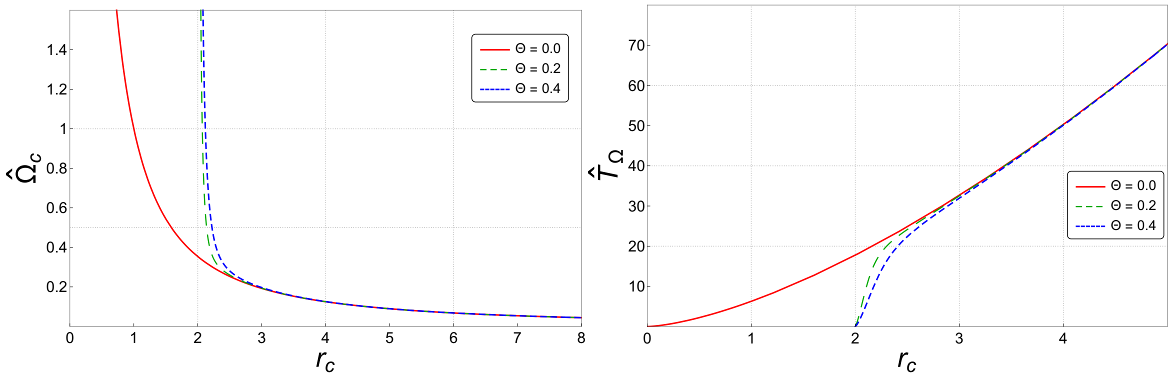

Figure 4.11: The behavior of the orbital velocity (left panel) and orbital time scale (right panel) for a massive test particle with different values of NC parameters Θ.

period is smaller compared to the commutative case (right panel), and as we see, the non-commutativity decreases the orbital time scale until it reaches zero at the singularity of the NC Schwarzschild BH, while at the large orbits $r_c \gg 3$, this effect vanishes.

4.2.3.2 *Lyapunov exponents*

In order to describe the NC spacetime proprieties around the NC Schwarzschild BH, it is interesting to study the classification of both stable and unstable circular orbits. In this context, the Lyapunov exponent [33] has a huge application in GR, where it is considered a bridge between the non-linear dynamics and the non-linear GR. Moreover, the Lyapunov exponent $\hat{\lambda}$ measures the average rate of separation between two nearby geodesics in phase space, and their stability can be determined by checking the nature of $\hat{\lambda}$, in which the circular orbit is stable and marginal stable when $\hat{\lambda}_p$ (or $\hat{\lambda}_c$) are imaginary and zero, respectively, and is unstable for $\hat{\lambda}_p$ (or $\hat{\lambda}_c$) real [40, 43]. In the NC spacetime, the proper time Lyapunov exponents $\hat{\lambda}_p$ and coordinate time Lyapunov exponents $\hat{\lambda}_c$ can be written respectively as follow [36, 40, 42, 43]

$$\hat{\lambda}_p = \pm\sqrt{\frac{-V_{eff}(r,\Theta)''}{2}}, \quad \hat{\lambda}_c = \pm\sqrt{\frac{-V_{eff}(r,\Theta)''}{2\dot{t}^2}}. \tag{4.29}$$

Using the NC effective potential (4.12) for a massive particle together with (4.4a), (4.22) and (4.23), we find

$$\hat{\lambda}_p = \sqrt{-\frac{m(r_c-6m)}{(r_c-3m)r_c^3} + \left(\frac{Z(r_c)+P(r_c)\sqrt{1-\frac{2m}{r_c}}}{32(r_c-2m)^3 r_c^6 (r_c-3m)^2}\right)\Theta^2}\,, \tag{4.30a}$$

$$\hat{\lambda}_c = \sqrt{-\frac{-m(r_c-6m)}{r_c^4} + \left(\frac{Y(r_c)+N(r_c)\sqrt{1-\frac{2m}{r_c}}}{32(r_c-2m)^3 r_c^7}\right)\Theta^2}\,. \tag{4.30b}$$

where

$$
\begin{aligned}
Z(r_c) &= 16416m^7 - 38544m^6r_c + 34992m^5r_c^2 - 16116m^4r_c^3 + 4076m^3r_c^4 - 551m^2r_c^5 \\
&\quad + 32mr_c^6, && (4.31a)\\
P(r_c) &= 3564m^6r_c - 8058m^5r_c^2 + 7070m^4r_c^3 - 2910m^3r_c^4 + 517m^2r_c^5 - 24mr_c^6, && (4.31b)\\
Y(r_c) &= 8880m^6 - 16568m^5r_c + 11200m^4r_c^2 - 3470m^3r_c^3 + 515m^2r_c^4 - 32mr_c^5, && (4.31c)\\
N(r_c) &= 1668m^5r_c - 2870m^4r_c^2 + 1808m^3r_c^3 - 473m^2r_c^4 + 24mr_c^5, && (4.31d)
\end{aligned}
$$

The commutative expressions of $\hat{\lambda}_p$ and $\hat{\lambda}_c$ are recovered when $\Theta = 0$ [40, 42].

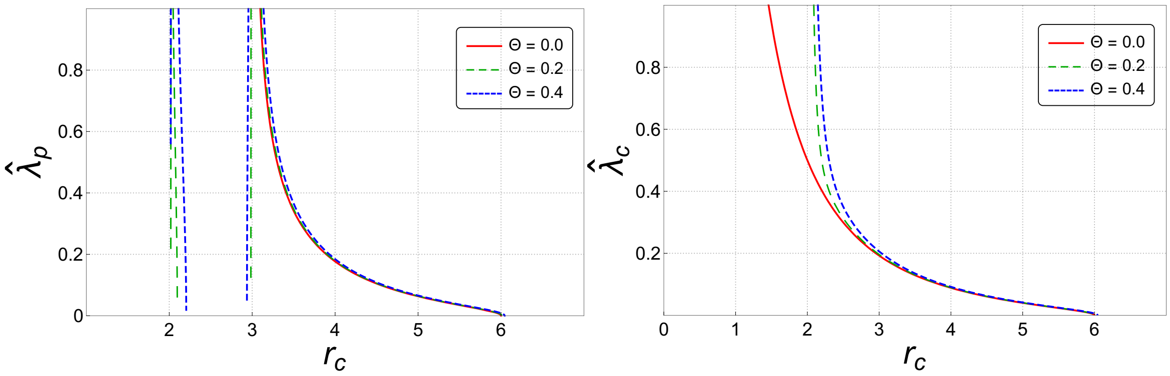

Figure 4.12: The behavior of the proper time (left panel) and coordinate time (right panel) Lyapunov exponents for a massive particle as a function of circular orbits r_c.

Fig. 4.12 shows the instability of orbits measured by Lyapunov exponents, which is described by the behavior of the proper (left panel) and coordinate time (right panel) for a massive particle in the NC Schwarzschild spacetime. As we see now, a new behavior appears in the NC spacetime a for both $\hat{\lambda}_p$ (left panel) and $\hat{\lambda}_c$ (right panel). It is clear that, in the right panel, we show the instability of the orbits in the region between the singularity and the NC ISCO, $2m < r_c \leq r^{ISCO}_{outer}$, which is measured by the coordinate time Lyapunov exponents in the NC space time, where that means $\hat{\lambda}_c$ is real in this region, and the non-commutativity increases the instability of the orbits near the event horizon and decreases when we are far from the event horizon $r_c > r_h^{NC}$, until reaching zero at the outer ISCO r^{ISCO}_{outer}. While, in the left panel, we show a different behavior to the coordinate time (see right panel), in which the proper time Lyapunov exponents in the NC spacetime measured the instability of circular orbits in two regions separated by an imaginary part of $\hat{\lambda}_p$, where $\hat{\lambda}_p$ is real in two regions $2m < r_c \leq r^{ISCO}_{inner}$ and $r_c^{uns} < r_c \leq r^{ISCO}_{outer}$, which means that the circular orbit is unstable and is separated by a stable region with $\hat{\lambda}_p$ imaginary in $r^{ISCO}_{inner} \leq r_c \leq r_c^{uns}$, and this result coincides with the one obtained in the Table. 4.1 and 4.2, where the new circular orbit near the event horizon is stable.

The ratio proper/coordinate time of the Lyapunov exponent can be computed using (4.30a) and (4.30b), which can be written as follows:

$$\frac{\hat{\lambda}_p}{\hat{\lambda}_c} = \sqrt{\frac{r_c}{(r_c - 3m)} + \left(\frac{Y(r_c)(3m - r_c) - Z(r_c) + (N(r_c)(3m - r_c) - P(r_c))\sqrt{1 - \frac{2m}{r_c}}}{32m(r_c - 2m)^3(r_c - 3m)^2(r_c - 6m)r_c^2} \right) \Theta^2}, \tag{4.32}$$

The commutative expression can be recovered when $\Theta = 0$ [40, 42].

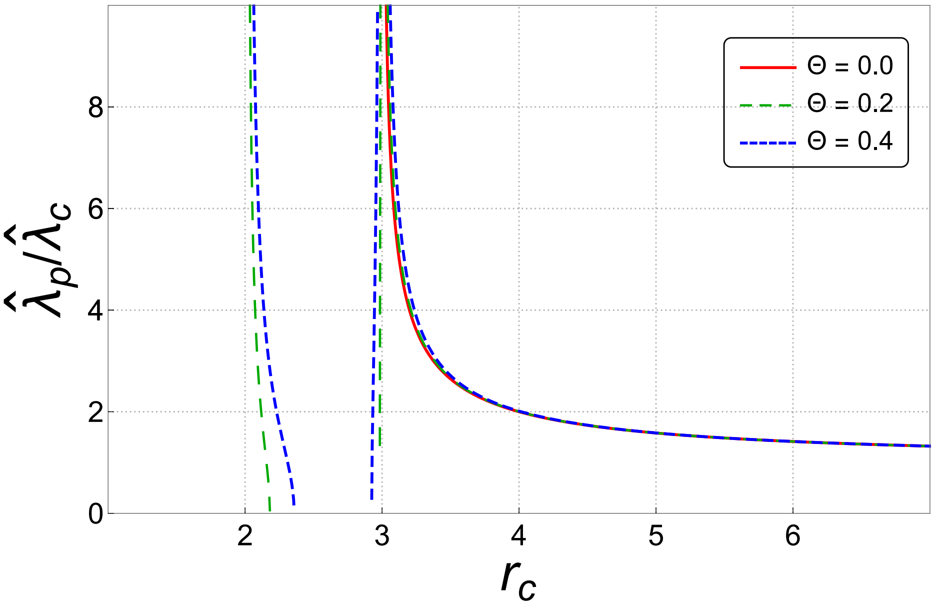

Figure 4.13: The behavior of the ratio proper/coordinate time of Lyapunov exponent for a massive particle in NC spacetime.

In Fig. 4.13, we show the behavior of the ratio proper time to the coordinate time of the Lyapunov exponent as a function of the circular orbits r_c in the NC spacetime. It is clear that the ratio $\hat{\lambda}_p/\hat{\lambda}_c$ is real in two regions and separated by an imaginary one, which means the unstable regions are separated by a stable one (see Fig. 4.9), and that is similar to the case of the proper time Lyapunov exponent.

4.2.4 *NC effect on the orbital motion*

As we see above, the non-commutativity affects the stability of circular orbits around NC Schwarzschild BH, so the investigation of the geodesic equation is important for more detailed analysis on the effect of this geometry. In which follow, we need to write the equation of motion (4.11) as a function of ϕ. To achieve this, we use the angular momentum condition Eq. (4.4b), and then we obtain

$$\frac{dr}{d\tau} = \frac{dr}{d\phi}\frac{d\phi}{d\tau} = \frac{l}{\hat{g}_{\phi\phi}(r,\Theta)}\frac{dr}{d\phi} \tag{4.33}$$

We substitute this into Eq. (4.11), and we obtain:

$$\left(\frac{dr}{d\phi}\right)^2 = -\frac{\hat{g}^2_{\phi\phi}(r,\Theta)}{l^2}V_{eff}(r,\Theta) \tag{4.34}$$

where we use the relations (4.11), (4.12), and (4.2d) in the case of a massive particle, $h = m_0^2$, then we obtain:

$$\begin{aligned}\left(\frac{dr}{d\phi}\right)^2 =& \frac{r^4}{l^2}E^2 - \frac{r^4}{l^2}\left(1-\frac{2m}{r}\right)\left(\frac{l^2}{r^2}+hc^2\right) - \Theta^2\Bigg\{-\Bigg(\frac{5}{8}-\frac{3}{8}\sqrt{1-\frac{2m}{r}}+\frac{m}{16r}\left(-17+\frac{5}{\sqrt{1-\frac{2m}{r}}}\right)\\ &+\frac{m^2\sqrt{1-\frac{2m}{r}}}{(-2m+r)^2}\Bigg)\left(1-\frac{2m}{r}\right)+\frac{E^2}{l^2}\Bigg(\frac{(m^2(-49+13\sqrt{1-\frac{2m}{r}})r+2m(13-3\sqrt{1-\frac{2m}{r}})r^2)}{16r^5(1-\frac{2m}{r})^2}\\ &+\frac{64m^3}{16r^5(1-\frac{2m}{r})^2}\Bigg)-\left(\frac{l^2}{r^2}+hc^2\right)\Bigg(\frac{m(12m^2+m(-14+\sqrt{1-\frac{2m}{r}})r-(5+\sqrt{1-\frac{2m}{r}}))r^2}{8r^5(1-\frac{2m}{r})}\Bigg)\\ &+\frac{1}{l^2}\Bigg(\frac{5}{8}-\frac{3}{8}\sqrt{1-\frac{2m}{r}}+\frac{m}{16r}\left(-17+\frac{5}{\sqrt{1-\frac{2m}{r}}}\right)+\frac{m^2\sqrt{1-\frac{2m}{r}}}{(-2m+r)^2}\Bigg)\Bigg(\left(1-\frac{2m}{r}\right)\left(\frac{l^2}{r^2}+hc^2\right)\\ &-E^2\Bigg)\Bigg\}+\mathcal{O}(\Theta^4),\end{aligned} \tag{4.35}$$

We define a new variable, $u = \frac{1}{r}$; thus, we find

$$\begin{aligned}\left(\frac{du}{d\phi}\right)^2 =& \frac{(E^2-m_0^2c^2)}{l^2}+\frac{2mm_0^2c^2}{l^2}u-u^2+2mu^3-\Theta^2\Bigg\{-u^4(1-2mu)\Bigg(\frac{5}{8}-\frac{3}{8}\sqrt{1-2mu}\\ &+\frac{1}{16}mu\left(-17+\frac{5}{\sqrt{1-2mu}}\right)+\frac{m^2u^2}{(1-2mu)^{\frac{3}{2}}}\Bigg)-\frac{2u^2}{l^2}\Big((-1+2mu)(m_0^2c^2+l^2u^2)\\ &+E^2\Big)\times\Bigg(\frac{5}{8}-\frac{3}{8}\sqrt{1-2mu}+\frac{1}{16}mu\left(-17+\frac{5}{\sqrt{1-2mu}}\right)+\frac{m^2u^2}{(1-2mu)^{\frac{3}{2}}}\Bigg)\\ &+\Bigg(\frac{E^2mu^3(64u^2m^2+mu(-49+13\sqrt{1-2mu})+2(13-3\sqrt{1-2mu}))}{16l^2(1-2mu)^2}\Bigg)\\ &+\frac{mu^3(m_0^2c^2+l^2u^2)(12u^2m^2+mu(-14+\sqrt{1-2mu})-(5+\sqrt{1-2mu}))}{8l^2(1-2mu)}\Bigg\}\\ &+\mathcal{O}(\Theta^4),\end{aligned} \tag{4.36}$$

Let's now rewrite the above equation in linear form using the following approximation $mu \ll 1$, and we stop at 3^{rd} order in u, and hence we find:

$$\begin{aligned}\left(\frac{du}{d\phi}\right)^2 =& \frac{(E^2-m_0^2c^2)}{l^2}+\frac{2mm_0^2c^2}{l^2}u-u^2+2mu^3+\frac{\Theta^2}{2l^2}\{(E^2-m_0^2c^2)u^2\\ &+m(5m_0^2c^2-4E^2)u^3\},\end{aligned} \tag{4.37}$$

The derivative of the above equation with respect to ϕ gives us

$$\frac{d^2u}{d\phi^2}+u=\frac{mm_0^2c^2}{l^2}+3mu^2+\frac{\Theta^2}{2l^2}\left\{(E^2-m_0^2c^2)u+\frac{3m}{2}(5m_0^2c^2-4E^2)u^2\right\}. \tag{4.38}$$

where this equation is the NC geodesic equation in NC Schwarzschild spacetime.

The analytical solution to this equation can be obtained using the approximation method. For that, let's rewrite the equation (4.38) in this form:

$$\frac{d^2u}{d\phi^2}+\omega^2u=\frac{mm_0^2c^2}{l^2}+3m'u^2, \tag{4.39}$$

where

$$\omega^2=1-\frac{2\Theta^2}{4l^2}(E^2-m_0^2c^2), \tag{4.40a}$$

$$m'=m\left[1+\Theta^2\left(\frac{5m_0^2c^2-4E^2}{4l^2}\right)\right]. \tag{4.40b}$$

This equation can be solved using the same method in Sec. 1.2, where we use the approximation solution [224].

$$u(\phi)=\frac{mm_0^2}{l^2\omega^2}\left(1+ecos\left(\omega\phi-\frac{3m'mm_0^2}{l^2\omega^3}\phi\right)\right). \tag{4.41}$$

where e is the eccentricity of the orbit. Note that when $\Theta=0$, the commutative solution is recover (1.24) (for the case $m_0=1$).

The plot of some orbits of a massive particle around a NC Schwarzschild black hole described by the geodesic equation (4.41) are shown in Fig. 4.14 for different values of l and E and with a fixed black hole mass $m=3/14$ and the NC parameter $\Theta=0.1, 0.2, 0.3$ (left to the right) compared with the commutative case $\Theta=0$. It is clear that in rows 1, 2, 3, and 4, the non-commutativity of the spacetime affected the orbits of the massive test particle, and this appears in the deformation on the periastron advance of the particle orbit.

4.3 NULL GEODESIC EQUATION IN THE NC SCHWARZSCHILD SPACETIME

This section is for studying the effect of non-commutativity in the radial and the circular motion of a massless test particle in the equatorial plane of NC Schwarzschild spacetime.

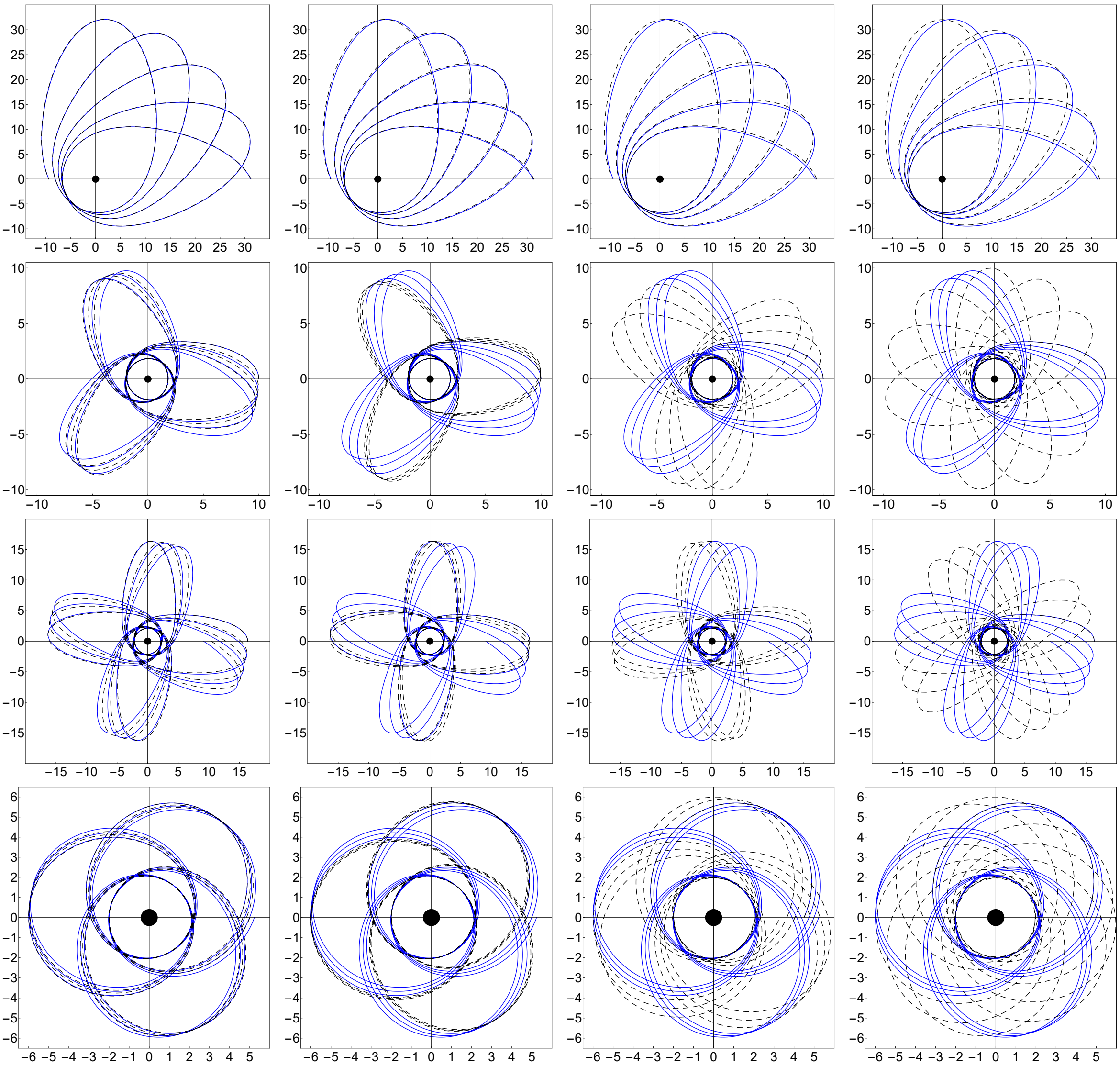

Figure 4.14: Time-like geodesic for a massive test particle $h = 1$ around a NC Schwarzschild black hole, with $\Theta = 0.1, 0.2, 0.3, 0.4$ (left to right) and fixed mass $m = \frac{3}{14}$ and varying other parameters in the plan $\theta = \frac{\pi}{2}$: (rows 1), $l = 1.586$, $E = 0.993$; (rows 2), $l = 0.915$, $E = 0.975$; (rows 3) $l = 0.99$, $E = 0.9828$; (rows 4) $l = 0.915$, $E = 0.975$.

4.3.1 *Radial motion of massless particles*

The radial motion for a massless particle in the NC Schwarzschild spacetime can be studied using the NC effective potential (4.12) with $l = 0$ and $h = 0$, and it is written as follows:

$$\left(\frac{dr}{d\tau}\right)^2 = E^2 - \Theta^2 \left\{ E^2 \left(\frac{64m^3 + m^2(-49 + 13\sqrt{1-\frac{2m}{r}})r + 2m(13 - 3\sqrt{1-\frac{2m}{r}})r^2}{16r^5(1-\frac{2m}{r})^2} \right) \right\} + \mathcal{O}(\Theta^4). \tag{4.42}$$

In the case of $\Theta = 0$, the commutative expression is recovered. Let's now consider a photon emitted from the point $r = r_0$ in free fall into the NC Schwarzschild BH with $E = 1$. The affine parameter τ and coordinate time $\hat{t}$ in this case are defined by

$$\hat{\tau} = -\int_{r_0}^{r} \left(1 - \Theta^2 \left\{ \frac{64m^3 + m^2(-49 + 13\sqrt{1-\frac{2m}{r}})r + 2m(13 - 3\sqrt{1-\frac{2m}{r}})r^2}{16r^5(1-\frac{2m}{r})^2} \right\} \right)^{-1/2}, \tag{4.43a}$$

$$\hat{t} = -\int_{r_0}^{r} (\hat{g}_{00})^{-1} \left(1 - \Theta^2 \left\{ \frac{64m^3 + m^2(-49 + 13\sqrt{1-\frac{2m}{r}})r + 2m(13 - 3\sqrt{1-\frac{2m}{r}})r^2}{16r^5(1-\frac{2m}{r})^2} \right\} \right)^{-1/2}. \tag{4.43b}$$

The integration of both above equations is evaluated at the leading order in Θ, which gives

$$\hat{\tau} = r_0 + \Theta^2 \left\{ 25Log\left(\frac{r_0}{(r_0-2m)}\right) - \frac{1}{128m}\left(\frac{32m^2 + 15mr_0 + 8r_0^2}{r_0^2} + \left(1 - \frac{2m}{r_0}\right)^{-1/2} \right.\right.$$
$$\left.\left. - \left(1 - \frac{2m}{r_0}\right)^{1/2}\right) - \frac{13}{3}\left(1 - \frac{2m}{r_0}\right)^{3/2} - \frac{35}{2}\left(\frac{r_0}{(r_0-2m)}\right) \right\} - (r_0 \to r), \tag{4.44a}$$

$$\hat{t} = r_0 + 2mLog\left(\frac{r_0}{2m} - 1\right) - \Theta^2 \left\{ \frac{224m^2 - 201mr_0 + 63r_0^2}{128r_0(r_0-2m)^2} + \frac{63}{m}Log\left(\frac{r_0}{(r_0-2m)}\right) \right.$$
$$\left. + \frac{(17m^2 - 24mr_0 + 8r_0^2)\sqrt{1-\frac{2m}{r_0}}}{m(r_0-2m)^2} \right\} - (r_0 \to r). \tag{4.44b}$$

When $\Theta = 0$, the commutative expression of both the affine parameter and the coordinate time of a massless particle are recovered [8].

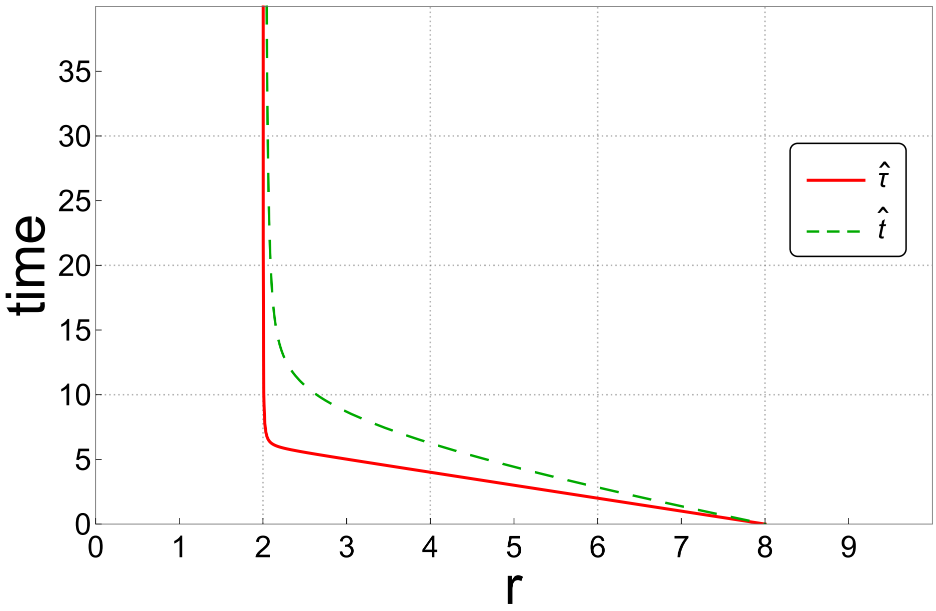

Figure 4.15: The behavior of the affine parameter and the coordinate time along the radial null geodesic of a photon in the NC Schwarzschild black hole as function of r.

In Fig. 4.15, we show the behavior of both the affine parameter $\hat{\tau}$ and the coordinate time $\hat{t}$ along a radial null geodesic. For the free fall of a photon from $r = r_0$ falling into the NC Schwarzschild BH, it is seen that the photons take an infinite affine parameter to reach the singularity, contrary to the commutative case [8, 225], in the case of the NC spacetime in the affine parameter framework, and it's the same case for the time coordinate, which takes an infinite time to reach the NC event horizon, which is the same behavior as in the commutative case for the time coordinate [8]. It is worth noting that the non-commutativity prevents the photons from reaching the singularity only after an infinite proper time τ, and that means the photons cannot reach the singularity for a finite time, which is the same observation as the massive test particle in the above Sec. 4.2.

4.3.2 *Circular motion of massless particles*

In which follows, we focus on the null circular motion of a photon in the equatorial plane around the NC Schwarzschild BH. The NC effective potential in this case is given by (4.12) with $h = 0$.

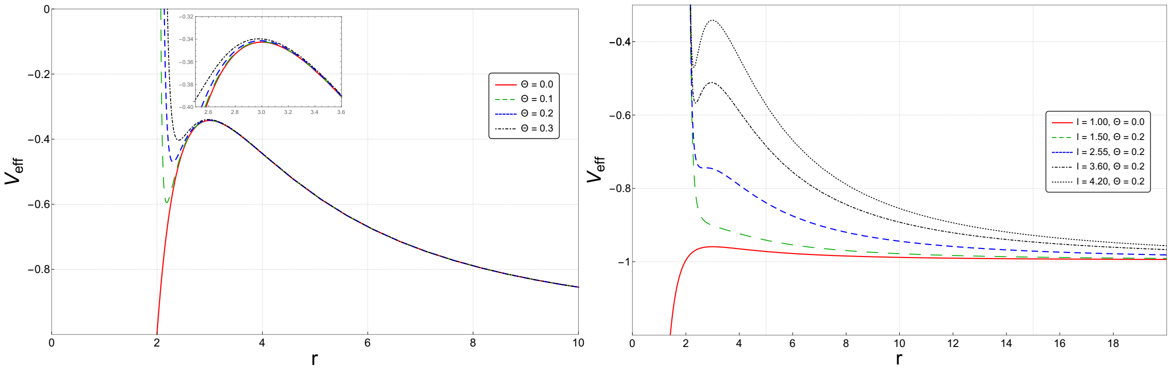

Figure 4.16: The behavior of the effective potential for massless particle with different values of NC parameters Θ and fixed: $E = 0.998$, $m = 1$, $l = 4.2$ (left panel), and with different angular momentum l and fixed $E = 0.998$, $m = 1$, $\Theta = 0.2$ (right panel).

The variation of the NC effective potential for a massless particle (photon) as a function of r_c is shown in Fig. 4.16, for different values of the NC parameters Θ (left panel) and for the angular momentum l (right panel). It is clear that, in the NC spacetime, the effective potential shows a new minimum appears near the event horizon in a similar way as for the massive test particle case (see Sec. 4.2), while for the photons, there are only two extrema located outside the event horizon, which are a minimum and a maximum, and that allows us to interpret this new minimum as a new SCO, which means a new stable photon sphere near the event horizon in this geometry. It is clear that, when Θ is increasing, the new minimum of the effective potential shifts away from the event horizon, and this effect becomes insignificant as we move further from the event horizon ($r \gg r_h^{NC}$). In the right panel, we show that in the NC spacetime, we have a condition in angular momentum l in which the effective potential has an extremum, contrary to the commutative case where the effective potential has a maximum, whatever the value of l, while in this geometry $\Theta =$

0.2 this potential has always two extremums for the critical value of angular momentum $l^{crit} \geq 2.55$, where this value depends on Θ. Finally, in the NC Schwarzschild spacetime, there is always a two-photon sphere, in which the inner one is stable while the outer is the usual unstable photon sphere.

4.3.3 *Stability condition and photon sphere*

In the case of a massless particle, the circular orbit subjects to the same conditions as the massive one (4.19) and (4.20), where we use the NC effective potential (4.12) with $h = 0$, and that leads to the ratio between the energy E_c and the angular momentum l_c for the circular orbit by the following expression:

$$\frac{1}{D_c} = \frac{E_c}{l_c} = \sqrt{\frac{r_c - 2m}{r_c^3} + \left(\frac{J(r_c) + G(r_c)\sqrt{1 - \frac{2m}{r_c}}}{16 r_c^6 (r_c - 2m)} \right) \Theta^2}. \tag{4.45}$$

where D_c is the impact parameter, and

$$J(r_c) = 156m^3 - 185m^2 r_c + 73m r_c^2 - 10 r_c^3, \quad G(r_c) = 33m^2 r_c - 37m r_c^2 + 6 r_c^3. \tag{4.46}$$

Table 4.3: Some numerical values of unstable r_{uns} and new stable circular orbit r_{sta} of photon sphere in the NC spacetime with different parameter Θ and fixed $E = 0.998$, $l = 4.2$, $m = 1$.

Θ	0	0.10	0.15	0.20	0.25	0.30
r_{sta}(new)		2.18400	2.24624	2.30383	2.35865	2.41183
r_{uns}	3.	2.99782	2.99504	2.99101	2.98559	2.97855

The numerical solution of equation (4.20) is presented in Table. 4.3, which represents the variation of stable and unstable circular orbits of the photon sphere as a function of some values of Θ, and when Θ increases, these two types of orbits get closer to each other for $3.29 \leq l \leq 4.48$ (the condition on l depends on $0 \leq \Theta \leq 0.3$), in which the stable circular orbit is increasing and these two orbits get closer to each other for $3.29 \leq l \leq 4.48$ (the condition on l depends on $0 \leq \Theta \leq 0.3$), which mean the stable circular orbit increasing and the unstable one decreasing, while for the case of $l > 4.48$, these two orbits increase both of them with increasing Θ.

It is clear that, in Fig. 4.17 (two left panels), the new null SCO increases while the unstable one decreases as the NC parameter Θ increases. Therefore, the unstable orbit of the photon has a smaller radius in NC spacetime and decreases as the NC parameter increases for the case $l < 4.48$, while for $l \geq 4.48$ this orbit is greater than in the commutative case, where in the commutative case this orbit is independent of the angular momentum l, and that is due to the presence of the non-commutativity effect that modified the gravitational field. For the two right panels in Fig. 4.17, the circular orbit of the photon depends on the

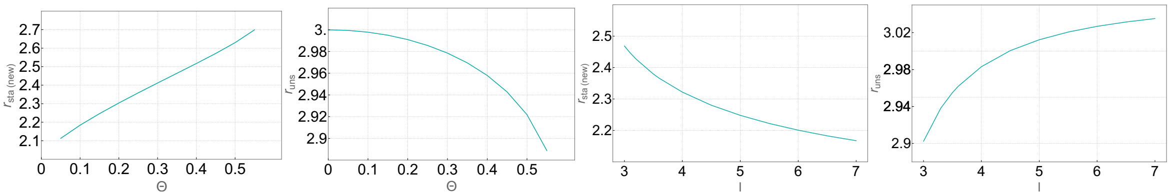

Figure 4.17: The behavior of the photon sphere radius in NC spacetime. stable and unstable circular orbits as a function of Θ and for fixed $l = 4.2$, $E = 1$, $m = 1$ (two left panels), as a function of l and for fixed $\Theta = 0.3$, $E = 1$, $m = 1$ (two right panels).

angular momentum l in this geometry, in which the new stable circular orbit decreases as the angular momentum l increases, while the unstable one increases.

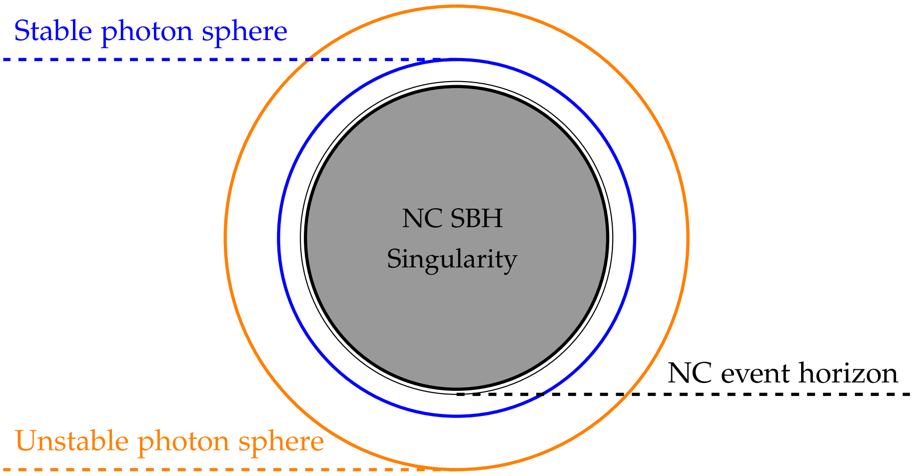

Figure 4.18: The schematic picture of the stable/unstable photon sphere around the NC Schwarzschild black hole.

4.3.4 *Lyapunov exponents*

In which follow we use only the coordinate time Lyapunov exponent, and that because the photon doesn't have a proper time.

In this case, for a null circular orbit, the NC angular frequency and the NC time period in coordinate time are given by the following equations: (4.25) and (4.28), respectively.

$$\hat{\Omega}_c^{Null} = \frac{1}{D_c}, \quad \hat{T}_{\hat{\Omega}}^{Null} = 2\pi D_c \tag{4.47}$$

The coordinate time Lyapunov exponent for the null circular orbit of a photon around NC Schwarzschild BH can be obtained using (4.29), which gives us

$$\hat{\lambda}_c^{Null} = \sqrt{-\frac{3((-4m+r_c)(-2m+r_c))}{r_c^4} + \left(\frac{O(r_c) + I(r_c)\sqrt{1-\frac{2m}{r_c}}}{32(r_c-2m)^2 r_c^7}\right)\Theta^2}. \tag{4.48}$$

where

$$O(r_c) = -19488m^5 + 39000m^4 r_c - 29076m^3 r_c^2 + 9958m^2 r_c^3 - 1716m r_c^4 + 140 r_c^5, \qquad (4.49a)$$

$$I(r_c) = -3171m^4 r_c + 5773m^3 r_c^2 - 3908m^2 r_c^3 + 1080m r_c^4 - 84 r_c^5. \qquad (4.49b)$$

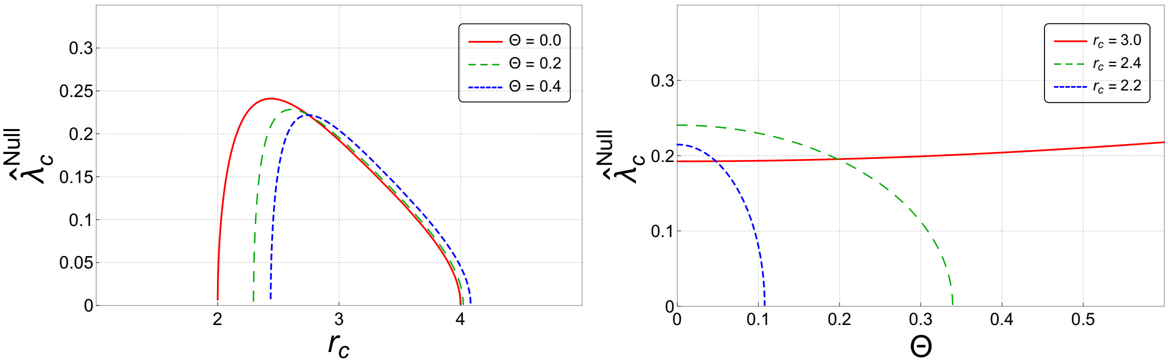

Figure 4.19: The behavior of the coordinate time Lyapunov exponent for massless particles as a function of r_c (left panel) and as a function of the NC parameters Θ (right panel).

The behavior of the Lyapunov exponent $\hat{\lambda}_c$ for photon in the coordinate time is shown in Fig. 4.19, as a function of r_c (left panel) and as a function of the NC parameters Θ (right panel). It is clear that in the left panel, the instability increases slowly from $r_c = 4$ until it reaches the maximum, then decreases rapidly as r_c decreases until it reaches zero at $r_c = 2$ (near the event horizon), and this maximum decreases and shifts away from the event horizon as Θ increases. It is worth noting that for the circular orbits near the event horizon in the NC geometry, their instability is smaller than in the commutative case, while when we move away from the event horizon, this observation is reflected. Furthermore, in the NC spacetime the profile of the instability is shifted away from the event horizon, compared to the commutative case in which the instability became zero at $r_c = 2$, this behavior left some SCO near the NC event horizon, and that is agree with what we find in the above discussion (see Table. 4.3) concerning the new stable photon sphere (see Fig. 4.17 and 4.18) around NC Schwarzschild BH, and the same observation can be found in other theory of non-commutativity as in Ref. [223], but in this theory the orbit is located inside the NC event horizon, which can't seen as new SCO of photons around NC Schwarzschild BH. In addition, the behavior of $\hat{\lambda}_c$ for some orbits r_c as a function of the NC parameter Θ is shown in the right panel of Fig. 4.19. As we see, in the NC spacetime, the orbit $r_c = 3$ is also unstable, and in this geometry, the instability of this orbit is greater than in the commutative case. For the other new circular orbit that emerged in the NC spacetime near the event horizon, there was less instability, and it decreased as Θ increased before going to zero for specified values of Θ. This indicates that some circular orbits near the event horizon in NC spacetime are stable.

Also, another quantity that measured the instability of the orbits was the so-called instability exponent of null circular orbits, where this quantity in NC spacetime is defined by the ratio of Lyapunov exponent $\hat{\lambda}_c^{Null}$ to angular frequency $\hat{\Omega}_c^{Null}$ in the coordinate time, which is given by the following expression:

$$\frac{\hat{\lambda}_c^{Null}}{\hat{\Omega}_c^{Null}} = \left(\frac{3(4m-r_c)}{r_c} + \left(\frac{O(r_c) + 6J(r_c)(8m^2-6mr_c+r_c^2) + 6G(r_c)(8m^2-6mr_c+r_c^2)\sqrt{1-\frac{2m}{r_c}}}{32(r_c-2m)^3 r_c^4} \right.\right.$$
$$\left.\left. + \frac{I(r_c)(8m^2-6mr_c+r_c^2)\sqrt{1-\frac{2m}{r_c}}}{32(r_c-2m)^3 r_c^4} \right) \Theta^2 \right)^{1/2} . \tag{4.50}$$

In Fig. 4.20, we show the behavior of the ratio $\hat{\lambda}_c^{Null}/\hat{\Omega}_c^{Null}$ as a function of r_c for different

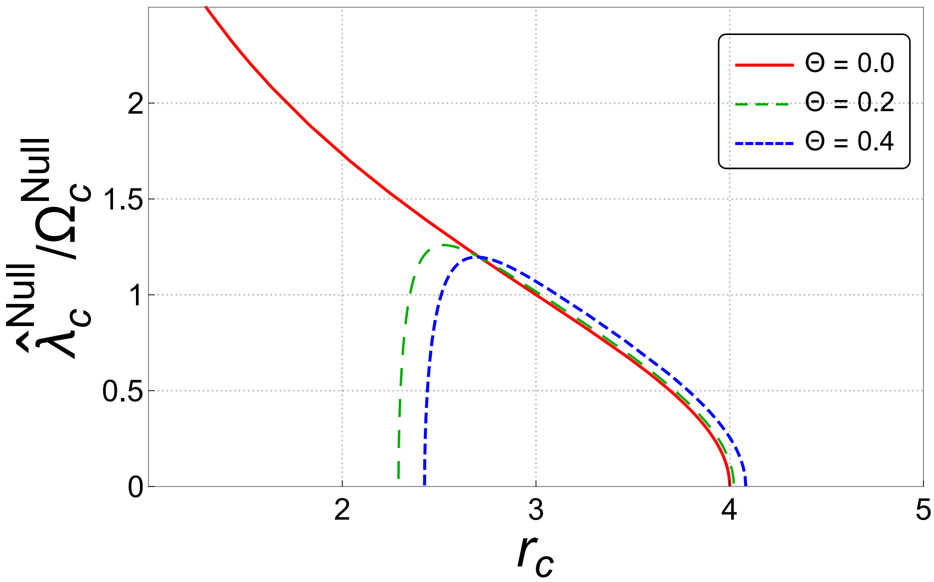

Figure 4.20: The behavior of $\frac{\hat{\lambda}_c^{Null}}{\hat{\Omega}_c^{Null}}$ as a function of r_c.

NC parameter Θ. It is clear that, in the NC case (for $\Theta \neq 0$), we observe the same behavior as in Fig. 4.19, while this behavior disappears when $\Theta = 0$ (in the commutative case), which means the orbits near the event horizon in the NC spacetime are stable, contrary to the results obtained in Ref. [223].

Finally, we check the behavior critical exponent $\hat{\gamma}$ as a final analysis of the null circular orbit instability around NC Schwarzschild BH, which is defined as a ratio of the Lyapunov timescale $\hat{T}_{\hat{\lambda}} = \frac{1}{\hat{\lambda}}$ to the orbital timescale $\hat{T}_{\hat{\Omega}} = \frac{2\pi}{\hat{\Omega}}$ [34–36], in this case we find

$$\hat{\gamma}^{Null} = \frac{T_{\hat{\lambda}}^{Null}}{T_{\hat{\Omega}}^{Null}} = \frac{1}{2\pi\sqrt{\frac{3(4m-r_c)}{r_c} + \left(\frac{O(r_c)+6J(r_c)(8m^2-6mr_c+r_c^2)+(I(r_c)+6G(r_c)(8m^2-6mr_c+r_c^2))\sqrt{1-\frac{2m}{r_c}}}{32(r_c-2m)^3 r_c^4} \right)\Theta^2}} . \tag{4.51}$$

The commutative expression can be obtained when $\Theta = 0$.

Numerical values of the critical exponent $\hat{\gamma}^{Null}$ for different ranges of the photon orbit r_c with different NC parameter Θ are shown in Table. 4.4. It is clear that $\hat{\gamma}^{Null}$ in this table shows both real and imaginary values, in which the real positive values of this quantity for

Table 4.4: Some numerical values of the critical exponent $\hat{\gamma}^{Null}$ for unstable r_{uns} and new stable circular orbit r_{sta} of photon sphere in the NC spacetime with different parameter Θ with $m = 1$.

	Θ	$r_c = 3$	$r_c = 2.4$	$r_c = 2.3$	$r_c = 2.2$
	0.0	0.159155	//	//	//
	0.1	0.158439	0.117291	0.121293	0.251639
$\hat{\gamma}^{Null}$	0.2	0.156349	0.136225	0.328429	0. -0.0662942 i
	0.3	0.153042	0.210585	0. -0.10626 i	0. -0.0397438 i
	0.4	0.148746	0.-0.216564 i	0. -0.0665877 i	0. -0.0288573 i

the different range of r_c correspond to unstable circular orbits [35], while the imaginary ones correspond to the stable ones. It is worth noting that the photon sphere located at $r_c = 3$ around the Schwarzschild BH is always unstable in both commutative and NC spacetime. Moreover, this instability means that the Lyapunov timescale is shorter than the orbital timescale ($\hat{T}_{\hat{\lambda}} < \hat{T}_{\hat{\Omega}}$) [34] (see the definition (4.51)). Also, we show that the values of $\hat{\lambda}^{Null}$ decrease when the NC parameter increases for $r_c = 3$, where that means the non-commutativity increases the instability of this orbit, where the smallest values of $\hat{\lambda}^{Null}$ indicate a strong Lyapunov instability [36], which agrees with our discussion for the right panel in Fig. 4.19, while the imaginary values that correspond to the SCO coincide with the new minimum of the effective potential for $l = 5.2$ (closer to the values of Table. 4.3), where that shows the stability of the new stable photon sphere around NC Schwarzschild BH and proves the instability of the external photon sphere in both geometry.

4.3.5 *Black hole shadow*

In which we are interested in studying the black hole shadow for one kind of motion of photons, which is the circular motion in the equatorial plane $\theta = \pi/2$, it is easy to show the relation between the black hole shadow R_{shadow} and the impact parameter D_c, which are related by the relation $R_{shadow} = D_c|_{r=r_{ps}}$, where r_{ps}^{uns} is the radius of the external unstable photon sphere (see Fig. 4.18), and it can be obtained by solving (4.20), the analytical solution to this condition in the leading order on Θ and m, written as follows:

$$r_{ps}^{uns} = 3m - \left(\frac{-38 + 540 D_c^2 m^2}{288\, m} \right) \Theta^2 . \tag{4.52}$$

It is worth noting that the new stable photon sphere can be obtained only by numerical solution (see Tab. 4.3), and their shadow can't be observed because the photon is orbiting in SCO around the NC Schwarzschild BH. Using this expression, we can express the radius of the NC Schwarzschild BH shadow.

$$R_{shadow} = 3\sqrt{3}m \left(1 + \frac{(1 + 2\sqrt{3})}{72\, m^2} \Theta^2 \right) . \tag{4.53}$$

When $\Theta = 0$, we obtain the commutative expression.

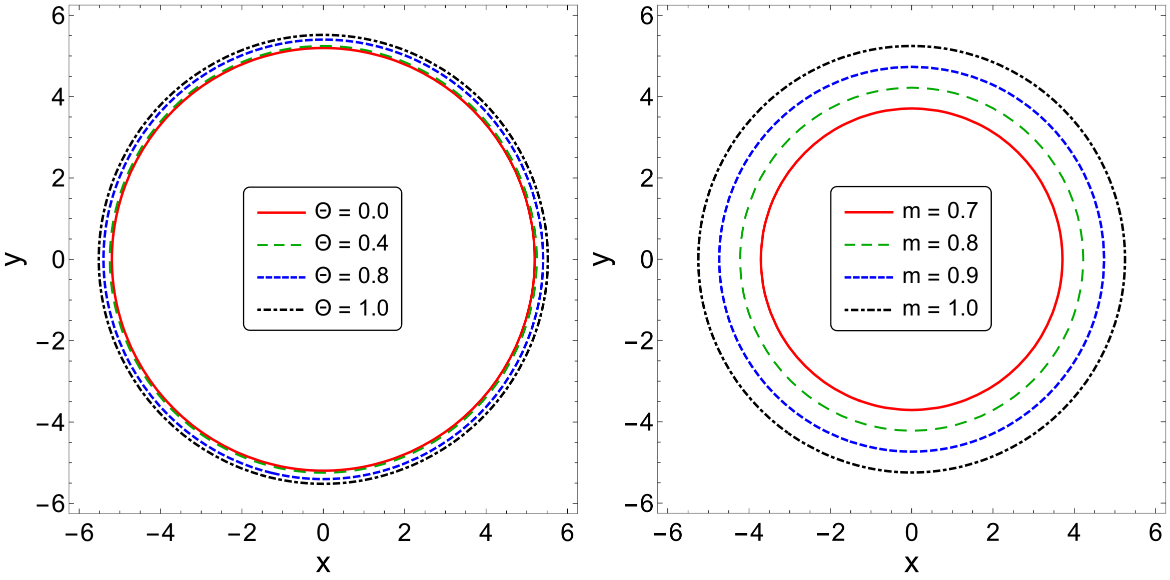

Figure 4.21: The Schwarzschild black hole shadow in the NC spacetime, for different values of NC parameter Θ (left panel) with $m = 1$, and for different values of black hole mass m (right panel) with $\Theta = 0.4$.

The influence of the NC parameter (left panel) and the BH mass (right panel) on the radius of the NC Schwarzschild BH shadow is depicted in Fig. 4.21. It is clear that, in the left panel, the non-commutativity increases the radius of the NC Schwarzschild BH shadow, in which this radius increases with increasing Θ, and we can see the same observation in the right panel for the fixed Θ and increasing in the BH mass m. Moreover, the effect of non-commutativity on the shadow radius is similar to the effect of black hole mass, where the NC parameter plays a similar role as a mass, and that's what we expected in our previous discussion (see 3 and SubSec. 4.2.3), and that means the non-commutativity increases the gravitational field. It is worth noting that the same observation on the noncommutativity effect on the radius of the BH shadow was obtained in [166], in which the authors used the NC correction to the black hole mass using gauge theory of gravity with negligence of the deformed metric in the calculation. However, in our case, we use the gauge theory and the non-diagonal tetrad matrix to calculate the NC Schwarzschild metric, which is used in our calculation to describe the radius of the NC Schwarzschild BH shadow, and the same effect is observed in both approaches.

4.4 NON-COMMUTATIVE REISSNER-NORDSTRÖM SPACETIME

On the equatorial plane $\theta = \frac{\pi}{2}$, around a deformed R-N black hole is described by the line element (4.1). In this case, the components of the deformed metric $\hat{g}_{\mu\nu}$ for $a = 0$ and $b = \Theta$ are given by

$$\begin{aligned}
-\hat{g}_{00} = {} & \left(1 - \frac{2m}{r} + \frac{Q^2}{r^2}\right) + \Bigg\{ \frac{2Q^2r^2\left(-15m\left(-7+\sqrt{1-\frac{2m}{r}+\frac{Q^2}{r^2}}\right) - 56Q^6 - 284Q^2r^2m^2\right)}{32r^6(Q^2-2mr+r^2)} \\
& + \frac{mr^3\left(88m^2 - 8r^2\left(-2+\sqrt{1-\frac{2m}{r}+\frac{Q^2}{r^2}}\right) + mr\left(-77+15\sqrt{1-\frac{2m}{r}+\frac{Q^2}{r^2}}\right)\right)}{32r^6(Q^2-2mr+r^2)} \\
& + \frac{12Q^2r^4\left(-3+\sqrt{1-\frac{2m}{r}+\frac{Q^2}{r^2}}\right)}{32r^6(Q^2-2mr+r^2)} \Bigg\} \Theta^2 + \mathcal{O}(\Theta^4)
\end{aligned} \tag{4.54a}$$

$$\begin{aligned}
\hat{g}_{11} = {} & \left(1 - \frac{2m}{r} + \frac{Q^2}{r^2}\right)^{-1} + \Bigg\{ \frac{(Q^2-mr)^2\left(8Q^2 - r\left(16m + r\left(-17+\sqrt{1-\frac{2m}{r}+\frac{Q^2}{r^2}}\right)\right)\right)}{32r^2(Q^2-2mr+r^2)^2} \\
& + \frac{r\left(-m^2r - 3Q^2r + 2m\left(Q^2+r^2\right)\right)\left(-4Q^2 + r\left(8m + r\left(5+\sqrt{1-\frac{2m}{r}+\frac{Q^2}{r^2}}\right)\right)\right)}{32r^2(Q^2-2mr+r^2)^3} \Bigg\} \Theta^2 + \mathcal{O}(\Theta^4)
\end{aligned} \tag{4.54b}$$

$$\begin{aligned}
\hat{g}_{22} = {} & r^2 + \Bigg\{ \frac{8Q^6 + mr^3\left(-8m^2 + 2mr\left(5-3\sqrt{1-\frac{2m}{r}+\frac{Q^2}{r^2}}\right) + r^2\left(-3+5\sqrt{1-\frac{2m}{r}+\frac{Q^2}{r^2}}\right)\right)}{16r^2(Q^2-2mr+r^2)^2} \\
& + \frac{Q^2r^2\left(r^2\left(7-5\sqrt{1-\frac{2m}{r}+\frac{Q^2}{r^2}}\right) + 3mr\left(-11+3\sqrt{1-\frac{2m}{r}+\frac{Q^2}{r^2}}\right)\right) - 32Q^4mr + 36Q^2m^2r^2}{16r^2(Q^2-2mr+r^2)^2} \\
& - \frac{Q^4r\left(3r\left(-5+\sqrt{1-\frac{2m}{r}+\frac{Q^2}{r^2}}\right)\right)}{16r^2(Q^2-2mr+r^2)^2} \Bigg\} \Theta^2 + \mathcal{O}(\Theta^4)
\end{aligned} \tag{4.54c}$$

$$\begin{aligned}
\hat{g}_{33} = {} & r^2 + \Bigg\{ \frac{Q^2r^2\left(184m^2 + 3r^2\left(16-11\sqrt{1-\frac{2m}{r}+\frac{Q^2}{r^2}}\right) + mr\left(-188+39\sqrt{1-\frac{2m}{r}+\frac{Q^2}{r^2}}\right)\right)}{16r^2(Q^2-2mr+r^2)^2} \\
& + \frac{r^3\left(2r^3\left(5-3\sqrt{1-\frac{2m}{r}+\frac{Q^2}{r^2}}\right) - 18m^2r\left(-6+\sqrt{1-\frac{2m}{r}+\frac{Q^2}{r^2}}\right) + 29mr^2\sqrt{1-\frac{2m}{r}+\frac{Q^2}{r^2}}\right)}{16r^2(Q^2-2mr+r^2)^2} \\
& + \frac{Q^4r\left(-135m + r\left(68-11\sqrt{1-\frac{2m}{r}+\frac{Q^2}{r^2}}\right)\right) + 30Q^6 - 68m^3r^3 - 57mr^2}{16r^2(Q^2-2mr+r^2)^2} \Bigg\} \Theta^2 + \mathcal{O}(\Theta^4)
\end{aligned} \tag{4.54d}$$

This deformed metric is used as background for the study of geodesic in the equatorial plan around the RN BH in the next sections.

For a Lagrangian of a massive neutral particle moving the NC RN spacetime, it can be written as for the Schwarzschild case (4.3), where use the above deformed metric of RN spacetime. Since the same Lagrangian is independent of t and ϕ, we have the same two conserved quantities, (1.14) and (1.15), where we use the components $\hat{g}_{00}$ and $\hat{g}_{33}$ given by (4.54a) and (4.54d), respectively. The NC effective potential of massive neutral particle in NC RN spacetime can be obtained following the same steps in previous section Sec. 4.2, and it can be obtained by substituting the components (4.54a), (4.54b), and (4.54d) into the equation (4.10), then we get

$$
\begin{aligned}
V_{eff}(r,\Theta) = {} & \left(1-\frac{2m}{r}+\frac{Q^2}{r^2}\right)\left(\frac{l^2}{r^2}+h\right)-E^2+\Theta^2\Bigg\{E^2\Bigg(\frac{2mQ^2r^3\left(77-13\sqrt{1-\frac{2m}{r}+\frac{Q^2}{r^2}}\right)}{16r^4(Q^2+-2mr+r^2)^2}\\
& +\frac{3Q^2r^4\left(-17+3\sqrt{1-\frac{2m}{r}+\frac{Q^2}{r^2}}\right)+2Q^4r^2\left(-32+5\sqrt{1-\frac{2m}{r}+\frac{Q^2}{r^2}}\right)+64m^3r^3-48Q^6}{16r^4(Q^2+-2mr+r^2)^2}\\
& +\frac{192mQ^4r-224m^2Q^2r^2-m^2r^4\left(49-13\sqrt{1-\frac{2m}{r}+\frac{Q^2}{r^2}}\right)+2mr^5\left(13-3\sqrt{1-\frac{2m}{r}+\frac{Q^2}{r^2}}\right)}{16r^4(Q^2+-2mr+r^2)^2}\Bigg)\\
& -\left(h+\frac{l^2}{r^2}\right)\Bigg(\frac{\left((-4Q^2+8mr)+r^2\left(5+\sqrt{1-\frac{2m}{r}+\frac{Q^2}{r^2}}\right)\right)r(-m^2r-3Q^2r+2m(q^2+r^2))}{16r^6(Q^2+-2mr+r^2)}\\
& +\frac{8Q^2(Q^2-mr)^2-r(Q^2-mr)^2\left(16m+r\left(-17+\sqrt{1-\frac{2m}{r}+\frac{Q^2}{r^2}}\right)\right)}{16r^6(Q^2+-2mr+r^2)}\Bigg)\\
& -\frac{l^2}{r^4}\Bigg(\frac{Q^2r\left(m\left(39-75\sqrt{1-\frac{2m}{r}+\frac{Q^2}{r^2}}\right)+r\left(-33+38\sqrt{1-\frac{2m}{r}+\frac{Q^2}{r^2}}\right)\right)-11Q^4}{16r^3\sqrt{Q^2+-2mr+r^2}}\\
& +\frac{30Q^4\sqrt{1-\frac{2m}{r}+\frac{Q^2}{r^2}}+r^2\left(mr\left(29-37\sqrt{1-\frac{2m}{r}+\frac{Q^2}{r^2}}\right)+2r^2\left(-3+5\sqrt{1-\frac{2m}{r}+\frac{Q^2}{r^2}}\right)\right)}{16r^3\sqrt{Q^2+-2mr+r^2}}\\
& +\frac{2mr^2\left(-9+17\sqrt{1-\frac{2m}{r}+\frac{Q^2}{r^2}}\right)}{16r^3\sqrt{Q^2+-2mr+r^2}}\Bigg)\Bigg\}+\mathcal{O}(\Theta^4)
\end{aligned}
\tag{4.55}
$$

When $\Theta \to 0$, we recover the commutative effective potential [8].

$$
V_{eff}(r,\Theta=0)=\left(1-\frac{2m}{r}+\frac{Q^2}{r^2}\right)\left(\frac{l^2}{r^2}+h\right)-E^2 \tag{4.56}
$$

and for the case $Q=0$, we obtain the previous NC effective potential in the Schwarzschild spacetime (4.12).

4.5 TIME-LIKE GEODESIC MOTION OF NEUTRAL PARTICLE AROUND A NC RN BLACK HOLE

In which follow, we investigate the effect of this geometry on the circular motion for the case of a uncharged/charged massive test particle around the NC RN BH, where we present a detailed analysis of this kind of motion.

4.5.1 *Circular orbit and stability condition*

The orbital motion of a neutral massive test particle around the NC RN BH is studied by analyzing the behavior of the NC effective potential (4.55) with $l \neq 0$ and $h = 1$, $c = 1$. The behavior of the commutative effective potential of a neutral massive particle is shown in Fig. 4.22 for different values of parameters Q (left panel) and l (right panel). As we see in the left panel, the effective potential in the RN spacetime shows a new minimum, which means two minimums and one maximum, and that is similar to the NC Schwarzschild spacetime in Sec. 4.2 (see Fig. 4.4), where these two types of BH predict a new minimum in the effective potential. Moreover, the effective potential has always a minimum, whatever the values of l (right panel) in commutative RN spacetime. Unfortunately, this new minimum in the commutative RN spacetime is located inside the event horizon (see Ref. [220]), and that leads to a difficult physical interpretation where we can't see it as new orbits. The influence of parameters (Q, Θ, and l) on the NC effective potential of a neutral massive test particle as a function of r is shown in Figs. 4.23 and 4.24. It is clear that, in NC RN spacetime, this minimum is shifted outside the event horizon as in the Schwarzschild case (see Fig. 4.4), so that can be seen as a new SCO near the event horizon in the same way as the Schwarzschild black hole in Sec. 4.2. Unlike in the commutative charged BH, where this minimum is always inside the event horizon whatever the values of Q and l, [211, 212, 219, 220, 226]. As we see, the increase in the NC parameter Θ for the Q constant

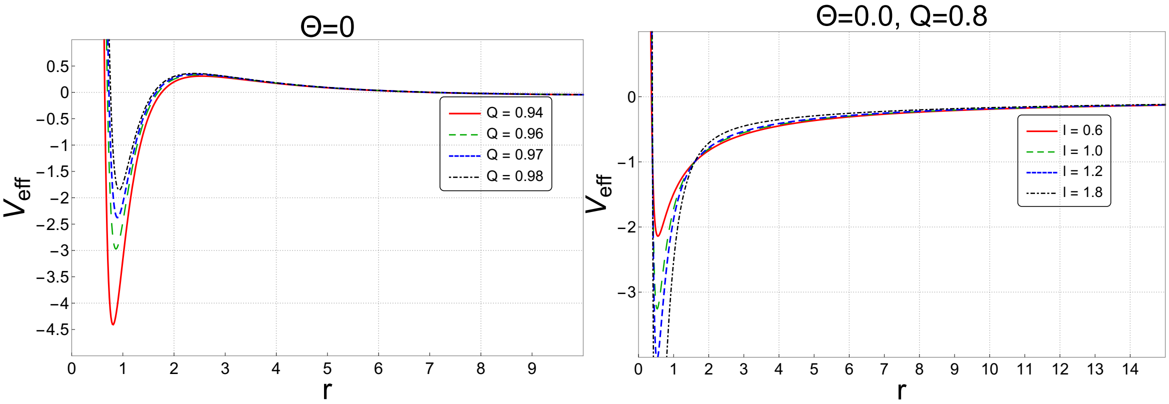

Figure 4.22: The behaviors of the commutative effective potential $\Theta = 0$ for a massive particle as a function of r. **Left panel:** different Q and fixed: $E = 0.998$, $m = 1$, $l = 4.2$. **Right panel:** different l and fixed: $E = 0.998$, $Q = 0.8$, $m = 1$.

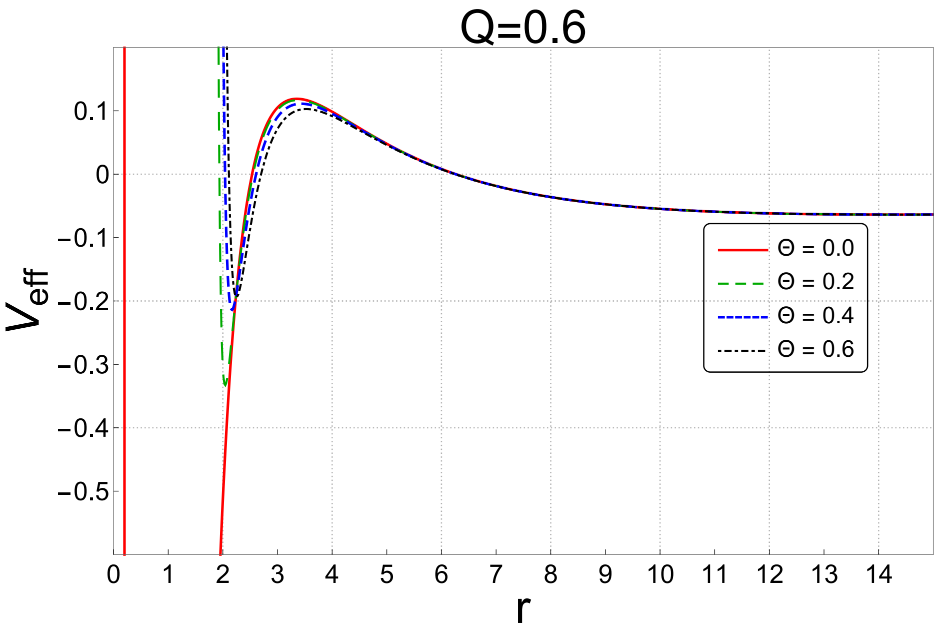

Figure 4.23: The behaviors of the NC effective potential for a massive particle as a function of r, with different Θ and fixed: $E = 0.998$, $m = 1$, $l = 4.2$.

leads to a decrease in the pick of the maximum and depth of the new minimum, which are shifted off the event horizon.

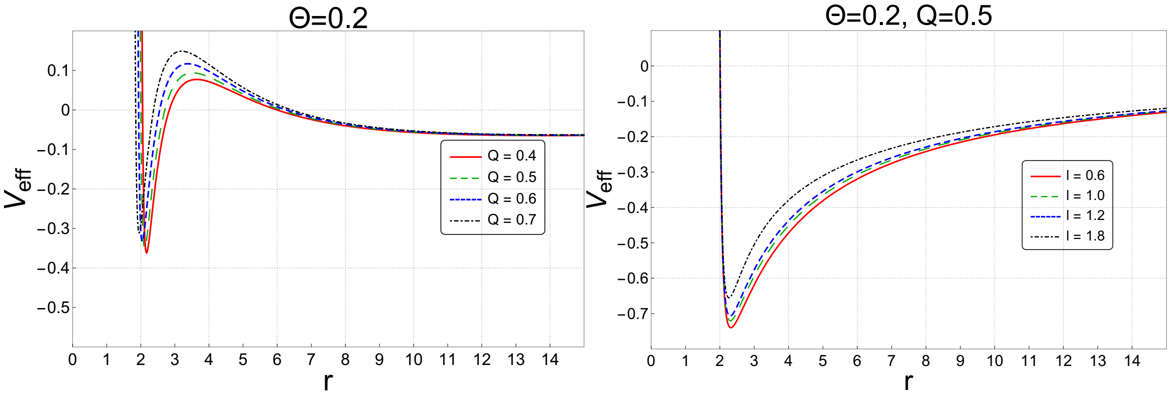

Figure 4.24: The behaviors of the NC effective potential for a massive particle as a function of r. **Left panel:** different Q and fixed: $E = 0.998$, $m = 1$, $l = 4.2$, $\Theta = 0.2$. **Right panel:** different l and fixed: $E = 0.998$, $m = 1$, $Q = 0.5$, $\Theta = 0.2$.

While, when we increase in the electric charge Q and we take a NC parameter constant (left panel Fig. 4.24), the maximum of the effective potential increases and the depth of this new minimum decreases compared to the commutative case. Also in the NC case of RN spacetime, the effective potential always has a minimum, whatever the value of l, and we can see that the depth of this minimum is smaller compared to the commutative case (see right panel Fig. 4.22). Note that, when we increase the angular momentum l, the depth of the minimum decreases and remains closer to the event horizon in the outside region. In addition, the NC parameter Θ can be seen to play an inverse role of the electric charge Q, but there is some similarity between them, and in this geometry, the new minimum is now shifted outside the event horizon for the RN black hole and gives us a multiple SCO separated by an unstable region, and this indicates that the non-commutativity solves the problem posed in Ref. [220] and leads to a new prediction of stable orbits near the event horizon. In addition, the RN spacetime is similar to the NC Schwarzschild spacetime for uncharged particles (see Fig. 4.4 and 4.22).

In order to obtain the circular orbits in this geometry, our effective potential must satisfy the following conditions, which are given by (4.19) and (4.20).

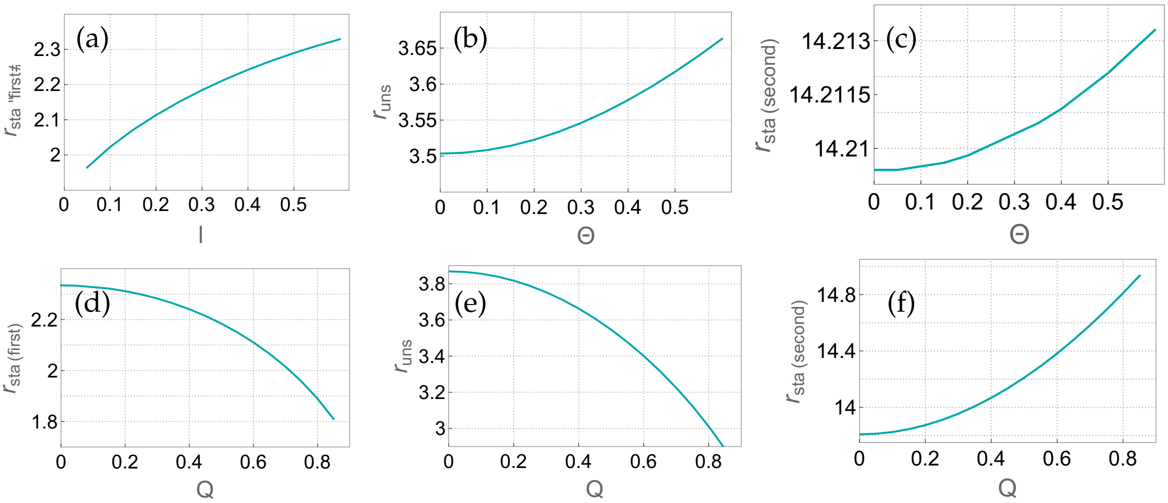

Figure 4.25: The behaviors of the radius of circular orbits for a particle in the NC RN spacetime. Unstable and multiple stable circular orbit as function of Θ and for fixed $l = 4.2$, $E = 0.998$, $m = 1$, $Q = 0.5$ in (a), (b) and (c), and as function of Q and for fixed $\Theta = 0.3$, $E = 0.998$, $l = 4.2$, $m = 1$ in (d), (e) and (f).

It is clear that, from Fig. 4.25, we can see that all types of circular motion (unstable and multiple stable) around the NC RN BH have the same behaviors as a function of Θ, in which their increases with Θ increases, while for increasing in the electric charge Q, the first stable and the unstable circular orbits decrease, and the second SCO increases.

The stability of these orbits and the ISCO for a massive neutral test particle can be obtained by the condition (4.21), which must be satisfied by the effective potential. The numerical solution to this condition in the commutative RN spacetime shows that, for $l^{C}_{ISCO} = 2\sqrt{2.785123}$ and $Q = 0.5$, we get $r^{C}_{ISCO} \geqslant 5.60664$, while in the NC RN spacetime, for $\Theta = 0.3$ and $l^{NC}_{ISCO} = 2\sqrt{2.78732967}$ we get two of region of SCO $r^{NC}_{h} \ll r^{NC}_{SCO} \leqslant 2.45336$ and $r^{NC}_{SCO} \geqslant 5.62175$ and separated by unstable region $2.45336 < r_c < 5.62175$, where that is correspond to a multiple SCO around NC RN BH.

As we can see, non-commutativity predicted a new SCO near the event horizon in the both NC Schwarzschild spacetime (see Sec. 4.2) and in the NC RN spacetime. A similar result can be found in Refs. [227, 228].

Let's now define the expression of the energy E^2_c and angular momentum l^2_c for this kind of motion of a neutral massive test particle. These quantities can be obtained using

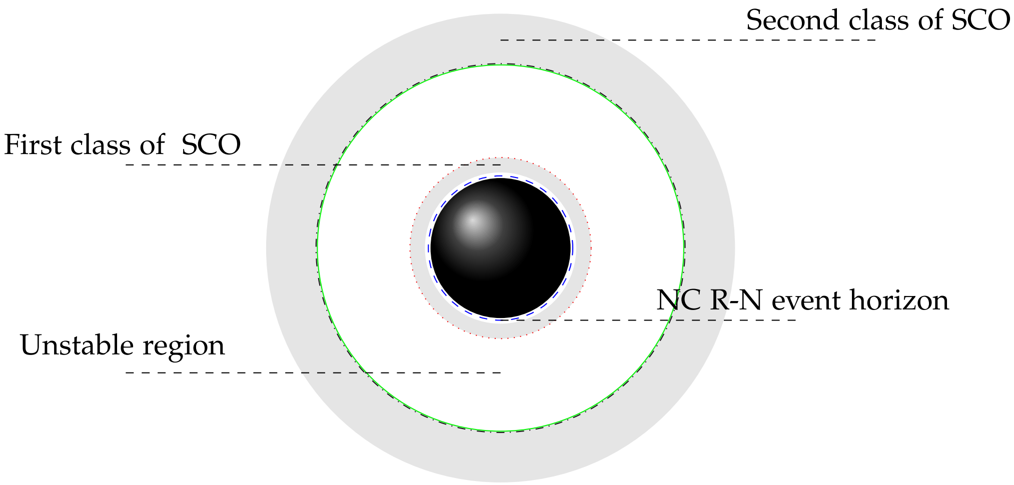

Figure 4.26: The first and second bound of stable circular orbits around the NC RN black hole.

the conditions (4.19), (4.20), and (4.21). Their expressions in the leading order in Θ are written as follows:

$$E_c^2 \simeq \frac{(Q^2-2mr_c+r_c^2)^2}{r_c^2(2Q^2-3mr_c+r_c^2)} + \left(\frac{\mathcal{X}(r_c)+\mathcal{G}(r_c)\sqrt{1-\frac{2m}{r_c}+\frac{Q^2}{r_c}}}{32r_c^6(2Q^2-3mr_c+r_c^2)^2\sqrt{1-\frac{2m}{r_c}+\frac{Q^2}{r_c}}} \right)\Theta^2 + \mathcal{O}(\Theta^4), \tag{4.57a}$$

$$l_c^2 \simeq \frac{(mr_c^3-Q^2r_c^2)}{2Q^2-3mr_c+r_c^2} + \left(\frac{\mathcal{W}(r_c)+\mathcal{V}(r_c)\sqrt{1-\frac{2m}{r_c}+\frac{Q^2}{r_c^2}}}{32r_c^2\mathcal{V}_0(r_c)^2(Q^2+r_c(-2m+r_c))\sqrt{1-\frac{2m}{r_c}+\frac{Q^2}{r_c^2}}} \right)\Theta^2 + \mathcal{O}(\Theta^4). \tag{4.57b}$$

where the functions $\mathcal{X}(r_c)$, $\mathcal{G}(r_c)$, $\mathcal{W}(r_c)$, $\mathcal{V}(r_c)$ and $\mathcal{V}_0(r_c)$ are provided in Appendix B.1.

At the limit $\Theta \to 0$, we recover the commutative case of a neutral particle in RN spacetime [219, 229], and the Schwarzschild case (see (4.22) and (4.23)) can be recovered when we set $Q = 0$.

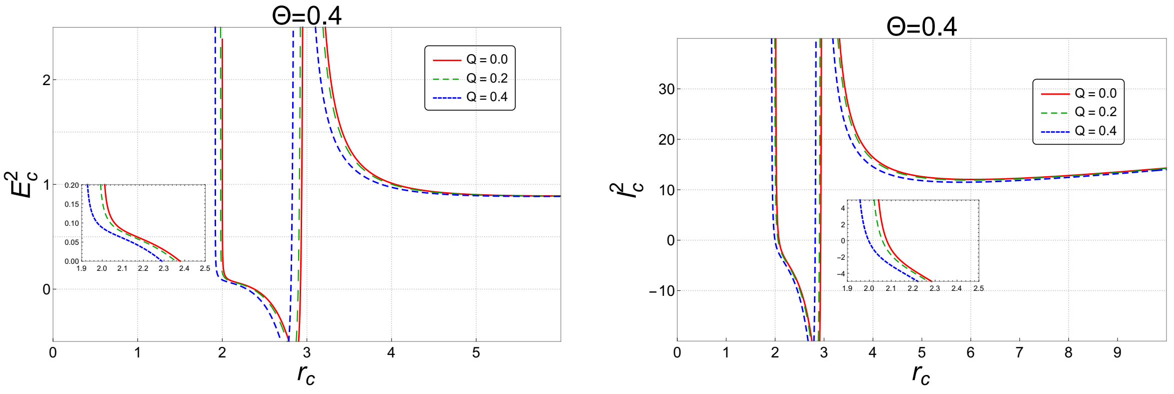

Figure 4.27: Radial dependence of the energy E_c^2 (left panel) and the angular momentum l_c^2 (right panel) of a neutral test particle orbiting around an NC RN black hole, for different values of electric charge Q and for fixed NC parameter Θ.

Fig. 4.27 shows the behaviors of the energy E_c^2 (left panel) and the angular momentum l_c^2 (right panel) of a circular orbit for a neutral particle around the NC RN BH as a function of r, with fixed Θ and different values of the electric charge Q. It is clear that, in NC RN spacetime, we get a new behavior on the energy E_c^2 and the angular momentum l_c^2, as well as in the case of NC Schwarzschild spacetime, where we have a new region of positive values of $E_c^2 > 0$ and $l_c^2 > 0$ near the event horizon compared to the unphysical region in the commutative case (where E_c^2 and l_c^2 are negatives), and that explains the emerge of the new SCO in this geometry. As we see, the effect of the electric charge Q in the NC spacetime is significant in the energy and the angular momentum, in which the behavior of these two quantities is shifted toward the event horizon, and that gives us more condition on the circular orbits.

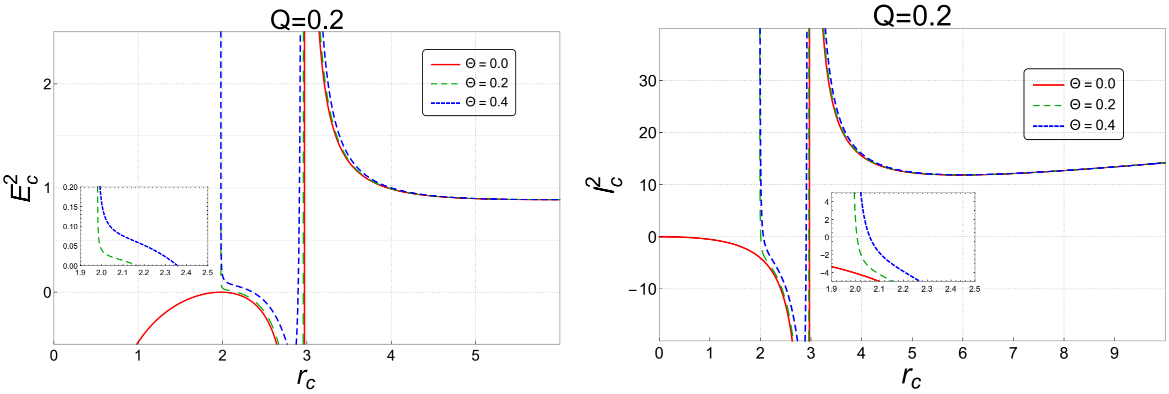

Figure 4.28: Radial dependence of the energy E_c^2 (left panel) and the angular momentum l_c^2 (right panel) of a neutral test particle orbiting around an NC RN black hole, for different values of NC parameter Θ and for fixed electric charge Q.

The effect of the NC parameter on the behaviors of the energy E_c^2 (left panel) and the angular momentum l_c^2 (right panel) is shown in Fig. 4.28. It is clear that the more we increase in Θ, the more we get new SCO near the event horizon, where the increase of Θ, the behaviors of E_c^2, and l_c^2 are shifted away from the event horizon.

4.5.2 *NC effect on the orbital motion*

In order to obtain a geodesic equation of a neutral massive particle ($h = m_0^2$) in the NC RN spacetime, we follow the same steps in SubSec. 4.2.4, where we use the radial equation (4.34) together with the deformed metric component (4.54d) and the effective potential (4.55). Let's use the new variable defined by $u = \frac{1}{r}$ and use the fact that $mu \ll 1$ and $\Theta \ll 1$ in order to write our equation in linear form. Then we stop at the 3^{rd} order in u in the NC correction term, and with some algebra, the orbital equation can be written as follows:

$$\left(\frac{du}{d\phi}\right)^2 = \frac{(E^2 - m_0^2c^2)}{l^2} + \frac{2mm_0^2c^2}{l^2}u - u^2 - \frac{Q^2m_0^2c^2}{l^2}u^2 + 2mu^3 - Q^2u^4 + \frac{\Theta^2}{2l^2}\left\{(E^2 - m_0^2c^2)u^2 + m(5m_0^2c^2 - 4E^2)u^3\right\} \tag{4.58}$$

Derive the above equation with respect to ϕ; in this case, the NC geodesic equation around a RN BH for a neutral particle is given by

$$\frac{d^2u}{d\phi^2} + \omega'^2 u = \frac{mm_0^2c^2}{l^2} + 3m'u^2 - 2Q^2u^3 \tag{4.59}$$

with

$$\omega'^2 = 1 + \frac{Q^2m_0^2c^2}{l^2} - \frac{\Theta^2}{2l^2}(E^2 - m_0^2c^2), \tag{4.60a}$$

$$m' = m\left[1 + \Theta^2\left(\frac{5m_0^2c^2 - 4E^2}{4l^2}\right)\right]. \tag{4.60b}$$

Not that, when $Q = 0$, we get the geodesic equation in the NC Schwarzschild spacetime (4.39), and for $\Theta = 0$, we get the usual equation of massive test particles in the Schwarzschild spacetime [8, 179].

The general solution to this equation can be expressed by using the approximation solution [224].

$$u(\phi) = \frac{mm_0^2}{l^2\omega'^2}\left(1 + e\cos\left(\omega'\phi - \frac{3m'mm_0^2}{l^2\omega'^3}\left(1 - \frac{Q^2}{l^2}\right)\phi\right)\right). \tag{4.61}$$

In Fig. 4.29, we show the circular orbit motion of a neutral massive test particle in the NC RN spacetime, described by the geodesic solution (4.61), with a given $m = 3/14$, $E = 0.993$, l, Q, and Θ (black dashed-line), and compared to the commutative case $\Theta = 0$ (blue solid-line) and uncharged black hole $Q = 0$ (left panel). It is clear that the non-commutativity effect is negligible for a large value of l; in both cases, Schwarzschild BH $Q = 0$ (left panel) and RN BH $Q = 0.2$ (right panel).

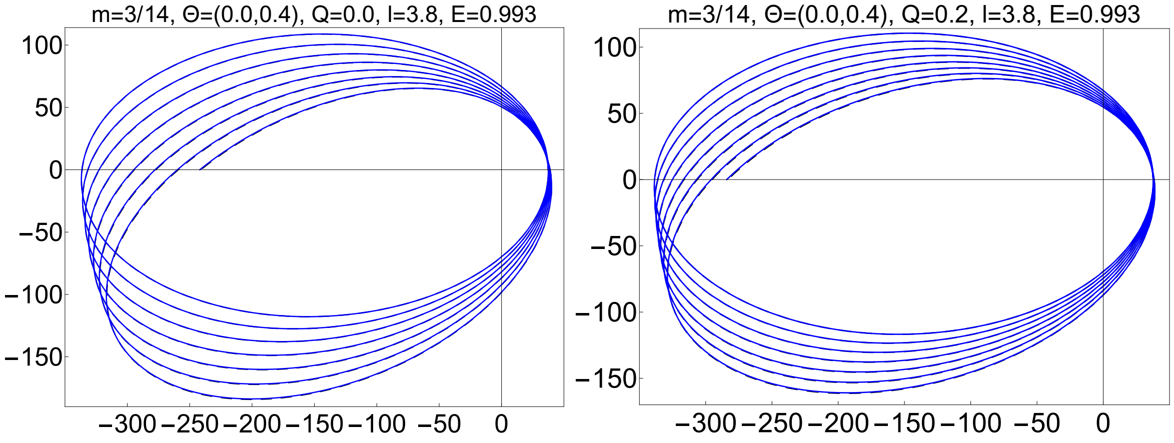

Figure 4.29: Time-like geodesic for a massive particle around Schwarzschild black hole $Q = 0$ and RN black hole $Q = 0.2$ with $m = 3/14$, $E = 0.993$, $l = 3.8$, and $\Theta = 0, 0.4$.

Some of the periodic orbits of a neutral massive test particle around the NC RN BH are shown in Fig. 4.30, where the plots are made with different l, Q, and Θ for a given m, E.

Here we examine the NC effect in the Schwarzschild BH $Q = 0$ and RN one $Q \neq 0$ for the periodic orbits. As we see, for a smaller value of l, the non-commutativity affected the particle motion, whereas the NC geometry affected only the periastron advance of the particle orbit in both cases of RN/Schwarzschild BH.

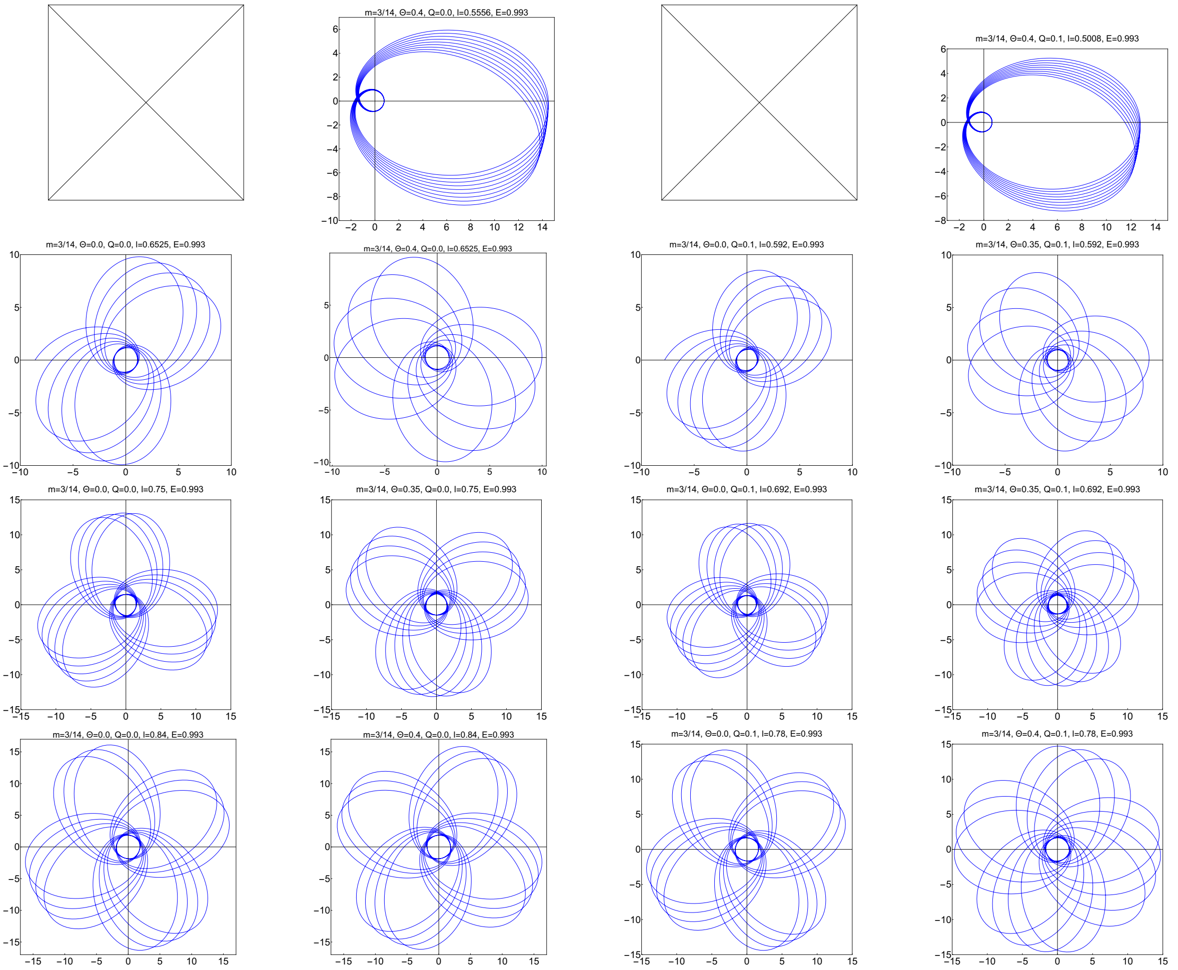
m=3/14, Θ=0.4, Q=0.0, l=0.5556, E=0.993

m=3/14, Θ=0.4, Q=0.1, l=0.5008, E=0.993

m=3/14, Θ=0.0, Q=0.0, l=0.6525, E=0.993

m=3/14, Θ=0.4, Q=0.0, l=0.6525, E=0.993

m=3/14, Θ=0.0, Q=0.1, l=0.592, E=0.993

m=3/14, Θ=0.35, Q=0.1, l=0.592, E=0.993

m=3/14, Θ=0.0, Q=0.0, l=0.75, E=0.993

m=3/14, Θ=0.35, Q=0.0, l=0.75, E=0.993

m=3/14, Θ=0.0, Q=0.1, l=0.692, E=0.993

m=3/14, Θ=0.35, Q=0.1, l=0.692, E=0.993

m=3/14, Θ=0.0, Q=0.0, l=0.84, E=0.993

m=3/14, Θ=0.4, Q=0.0, l=0.84, E=0.993

m=3/14, Θ=0.0, Q=0.1, l=0.78, E=0.993

m=3/14, Θ=0.4, Q=0.1, l=0.78, E=0.993

Figure 4.30: Periodic orbits of neutral massive particle around Schwarzschild and Reissner-Nordeström black hole for fixed mass $m = 3/14$ and energy $E = 0.993$ and varying other parameters l, Q, and Θ.

4.6 TIME-LIKE GEODESIC EQUATION OF CHARGED PARTICLE AROUND A RN BLACK HOLE

In which follow we investigate the motion of a charged massive test particle around the NC RN BH, and its motion can be described by the following Lagrangian

$$\hat{\mathcal{L}} = \frac{1}{2}\hat{g}_{\mu\nu}\dot{x}^{\mu}\dot{x}^{\nu} + q\hat{A}_{\mu}\dot{x}^{\mu} = \frac{1}{2}\left(\hat{g}_{tt}(r,\Theta)c^2\dot{t}^2 + \hat{g}_{rr}(r,\Theta)\dot{r}^2 + \hat{g}_{\phi\phi}(r,\Theta)\dot{\phi}^2\right) + q\hat{A}_t\dot{t} \tag{4.62}$$

where q is the electric charge of the test particle, and $\hat{A}_t$ is the NC electric potential deformed via the SW maps [160], which generated by the NC RN BH (see SubSec. 2.2.3). For a statically charged BH, the only potential generated by the total electric charge Q is the Coulomb potential.

$$\hat{A}_t = A_t + A_t^{(1)} + A_t^{(2)} + ..., \tag{4.63}$$

where A_t is the commutative Coulomb potential, and $A_t^{(1)}$ and $A_t^{(2)}$ are the first and second order corrections in Θ obtained by using SW map, as defined in Eqs. (2.25b) and (2.26b), respectively. For our choice of NC parameter matrix and the Coulomb potential, the NC corrections to the deformed potential are zero: $A_t^{(1)} = A_t^{(2)} = 0$, and that means $\hat{A}_t = A_t = \frac{Q}{r}$. However, for the non-static BH or another type of potential, we the NC corrections must be considered in the calculation.

From our Lagrangian (4.62), we get two conserved quantities, which are

$$\dot{t} = \frac{E_0 - qA_t}{c^2 \hat{g}_{tt}(r,\Theta)}, \quad \dot{\phi} = \frac{l}{\hat{g}_{\phi\phi}(r,\Theta)} \tag{4.64}$$

Using these conserved quantities together with the invariant quantity $\hat{g}_{\mu\nu}\dot{x}^\mu \dot{x}^\nu = -h$, after some algebra, we find

$$\dot{r}^2 = -\frac{\left(E - \frac{q}{c}A_t\right)^2}{\hat{g}_{tt}(r,\Theta)\hat{g}_{rr}(r,\Theta)} - \frac{1}{\hat{g}_{rr}(r,\Theta)}\left(\frac{l^2}{\hat{g}_{\phi\phi}(r,\Theta)} + hc^2\right) \tag{4.65}$$

and the deformed effective potential at the second-order in Θ is written as follows:

$$\begin{aligned}
V_{eff}(r,\Theta) = {} & \left(1 - \frac{2m}{r} + \frac{Q^2}{r^2}\right)\left(\frac{l^2}{r^2} + h\right) - \left(E - \frac{qQ}{c\,r}\right)^2 + \Theta^2 \left\{ \left(\frac{2mQ^2r^3\left(77 - 13\sqrt{1 - \frac{2m}{r} + \frac{Q^2}{r^2}}\right)}{16r^4(Q^2 + -2mr + r^2)^2} \right.\right. \\
& + \frac{192mQ^4r - 48Q^6 - 3Q^2r^4\left(17 - 3\sqrt{1 - \frac{2m}{r} + \frac{Q^2}{r^2}}\right) - 2Q^4r^2\left(32 - 5\sqrt{1 - \frac{2m}{r} + \frac{Q^2}{r^2}}\right)}{16r^4(Q^2 + -2mr + r^2)^2} \\
& \left. + \frac{64m^3r^3 - 224m^2Q^2r^2 - m^2r^4\left(49 - 13\sqrt{1 - \frac{2m}{r} + \frac{Q^2}{r^2}}\right) + 2mr^5\left(13 - 3\sqrt{1 - \frac{2m}{r} + \frac{Q^2}{r^2}}\right)}{16r^4(Q^2 + -2mr + r^2)^2} \right) \\
& \times \left(E - \frac{qQ}{c\,r}\right)^2 - \left(\frac{8Q^2(Q^2 - mr)^2 - r(Q^2 - mr)^2\left(16m + r\left(-17 + \sqrt{1 - \frac{2m}{r} + \frac{Q^2}{r^2}}\right)\right)}{16r^6(Q^2 + -2mr + r^2)} \right. \\
& \left. + \frac{r(-m^2r - 3Q^2r + 2m(Q^2 + r^2))\left((-4Q^2 + 8mr) + r^2\left(5 + \sqrt{1 - \frac{2m}{r} + \frac{Q^2}{r^2}}\right)\right)}{16r^6(Q^2 + -2mr + r^2)} \right) \\
& \times \left(\frac{l^2}{r^2} + hc^2\right) - \frac{l^2}{r^4}\left(\frac{2mr^2\left(-9 + 17\sqrt{1 - \frac{2m}{r} + \frac{Q^2}{r^2}}\right) + Q^4\left(-11 + 30\sqrt{1 - \frac{2m}{r} + \frac{Q^2}{r^2}}\right)}{16r^3\sqrt{Q^2 + -2mr + r^2}} \right. \\
& + \frac{r^2\left(mr\left(29 - 37\sqrt{1 - \frac{2m}{r} + \frac{Q^2}{r^2}}\right) + 2r^2\left(-3 + 5\sqrt{1 - \frac{2m}{r} + \frac{Q^2}{r^2}}\right)\right)}{16r^3\sqrt{Q^2 + -2mr + r^2}} \\
& \left.\left. + \frac{Q^2r\left(m\left(39 - 75\sqrt{1 - \frac{2m}{r} + \frac{Q^2}{r^2}}\right) + r\left(-33 + 38\sqrt{1 - \frac{2m}{r} + \frac{Q^2}{r^2}}\right)\right)}{16r^3\sqrt{Q^2 + -2mr + r^2}} \right) \right\}.
\end{aligned} \tag{4.66}$$

Not that for the commutative case $\Theta = 0$, we obtain the ordinary effective potential.

$$V_{eff}(r,\Theta = 0) = \left(1 - \frac{2m}{r} + \frac{Q^2}{r^2}\right)\left(\frac{l^2}{r^2} + hc^2\right) - \left(E - \frac{qQ}{c\,r}\right)^2 \tag{4.67}$$

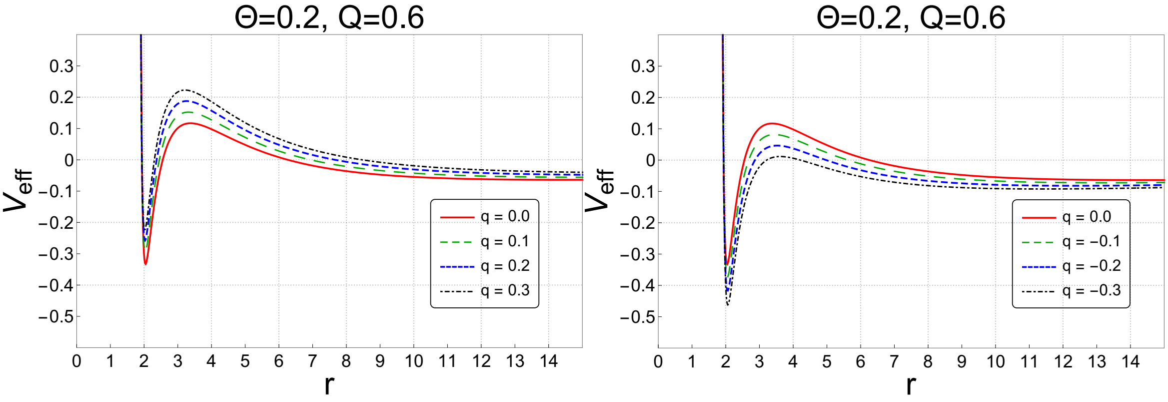

Figure 4.31: The behaviors of the effective potential for charged massive particle as a function of r, for different electric charges of the test particle q and fixed: $E = 0.998$, $m = 1$, $l = 4.2$.

In Fig. 4.31, we show the behavior of the effective potential as a function of r for different values of the electric charge q of a test particle, for a positive (left panel) and a negative charge (right panel). It is clear that, for the positive electric charge $q > 0$, the pick of the NC effective potential increases, and that means a repulsive electric interaction, while for the negative electric ones $q < 0$, this pick decreases, and that means an attractive electric interaction.

As we see before, for a classification of the circular orbits, our effective potential (4.66) must satisfy the same conditions as (4.19) and (4.20), and their stability can be determined by solving (4.21).

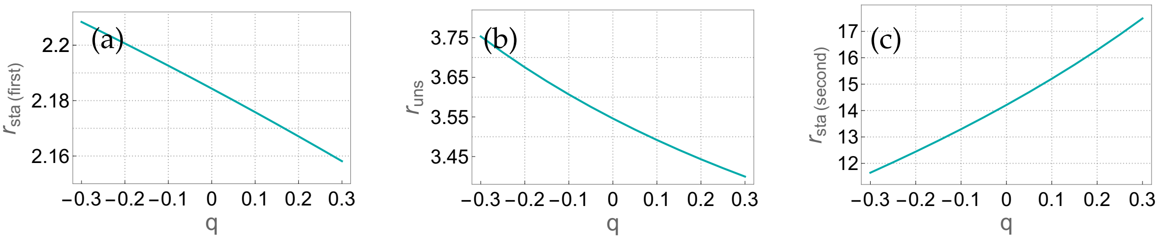

Figure 4.32: The behaviors of the radius of circular orbits for a particle in the NC RN spacetime. Unstable and multiple stable circular orbit as a function of q and for fixed $l = 4.2$, $E = 0.998$, $m = 1$, and $Q = 0.5$.

The behavior of the circular orbit radius in NC spacetime as a function of the electric charge of a test particle q is shown in Fig. 4.32. As we see, for a negative value of $q < 0$, the new SCO (left panel) is greater than in the positive range and is decreasing when q increases, and that means the range of SCO is greater for a particle with negative electric charge, which corresponds to the attractive force exerted by the charged BH on this particle, while for a particle with positive charge $q > 0$, this new SCO became smaller than for the negative $q < 0$, and that means this particle can be orbiting in stable orbits closer to the event horizon, and that is due to the presence of the repulsive force. Moreover, the same behavior exists for the unstable circular orbits (middle panel), in which the range of the unstable orbits is greater for the attractive force than for the repulsive one. However, this behavior is reversed for the external SCO (right panel), in which the radius of SCO for a negative electric charge $q < 0$ of the test particle is smaller than the positive case, which means that for the attractive interaction, this particle can orbit closer to this BH, while for the repulsive one, this particle orbits in a large SCO.

The expressions of energy and angular momentum for a circular orbit of a charged massive test particle can be obtained using the same conditions (4.19), (4.20) and (4.21) with the above NC effective potential (4.66). With some algebra, we find

$$\begin{aligned} E_c^2 \simeq & \frac{1}{r_c^2}\left(-qQ + r\sqrt{\frac{\left(1-\frac{2m}{r_c}+\frac{Q^2}{r_c^2}\right)\mathcal{V}_1(r_c)}{\mathcal{V}_2(r_c)}}\right)^2 + \left(qQ - r\sqrt{\frac{\left(1-\frac{2m}{r_c}+\frac{Q^2}{r_c^2}\right)\mathcal{V}_1(r_c)}{\mathcal{V}_2(r_c)}}\right) \\ & \times\sqrt{\frac{\left(1-\frac{2m}{r_c}+\frac{Q^2}{r_c^2}\right)\mathcal{V}_1(r_c)}{\mathcal{V}_2(r_c)}}\left(\frac{\mathcal{X}_1(r_c)+\mathcal{G}_1(r_c)\sqrt{1-\frac{2m}{r_c}+\frac{Q^2}{r_c}}}{16r_c^6(Q^2-2mr_c+r_c^2)\mathcal{V}_1(r_c)\mathcal{V}_2(r_c)}\right)\Theta^2+\mathcal{O}(\Theta^4), \end{aligned} \tag{4.68a}$$

$$\begin{aligned} l_c^2 \simeq & -\frac{2r_c^2\left(2Q^2 - mr_c + qQr\sqrt{1-\frac{2m}{r_c}+\frac{Q^2}{r_c^2}}\right)}{\mathcal{V}_2(r_c)} \\ & + \left(\frac{\mathcal{X}_2(r_c)+\mathcal{G}_2(r_c)\sqrt{1-\frac{2m}{r_c}+\frac{Q^2}{r_c^2}}}{16r_c^3(Q^2-2mr_c+r_c^2)\mathcal{V}_{(}r_c)^2\sqrt{1-\frac{2m}{r_c}+\frac{Q^2}{r_c^2}}}\right)\Theta^2+\mathcal{O}(\Theta^4). \end{aligned} \tag{4.68b}$$

where the explicit expressions for the functions $\mathcal{G}_1(r_c)$, $\mathcal{G}_2(r_c)$, $\mathcal{X}_1(r_c)$, $\mathcal{X}_2(r_c)$, $\mathcal{V}_1(r_c)$, and $\mathcal{V}_2(r_c)$ are provided in Appendix B.2.

For the limit $\Theta \to 0$, we recover the commutative case, and for the neutral particle $q = 0$, we get the same above expression as (4.57a) and (4.57b).

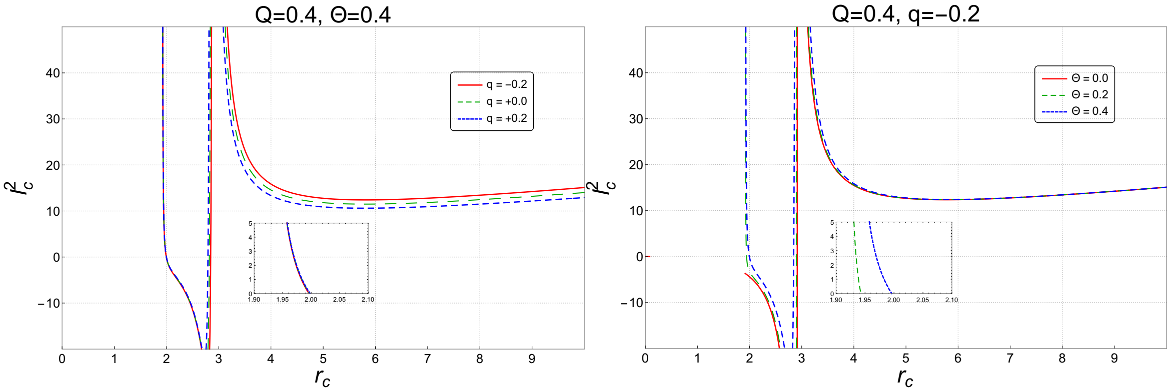

Figure 4.33: Radial dependence of the angular momentum l_c^2 of a charged test particle orbiting around an NC RN black hole for different values of electric charge of test particle q (left panel) and for different values of NC parameter Θ (right panel).

In Fig. 4.33, we show the behavior of the angular momentum l_c^2 for a charged particle around NC RN BH as a function of r_c, for different electric charge q and fixed Θ (left panel), and for different Θ and fixed q. It is clear that, for the angular momentum of a charged massive test particle, we get the same behavior as in the uncharged particle case (see Figs. 4.27 and 4.28), where in the NC spacetime, we have positive values of the angular momentum $l_c^2 > 0$ near the event horizon, which explain the presence of the new SCO in this region. As we see, the effect of the particle electric charge q is significant only for the external region $r_c > 3$ and is negligible in the region near the event horizon. While the effect of the non-commutativity is significant in the region near the event horizon and negligible for the external region, the increase in Θ shifted the angular momentum behavior away from the event horizon, which led to a new condition on the SCO.

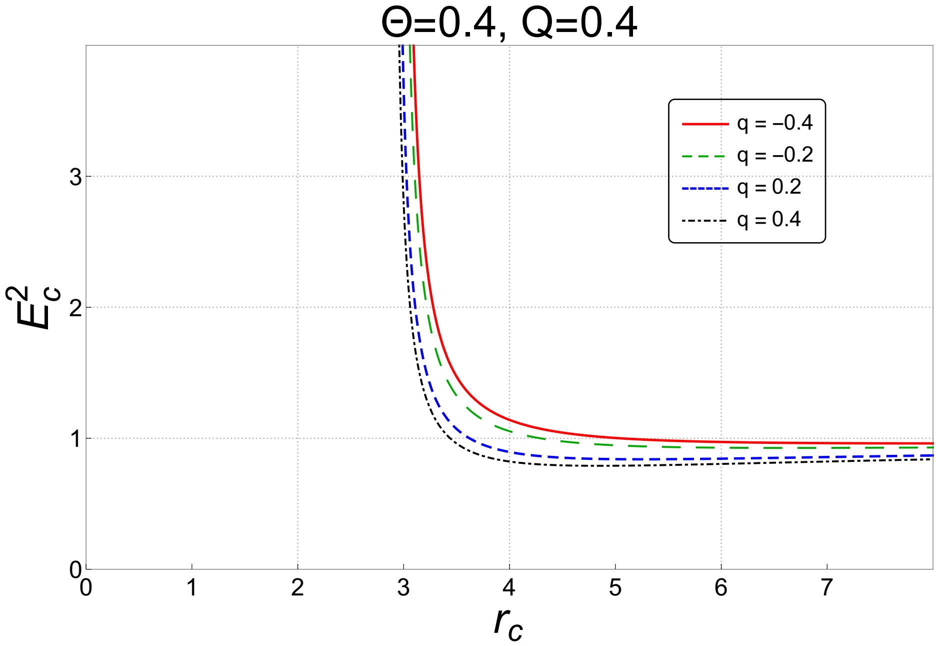

Figure 4.34: Radial dependence of the energy E_c^2 of a charged test particle orbiting around an NC RN BH for different values of electric charge of test particle q and a fixed NC parameter Θ.

The behavior of the energy E_c^2 of a charged test particle orbiting around an NC RN BH as a function of r_c for different values of electric charge of the test particle q and fixed Θ and Q. It is clear that the energy behavior is unphysical (E_c^2<0) for the region $r_c < 3$ for the charged test particle, and that due to the many approximations made to calculate the analytical expression, for an exact solution, we believe that a physical solution appears near the event horizon as the behavior of angular momentum.

4.6.1 *NC effect on the circular orbits of charged particles*

In a similar way as we see in SubSec. 4.2.4, we can express the NC geodesic equation of a charged q massive test particle $h = m_0^2$ in the deformed RN spacetime, where we insert the NC effective potential (4.66) and the metric component (4.54d) inside the radial equation

(4.34). The geodesic equation at 3^{rd} order in u the NC correction term (where we use this fact $\Theta^2 u \ll 1$), we obtain

$$\begin{aligned}\left(\frac{du}{d\phi}\right)^2 &= \frac{(E^2 - m_0^2c^2)}{l^2} + 2\left(\frac{mm_0^2c^2 - EqQ}{l^2}\right)u - u^2 - \frac{Q^2(m_0^2c^2 - q^2)}{l^2}u^2 + 2mu^3 \\ &\quad - Q^2u^4 + \frac{\Theta^2}{2l^2}\left\{(E^2 - m_0^2c^2)u^2 + \left(m(5m_0^2c^2 - 4E^2) - 2EqQ\right)u^3\right\} \qquad (4.69)\end{aligned}$$

The final geodesic equation for a charged massive test particle around NC RN BH can be obtained by deriving the above equation with respect to ϕ.

$$\frac{d^2u}{d\phi^2} + \omega''^2 u = \frac{m''}{l^2} + 3\mathfrak{m}u^2 - 2Q^2u^3 \qquad (4.70)$$

where the parameters ω' and $\mathfrak{m}$ are defined as

$$\omega''^2 = 1 + \frac{Q^2(m_0^2c^2 - q^2)}{l^2} - \frac{\Theta^2}{2l^2}(E^2 - m_0^2c^2), \qquad (4.71a)$$

$$m'' = mm_0^2c^2 - EqQ, \qquad (4.71b)$$

$$\mathfrak{m} = m\left[1 + \frac{\Theta^2}{2l^2}\left(\frac{5m_0^2c^2 - 4E^2}{2} - \frac{EqQ}{m}\right)\right]. \qquad (4.71c)$$

By applying the same approximation method [224], the general solution to the above equation can be expressed as follows:

$$u(\phi) = \frac{m''}{l^2\omega''^2}\left(1 + e\cos\left(\omega''\phi - \frac{3\mathfrak{m}m''}{l^2\omega''^3}\left(1 - \frac{Q^2}{l^2}\right)\phi\right)\right). \qquad (4.72)$$

It is clear that, for the case of $q = 0$, this solution is reduced to the one obtained for the uncharged test particle (4.61).

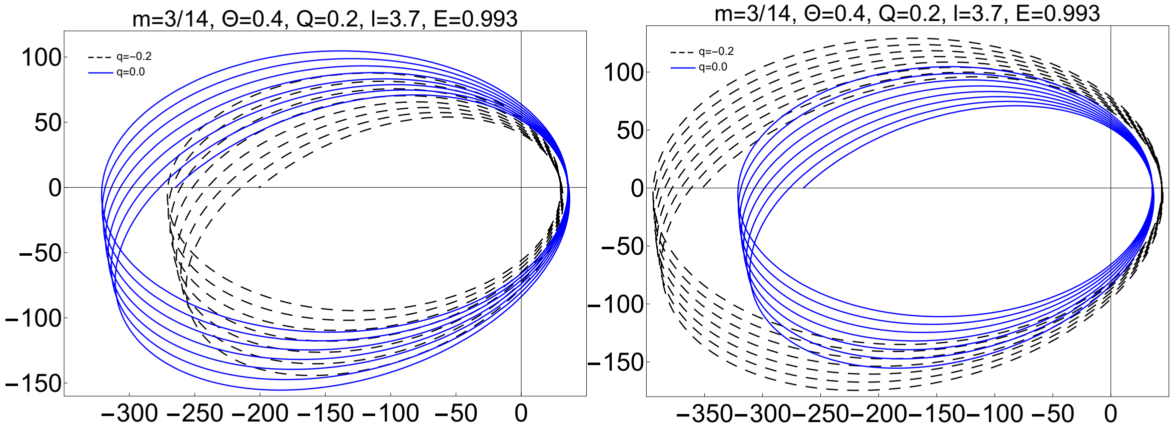

Figure 4.35: Time-like geodesic for charged massive test particle around NC RN black hole $Q = 0.2$ with $m = 3/14$, $E = 0.993$, $l = 3.7$, and $\Theta = 0.4$ for different particle electric charge $q = -0.2, 0.0, 0.2$.

In Fig. 4.35, we show a comparison for a charged uncharged particle in the orbit around the NC RN BH for a particular solution (4.72) with a given $m = 3/14$, $E = 0.993$, $l = 3.7$, $Q = 0.2$, and $\Theta = 0.4$. It is clear that, in the case of the opposite sign between the particle and BH electric charge, both gravitational and Coulomb forces are attractive and that this explains the decreases in major semi-axes of the charged particle $q \neq 0$ orbit compared to the neutral particle orbit $q = 0$ (see left panel Fig. 4.35). However, for the same sign of the electric charge for both a particle and BH, the Coulomb force is repulsive while the gravitational force is attractive as before; in this case, we observe inverse behavior as before, where the Coulomb force dominates and the major semi-axis of the charged particle orbit is greater than in the neutral case (see right panel Fig. 4.35).

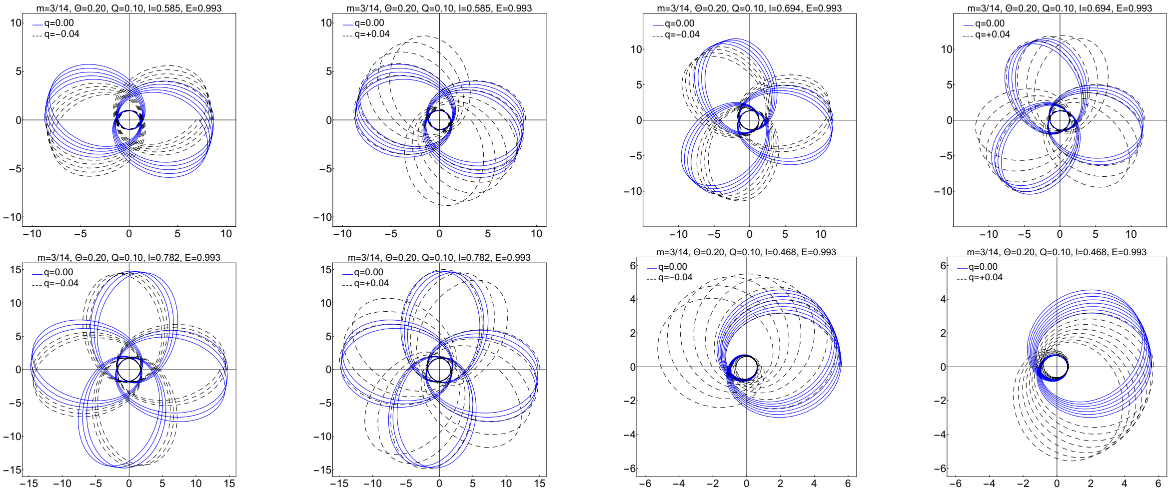

Figure 4.36: Periodic orbits of charged massive test particle around NC RN black hole for fixed $m = 3/14$, $E = 0.993$, $\Theta = 0.2$, $Q = 0.1$ and varying other parameters l and q.

Some periodic orbits of a charged massive particle in the NC RN spacetime with a given $m = 3/14$, $E = 0.993$, $\Theta = 0.2$, $Q = 0.1$, and varying the parameters l and q are shown in Fig. 4.36. Here, we compare the periodic orbits between the charged and an uncharged massive test particle around NC RN BH. As we see, the electric charge q of the massive test particle has a significant effect on its motion for both smaller and larger values of l (see Fig. 4.36), where this particle's electric charge affects the major semi-axis and the periastron advance of its orbit, and the Coulomb force dominates in both cases of attractive and repulsive interaction.

4.7 CONSTRAINT ON THE NC PARAMETER Θ FROM SOME ASTROPHYSICAL SYSTEMS

In the astrophysics field, the geodesic equation has a huge application and importance in the study and understanding of orbital motion around compact, massive objects. In which we give an estimation of the NC parameter Θ based on the four classical experimental tests of general relativity.

4.7.1 *Gravitational periastron advance in NC spacetime*

As we see in the previous sections, we have studied the geodesic motion in different cases in this geometry, in which we obtained periastron advanced analytical expressions for different cases.

4.7.1.1 *NC periastron advance in different cases*

In order to obtain the analytical expression of the NC orbital precession, we need to write our geodesic equations for the previous cases. (4.38), (4.59), and (4.70) into the perturbation form of the Keplerian trajectory equation [230],

$$\frac{d^2u}{d\phi^2} + u = \frac{m}{\tilde{l}^2} + \frac{g(u)}{\tilde{l}^2}, \tag{4.73}$$

where $\tilde{l} = \frac{l}{m_0 c}$, and $\frac{g(u)}{\tilde{l}^2}$ is defined for each geodesic equation (4.38), (4.59) and (4.70). According to Ref. [230], the deviation angle after one revolution is given by

$$\Delta\phi = \frac{\pi g_1}{\tilde{l}^2}. \tag{4.74}$$

where $g_1 = \frac{dg(u)}{du}\,|_{u=\frac{1}{b}}$, and the distance b is given by $b = \alpha(1-e^2)$, with e and α denoting the eccentricity of the movement and the major semi-axis. In Schwarzschild spacetime, the function $g(u)$ is given by

$$\frac{g(u)}{\tilde{l}^2} = 3mu^2 + \frac{\Theta^2}{2l^2}\left\{(E^2 - m_0^2c^2)u + \frac{3m}{2}(5m_0^2c^2 - 4E^2)u^2\right\}. \tag{4.75}$$

Using this relation together with (4.74), we find the NC deviation angle.

$$\Delta\phi = \frac{6\pi GM}{c^2\alpha(1-e^2)} + \pi\Theta^2\left[\frac{(E_0^2/c^2 - m_0^2c^2)}{2m\alpha(1-e^2)} + \frac{6(m_0^2c^2 - E_0^2/c^2)}{\alpha^2(1-e^2)^2} + \frac{3m_0^2c^2}{2\alpha^2(1-e^2)^2}\right]. \tag{4.76}$$

This result is quite close to the one obtained in Ref. [137], where the authors use only the star product, while in our case we use the SW map together with the star product. By using the relativistic relation of dispersion, we obtain

$$\Delta\phi = \frac{6\pi GM}{c^2\alpha(1-e^2)} + \pi\Theta^2\left[\frac{m_0^2v^2c^2}{2GM\alpha(1-e^2)} - \frac{6m_0^2v^2}{\alpha^2(1-e^2)^2} + \frac{3m_0^2c^2}{2\alpha^2(1-e^2)^2}\right]. \tag{4.77}$$

It is clear that, for $\Theta = 0$, we recover the commutative expression of general relativity predictions.

For a neutral particle in the NC RN spacetime, the function $g(u)$ is given by

$$\frac{g(u)}{\tilde{l}^2} = -\frac{Q^2m_0^2c^2}{l^2}u + \frac{\Theta^2}{2l^2}(E^2 - m_0^2c^2)u + 3m'u^2 - 2Q^2u^3. \tag{4.78}$$

In a similar way, by using the above equation together with (4.74), we obtain the NC precession of the neutral massive test particle.

$$\begin{aligned}\Delta\phi = {} & \frac{6\pi G\,M}{c^2\,\alpha(1-e^2)} - \frac{\pi k\,Q^2}{M\,c^2\,\alpha(1-e^2)} - \frac{6\pi G\,k\,Q^2}{c^4\,\alpha^2(1-e^2)^2} + \frac{\pi\,c^2\Theta^2}{2G\,M\,\alpha(1-e^2)}\left\{(E_0^2/c^2 - m_0^2c^2)\right. \\ & \left. + \frac{3G\,M(5m_0^2c^2 - 4E_0^2/c^2)}{c^2\,\alpha(1-e^2)}\right\}.\end{aligned} \tag{4.79}$$

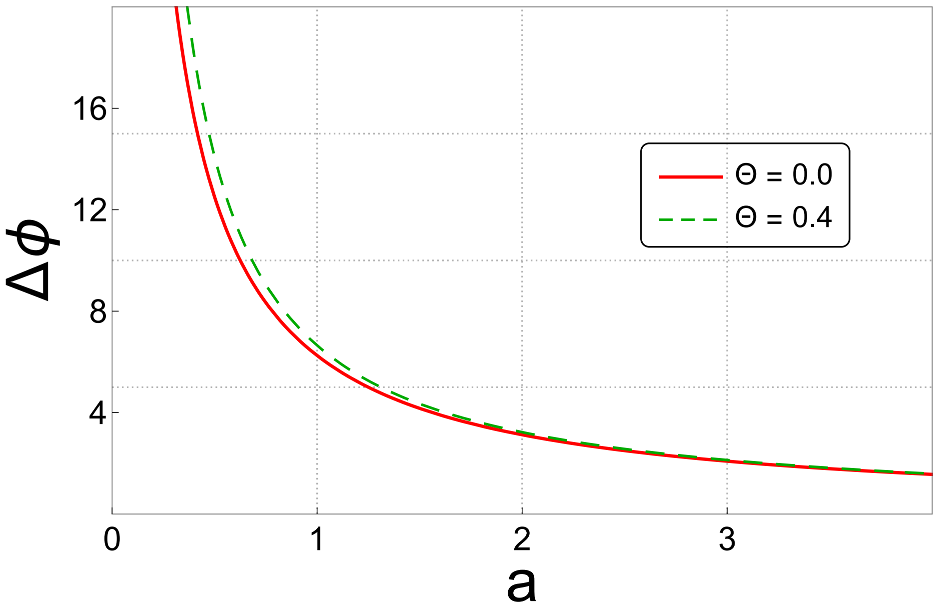

Figure 4.37: Behaviors of the gravitational periastron advance of Mercury in the NC spacetime.

It is clear that, when $\Theta = 0$, we recover the commutative expression. It is worth noting that the first two terms of this expression are coincident with the result [209, 231], while in our case we find three terms in the commutative spacetime, where this third term emerges from the term of the order u^4 in the geodesic equation (4.59). Another note: for the uncharged BH ($Q = 0$), we recover the result obtained in the NC Schwarzschild spacetime (4.76).

Therefore, the function $g(u)$ for a charged massive test particle is given by

$$\frac{g(u)}{\tilde{l}^2} = -\frac{Q^2(m_0^2c^2 - q^2)}{l^2}u + \frac{\Theta^2}{2l^2}(E^2 - m_0^2c^2)u + 3\mathfrak{m}u^2 - 2Q^2u^3. \tag{4.80}$$

In the same way, the NC precession of the charged massive test particle is given by

$$\begin{aligned}\Delta\phi = &\frac{6\pi G\,M}{c^2\,\alpha(1-e^2)} - \frac{\pi k\,Q^2}{M\,c^2\,\alpha(1-e^2)} - \frac{6\pi G\,k\,Q^2}{c^4\,\alpha^2(1-e^2)^2} + \frac{\pi Q^2\,q^2}{m\alpha(1-e^2)} \\ &+ \frac{\pi c^2\,\Theta^2}{2G\,M\alpha(1-e^2)}\left\{(E_0^2/c^2 - m_0^2c^2) + \frac{3G\,M(5m_0^2c^2 - 4E_0^2/c^2)}{c^2\alpha(1-e^2)} - \frac{6E_0/c\,k\,q\,Q}{c^2\,\alpha(1-e^2)}\right\}.\end{aligned} \tag{4.81}$$

For the uncharged test particle $q = 0$, we recover the result in (4.79).

4.7.1.2 *Schwarzschild spacetime*

As a first numerical application in Schwarzschild spacetime, we take the problem of Mercury orbit and use Eq. (4.77). The NC perihelion shift for the Mercury planet is given by

$$\mid\delta\phi_{NC}\mid = \left(1.96689 \times 10^{43}\right)\Theta^2 Kg^2.s^{-2} \tag{4.82}$$

The experimental (observation) and theoretical (GR) predictions of the perihelion shift for the Mercury planet are given in Ref. [184].

$$\delta\phi_{obs} = 2\pi\,(7.98734 \pm 0.00037) \times 10^{-8} rad/rev \tag{4.83a}$$
$$\delta\phi_{GR} = 2\pi\,(7.98743) \times 10^{-8} rad/rev \tag{4.83b}$$

As a first estimation of Θ, we compare the NC correction (4.82) to the observable data (4.83a) ($\mid \delta\phi_{NC} \mid \approx \delta\phi_{obs}$) and we find

$$\Theta \approx 1.597 \times 10^{-25} s.Kg^{-1}, \tag{4.84}$$

or equivalently:

$$\Theta^{\mathrm{Phy}} \equiv \sqrt{\hbar\Theta} \approx 4.104 \times 10^{-30} m. \tag{4.85}$$

The lower bound for Θ is defined as follows:

$$\mid \delta\phi_{NC} \mid \quad \leq \quad \mid \delta\phi_{GR} - \delta\phi_{obs} \mid \approx 2\pi (9 \times 10^{-13}) rad/rev. \tag{4.86}$$

Thus, we get:

$$\Theta \leq 5.652 \times 10^{-28} s.kg^{-1}, \tag{4.87}$$

or equivalently:

$$\Theta^{\mathrm{Phy}} \leq 2.441 \times 10^{-31} m. \tag{4.88}$$

As we see, our estimation of the NC parameter Θ is very small, as expected from this theory, and it is remarkable that our result is very close to the one obtained in Ref. [136, 232], where the authors use the NC flat space as a framework in classical mechanics. It is worth noting that our result is different from the one obtained in Ref. [232] with an order of 10^{-1}, which occurs because we are using curved spacetime. Furthermore, in Ref. [136], the authors include a new degree of freedom, γ, in which, with the use of a specific value of γ, one can obtain the same result as ours. For other planets in our solar system, we use the experimental data in Refs. [184–186], where the lower bound in the NC parameter is obtained as follows:

As we see in Table 4.5, the lower bound of the physical NC parameter Θ^{Phy} is in the same order for the planetary orbit of our solar system $\Theta^{\mathrm{Phy}} \sim 10^{-31}\, m$. Moreover, our results lead us to the same conclusion in Ref. [232]: that the solar system is very sensitive to the NC parameter, and that means any small change in Θ implies a sensible change at a large scale. In this way, the NC parameter plays the role of a fundamental constant of our solar system, which describes the microstructure of spacetime in this region.

Comparing our result with the Planck length, we find that $\Theta^{\mathrm{Phy}} > L_P$. The NC parameter also has a lower bound, which is the Planck scale L_P:

$$\Theta^{\mathrm{Phy}} \leq (3.5808 \times 10^{4}) L_P. \tag{4.89}$$

Table 4.5: Some observable values for different planets of our solar system are: mass of the planet (M), semi-major axis (α), eccentricity (e), orbital period (T), and orbital precession in columns 2–6, respectively. The prediction of the orbital precession in general relativity is in column 7, and in the finale column we give the lower bound for the non-commutative parameter Θ^{Phy}.

Planet	Mass	α	e	T	$\Delta\phi_{obs}$	$\Delta\phi_{GR}$	L.b of Θ^{Phy}
	$(10^{24}Kg)$	(AU)		$(\frac{rev}{centry})$	$(\frac{arc-sec}{centry})$	$(\frac{arc-sec}{centry})$	$(10^{-31}m)$
Mercury	$0,3301$	0.39	0.206	415.203	42.9800 ± 0.0020	42.9805	≤ 02.441
Venus	$4,8675$	0.72	0.007	162.574	8.6247 ± 0.0005	8.6283	≤ 01.805
Earth	$5,9724$	1.00	0.017	100	3.8387 ± 0.0004	3.8399	≤ 01.635
Mars	6.44171	1.52	0.093	53.175	1.3565 ± 0.0004	1.3514	≤ 10.348
Jupiter	1898.19	5.20	0.048	8.431	0.0700 ± 0.0040	0.0623	≤ 00.617
Saturn	568.34	9.54	0.056	3.396	0.0140 ± 0.0020	0.0137	≤ 00.844

In the natural units, the upper bound of the energy in the presence of non-commutativity is given by

$$3.39 \times 10^{14} Gev \leq \frac{1}{\Theta^{\text{Phy}}}. \tag{4.90}$$

which also has an upper bound given by Planck energy E_P.

As a second example, we consider a strong gravitational system, where we take the motion of a $S2$ star with a mass of $10 - 15\, M_\odot$ that orbits around a supermassive BH Sagittarius A (SgrA*) with a mass of $M = 4.260 \times 10^6 M_\odot$, and this star $S2$ completes one orbit around SgrA* in $16.052\, yer$ with major semi-axis $\alpha = 970\, UA$ [233]. The experimental observation of the perihelion shift for the $S2$ star is given in Refs. [210, 233] by,

$$\delta\phi_{obs} = 48.506\, f_{SP} (''/yer) \tag{4.91}$$

where f_{SP} is the observational fitting parameter for this system and is confined between these two values: $f_{SP,min} = 0.9$ and $f_{SP,max} = 1.2$ [210]. The theoretical prediction from the commutative term of Eq. (4.77)

$$\delta\phi_{GR} = 2\pi\, (5.98378) \times 10^{-4} rad/rev \tag{4.92}$$

and the NC perihelion shift is given by

$$\mid \delta\phi_{NC} \mid = \left(3.58067 \times 10^{53}\right) \Theta^2 Kg^2.s^{-2} \tag{4.93}$$

The lower bound for Θ can be computed using the fitting parameter $f_{SP} = 1$:

$$\sqrt{\hbar\Theta} \leq 2.6166 \times 10^{-32} m \tag{4.94}$$

As we see, this result is smaller than the result obtained using the Mercury-Sun system (4.88), and that is due to the use of a strong gravitational field created by supermassive BH $SgrA^*$ in the center of galactic. Moreover, if one uses another experimental data as in

Refs. [5, 210, 233, 234], we get new results that are confined between $\sqrt{\hbar\Theta} \propto 10^{-31}m$ and $\sqrt{\hbar\Theta} \propto 10^{-32}m$, and that leads us to this conclusion: to get a better estimation of the NC parameter Θ, it is very important to use an experimental measurement with good accuracy.

4.7.1.3 *Uncharged massive test body case in RN spacetime*

For the case of an uncharged massive test body, we must use (4.79) to find a lower bound for the NC parameter Θ.

Firstly, we take the same previous example of the Mercury plant around the sun. In the RN spacetime, we take the possibility of the Sun's having an electric charge $Q_\odot$, where its electric charge has some constraint as in Ref. [234] ($0.48 \times 10^{18} \leqslant Q_\odot \leqslant 1.5 \times 10^{18}\,C$). For a numerical application to the NC perihelion shift of the Mercury planet, we find

$$\mid \delta\phi_{NC} \mid = \left(1.96689 \times 10^{43}\right) \Theta^2 Kg^2.s^{-2} \tag{4.95}$$

The experimental observation of the perihelion shift for Mercury orbits [184, 235] and the commutative theoretical prediction from Eq. (4.79) with the sun's electric charge ($Q_\odot = 1.5 \times 10^{18}\,C$) [234] are given by

$$\delta\phi_{obs} = 2\pi\,(7.98734 \pm 0.00037) \times 10^{-8} rad/rev \tag{4.96}$$

$$\delta\phi_{RN} = 2\pi\,(7.98732) \times 10^{-8} rad/rev \tag{4.97}$$

The lower bound of Θ is defined as follows:

$$\mid \delta\phi_{NC} \mid \quad \leq \quad \mid \delta\phi_{RN} - \delta\phi_{obs} \mid \approx 2\pi(2 \times 10^{-13}) rad/rev \tag{4.98}$$

So we get:

$$\sqrt{\hbar\Theta} \leq 1.63266 \times 10^{-31} m \tag{4.99}$$

As we see, this result is smaller but in the same order as the one obtained for uncharged sun in Schwarzschild spacetime (4.88). This lower bound can be reduced to the order $\sqrt{\hbar\Theta} \propto 10^{-32}$ if we choose a particular value of the sun's charge: $Q_\odot = 1.35 \times 10^{18}\,C$.

For the second example, we take the same system of $S2$ stars orbiting around a supermassive BH $SgrA^*$, with the possibility that BH $SgrA^*$ is charged electrically (see Ref. [234]), where the authors predicted that the electric charge of $SgrA^*$ is given by $Q_{SgrA^*} \leqslant 3.6 \times 10^{27}\,C$. The theoretical prediction of perihelion shift for this system can be obtained using the commutative term of Eq. (4.79).

$$\delta\phi_{RN} = 2\pi\,(5.98359) \times 10^{-4} rad/rev \tag{4.100}$$

with $Q_{SgrA^*} \propto 10^{25}\,C$, so the lower bound of Θ for the case $f_{SP} = 1$ is given by

$$\sqrt{\hbar\Theta} \leq 2.575 \times 10^{-32} m \tag{4.101}$$

This result is shifted with a coefficient of 0.0416 from the case of an uncharged supermassive black hole $SgrA^{*}$ with the same order (4.94), in which the effect of the electric charge is so small and can be considered negligible. Also, if we vary the electric charge Q, we obtain a lower bound on Θ between $\sqrt{\hbar\Theta} \propto 10^{-31}m$ and $\sqrt{\hbar\Theta} \propto 10^{-32}m$.

4.7.1.4 *Charged massive test body case in RN spacetime*

In the possibility that the massive test object is charged electrically, we must use Eq(4.81). As a numerical application, we take the same example system as before for our Mercury-Sun system, and we take into account that the Mercury planet has an electric charge of q, which is expected to be in the order of $q \leqslant 3.89 \times 10^{9}\,C$ [235]. The effect of the electric charge of the Mercury planet q is negligible in the commutative and in the NC term, and the result is the same as in the case of the uncharged test body $q = 0$ (4.99), which means the electric charge of the test particle does not affect the properties of spacetime.

4.7.2 *Gravitational red-shift*

The gravitational red-shift, also known as the Einstein effect, and its analytical expression in the NC Schwarzschild spacetime can be obtained by following the same steps as in Sec. 1.2, where we use the NC line element in the equatorial plane (4.1), and after some calculation we find

$$\hat{z} = \sqrt{\left|\frac{\hat{g}_{00}(r_2,\Theta)}{\hat{g}_{00}(r_1,\Theta)}\right|} - 1 \tag{4.102}$$

When $\Theta = 0$, we recover the commutative expression (1.37).

For an asymptotic observer $r_2 \to \infty$, the measured red-shift for the NC Schwarzschild black hole is given by $\hat{z}$:

$$\hat{z} = z\left[1 - \left(\frac{z+1}{z}\right)\frac{m\left(88m^2 + mr_1\left(-77 + 15\sqrt{1-\frac{2m}{r_1}}\right) - 8r_1^2\left(-2+\sqrt{1-\frac{2m}{r_1}}\right)\right)}{32r_1^3(r_1-2m)^2}\Theta^2\right], \tag{4.103}$$

where z is the commutative red-shift, which is given by (1.37) with $r_2 \to \infty$ and $m = GM$.

In Fig. 4.38, we show the effect of non-commutativity on the gravitational red-shift. As we see the non-commutativity affect the red-shift behavior near the event horizon, and when we move away from this region, their effect becomes negligible.

In order to obtain an estimation of the NC parameter, we use the proposition proposed in Ref. [236], which states that the NC correction should be smaller than the accuracy of the experimental measurements, which is 7×10^{-9}, so we get

$$\begin{aligned}\left|\frac{\hat{z}-z}{z}\right| &= \left(\frac{z+1}{z}\right)\frac{m\left(88m^2 + mr_1\left(-77 + 15\sqrt{1-\frac{2m}{r_1}}\right) - 8r_1^2\left(-2+\sqrt{1-\frac{2m}{r_1}}\right)\right)}{32r_1^3(r_1-2m)^2}\Theta^2,\\ &\leqslant 7\times 10^{-9}.\end{aligned} \tag{4.104}$$

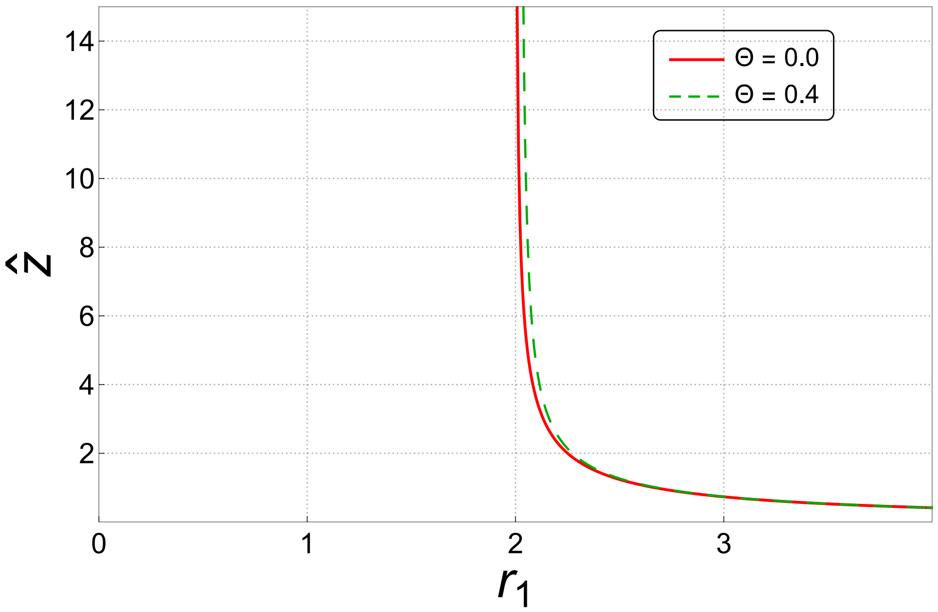

Figure 4.38: Behavior of the gravitational red-shift in NC spacetime.

The upper bound for Θ can be written as follows:

$$\Theta^2 \leqslant \frac{7\times 10^{-9}\times\left(\frac{z}{z+1}\right)32r_1^3(r_1-2GM)^2}{GM\left(88(GM)^2+GMr_1\left(-77+15\sqrt{1-\frac{2GM}{r_1}}\right)-8r_1^2\left(-2+\sqrt{1-\frac{2GM}{r_1}}\right)\right)}, \tag{4.105}$$

As a numerical application, we follow the same step as in Ref. [237], where we use the data of a typical micro BH, with a radius and mass given by $r_1 \sim 1.5\times 10^{-3}\,m$ and $GM \sim 5\times 10^{-4}\,m$, respectively. According to Ref. [238], for a space-space NC matrix, the obtained result should be multiplied by the square of the scale factor at the end of inflation $\alpha \approx 10^{-29}$ to obtain a physical result, so we get

$$\Theta^{\mathrm{Phy}} = \sqrt{\alpha^2\Theta^2} \leqslant 2.09\times 10^{-36}\,m. \tag{4.106}$$

Our estimation of this case shows better results compared to the one obtained from the study of the perihelion shift of orbit, where this result is different from the previous one by 10^{-4}, and that is around the Planck scale. It is worth noting that the estimation of Θ depends on the accuracy of the experimental measurements. For example, if one uses another experiment with different accuracy, such as 7×10^{-5} [239], in this case the NC parameter is given by

$$\Theta^{\mathrm{Phy}} = \sqrt{\alpha^2\Theta^2} \leqslant 2.09\times 10^{-34}\,m. \tag{4.107}$$

As we see, the accuracy of the experimental measurements is very important to test the effect of non-commutativity and get a good estimation for Θ. In this case, the NC parameter is close to the Planck scale and deviates by 10^{-2} from the one obtained in (4.94).

4.7.3 *Gravitational deflection of light*

In which follow we investigate the effect of non-commutativity on the deflection of light, where we follow the same steps as in Sec. 1.2. For that, we use Eq. (4.5), together with the conserved quantity (4.4b), to obtain the Eq of ϕ as a function of r. With some algebra, we find

$$\Delta\hat{\phi} = 2\int_b^\infty \sqrt{\frac{\hat{g}_{11}(r)}{\hat{g}_{33}(r)}} \left(\frac{\hat{g}_{33}(r)}{\hat{g}_{33}(b)}\left|\frac{\hat{g}_{00}(b)}{\hat{g}_{00}(r)}\right| - 1\right) dr - \pi. \tag{4.108}$$

To compute this integral, we need to expand our expression on the first order in m/r and in m/b for the commutative term, and in the leading order in the NC correction, with $m = GM$.

$$\Delta\hat{\phi} \approx 2\int_b^\infty \frac{1}{r\sqrt{\left(\frac{r}{b}\right)^2 - 1}} \Bigg[1 + \frac{m}{r} + \frac{mr}{b(b+r)} + \Bigg(\frac{b^4(7m-2r) + b^3(7m-2r)r}{16b^3r^3(b+r)} + \frac{br^3(-5m+2r) + b^2r^2(-3m+2r) - 5mr^4}{16b^3r^3(b+r)}\Bigg)\Theta^2 + ...\Bigg] dr - \pi, \tag{4.109}$$

After integrating the above equation, we get:

$$\Delta\hat{\phi} = \frac{4GM}{b} - \frac{8GM - 3b\pi + 6GM\pi}{48\,b^3}\Theta^2. \tag{4.110}$$

The above expression represents the NC gravitational deflection of light, and when $\Theta = 0$, we recover the commutative expression (1.32).

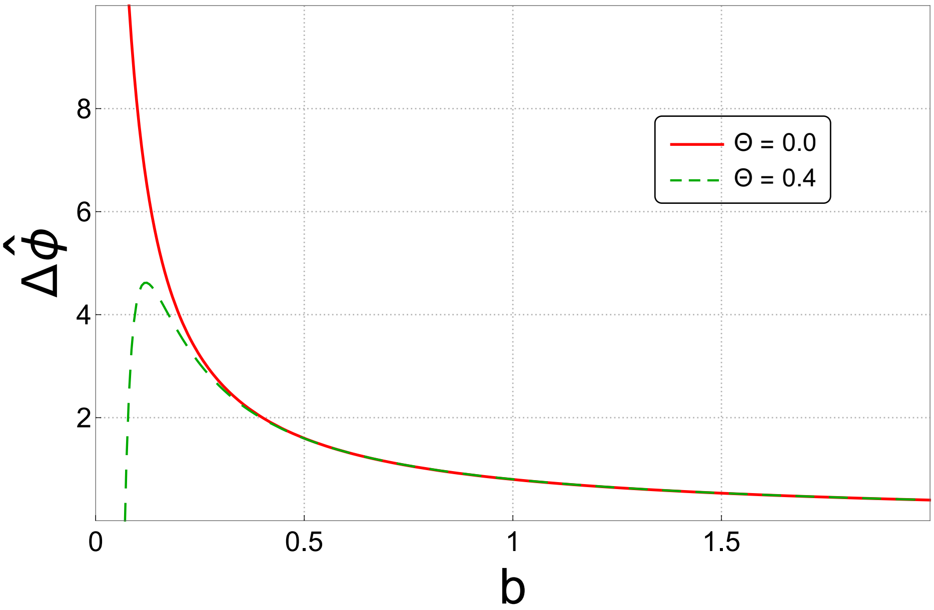

Figure 4.39: Behavior of the gravitational deflection of light in NC spacetime

In Fig. 4.39, we show the behavior of the light deflection in the NC Schwarzschild spacetime. It is clear that the non-commutativity removes the divergence of the light deflection for a smaller impact parameter b, and for large values of b, the NC effect becomes negligible.

In order to give an estimation to the NC parameter for this phenomenon, we use the fact that the NC correction should be smaller than the accuracy of the measurements, which is 2.91×10^{-7} [240].

$$\left|\frac{\Delta\hat{\phi} - \Delta\phi}{\Delta\phi}\right| = \frac{3b\pi - 2m(4+3\pi)}{194GM\,b^2}\Theta^2 \leqslant 2.91 \times 10^{-7}, \tag{4.111}$$

So the upper bond of Θ is:

$$\Theta^2 \leqslant 2.91 \times 10^{-7}\,\frac{194GM\,b^2}{3b\pi - 2m(4+3\pi)}. \tag{4.112}$$

For numerical application, using the radius $r_1 \equiv b = 1.5 \times 10^{-3}\,m$ of the micro-BH, we get:

$$\Theta^{\text{Phy}} = \sqrt{\alpha^2\Theta^2} \leqslant 7.787 \times 10^{-35}\,m. \tag{4.113}$$

When we use the gravitational deflection of light, we find that the estimation of Θ is in the Planck scale, and it is different with an order of 10^{-1} form (4.106)-(4.107) using the red shift and with a difference of order of 10^{-3} from the obtained one using the perihelion shift (4.94).

4.7.4 *Gravitational time delay (Shapiro effect)*

For the NC gravitational time delay, we follow the same steps as in Sec. 1.2, where we use Eq. (4.5), together with the first conserved quantity (4.4a), to obtain the Eq of coordinate time t as a function of r. Supposing now that the same example of a radar signal travels from the Earth $r = r_E$ to Venus $r = r_V$ (see Fig. 1.5), then the time delay is given by

$$\Delta\hat{t} = 2\left[\hat{t}(r_E, b) + \hat{t}(r_V, b) - \sqrt{b - r_E} - \sqrt{b - r_V}\right], \tag{4.114}$$

with:

$$t(r,b) = \int_b^r \sqrt{\frac{g_{11}(r')}{|g_{00}(r')|}}\left(1 - \frac{g_{33}(b)\,|g_{00}(r')|}{g_{33}(r')\,g_{00}(b)}\right)^{-1/2} dr', \tag{4.115}$$

As a first step, we expand the above expression in linear form and stop in the leading order in m/r and m/b.

$$\begin{aligned}\hat{t}(r,b) \approx \int_b^r \frac{r}{\sqrt{r^2 - b^2}}\Bigg[1 + \frac{2m}{r} + \frac{m\,b}{r\,(r+b)} + \Bigg(\frac{1}{8r^2} - \frac{3m}{16br(r+b)} + \frac{bm}{16r^3(b+r)} \\ - \frac{m}{16r^2(b+r)}\Bigg)\Theta^2 + \ldots\Bigg]\,dr'.\end{aligned} \tag{4.116}$$

The integral of the above equation is given by

$$\hat{t}(r,b) = \sqrt{r^2-b^2} + 2m \ln\left(\frac{r+\sqrt{r^2-b^2}}{b}\right) + m\left(\frac{r-b}{r+b}\right)^{1/2} + \left(\frac{m}{16b\,r}\left(\frac{r-b}{r+b}\right)^{1/2} + \frac{b-m}{8b^2}\arctan\left(\sqrt{\frac{r^2}{b^2}-1}\right)\right)\Theta^2. \tag{4.117}$$

We take into consideration that $r_E \gg b$ and $r_V \gg b$, so we get:

$$\hat{t}(r_E,b) - \sqrt{r_E^2-b^2} \approx 2m \ln\left(\frac{2r_E}{b}\right) + m + \Theta^2\left(\frac{m}{16br_E} + \frac{b-m}{8b^2}\arctan\left(\frac{r_E}{b}\right)\right), \tag{4.118}$$

Inserting the above equation in the relation (4.117), we get the total expression of the gravitational time delay in the NC spacetime.

$$\Delta\hat{t} \approx 4GM\left[\ln\left(\frac{4r_E\,r_V}{b^2}\right)+1\right] + \frac{GM}{8b^2}\left(\frac{b-GM}{GM}\left(\arctan\left(\frac{r_E}{b}\right)+\arctan\left(\frac{r_V}{b}\right)\right) + \frac{b(r_E+r_V)}{2r_E r_V}\right)\Theta^2. \tag{4.119}$$

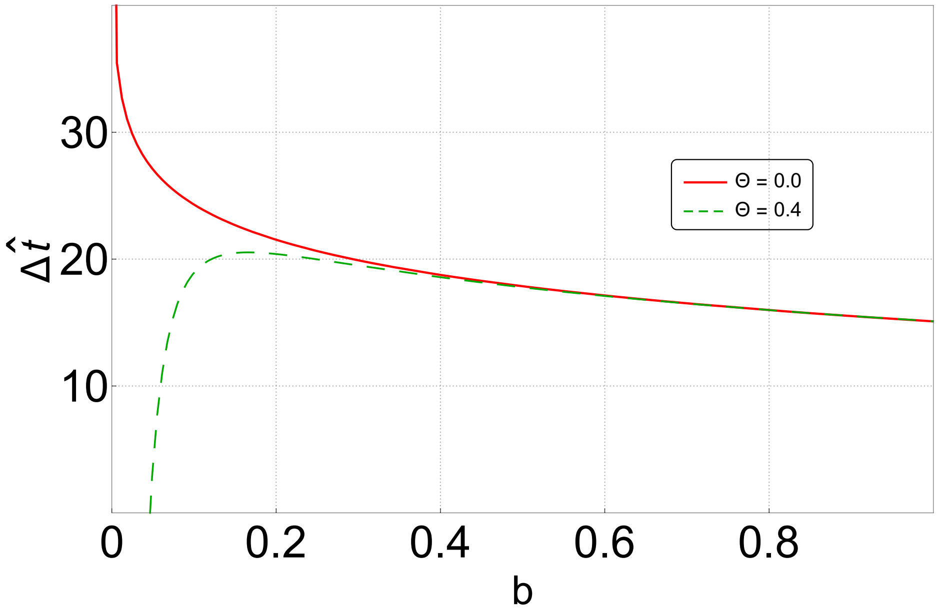

Figure 4.40: Behavior of the gravitational time delay in the NC spacetime.

For the estimation of Θ for Shapiro time delay, we use the fact that the NC correction should be smaller than the accuracy of the measurements, which is 2.91×10^{-7} [240].

$$\left|\frac{\Delta\hat{t}-\Delta t}{\Delta t}\right| = \frac{\left(\frac{b-GM}{GM}\left(\arctan\left(\frac{r_E}{b}\right)+\arctan\left(\frac{r_V}{b}\right)\right) + \frac{b(r_E+r_V)}{r_E r_V}\right)}{32b^2\left[\ln\left(\frac{4r_E\,r_V}{b^2}\right)+1\right]}\Theta^2 \leqslant 2.91\times 10^{-7}, \tag{4.120}$$

So the upper bound expression of Θ is given by:

$$\Theta^2 \leqslant 2.91\times10^{-7}\frac{32b^2\left[\ln\left(\frac{4r_E r_V}{b^2}\right)+1\right]}{\left(\frac{b-GM}{GM}\left(\arctan\left(\frac{r_E}{b}\right)+\arctan\left(\frac{r_V}{b}\right)\right)+\frac{b(r_E+r_V)}{r_E r_V}\right)}, \tag{4.121}$$

For the scale of the micro-BH, the ration $\frac{4r_E r_V}{b^2}$ is the same at the solar system scale, so the numerical application gives us

$$\Theta^{\text{Phy}} \leqslant 4.089\times10^{-34}\,m \tag{4.122}$$

Another result shows that the NC parameter is closer to the Planck scale. For the different experimental tests of GR, the non-commutativity affects the spacetime at the Planck scale.

4.7.5 *Results and discussion*

As we see in the previous subsections, the estimation of the NC parameter Θ based on the four classical tests of GR shows good results, in which this parameter is located around the Planck scale. We summarize our results in the following Table 4.6:

Table 4.6: Upper bound on the NC parameter Θ^{Phy} for the classical tests of general relativity.

Experiment	Physical bound on Θ^{Phy} (m)
Periastron advance	$\Theta^{\text{Phy}} \leqslant (2.378\times10^{-31} - 2.6166\times10^{-32})$
Red-shift	$\Theta^{\text{Phy}} \leqslant 2.09\times(10^{-34} - 10^{-36})$
Deflection of light	$\Theta^{\text{Phy}} \leqslant 7.787\times10^{-35}$
Time delay	$\Theta^{\text{Phy}} \leqslant 4.089\times10^{-34}$

As a first application, we chose the periastron advance of mercury and then generalized it to our solar system, where the NC parameter acts as a fundamental constant for several planets and is found in the order of $\sim 10^{-31}\,m$. The extend of this application to a strong gravitational system as the star $S2$ around SgrA* shows a better estimation of the NC parameter, which is found in order of $\sim 10^{-32}m$. It is worth noting that, when we generalized the periastron advance to a RN spacetime, we found that, in the case of using the electric charge, our results did not exceed the same order as those of an uncharged gravitational source. We also found that the electric charge of a massive test body had a negligible effect on the estimation of NC. Secondly, we use red-shift, light deflection, and time delay to obtain an estimation of the NC parameter. We use a microscopic system, where we choose the data of a microscopic BH at the early universe[3]. In the case of the red-shift, we find that the NC parameter is in order between $10^{-34}\,m$ and $10^{-36}\,m$; this difference is due to the accuracy of the measurement used, while in the case of light deflection and time delay, we obtain an estimation of Θ in order of 10^{-35} and 10^{-34}, respectively. Moreover, the

---

[3] For the experimental tests that use a radio wave or a light bound, we cannot use a macroscopic system because the NC correction term is so small to be detected experimentally.

most stringent constraint comes from the light deflection, which gives us $\Theta^{\text{Phy}} \sim 10^{-35} m$. However, we confirm that the non-commutativity of spacetime appears in the Planck scale.

5

THERMODYNAMICS PROPRIETIES OF THE DEFORMED BLACK HOLE

In this present chapter, we investigate in detail the thermodynamic properties of the deformed Schwarzschild BH in the presence of non-commutativity for a different choice of the NC matrix (see Chap. 3). In this study, we are interested in two approaches to BH thermodynamics in the NC geometry and for different scenarios. First, we use the classical approach [170, 172] to investigate its thermal stability and phase transition in different cases. Then, we present a new treatment of non-commutativity that allows us to establish a similarity between the RN BH and the NC Schwarzschild BH [172]. Also, we present the discussion of thermal stability and phase transition of the NC Schwarzschild BH inside a spherical isothermal cavity [171]. In the second approach, we study Hawking radiation as a quantum tunneling process of massless particles from BH in the context of NC gauge theory, in which we investigate two scenarios, thermal and non-thermal radiation [173]. Finally, we examine some of the BH phenomenology quantities inspired by the NC.

This chapter is organized as follows: In Sect. 5.1, we present a detailed study of the influence of non-commutativity on the thermodynamic properties of the deformed Schwarzschild BH, using the classical approach of BH thermodynamics, then investigate their stability and phase transition, and also establish a connection between this geometry and the electric charge of RN BH, where we deal with this geometry with different scenarios. In Sect. 5.3, we study the thermal stability and phase transition of NC Schwarzschild BH inside a spherical isothermal cavity. In Sect. 5.4, we present a detailed analysis of the quantum tunneling process of massless particles from the NC Schwarzschild BH, and we also show the effect of this geometry on the number of particles that are emitted in two scenarios of pure thermal and non-thermal radiation. In Sects. 5.5, we show the NC effect on the evaporation process of the Schwarzschild BH, where we study their luminosity, energy emission rate, and BH lifetime.

5.1 CLASSICAL BLACK HOLE THERMODYNAMICS IN NC SPACETIME

In this section, we investigate the thermodynamic properties of the deformed Schwarzschild BH (see Sec. 3.2) in the context of the NC gauge theory. This study allows us to understand the non-commutativity of spacetime, which leads to a better understanding of the quantum effect of gravity on BH physics. In this investigation, we use the classical approach of BH thermodynamics, which is based on the geometry and laws of BH mechanics (see Sec. 1.3). In this context, the NC first law of BH thermodynamics for Schwarzschild case has become

$$d\hat{m} = \hat{T} d\hat{S} \,. \tag{5.1}$$

where $\hat{m}$, $\hat{T}$, and $\hat{S}$ are the mass, temperature, and entropy of the NC Schwarzschild BH, respectively. In which follow, we use the deformed metric of Schwarzschild spacetime given in Sec. 3.2.

5.1.1 *Mass, temperature, and entropy of the NC Schwarzschild black hole*

As a first step, we compute the BH ADM mass for the NC Schwarzschild one, and that can be obtained as a function of the NC parameter $\hat{M} = r_h^{\mathrm{NC}}/2$ [165, 166], which is easy to prove by solving the equation $1/\hat{g}_{11}(r_h^{\mathrm{NC}}) = 0$ for m. In the case of $a = 0$ and $b = \Theta$, the expression of this mass is a function of the event horizon r_h, Θ, and the observational angle θ, which is given by

$$\begin{aligned} \hat{M} &= \frac{r_h}{2} + \frac{3}{16 r_h}\Theta^2 \sin^2\theta \\ &= m + M^{\mathrm{NC}}(\theta,\Theta) \,, \end{aligned} \tag{5.2}$$

where $m = r_h/2$ is the commutative Schwarzschild mass and $M^{\mathrm{NC}}(\theta,\Theta)$ is the NC correction term that depends on the angle θ, which means this mass describes the partial mass contributed by the NC correction to this BH. Thus, the total mass of the NC BH can be computed as follows:

$$\hat{m} = \frac{1}{\int_0^{2\pi}\int_0^{\pi}\sqrt{\hat{g}_{22} * \hat{g}_{33}}\, d\theta\, d\varphi}\int_0^{2\pi}\int_0^{\pi}\hat{M}\,\sqrt{\hat{g}_{22} * \hat{g}_{33}}\, d\theta\, d\varphi \,. \tag{5.3}$$

Then, using the deformed components of the metric given by (3.9d) and (3.9e) in the same above condition, we obtain the expression of the NC BH mass up to second order in the NC parameter Θ.

$$\hat{m} = m + \frac{\Theta^2}{8\, r_h} \,, \tag{5.4}$$

It is clear that in the commutative limit $\Theta = 0$, we obtain the Schwarzschild BH mass.

The behavior of the NC Schwarzschild BH mass as a function of the event horizon for various values of the NC parameter Θ is shown in Fig. 5.1. As we see, the effect of the non-commutativity shows a new behavior of the BH mass, contrary to the commutative one,

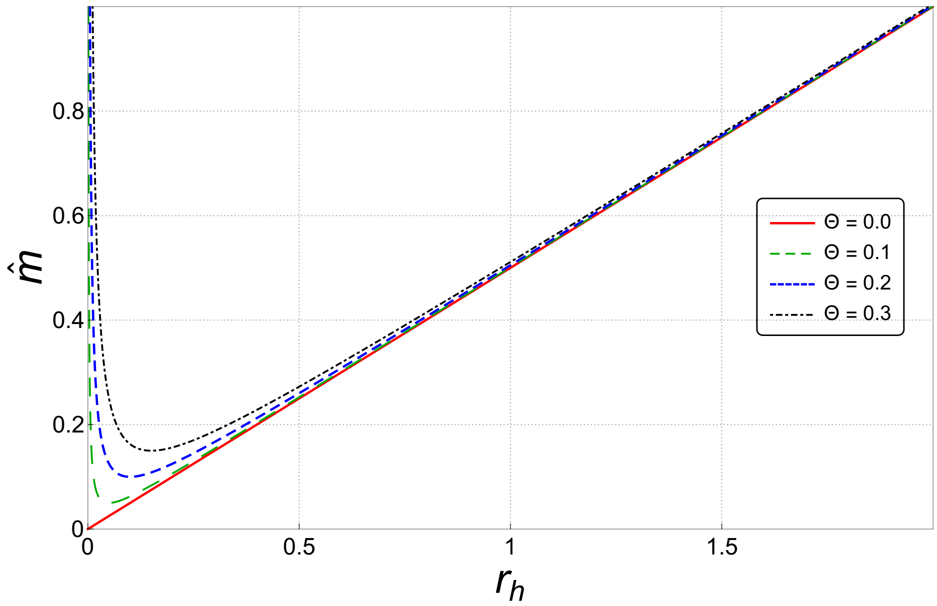

Figure 5.1: Behavior of BH mass as a function of r_h.

in which the behavior of the mass is in the linear depend with the event horizon radius $m = r_h/2$ and vanishes at the origin, while in the NC case this geometry prevents the mass from vanishing at the origin and presents a minimal value $\hat{m}_0 = 0.5\,\Theta$ away from the origin at $r_h = r_0 = 0.5\,\Theta$ (in this case the NC parameter Θ plays the role of the mass, as was found in our previous chapters (see Chap. 3 and 4)). This new minimum increases with the increase in the NC parameter Θ, and that means the non-commutativity prevents the mass from vanishing by creating a new minimum mass at the origin of the BH. It is clear that if $r_h \to 0$ then $\hat{m} \to \infty$, and this corresponds to the singularity of the BH at the origin of the commutative case and became an unphysical region because, as we see in Chap. 3, the noncommutativity shifted the singularity of the origin to a finite radius $r = 2m$. It is worth noting that the result of the effect of non-commutativity is a clear confirmation that the theory of GR links the geometry of spacetime and mass (gravity) together.

5.1.1.1 *Hawking temperature*

In the presence of non-commutativity, the geometry of the Schwarzschild BH is deformed, and this deformation leads to a modification in the geometrical quantities. In this context, the NC surface gravity $\hat{\kappa}$ of the deformed Schwarzschild BH is given by

$$\hat{\kappa} = -\frac{1}{2\sqrt{-\hat{g}_{00}(r,\Theta)\hat{g}_{11}(r,\Theta)}}\,\frac{\partial \hat{g}_{00}}{\partial r}\bigg|_{r=r_h^{\mathrm{NC}}}, \tag{5.5}$$

As we know, in the semi-classical framework, the Hawking temperature is related to the surface gravity by the relation (1.46); also, in the NC framework, the deformed Hawking temperature is related to the above deformed surface gravity by $\hat{T}_H = \frac{\hat{\kappa}}{2\pi}$. By using the deformed Schwarzschild metric given in Sec. 3.2 with $a, b \neq 0$ (see the schematic picture in

Fig. 3.2 for more detail on this geometry), we expanded our expression up to $(1/r^4)$, and we stopped at the second order in Θ. The NC Hawking temperature is given by

$$\hat{T}_H = \frac{1}{4\pi r_h} - \frac{3}{8\pi r_h^3}\left(a^2 + b^2 \sin^2\theta\right). \tag{5.6}$$

It is clear that the above expression depends on the observation angle θ and that due to the presence of non-commutativity, which deformed the symmetry of the BH and transformed into a spherical asymmetric. Moreover, this expression describes the four scenarios of BH in this geometry for different possibilities on a and b (see Fig. 3.2) for our choice of the NC matrix. It is worth noting that the NC Hawking temperature is the same as that in ordinary spacetime when $\theta = 0, \pi$ for the choice of $a = 0, b = \Theta$, which is actually a direct consequence of the NC parameter choice being perpendicular to the plane of rotation created by the non-commutativity of coordinates. Furthermore, the depends of NC temperature on the observational angle θ mean that the radiation of BH is not the same in all directions of observation in this geometry for $b \neq 0$, while in the case of $b = 0$ and $a = \Theta$ this particular result vanishes, and the BH has the same radiation in all directions as in the commutative case $a = b = 0$, where the commutative expression is recover (1.46).

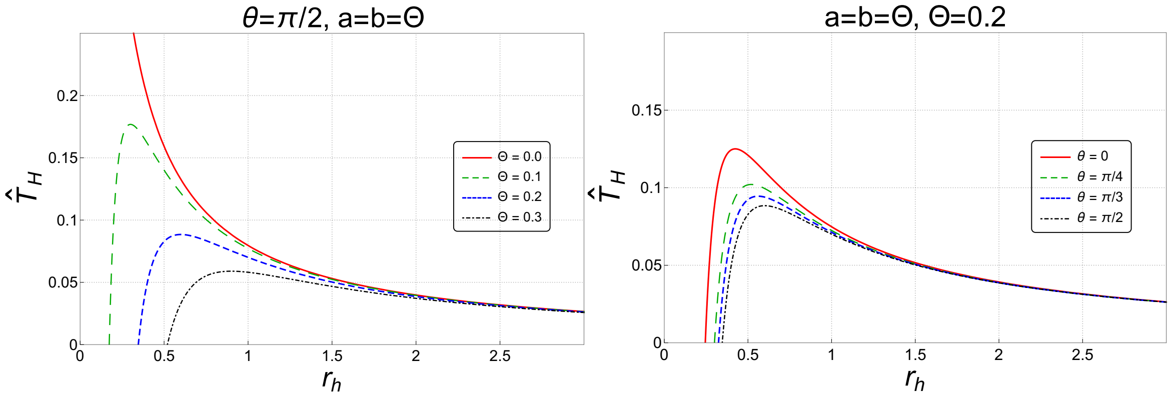

Figure 5.2: Behavior of NC Hawking temperature as a function of the event horizon r_h, with different Θ (left panel) and for different θ (right panel) for the case $a = b = \Theta$.

The behavior of Hawking temperature in the NC spacetime as a function of the event horizon r_h for the case $a = b = \Theta$ is shown in Fig. 5.2, for a different NC parameter Θ in the left panel and for a different observational angle Θ in the right panel. It is clear that from the left panel, the non-commutativity removes the divergence behavior that appears in the commutative spacetime, and this geometry cool-down the BH radiation. Moreover, in the right panel, we show the impact of our choice of non-commutativity, in which the radiation of the BH is note the same in all directions of observation, where the radiation at the poles of the NC Schwarzschild BH ($\theta = 0, \pi$) is more active compared to the equatorial plane, and that means the poles are more hot (high temperature) compared to the temperature emitting from the equatorial plan. This difference in temperatures between poles-equator increases during the BH evaporation. Also, we can see that, during the evaporation, the NC Hawking temperature of this deformed BH increases until it reaches a maximum value

$\hat{T}_H^{\max} = \frac{0.0177}{\Theta\sqrt{1+\sin^2\theta}}$ at the critical horizon radius $r_h^c = 2.12136\,\Theta\sqrt{1+\sin^2\theta}$, then quickly falls to zero at a new minimum of BH size $r_h^{\min} = 1.226\Theta\sqrt{1+\sin^2\theta}$, from this result and from the right panel, we can conclude that the BH stops radiation in the equator before the pols, and that led to a new scenario of evaporation.

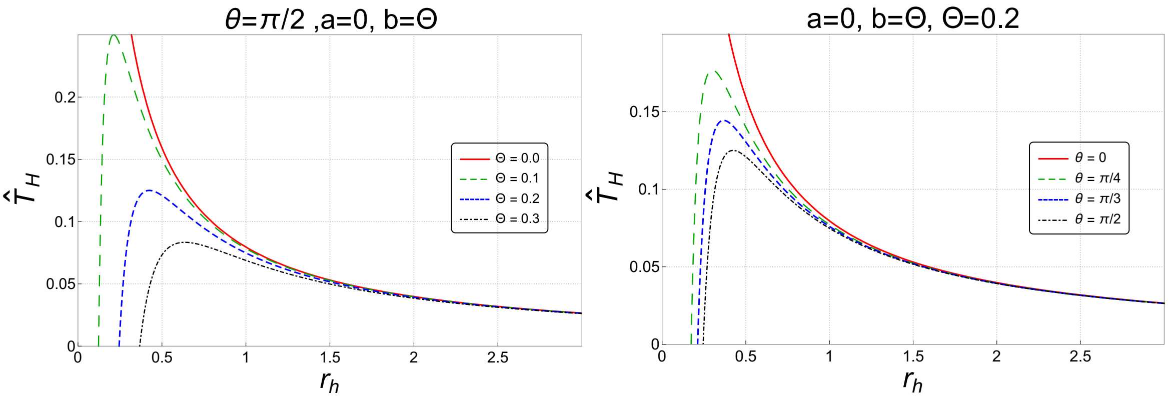

Figure 5.3: Behavior of NC Hawking temperature as a function of the event horizon r_h, with different Θ (left panel) and for different θ (right panel) for the case $a = 0$, $b = \Theta$.

In Fig. 5.3, we present the NC Hawking temperature for the cases $a = 0$ and $b = \Theta$, with different Θ in the left panel and for different θ in the right panel. As we see, the global behavior of these two scenarios is the same, except at the two poles ($\theta = 0, \pi$), where the NC effect vanishes. Another difference is in the maximum temperature and the minimum size of the BH, which are given by $\hat{T}_H^{\max} = \frac{0.025009}{\Theta\sin\theta}$, the critical size $r_h^c = 2.12132\,\Theta\sin\theta$, and the minimum size $r_h^{\min} = 1.2247\Theta\sin\theta$, and also in this scenario the BH stop radiation in the equator before their poles and the above one. Furthermore, for the cases $a = \Theta$ and $b = 0$, the deformed BH emit the same radiation in all directions, and the BH stop evaporation in all directions at the same time. At this point, we see all the possibilities of the radiation from the different scenarios of NC BHs present in Fig. 3.2.

It is worth noting that there are some models and observations that predicted the difference in temperature between the poles and the equator of the sun in the literature, e.g., [241–244]. This difference in temperature between poles-equator appears only in the NC spacetime, and it increases with Θ for small BHs as well (see Fig. 5.4).

In order to find an estimation of the NC parameter Θ, we use the temperature emitted from the total surface horizon of BH, and we take the choice of $a = 0$ and $b = \Theta$. This temperature can be computed as follows:

$$\begin{aligned}\hat{T}\left(r_h\right) &= \frac{1}{\int_0^{2\pi}\int_0^{\pi}\sqrt{\hat{g}_{22}\hat{g}_{33}}d\theta d\varphi}\int_0^{2\pi}\int_0^{\pi}\hat{T}\left(r_h,\theta\right)\sqrt{\hat{g}_{22}\hat{g}_{33}}d\theta d\varphi \\ &= \frac{1}{4\pi r_h} - \frac{\Theta^2}{4\pi r_h^3}\,. \end{aligned} \tag{5.7}$$

In the commutative limit $\Theta = 0$, we recover the Hawking temperature of the Schwarzschild BH (1.46).

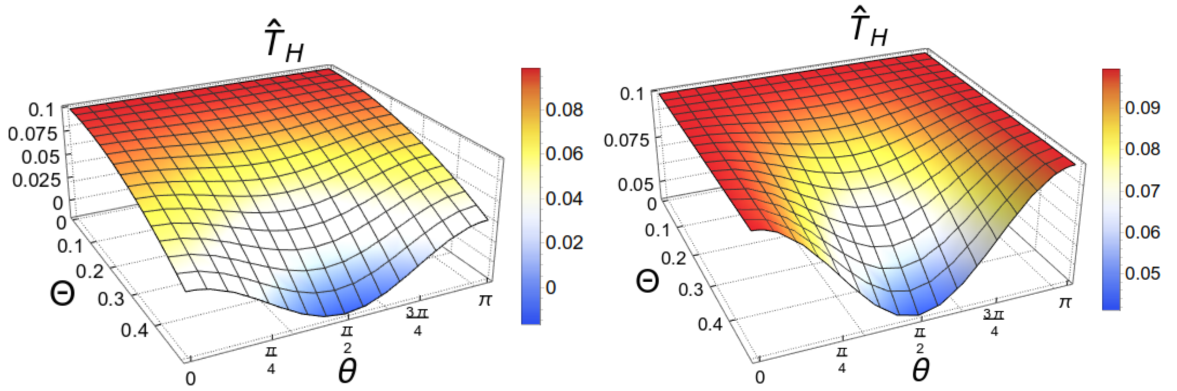

Figure 5.4: Behavior of NC temperature distribution as a function of the observation angle θ and NC parameter Θ, for the two cases, $a = b = \Theta$ (left panel) and $a = 0$, $b = \Theta$ (right panel), with $r_h = 0.8$.

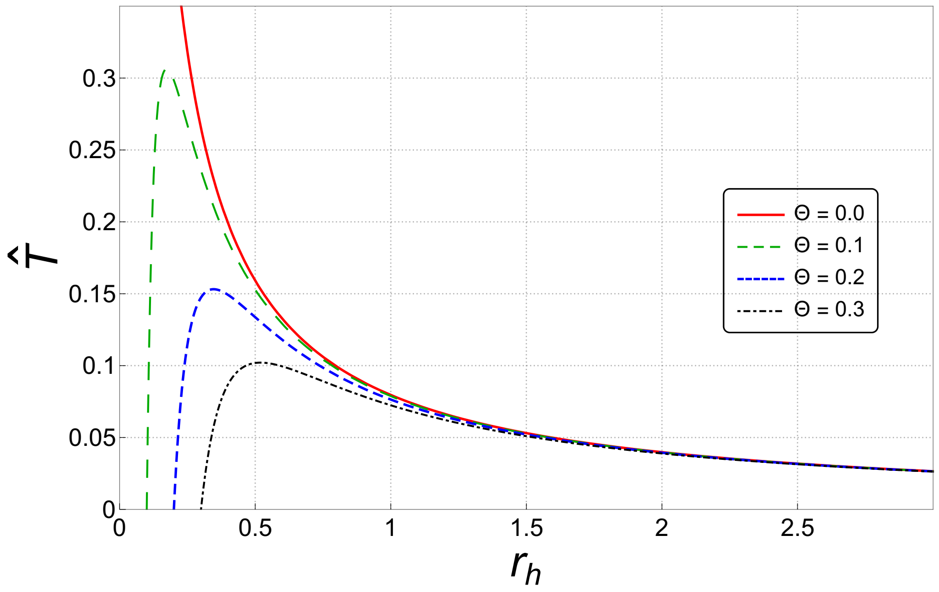

Figure 5.5: Behavior of NC temperature emitted from the surface horizon of the BH as a function of r_h, for the case $a = 0$, $b = \Theta$.

The behavior of the NC Hawking temperature emitted from the surface horizon of the NC Schwarzschild BH as a function of the event horizon r_h is shown in Fig. 5.5. As we see, we have the same behavior as the above scenarios, where the temperature emitted from the surface horizon increases to reach a maximum value $\hat{T}^{\max} = 0.031/\Theta$ at the critical horizon radius $r_h^c = 1.732\,\Theta$, then quickly falls to zero at the minimum horizon radius $r_h^{\min} = \Theta$, in which this BH cannot radiate anymore with this minimum, and that means there are no more processes of particle creation near the event horizon with $r_h = r_h^{\min}$, and that corresponds to the minimal mass $\hat{m}_0 = r_h^{min}/2 = 0.5\,\Theta$, which is called the remnant BH. The effect of this geometry is now clear, in which the non-commutativity removes the divergence behavior of the BH radiation that appears in the final stage of evaporation in a similar way to the electric charge of RN BH [245].

To get an estimation of the NC parameter Θ, we use the back-reaction point of the BH temperature. At this point, the thermal energy and the temperature are equivalent and are given by[1] $E^{\text{th}} = \hat{T}^{\text{max}}$ and at this point the mass of the BH $\hat{m} = \frac{G}{2} r_h^c = 0.866\,\Theta M_{\text{Planck}}^2$. The thermal energy and mass of the BH should be of the same order of magnitude at the critical point r_h^C for a significant result, and the NC parameter can be estimated as

$$\Theta \approx 1.523 \times 10^{-35} m \sim l_{\text{Planck}}\,. \tag{5.8}$$

The above value of the NC parameter Θ is close to the ones obtained in our previous Chap. 4. Moreover, this result is good according to the one obtained using the gravitational wave experimental data [246], which is on the Planck scale. It is clear that our results obtained using the gauge theory do not exceed the Planck scale. However, there exist few papers that study the BH thermodynamics in NC spaces where present a bound on the NC parameter of the order $\Theta \sim 10^{-1} l_{\text{Planck}}$, as in [145, 247–249], and that confirms the NC property of spacetime appears close to the Planck scale.

5.1.1.2 *Entropy*

In which follow, we use the choice[2] of $a = 0$ and $b = \Theta$. As we have observed so far, the non-commutativity modified the geometry structure of the Schwarzschild BH. Let's now turn to a second geometrical quantity, which is the NC BH area, and is defined by

$$A_h^{\text{NC}} = \int_0^{2\pi} \int_0^{\pi} \sqrt{\hat{g}_{22} * \hat{g}_{33}}\, d\theta\, d\phi\,. \tag{5.9}$$

The above integral can be computed by using the deformed metric components (3.9d) and (3.9e), and we take the result up to second order in Θ, then we obtain the NC area of the deformed Schwarzschild BH.

$$\begin{aligned} A_h^{\text{NC}} =& 2\pi \int_0^{\pi} \left[r_h^{\text{NC}} + \frac{3r_h^{\text{NC}} - m + \left(m + r_h^{\text{NC}}\right)\cos(2\theta)}{16\, r_h^{\text{NC}}} \right] \sin\theta\, d\theta, \\ =& 4\pi r_h^2 + \frac{5\pi}{2}\Theta^2 + \mathcal{O}(\Theta^4)\,. \end{aligned} \tag{5.10}$$

In order to obtain the expression of the NC entropy, we use the relation that relates the entropy with the area of the BH given in (1.47). In this case, we use the NC area $\hat{S} = A_h^{NC}/4$ given by the above expression. Thus, we get

$$\hat{S} = \pi r_h^2 + \frac{5\pi}{8}\Theta^2\,. \tag{5.11}$$

It is clear that, in the commutative spacetime $\Theta = 0$, the usual entropy of the Schwarzschild BH is recovered (1.47).

---

[1] In natural units system ($\hbar = k_B = c = 1$).

[2] The same calculations can be made for the others choice of a and b, and the only difference is in the correction factor, and the physics of the quantity is conserved for any choice of the NC matrix.

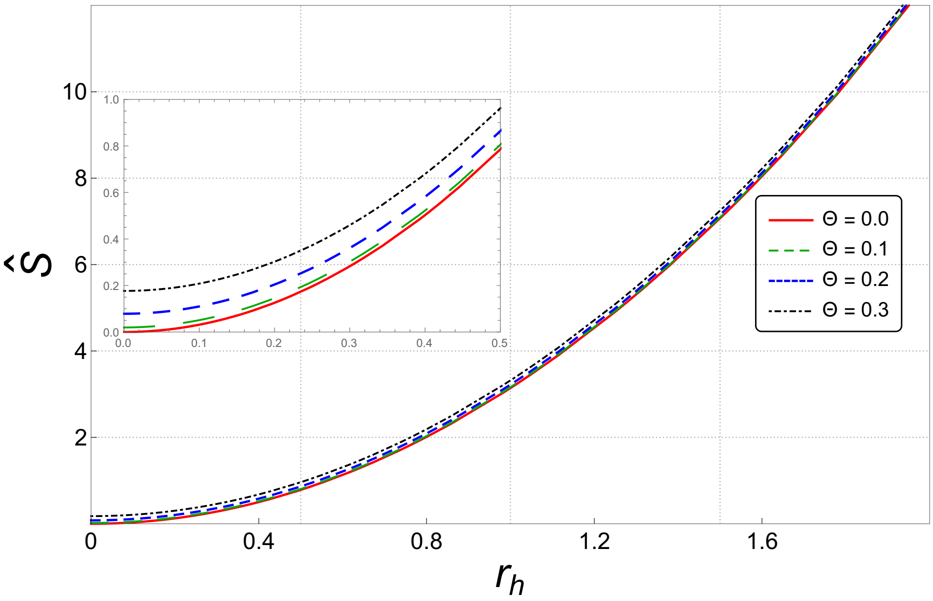

Figure 5.6: Behavior of NC entropy as a function of r_h.

The entropy behavior of the NC Schwarzschild BH as a function of the event horizon r_h is shown in Fig. 5.6. It is clear that we observe a significant difference between the commutative and NC entropy for smaller BH, and it becomes negligible for larger ones. Another important observation in this deformed entropy is the non-zero entropy (5.12) that appears in the final stage of evaporation, which is a consequence of the quantum structure of spacetime.

$$\lim_{r_h \to 0} \hat{S} = S_0^{\Theta} \approx \frac{5\pi}{8}\Theta^2. \tag{5.12}$$

The above expression emerges from the pure quantum structure of spacetime, which originates from non-commutativity. This remnant of entropy is a consequence of an existing BH that evaporated before, since the entropy is related to the area of the BH via $S_0^{\Theta} = A_0^{\Theta}/4$, which implies that, after the evaporation process, the NC BH still has a quantum area corresponding to quantum entropy[3]. This strange quantum object has a quantum area A_0^{Θ} with a minimal mass $\hat{m}_0 = 0.5\, l_p$ and a minimum size $r_h^{min} = l_P$, which can be considered a microscopic remnant BH.

5.1.2 *Heat capacity and phase transition*

In order to investigate the thermal stability of the NC Schwarzschild BH, we must check the behavior and signature of its heat capacity in this geometry. As a first step, we investigate the partial heat capacity; for that, we use the partial deformed Hawking temperature

---

[3] This note is valid only if the area law of BH is correct in the NC gauge theory, and we present the correct correction to the entropy in the following section

given by Eq. (5.6) to see the stability of each region from the equator to the poles and examine their phase transition. In this case, the heat capacity is given by

$$\begin{aligned}\hat{C} &= \hat{T}_H \left(\frac{\partial \hat{S}}{\partial \hat{T}_H}\right) = \hat{T}_H \left(\frac{\partial \hat{S}}{\partial r_h}\right) \left(\frac{\partial \hat{T}_H}{\partial r_h}\right)^{-1} \\ &= -2\pi r_h^2 \frac{(2r_h^2 - 3\Theta^2 \sin^2\theta)}{(2r_h^2 - 9\Theta^2 \sin^2\theta)}, \qquad (5.13)\end{aligned}$$

where we use the NC entropy (5.11) and the NC Hawking temperature (5.6). In Fig. 5.7,

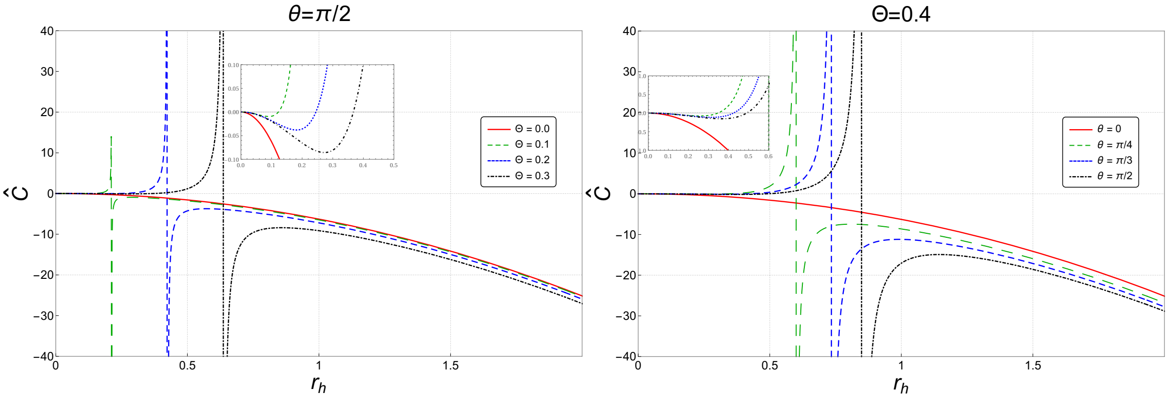

Figure 5.7: Behavior of Schwarzschild BH heat capacity as a function of the event horizon r_h, for different values of Θ (left panel) and for different values of θ (right panel).

we show the behavior of the NC heat capacity of the deformed Schwarzschild BH in NC spacetime. It is clear that in the commutative limit $\Theta = 0$, we recover the standard behavior of heat capacity, in which the phase transition of the Schwarzschild BH does not exist because their behavior is always negative. From the left panel of this figure, we see clearly that the heat capacity is equal to zero at $r_h = r_h^{\text{min}}$, which corresponds to the minimum size when the BH stop radiation (see Fig. 5.3), and that means this BH has one physical limitation point [250] and has a divergence at $r_h = r_h^{\text{crit}}$, where this corresponds to the back-reaction point of the BH radiation (in Fig. 5.3 corresponds to the maximum temperature), which implies one phase transition point. According to the right panel, we see that the physical limitation point r_h^{min} and the back reaction point r_h^{crit} are different from direction to the other, and that is due to the presence of the observational angle θ in our expression of the partial heat capacity (5.13). This indicates that the deformed BH with the choice $a = 0$ and $b = \Theta$ (even for $a = b = \Theta$) has a new scenario of evaporation, in which the phase transition r_h^{crit} occurs in the equator before the two poles. Also, this BH stops radiation r_h^{min} from the equator region before the other direction, and that means the evaporation of the deformed Schwarzschild BH in this geometry begins the evaporation from the equator and goes up to the two poles. It is worth noting that all limitation points r_h^{min} for different NC parameter Θ or different observational angle θ and also for the divergence points r_h^{crit} are consistent with the profiles of $\hat{T}_H - r_h$ in Fig. 5.3 for the left and right panels, respectively. For the investigation of stability, we leave it for the global analysis of the heat capacity.

Now we check the global heat capacity of this deformed BH for more information about the phase transition and its thermal stability. For that, we use the same above definition with the global temperature emitted from the surface horizon of the NC Schwarzschild BH

$$\hat{C} = -2\pi r_h^2 \frac{(r_h^2 - \Theta^2)}{(r_h^2 - 3\Theta^2)}, \tag{5.14}$$

In this case, we are using the Hawking temperature given by Eq. (5.7) and the entropy (Eq. (5.11)). The behavior of the global heat capacity emitted from the surface horizon of the NC Schwarzschild BH as a function of the event horizon r_h for different Θ is shown in Fig. 5.8. It is clear that the behavior of the global heat capacity is similar to the partial distribution of the radiation obtained above; the only differences are the points of physical limitation and the phase transition. In this case, the physical limitation point $r_h = r_h^{\text{min}}$ and the divergence at $r_h = r_h^{\text{crit}}$ are consistent with the point when the BH stop radiation and the point of the back-reaction in the profile $\hat{T} - r_h$ in Fig. 5.5. In this geometry, a non-equilibrium (unstable) system has a negative heat capacity for $r_h > r_h^{\text{crit}}$, which corresponds to a large massive BH, while for a system in equilibrium (a stable one), it has a positive heat capacity for $r_h^{\text{min}} < r_h < r_h^{\text{crit}}$, which corresponds to the smaller BH. As we see above, the divergence point r_h^{crit} of heat capacity describes a phase transition of the NC Schwarzschild BH in this geometry, and this point is increasing with the growth of Θ. Also, the stable stage $r_h^{\text{min}} < r_h < r_h^{\text{crit}}$, which has a positive heat capacity, increases with Θ, and that means the NC Schwarzschild BH takes longer to stop radiating and evaporating for the large values of Θ.

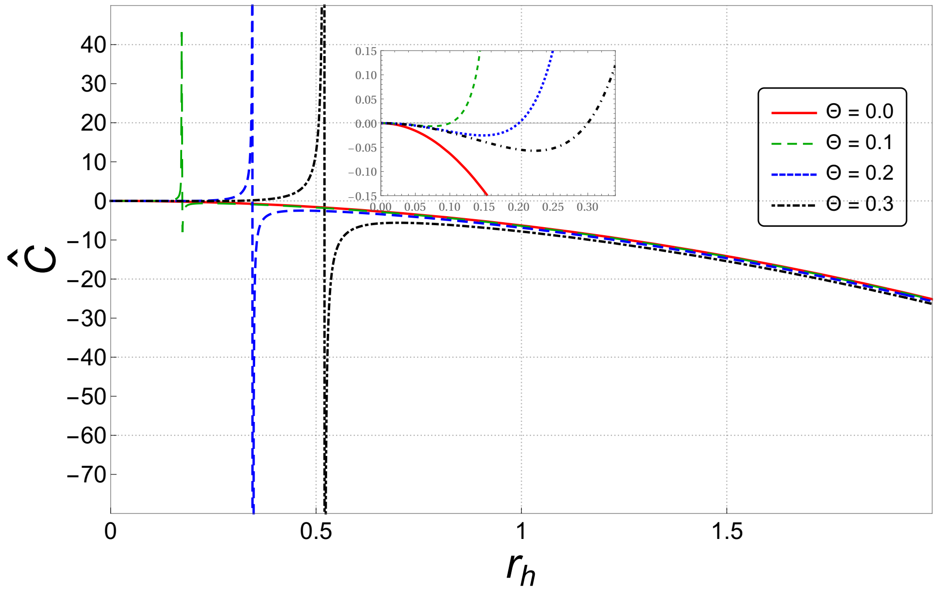

Figure 5.8: Behavior of the global heat capacity as a function of r_h in the case of $a = 0$ end $b = \Theta$.

5.1.3 *Helmholtz free energy and black hole stability*

For more details on the phase transition and thermal stability, we need to analyze the Helmholtz free energy, which is given as the Legendre transform of the ADM mass.

$$\hat{F} = \hat{m} - \hat{T}\hat{S}. \tag{5.15}$$

where we use the global temperature that is emitted by the surface horizon of the BH given by Eq. (5.7).

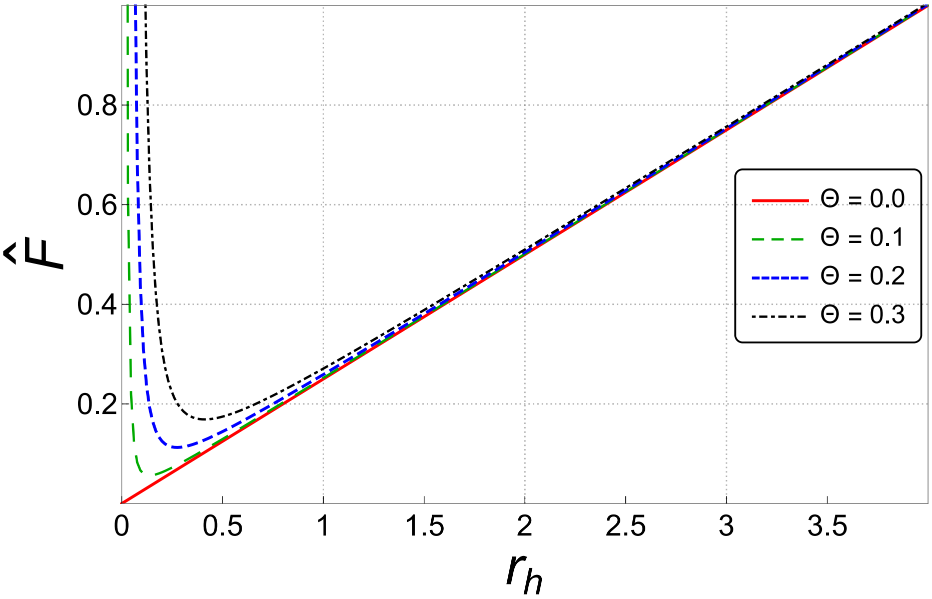

Figure 5.9: Behavior of Helmholtz free energy $\hat{F}$ as a function of r_h in NC spacetime.

In Fig. 5.9, we plot the behavior of Helmholtz free energy of the NC Schwarzschild BH as a function of the event horizon r_h. As we see, in the NC spacetime, the Helmholtz free energy behavior has a minimum, which is given by

$$\frac{\partial \hat{F}}{\partial r_h} = 0\,, \tag{5.16}$$

and the location of this minimum increases with the increase of the NC parameter Θ, which corresponds to a stable region. This result is consistent with the profile $\hat{C} - r_h$ obtained in Fig. 5.8, which means that a smaller BH is more stable compared to a larger one.

The effect of temperature on the NC Helmholtz free energy is shown in Fig. 5.10, where we plot the following expression for different Hawking temperatures $\hat{T}$

$$\hat{F} = \frac{r_h}{2} - \pi r_h^2 \hat{T} + \Theta^2 \left(\frac{1}{8 r_h} - \frac{5\pi}{8} \hat{T} \right). \tag{5.17}$$

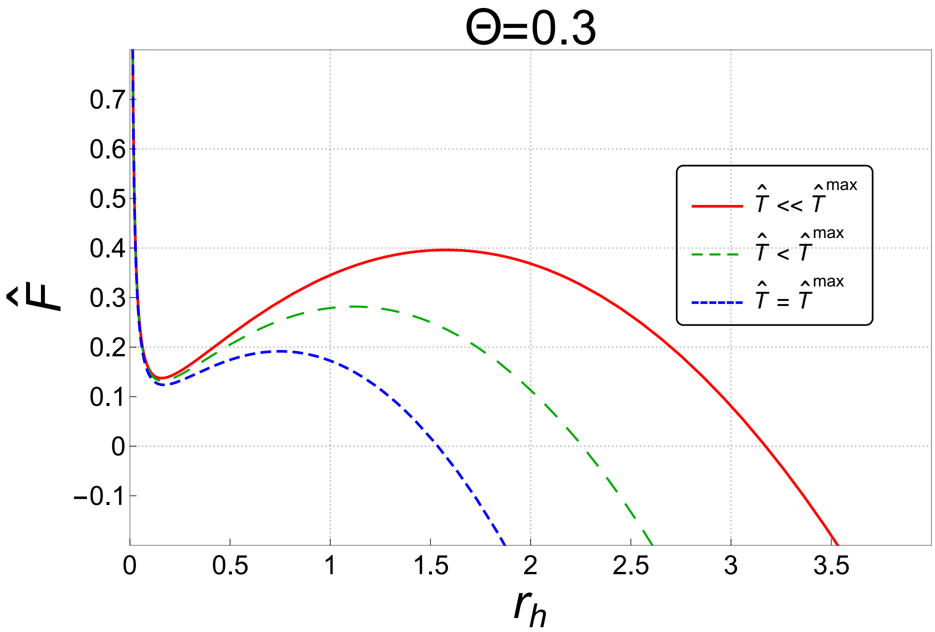

Figure 5.10: Behavior of Helmholtz free energy $\hat{F}$ as a function of r_h in NC spacetime for different Hawking temperatures $\hat{T}$.

In Fig. 5.10, we plot the behavior of the NC Helmholtz free energy for different values of Hawking temperature. It is clear that when taking into account the Hawking temperature, a new extremum appears in the behavior of the Helmholtz free energy, which results in two extrema (stable and unstable), where we can obtain their location by solving Eq. (5.16). From this behavior, we conclude that a maximum Helmholtz free energy corresponds to a large BH, which is unstable thermodynamically, while a minimum Helmholtz free energy corresponds to a smaller one, which is stable thermodynamically, contrary to the commutative Schwarzschild BH, which is always unstable.

The behavior of the NC Helmholtz free energy $\hat{F}$ as a function of the NC Hawking temperature $\hat{T}$ for different values of Θ is shown in Fig. 5.11. As we see in this geometry, the Helmholtz free energy decreases rapidly with increases in Hawking temperatures (from infinity at $\hat{T} \sim 0$) until it reaches the maximum temperature $\hat{T}^{max}$. Moreover, when the temperature bounces back from a maximum $\hat{T}^{\mathrm{max}}$, the free energy starts to increase at a slow rate, and this rate becomes more rapidly when we increase Θ, while in the commutative case $\Theta = 0$, the Helmholtz free energy does not change its behavior during the BH evaporation. It is worth noting that this behavior is similar to the one obtained with a modified first law of BH thermodynamics, where we take into account the surface tension as in Refs. [67–69]. However, in our results, this behavior emerges from the quantum properties of spacetime in the NC Schwarzschild spacetime. According to these works, non-commutativity can be seen as a spacetime tension on the quantum scale.

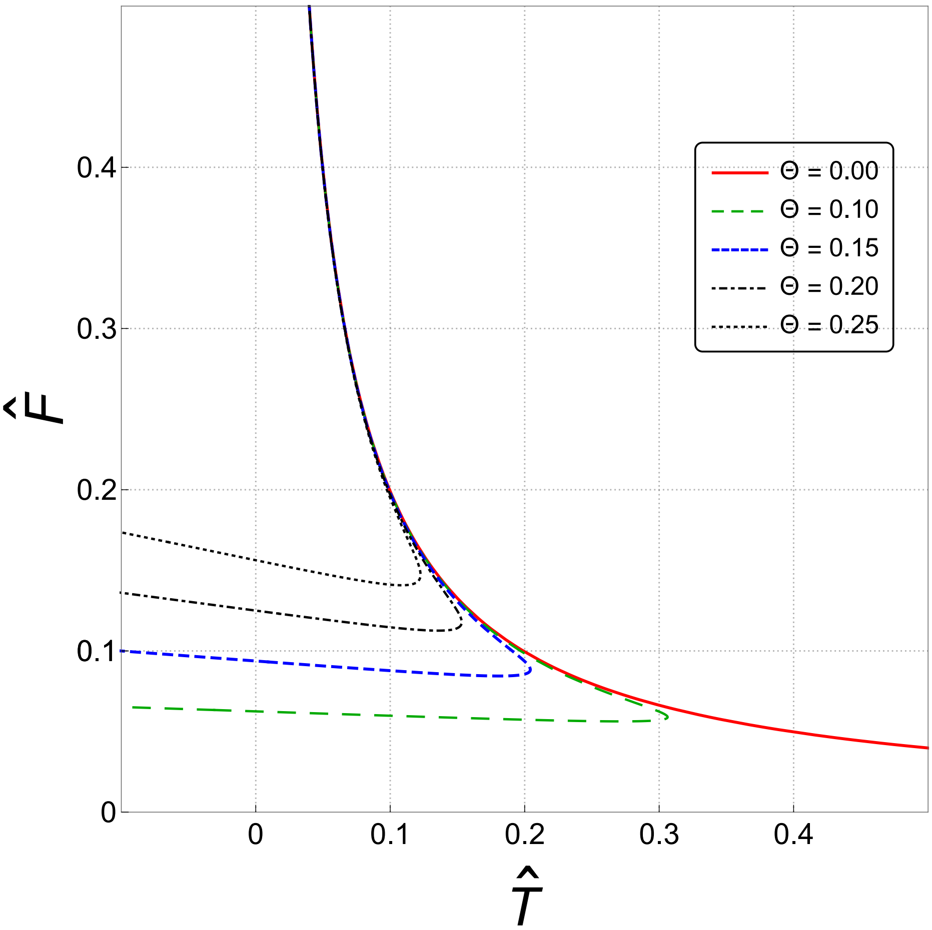

Figure 5.11: Behavior of the Helmholtz free energy $\hat{F}$ as a function of the NC Hawking temperature $\hat{T}$.

5.1.4 *The black hole pressure and Hawking-Page-like phase transition*

The authors of the following recent papers [251–253], show that if one uses quantum gravitational corrections to the BH thermodynamics for the Schwarzschild case, these corrections lead to a pressure in this BH. In this context, our next step is motivated by the above papers, where in our case we consider the origin of the quantum correction for Schwarzschild BH to be the non-commutativity of spacetime. For that, we add the pressure of the BH by ad-hoc $\hat{P}d\hat{V}$ term to the first law of thermodynamics, (5.1), which can be written as follows:

$$d\hat{m} = \hat{T}d\hat{S} - \hat{P}d\hat{V}\,, \tag{5.18}$$

where $\hat{V}$ denotes the NC volume of deformed Schwarzschild BH, which is computed using the same step in (5.3) (we stop at the second order in Θ).

$$\begin{aligned}\hat{V} &= \frac{4\pi}{3}\frac{1}{\int_0^{2\pi}\int_0^{\pi}\sqrt{\hat{g}_{22}*\hat{g}_{33}}\,d\theta\,d\phi}\int_0^{2\pi}\int_0^{\pi}\left(r_h^{\mathrm{NC}}\right)^3\sqrt{\hat{g}_{22}*\hat{g}_{33}}\,d\theta\,d\phi\\ &= \frac{4\pi}{3}r_h^3 + \pi r_h\Theta^2 + \mathcal{O}(\Theta^4)\,,\end{aligned} \tag{5.19}$$

and its conjugate, the pressure $\hat{P}$

$$\hat{P} = -\left(\frac{\partial \hat{m}}{\partial \hat{V}}\right) = -\left(\frac{\partial \hat{m}}{\partial r_h}\right)\left(\frac{\partial \hat{V}}{\partial r_h}\right)^{-1}$$
$$= -\frac{1}{8\pi r_h^2} + \frac{\Theta^2}{16\pi r_h^4} + \mathcal{O}(\Theta^4)\,, \tag{5.20}$$

where $\frac{4\pi}{3} r_h^3$ and $P = -1/(8\pi r_h^2)$ are the commutative volume and pressure, respectively.

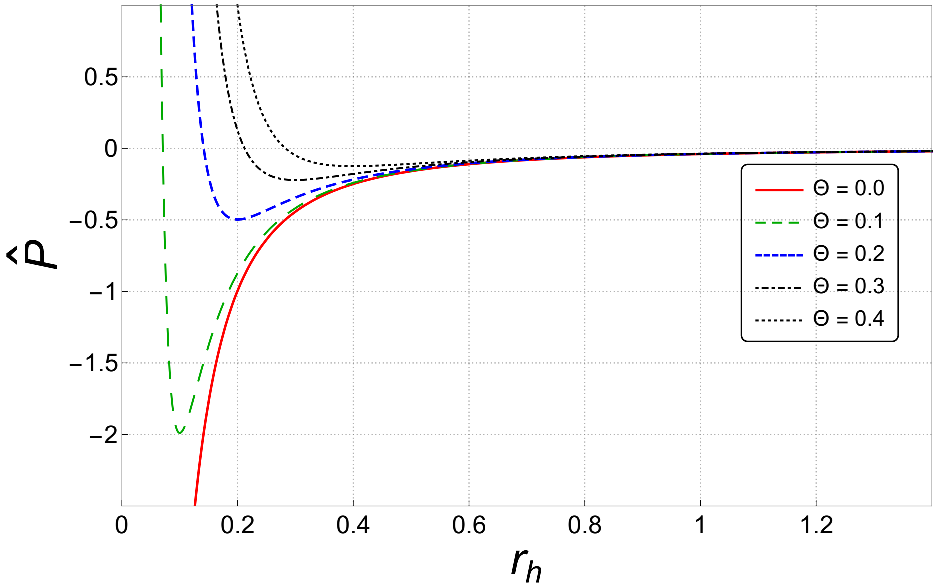

Figure 5.12: Behavior of pressure $\hat{P}$ as a function of r_h.

The behavior of the NC Schwarzschild BH pressure as a function of the event horizon r_h, with different values of the NC parameter Θ, is shown in Fig. 5.12. As we see, the non-commutativity shows a new behavior, where this geometry removes the divergence behavior of pressure, and during the evaporation process, the pressure behavior decreases rapidly until it reaches a new minimum value at the point $\left(-0.02/\Theta^2, \Theta\right)$, then starts to increase until it reaches a zero at $r_h = 0.71\Theta$. Moreover, that means the NC coordinates create a new minimum behavior for the pressure, which corresponds to a transition point associated with the interaction of this BH with NC spacetime. After this point, the effect of the NC spacetime pressure on the BH increases with decreasing of the event horizon r_h until reach the equilibrium point at $r_h = 0.71\Theta$. Note that, for a region where the pressure is negative and decreasing until it reaches its minimum at $r_h = \Theta$, it can be interpreted as the pressure exerted by the BH on spacetime. This pressure is induced by the radiation of the BH. While for the negative region between minimum $r_h = \theta$ and equilibrium point $r_h = 0.71\Theta$, the pressure is increasing, which can be interpreted as the pressure exerted by the spacetime on BH.

5.1.4.1 *Gibbs free energy*

In order to analyze the phase transition in the presence of pressure in the NC spacetime, we investigate the profile of Gibbs free energy. In this context, use the NC Helmholtz free energy $\hat{F}$ (see Eq. (5.15)) to compute the NC Gibbs free energy $\hat{G} = \hat{F} + \hat{P}\hat{V}$. Thus, we can write the NC Gibbs free energy as follows:

$$\hat{G} = \hat{m} - \hat{T}\hat{S} + \hat{V}\hat{P}\,. \tag{5.21}$$

The influence of pressure on Gibbs free energy is shown in Fig. 5.13, where we plot the following expression for different $\hat{P}$ and $\hat{T}$

$$\hat{G} = \frac{r_h}{2} + \frac{4\pi}{3} r_h^3 \hat{P} - \pi\, r_h^2\, \hat{T} + \Theta^2 \left(\frac{1}{8 r_h} + \pi\, r_h \hat{P} - \frac{5\pi}{8} \hat{T} \right). \tag{5.22}$$

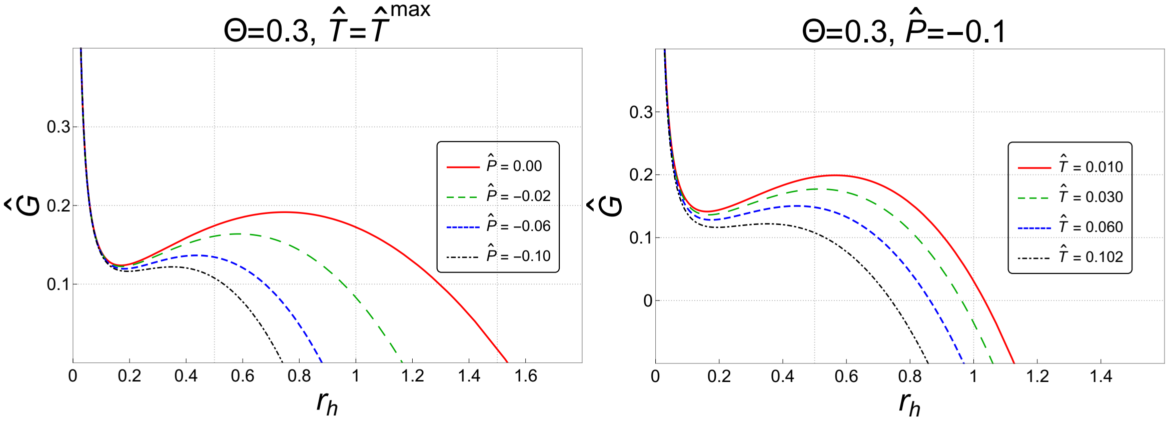

Figure 5.13: Behavior of Gibbs free energy $\hat{G}$ as a function of r_h in NC spacetime, for different values of pressure $\hat{P}$ (left panel) and different Hawking temperature $\hat{T}$ (right panel).

In this study, we are only interested in the negative pressure for the Schwarzschild BH (see Fig. 5.12). In Fig. 5.13, we show the behavior of the NC Gibbs free energy as a function of the event horizon r_h for different values of pressure (left panel) and for different values of temperature (right panel). As we see, the Gibbs free energy exhibits the same behavior as the one obtained with the Helmholtz free energy shown in Fig. 5.10, i.e., there are only two extrema for $\hat{G}$ (see left panel in Fig. 5.13) for $\hat{T} = \hat{T}^{\max}$ and $-0.10 \leqslant \hat{P} \leqslant 0$ in NC geometry, and as we see above, the minimum of free energy corresponds to the stable BH (smaller Schwarzschild BH) and the maximum one corresponds to the unstable one (larger Schwarzschild BH), and these extremum can be obtained by solving Eq. (5.16). It is worth noting that the two extrema of Gibbs free energy disappear when the pressure gets a value less than ($\hat{P} \ll -0.1$). Furthermore, when we fix pressure at ($\hat{P} = -0.10$) and we change the temperature in the range $0.010 < \hat{T} \leqslant 0.102 < \hat{T}^{\max}$, we observe the same Gibbs free energy behavior (see right panel in Fig. 5.13), i.e., two extrema. In this case, the depth of the minimum and the maximum of the NC Gibbs free energy decreases with the increase in temperature. As a consequence, a larger BH, which is an unstable one, evaporates to a smaller and more stable one, and this agrees with the analysis of the heat capacity profile $\hat{C} - r_h$ (see Fig. 5.7), which indicates a phase transition of Schwarzschild BH in the NC spacetime.

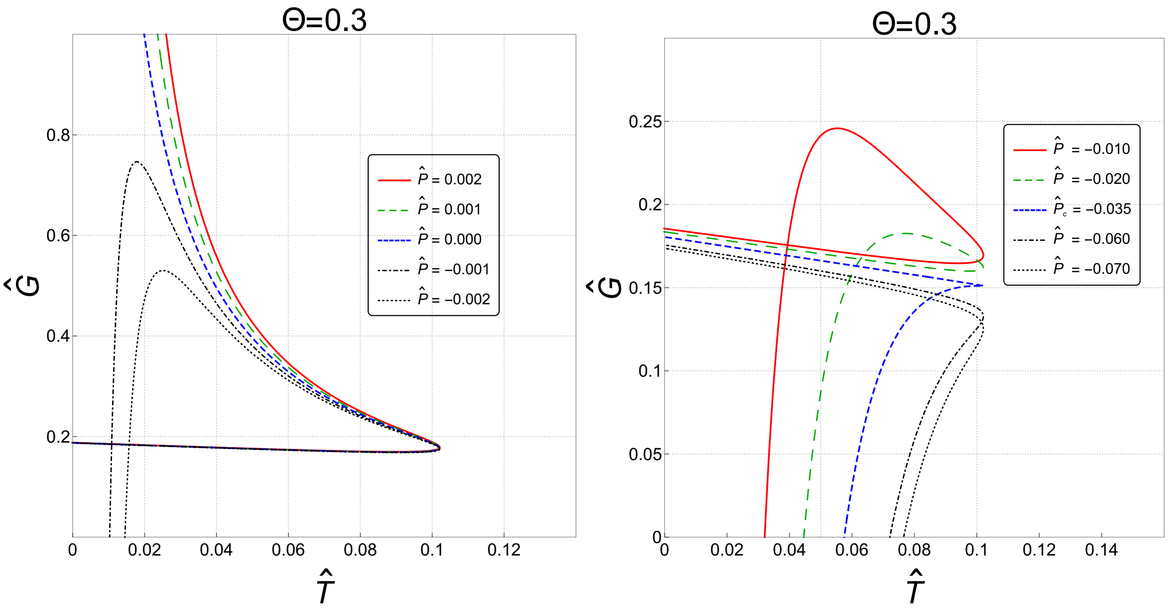

Figure 5.14: Behavior of Gibbs free energy $\hat{G}$ as a function of the NC Hawking temperature $\hat{T}$, for different values of NC pressure $\hat{P}$.

In Fig. 5.14, we show the behavior of Gibbs free energy as a function of the NC temperature for different values of pressure (left and right panels). As shown in the left panel, for $\hat{P} \geqslant 0$, the Gibbs free energy is consistent with the profile "$\hat{F} - \hat{T}$" in Fig. 5.11. For negative pressure, $\hat{P} \leqslant 0$, we observe new behavior in which the Gibbs free energy increases rapidly as the temperature increases, until it reaches a maximum free energy, then it starts to decrease until the temperature rises to a maximum $\hat{T}^{max}$. When the temperature bounces back, the Gibbs free energy increases at a slow rate, which coincides with the previous cases of positive pressure. $\hat{P} \geqslant 0$. It is worth noting that, when we decrease in the pressure, i.e., $\hat{P}_c < \hat{P} < 0$, we observe a similar behavior to the swallowtail structure as in the literature; for example, see Refs. [254–256], which can be seen as a quasi-swallowtail, where in our case we have smoother curves, and that is due to the presence of non-commutativity. Unfortunately, the quasi-swallowtail cannot be interpreted as tow-phase coexistence, and that is due to the absence of the intermediate BH during the evaporation process (see Fig. 5.13). However, at the critical point of pressure $\hat{P}_c = -0.035$, the quasi-swallowtail structure disappears and an inflection point occurs, and that corresponds to a second-order phase transition. At this point, the Hawking-Page-like phase transition occurs during the evaporation processes of the NC Schwarzschild BH, where that corresponds to the transition of the unstable BH (larger one) to a stable one (smaller BH), and that is consistent with the profiles "$\hat{G} - r_h$" in Fig. 5.13 and "$\hat{C} - r_h$" in Fig. 5.8. For values below the critical point of pressure $\hat{P} < \hat{P}_c$, the inflection point vanishes, which means there is no more phase transition in this case, and that means there is only one phase transition that occurs at the critical point $\hat{P} = \hat{P}_c$ during the evaporation of the NC Schwarzschild BH. It is worth noting that, in the literature, we find some papers that study the effect of some QG models on the phase transition of BHs inside an isothermal spherical cavity with a constant of radius R, as in Refs. [102, 103, 121, 257, 258], and these results show the exact swallowtail structure[4]. However, in this study, we show a quasi-swallowtail behavior with smoother curves ($\hat{P}_c < \hat{P} < 0$) without using a boundary condition as the spherical cavity in the above examples, but we find a Hawking-Page-like phase transition ($\hat{P} = \hat{P}_c$). This behavior emerges when we study the presence of the BH pressure in the NC spacetime.

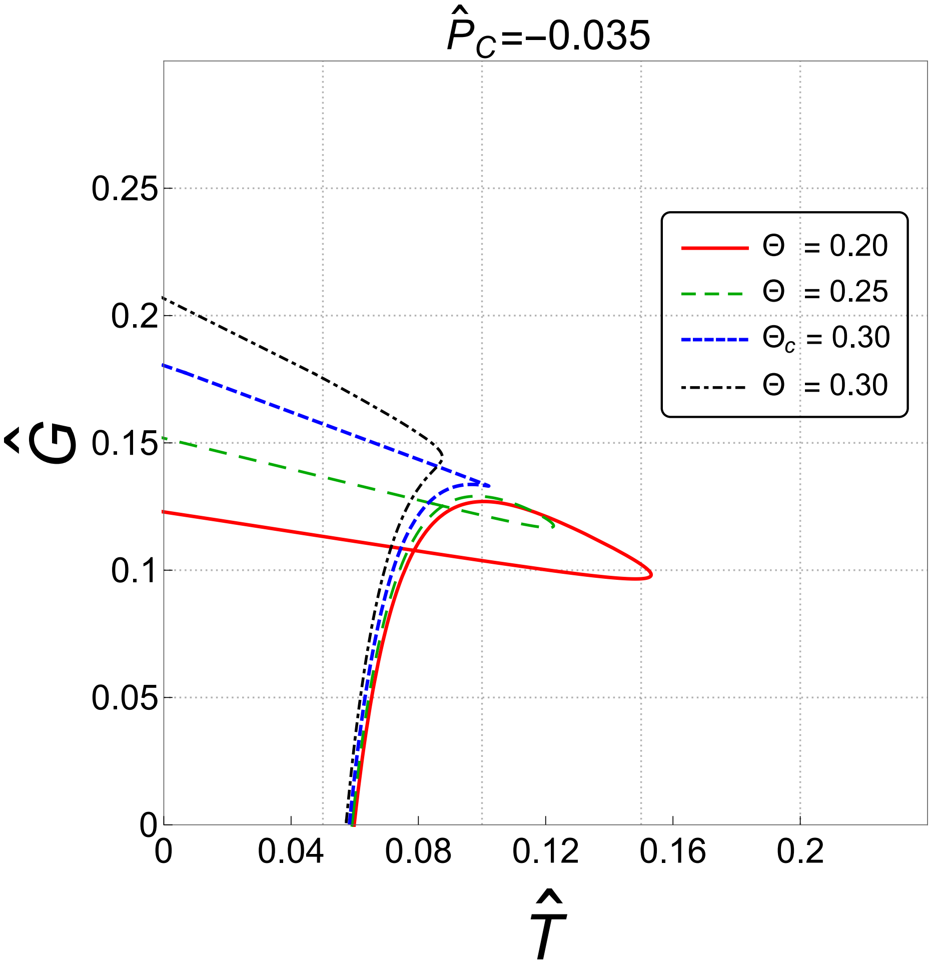

Figure 5.15: Behavior of Gibbs free energy $\hat{G}$ as a function of NC Hawking temperature $\hat{T}$, for different values of Θ.

In Fig. 5.15, we plot the Gibbs free energy as a function of Hawking temperature $\hat{T}$ in the NC spacetime for constant pressure $\hat{P}$ and different values of the NC parameter Θ. As we see, for the values of the NC parameter below the critical value $\Theta < \Theta_c$, we obtain the quasi-swallowtail structure with smoother curves. At a critical point, $\Theta_c = 0.30$, we can see that the vanish of the quasi-swallowtail structure and its replacement by an inflection point occur, which is a behavior similar to the Hawking-Page phase transition, and that indicates a phase transition of a larger BH (unstable) to a smaller one (stable). Then, for $\Theta > \Theta_c$, this inflection point disappears. This behavior is similar to the above one, which is presented in Fig. 5.14 (right panel), but with a difference in the order of the curves. We observe that the NC parameter Θ plays a role similar to a thermodynamic variable of a BH.

---

[4] Also, when we take into account the scenario of NC Schwarzschild BH inside an isothermal spherical cavity with radius R, we obtain an exact swallowtail behavior by just using the relation between free energy and mass, with no need of the ad-hoc term of pressure. We investigate this scenario in detail in the next Sec.

5.1.5 *Modified first law of the BH thermodynamics*

In what follows, we study the validity of the first law of BH thermodynamics in the NC gauge theory of gravity, where we are motivated by some issues that we found above, for example, the validity of the area law for the entropy and the equivalence of the deformed Hawking temperature resulting from the surface horizon with the one obtained from the first law (5.1). As in the commutative case, the NC BH also obeys the first law of thermodynamics because it is a thermodynamic system. The temperature $\hat{T}$ resulting from the first law of thermodynamics reads

$$\begin{aligned}\hat{T} &= \left(\frac{\partial \hat{m}}{\partial r_h}\right)\left(\frac{\partial \hat{S}}{\partial r_h}\right)^{-1} \\ &= \frac{1}{4\pi r_h} - \frac{\Theta^2}{16\pi r_h^3}\,.\end{aligned} \tag{5.23}$$

It is clear that $\hat{T}$ in Eq. (5.23) calculated by the first law is not the same as $\hat{T}$ in Eq. (5.7) calculated using surface gravity, and this difference is also observed in Ref. [166]. The possibility for solving this problem in this geometry is to use an ad-hoc term, in which the classical form of the first law is modified by an extra factor [170].

$$c\left(r_h, \Theta\right) d\hat{m} = \hat{T} d\hat{S}\,, \tag{5.24}$$

where $c\left(r_h, \Theta\right)$ is

$$c\left(r_h, \Theta\right) = 1 - \frac{3\Theta^2}{4r_h^2}\,. \tag{5.25}$$

If we substitute this value in Eq. (5.25) for $c\left(r_h, \Theta\right)$, we recover the area law. The correct NC correction to the entropy will be present in the next section, and for the next step, we keep working on the NC entropy resulting from the area law (5.11) in order to modify the first law of BH thermodynamic. In this context, we use the following decomposition of thermodynamic properties:

$$\hat{m} = m + \Theta^2 m^{(2)}, \tag{5.26a}$$

$$\hat{T} = T_H + \Theta^2 T^{(2)}, \tag{5.26b}$$

$$\hat{S} = S + \Theta^2 S^{(2)}. \tag{5.26c}$$

where $m^{(2)}$, $T^{(2)}$, and $S^{(2)}$ are the NC correction terms and can be obtained by comparison with the Eqs. (5.4), (5.7), and (5.11), respectively.

As we see above, in the NC gauge theory, the first law of BH thermodynamics is not respected, and that also means the Samarr formula of the ADM mass is not respected in this geometry. Starting from the classical form

$$\frac{1}{2}\hat{m} = \hat{T}_H \hat{S}, \tag{5.27}$$

By using the relations (5.26b) and (5.26c), we can separate the right hand of the above relation for the commutative terms and the NC terms, and then we find

$$\begin{aligned}\frac{1}{2}\hat{m} &= \left(T_H + \Theta^2 T^{(2)}\right)\left(S + \Theta^2 S^{(2)}\right)\\ &= T_H S + \Theta^2\left(T_H S^{(2)} + T^{(2)} S\right) + \mathcal{O}(\Theta^4)\\ &= T_H S + \Theta\mathcal{A}\end{aligned} \tag{5.28}$$

where $\mathcal{A}$ is a physical quantity conjugate to the NC parameter Θ, and in this case represent the NC corrections for the first law of thermodynamics. From the above relation (5.28), we can compute this physical quantity as follows:

$$\begin{aligned}\Theta\mathcal{A} &= \Theta^2\left(T_H S^{(2)} + T^{(2)} S\right)\\ &= -\frac{7\Theta^2}{32 r_h}.\end{aligned} \tag{5.29}$$

and we have

$$\begin{aligned}T_H S &= \frac{r_h}{4}\\ \frac{1}{2}\hat{m} &= \frac{r_h}{4} + \frac{\Theta^2}{16 r_h}.\end{aligned} \tag{5.30}$$

It is clear that, from Eqs. (5.29) and (5.30), the terms of NC correction in both sides of Eq. (5.28) are note equal, and that means in the NC gauge theory, the Samarr formula is note respected.

5.2 NC BH IN THE GRAND CANONICAL ENSEMBLE

As we saw earlier, in the NC gauge theory, the Samarr formula and the area law of entropy are not valid. In the next step, we present a modified Samarr formula in the NC gauge theory where we considered the non-commutativity as a thermodynamical variable in the first law of thermodynamics, which is motivated by the previous section, where we find that in the presence of the BH pressure, the NC parameter Θ plays the same role as a thermodynamical variable and the similarity between the non-commutativity effect on the temperature and the electric charge of RN BH[5], also by the Refs. [245, 259].

We start now with the first law of the BH thermodynamics (5.1), which can be written by differentiating the ADM mass (5.4), and we considered the NC parameter as geometrical charge, in a similar form of the electric charge of RN BH, [245, 259]

$$d\hat{m} = \hat{T} d\hat{S} + \mathcal{A} d\Theta, \tag{5.31}$$

---

[5] We investigate this similarity in detail in this section.

where Θ is the NC parameter and $\mathcal{A}$ his conjugate (which can be seen as a NC physical potential), which is defined as:

$$\mathcal{A} = \left(\frac{\partial \hat{m}}{\partial \Theta}\right)_{\hat{S}} \tag{5.32}$$

Using the expression of the ADM mass (5.4), we get

$$\mathcal{A} = \frac{\Theta}{4r_h}. \tag{5.33}$$

As we see, the NC physical potential $\mathcal{A}(r)$ conjugate to the NC parameter Θ is similar to the Coulomb potential $\phi(r)$ conjugate to the electric charge Q in the RN BH.

The Samarr formula of the modified first law, (5.31), can be represented in a similar form as in the case of the RN BH [245, 259].

$$\hat{m} = 2\hat{T}_H\hat{S} + \alpha\mathcal{A}\Theta, \tag{5.34}$$

where α is a factor, using the thermodynamic quantities in the previous section, we find

$$\begin{aligned} \hat{m} &= 2\left(\frac{r_h}{4} - \frac{7\Theta^2}{32r_h}\right) + \alpha\left(\frac{\Theta^2}{4r_h}\right), \\ &= \frac{r_h}{2} + \frac{-7+4\alpha}{16r_h}\Theta^2, \end{aligned} \tag{5.35}$$

By comparing the above equation with the NC ADM mass (5.4), we find that $\alpha = \frac{9}{4}$, so the modified Samarr formula in the NC gauge theory of gravity is written as follows:

$$\hat{m} = 2\hat{T}_H\hat{S} + \tilde{\mathcal{A}}\Theta, \tag{5.36}$$

where $\tilde{\mathcal{A}} = \frac{9}{4}\mathcal{A}$, in this case the Samarr formula is respected in the NC spacetime.

According to the modified first law of thermodynamics (5.31), in the same way as the electric charge [260], the new modified Gibbs free energy in the grand canonical ensemble (in the presence of the NC physical potential $\mathcal{A}(r_h)$) is written as follows:

$$\tilde{G} = \hat{m} - \hat{T}\hat{S} - \Theta\mathcal{A}. \tag{5.37}$$

The behavior of modified Gibbs $\tilde{G}$ free energy in the grand canonical ensemble as a function of the deformed Hawking temperature is shown in Fig. 5.16 for different values of the NC parameter. It is clear that we obtain a similar behavior to the Helmholtz free energy given in the profile $\hat{F} - \hat{T}$ (see Fig. 5.11), where the only difference is that the free energy is lower than obtained in Fig. 5.11 in the final stage of evaporation, which means that, when we take into account the presence of the NC physical potential $\mathcal{A}$, the BH is more stable thermodynamically compared to the one analyzed without $\mathcal{A}$ (see Fig. 5.11), and this potential has a significant effect of the free energy only in the final stage of evaporation. Moreover, in the grand canonical ensemble, the NC Schwarzschild BH is more stable thermodynamically in its final stage.

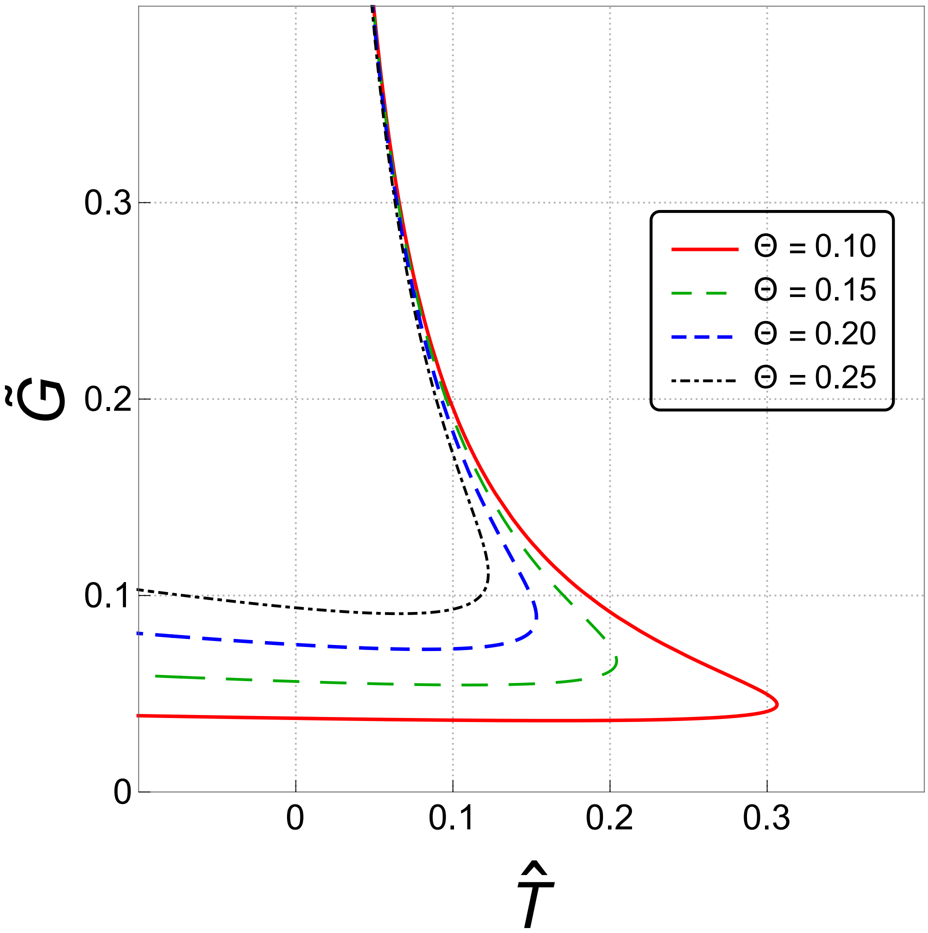

Figure 5.16: The behaviors of the modified Gibbs $\tilde{G}$ free energy in the grand canonical ensemble as a function of the NC Hawking temperature $\hat{T}$.

5.2.0.1 *Black hole pressure*

Now, we will take into account the presence of pressure and investigate the thermal stability in the presence of $\mathcal{A}(r)$. Let's now consider the presence of $\mathcal{A}(r)$ together with the pressure term in the relation (5.18), so we get

$$d\hat{M}_{ADM} = \hat{T}_H d\hat{S} + \mathcal{A} d\Theta - \hat{P} d\hat{V}. \tag{5.38}$$

According to the above modified first law of thermodynamics in the presence of pressure (5.38), we can define the new Gibbs free energy in the grand canonical ensemble by:

$$\tilde{G}_P = \hat{M}_{ADM} - \hat{T}_H \hat{S} - \Theta \mathcal{A} + \hat{P} \hat{V}. \tag{5.39}$$

In Fig. 5.17, we show the behavior of the modified Gibbs free energy in the grand canonical ensemble as a function of the NC Hawking temperature in the presence of pressure. As we see, a similar behavior is obtained with $\hat{G} - r_h$ (see Fig. 5.14) in the absence of NC physical potential $\mathcal{A} = 0$, while in the presence of $\mathcal{A}$ the modified Gibbs free energy has a lower energy compared to their absence, and that means this BH is more stable thermody-

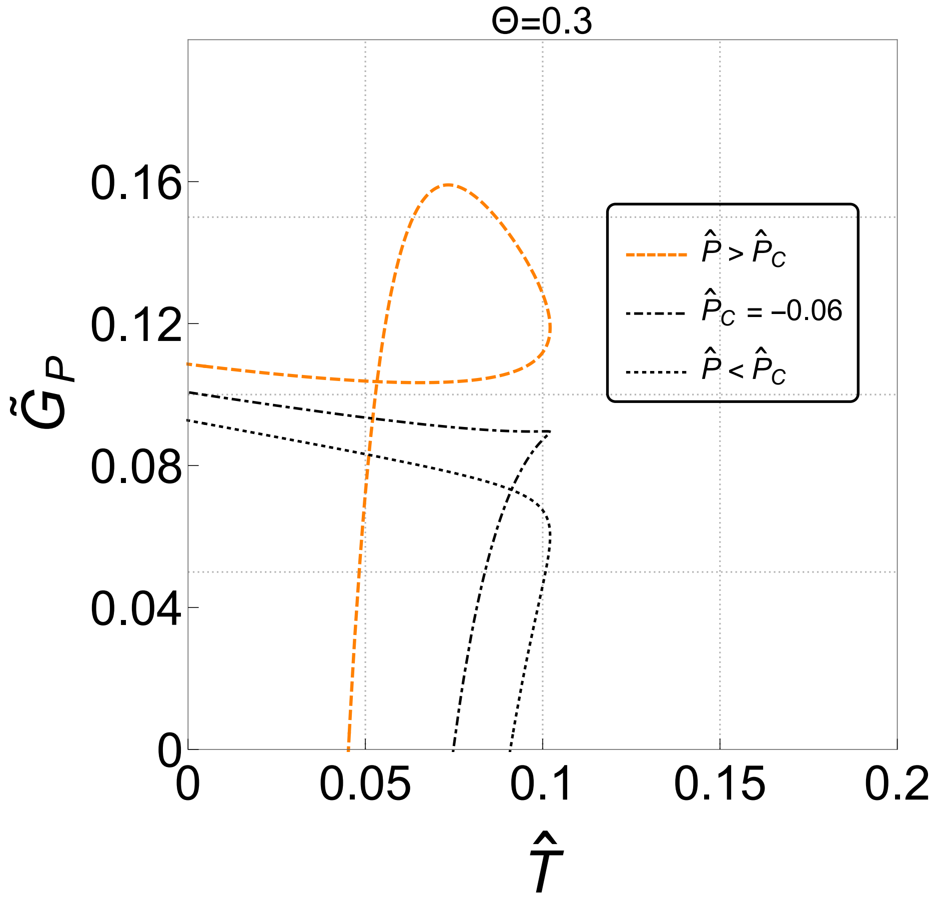

Figure 5.17: The behaviors of the modified Gibbs free energy in the grand canonical ensemble as a function of the NC Hawking temperature $\hat{T}$ in the presence of pressure.

namically in the presence of the NC physical potential $\mathcal{A}$ compared to its absence. Also, we observe the quasi-swallowtail structure with smother curves as before (for the case $\mathcal{A} = 0$). It is worth noting that the presence of the NC physical potential shifts the inflection point to a new critical point, $\hat{P}_c = -0.06$, at which the quasi-swallowtail structure disappears, and that means a second-order phase transition. In other words, the NC physical potential $\mathcal{A}$ is important for the thermal stability of the NC BH during his evaporation process.

5.2.1 *Similarity between non-commutativity and the electric charge of a black hole*

As we know, some of the quantum potential used as a correction to the BH geometry affects the quantum process of Hawking radiation [100, 108–110],...etc., as well as the electric potential in the RN BH [245, 259]. In a similar way, the NC geometry also affects this process [165, 166, 203, 247], in which this geometry plays a similar role as a thermodynamical potential, and that leads to a modification in the BH thermodynamics, as we saw above. In our previous subsection, in the grand canonical ensemble, we found an important observation that brought our attention to the similarity in the thermodynamic corrections between the effect of non-commutativity and the electric charge one of RN BH. We summarized them in the following table.

Table 5.1: Comparison of some thermodynamic properties between RN BH and NC Schwarzschild BH in the grand canonical ensemble.

Thermodynamic properties	RN BH [245]	NC Schwarzschild BH
ADM mass	$M = \frac{r_+}{2} + \frac{Q^2}{2r_+}$	$\hat{m} = \frac{r_h}{2} + \frac{\Theta^2}{8r_h}$
Hawking temperature	$T_H = \frac{1}{4\pi r_+} - \frac{Q^2}{4\pi r_+^3}$	$\hat{T} = \frac{1}{4\pi r_h} - \frac{\Theta^2}{4\pi r_h^3}$
Potential	$\phi = \frac{\phi}{r_+}$,	$\mathcal{A} = \frac{\Theta}{4r_h}$,

The similarity between the RN BH and the NC Schwarzschild BH in the grand canonical ensemble for some expressions of BH thermodynamic properties is shown in Table. 5.1. It is clear that, for the Hawking temperature, we see that both expressions are identically the same. Also, for the BH mass, we observe a similarity between the electric charge Q and the NC parameter Θ, where the non-commutativity term is shifted by a factor of $\frac{1}{4}$, and the same is true for the NC physical potential $\mathcal{A}$ and the electric one ϕ. Moreover, these results motivate us to treat the non-commutativity as a quantum potential in a similar way as the electric charge Q for the RN BH.

5.2.2 *State equation*

In which follow we present a new procedure in which we treat the NC BH as AdS RN BH to show the similarity between the NC parameter and the electric charge. As a first step, we define a new temperature and pressure as follows: $\tilde{t} = \frac{\hat{T}}{2}$ and $\tilde{p} = \frac{\hat{P}}{2}$, respectively, so the Eqs. (5.7) and (5.20) become

$$\tilde{t} = \frac{1}{8\pi r_h} - \frac{\Theta^2}{8\pi r_h^3}, \tag{5.40a}$$

$$\tilde{p} = -\frac{1}{16\pi r_h^2} + \frac{\Theta^2}{32\pi r_h^4}. \tag{5.40b}$$

We multiply Eq. (5.40b) by $2r_h$ and subtract from Eq. (5.40a) to obtain two new coupled equations for temperature and pressure in the following table, which we compare with the AdS and RN expressions [245].

Table 5.2: Comparison of state equation between AdS RN BH and the NC Schwarzschild BH.

Thermodynamic properties	RN BH [245, 256]	NC Schwarzschild BH
Temperature	$T = \frac{1}{4\pi r_h} + 2r_h P - \frac{Q^2}{4\pi r_h^3}$,	$\tilde{t} = \frac{1}{4\pi r_h} + 2r_h\tilde{p} - \frac{3\Theta^2}{16\pi r_h^3}$,
Pressure	$P = -\frac{1}{8\pi r_h^2} + \frac{T}{2r_h} + \frac{Q^2}{8\pi r_h^4}$,	$\tilde{p} = -\frac{1}{8\pi r_h^2} + \frac{\tilde{t}}{2r_h} + \frac{3\Theta^2}{32\pi r_h^4}$.

In Table. 5.2, we show a comparison between the NC Schwarzschild BH and the AdS RN BH for both state equations of temperature and pressure. It is clear that our result shows a good similarity between the expressions for both cases, and the only difference was observed in the third term, which allows us to make a comparison between the NC parameter Θ and the electric charge Q.

$$\Theta^2 = \frac{4}{3} Q^2. \tag{5.41}$$

It is worth noting that our result is different from the one obtained in Ref. [163], and that due to the different approach used, where we use the NC gauge theory of gravity, we agree with Ref. [163] for the possibility that the electric charge Q is related to the NC parameter Θ.

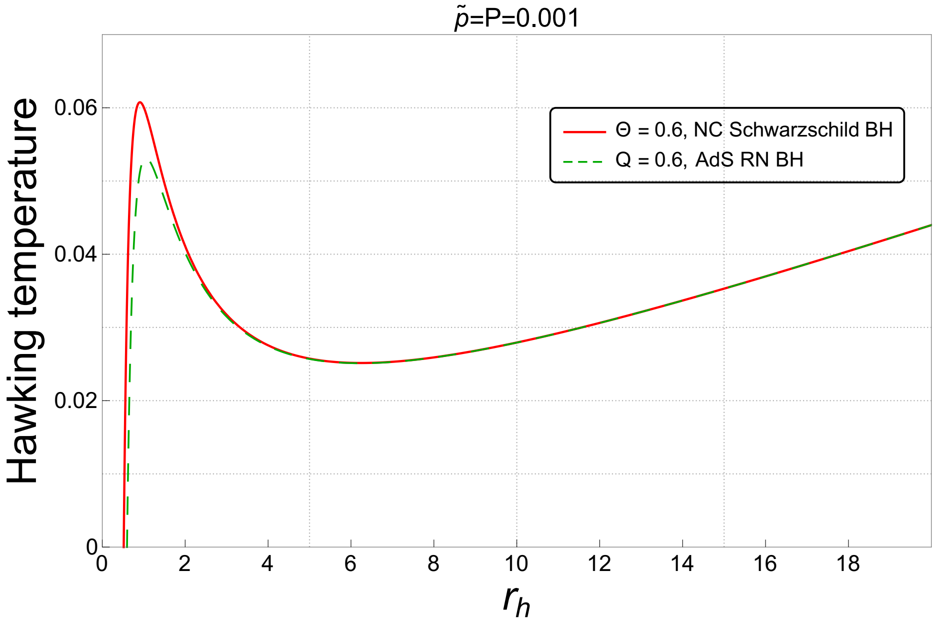

Figure 5.18: Hawking temperature for AdS RN BH compared to NC Schwarzschild BH as a function of the event horizon.

The comparison of the Hawking temperature behavior between the AdS RN BH and the NC Schwarzschild one is shown in Fig. 5.18, which is plotted as a function of r_h with a constant pressure. As we see, for a larger BH, the Hawking temperature is identical in both cases, while for a smaller one, we observe a significant difference in the final stage of BH evaporation, where the NC Schwarzschild BH is hotter compared to the AdS RN ($\tilde{t}^{max} > T^{max}$). We observe also that the AdS RN BH evaporate and stop radiation before the NC Schwarzschild one, and that means the remnant NC Schwarzschild BH is smaller than the remnant AdS RN one ($r_0^{NC-SBH} < r_0^{AdS-RNBH}$). Another important observation is that in this scenario, the NC Hawking temperature of Schwarzschild BH has a new minimum, which is not allowed in the previous profile $\hat{T} - r_h$ presented in Fig. 5.5, in which here the non-commutativity plays a similar role as a boundary condition, because we treated this effect of the NC pressure as external pressure applied by the NC spacetime on the deformed Schwarzschild BH, in a similar way to the cosmological constant in AdS RN BH. Also, during the evaporation process of the NC Schwarzschild BH, their temperature decreases until they reach the minimum $\tilde{t}^{min}_{local}$, and this minimum decreases with the increase in Θ. This behavior starts to increase during the evaporation to reach the maximum $\tilde{t}^{max}$, then quickly falls to zero at r_0, where the BH stop radiation at this point, and that means a remnant BH. It is worth noting that the change in temperature behavior starts from decreasing to reach a minimum, then increases from this minimum to reach a maximum and decreasing again, which indicates a two-phase transition of the NC Schwarzschild BH at the minimum and maximum points.

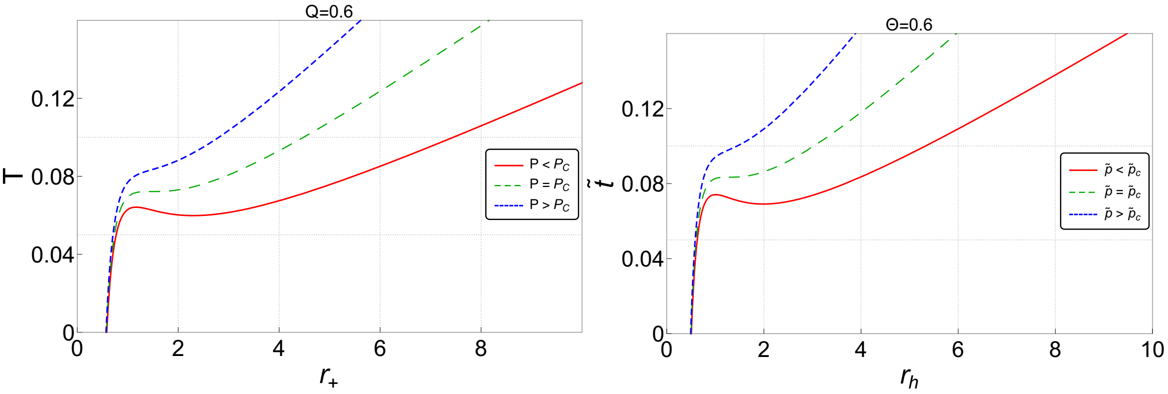

Figure 5.19: Hawking temperature for AdS RN BH (left panel) and NC Schwarzschild one (right panel) as a function of the event horizon r_h, with different values of pressure.

In Fig. 5.19, we show the influence of pressure on the Hawking temperature for the AdS RN BH (left panel) and the NC Schwarzschild one (right panel) as a function of the event horizon r_h. It is clear that we observe the same behavior in both cases, and that shows an important similarity between these two BHs, and the only difference was in the critical points of the thermodynamical proprieties, which we derived latterly.

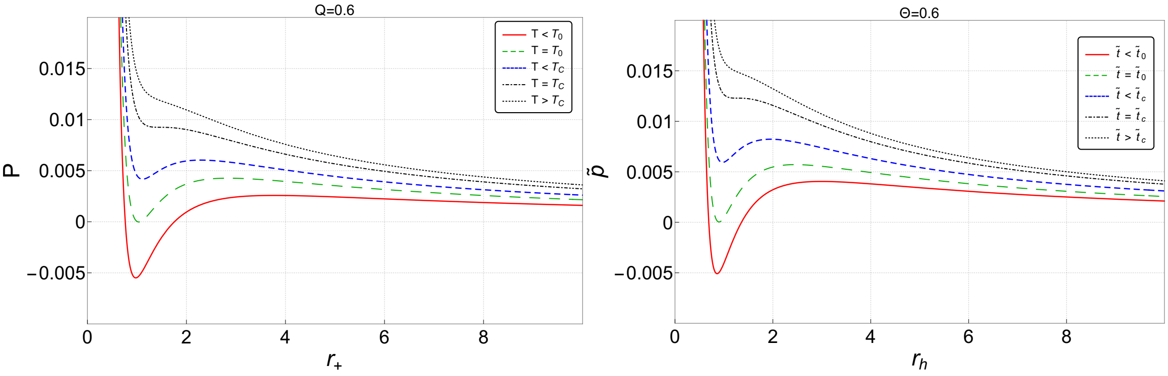

Figure 5.20: Black hole pressure for AdS RN (left panel) and NC Schwarzschild (right panel) as a function of the event horizon, with different values of temperature.

The behavior of the BH pressure for both cases of the AdS RN BH (left panel) and the NC Schwarzschild one (right panel) as a function of the event horizon and for different values of temperature are shown in Fig. 5.20. It is clear that, also for the pressure profile, we observe a similarity between the NC Schwarzschild BH and the AdS RN one, and the only difference is in the values of the critical points in each case, where an inflection point appears for $\tilde{t} < \tilde{t}_c$ and disappears for $\tilde{t} \geq \tilde{t}_c$. As we mentioned in our previous SubSec. 5.1.4, we interpreted the negative pressure as the pressure applying by the BH on his environment (spacetime for example), while the positive one represents the pressure applying by the environment (spacetime for example) on the BH. In the AdS RN BH the positive and negative pressure due to the positive and negative sign of the cosmological constant [261] (Fig. 5.20 left panel), in which the cosmological constant is identified as the pressure, see Refs. [245, 256, 261, 262]. However, in this study, we identify the deformed geometry induced by the presence of non-commutativity as external pressure applied to the NC Schwarzschild BH. According to discussion in SubSec. 5.1.4, we can see that, for $\tilde{p} < \tilde{p}_c$ (Fig. 5.19 right panel) and $\tilde{t} < \tilde{t}_c$ (Fig. 5.20 right panel), we can analyze the pressure behavior by comparing to the radiation activity of BH (see Fig. 5.19 right panel), where for large BH, their pressure is always positive and close to zero pressure, and this one is responsible for the increasing in temperature for a LBH which act as a boundary condition, at this moment the spacetime pressure applying on this BH. Then this pressure starts increasing until it reaches a maximum during the BH evaporation, and that is due to the decrease in the BH radiation, which corresponds to the minimum temperature (see temperature profile in Fig. 5.19 right panel), and that means the pressure applied by the non-commutativity of spacetime on the BH is greater than the pressure applied by the NC BH on the spacetime. This maximum doesn't take a long time to start decreasing until it reaches a minimum, and that is due to the increase in the BH radiation, which corresponds to the maximum temperature (see Fig. 5.19 right panel), where that means the pressure applying by BH on the spacetime is significant, but the dominant pressure in this case is the one applied by the spacetime on this BH. It is worth noting that, for some range of BH radius, the pressure became negative, and that means the BH pressure applying on the spacetime is completely dominated by the one applying by the spacetime on this BH. Moreover, when the BH stop radiation, this effect is reversed, in which the pressure increases rapidly to infinity. At this region, a remnant BH appears (see Fig. 5.19 right panel). As a conclusion, the profile shown in Fig. 5.20 (right panel) is the pressure applied between BH and spacetime in the NC geometry, and the study of the non-commutativity effect as an external pressure shows a new behavior of thermodynamic properties for the Schwarzschild BH and shows an important similarity with the AdS RN BH.

As in the commutative case, the critical point in the NC spacetime can also be obtained by solving the following system of equations for $\Theta \neq 0$:

$$\frac{\partial \tilde{t}}{\partial r_h} = 0, \quad \frac{\partial^2 \tilde{t}}{\partial r_h^2} = 0, \tag{5.42}$$

$$\frac{\partial \tilde{p}}{\partial r_h} = 0, \quad \frac{\partial^2 \tilde{p}}{\partial r_h^2} = 0. \tag{5.43}$$

We summarized in the following table the solution to the above equations.

Table 5.3: Critical parameter of AdS RN BH and NC Schwarzschild one.

Black holes type	size	volume	temperature	pressure
AdS RN BH [245, 256]	$r_c = \sqrt{6}Q$	$V_c = 8\sqrt{6}\pi Q^3$	$T_c = \frac{\sqrt{6}}{18\pi Q}$	$P_c = \frac{1}{96\pi Q^2}$
NC Schwarzschild BH	$r_c = \frac{3\sqrt{2}}{2}\Theta$	$\tilde{V}_c = 9\sqrt{2}\pi\Theta^3$	$\tilde{t}_c = \frac{\sqrt{2}}{9\pi\Theta}$	$\tilde{p}_c = \frac{1}{72\pi\Theta^2}$

5.2.3 *Phase transition and free energy*

In order to investigate the phase transition of the NC Schwarzschild BH in this scenario, we must check the signature of the heat capacity in this case. By using the new deformed Hawking temperature given in Table. 5.2, the new heat capacity can be written as follows:

$$\tilde{C} = \tilde{t}\frac{\partial \hat{S}}{\partial \tilde{t}} = \tilde{t}\left(\frac{\partial \hat{S}}{\partial r_h}\right)\left(\frac{\partial \tilde{t}}{r_h}\right)^{-1},$$

$$= \frac{2r_h^2\pi(4r_h^2 + 32r_h^4\tilde{p}\pi - 3\Theta^2)}{-4r_h^2 + 32r_h^4\tilde{p}\pi + 9\Theta^2}. \tag{5.44}$$

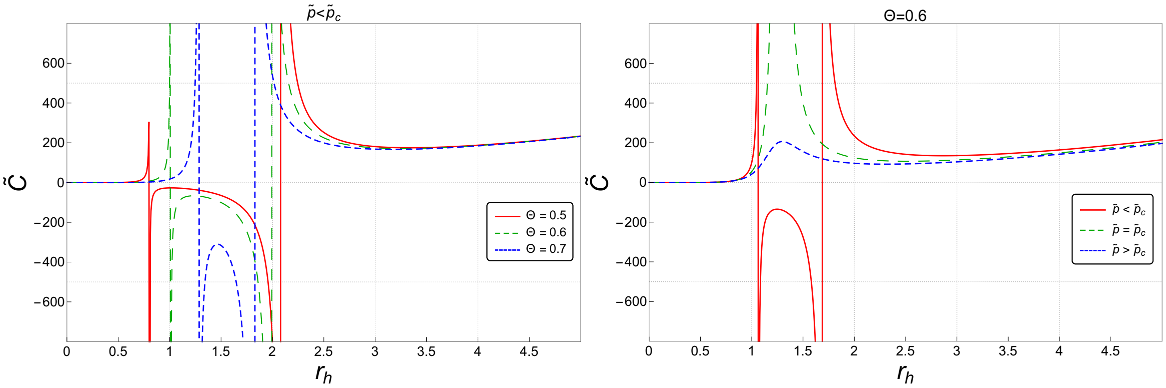

Figure 5.21: The heat capacity behavior of the NC Schwarzschild BH as a function of the event horizon r_h, for different Θ (left panel) and for different $\tilde{p}$ (right panel).

The behavior of the BH heat capacity for the NC Schwarzschild one as a function of the event horizon r_h, with different values of the NC parameter Θ (left panel) and for different values of the pressure $\tilde{p}$, is shown in Fig. 5.21. As we see in the left panel, for the case $\tilde{p} < \tilde{p}_c$, with the presence of non-commutativity, we observe three branches in the heat capacity behavior, in which two of them are stable and separated by a new unstable intermediate (IBH) region, where its caused by the external pressure due to the effect of the NC geometry, and that means the NC Schwarzschild BH has two phase transitions, and that is consistent with the profile $\tilde{t} - r_h$ (see right panel in Fig. 5.19), and this new region decreases with the increasing in the NC parameter Θ. It is worth noting that our result is similar to the ones obtained using some models of QG that study deformed BH inside an isothermal and spherical cavity [73, 102, 103, 121, 257]. However, in our case, we study the pressure as an external effect of the non-commutativity on the deformed BH, where in our previous SubSec. 5.1.4, the pressure is considered a BH pressure emerged from the non-commutativity, but in this scenario, the pressure is treated as an external potential of the non-commutativity, in the same way as the cosmological constant in the AdS RN BH [245]. For the other cases of $\tilde{p}$ shown in the right panel, where for the case $\tilde{p} = \tilde{p}_c$ (right panel panel), we observe that the unstable IBH disappear and the two stable regions (LBH and SBH) coexist at one inflexion point r_3, while for $\tilde{p} > \tilde{p}_c$ there are no more phase transitions at this point, with one single thermally stable region ($\tilde{C} > 0$).

It is clear that, for the cases of $\tilde{p} < \tilde{p}_c$, the NC Schwarzschild BH has only one physical limitation point [250] as we see in the previous scenario in SubSec. 5.1.2, in which $\tilde{C}$ is equal to zero at r_0 (this point is in depend with the value of Θ and $\tilde{p}$), where the other important points correspond to the divergence behavior of $\tilde{C}$ at $r_h = r_1$ and r_2 (which correspond to the maximum and the minimum temperature presented in the right panel of Fig. 5.19), and that implies two phase transition at these points.

Table 5.4: Region, heat capacity, state, and stability of the NC Schwarzschild BH for different branches.

Pressure	Branches	Region	Heat capacity	State	Stability
$\tilde{p} < \tilde{p}_c$	1	$r_h > r_2$	$\tilde{C} > 0$	LBH	stable
	2	$r_1 < r_h < r_2$	$\tilde{C} < 0$	IBH	unstable
	3	$r_0 < r_h < r_1$	$\tilde{C} > 0$	SBH	stable
$\tilde{p} = \tilde{p}_c$	1	$r_h > r_3$	$\tilde{C} > 0$	LBH	stable
	2	$r_h < r_3$	$\tilde{C} > 0$	SBH	stable
$\tilde{p} > \tilde{p}_c$	1	$r_h > r_0$	$\tilde{C} > 0$	-	stable

In Table. 5.4, we summarize the results of Fig. 5.21. As we see before, in this geometry for $\tilde{p} < \tilde{p}_c$, we get three branches in $\tilde{C}$, in which the LBH and SBH have a positive heat capacity for $r_h > r_2$ and $r_0 < r_h < r_1$, respectively, and that indicates this BH is in the equilibrium (stable) state, and these two regions are separated by a negative heat capacity region, which corresponds to IBH located in $r_1 < r_h < r_2$. Secondly, the phase transition of NC Schwarzschild BH in this geometry is described by the divergence of heat capacity at the critical points $r_h = r_2$ and r_1, which correspond to two phase transitions, and these two points getting closer to each other when we increase in Θ. Also, the stable stage located in $r_0 < r_h < r_1$ increases when Θ is increased, and that means the SBH takes longer to stop the evaporation process. However, for the case $\tilde{p} = \tilde{p}_c$, the heat capacity has only two branches, in which the stables LBH and SBH take longer to decay one to the other and inversely with one phase transition, and that is due to the equilibrium stability of these BHs, while for the last case $\tilde{p} > \tilde{p}_c$, there is no more phase transition and the heat capacity is always positive, which means that there is only one single thermally stable region.

5.2.3.1 *Free energy*

For in-depth details in the analysis of thermodynamic stability, we must investigate the Helmholtz free energy in this scenario. Firstly, we need to compute the new BH mass of this system; for that, we use the first law of thermodynamics [122, 260].

$$\begin{aligned} \tilde{m} &= \int \tilde{t} d\hat{S}, \\ &= \frac{r_h}{2} + \frac{4}{3}\pi r_h^3 \tilde{p} + \frac{3}{8r_h}\Theta^2. \end{aligned} \tag{5.45}$$

The Helmholtz free energy can be expressed as follows:

$$\tilde{F} = \tilde{m} - \tilde{t}\hat{S}, \tag{5.46}$$

where we use the above expression of the new mass (5.45), together with the entropy (5.11) and the new temperature given in Table. 5.2. The new Helmholtz free energy in this scenario can be expressed as follows:

$$\tilde{F} = \frac{r_h}{2} + \frac{4}{3}\pi r_h^3 \tilde{p} - \pi r_h^2 \tilde{t} + \Theta^2 \left(\frac{1}{8r_h} - \frac{5\pi}{8}\tilde{t} \right). \tag{5.47}$$

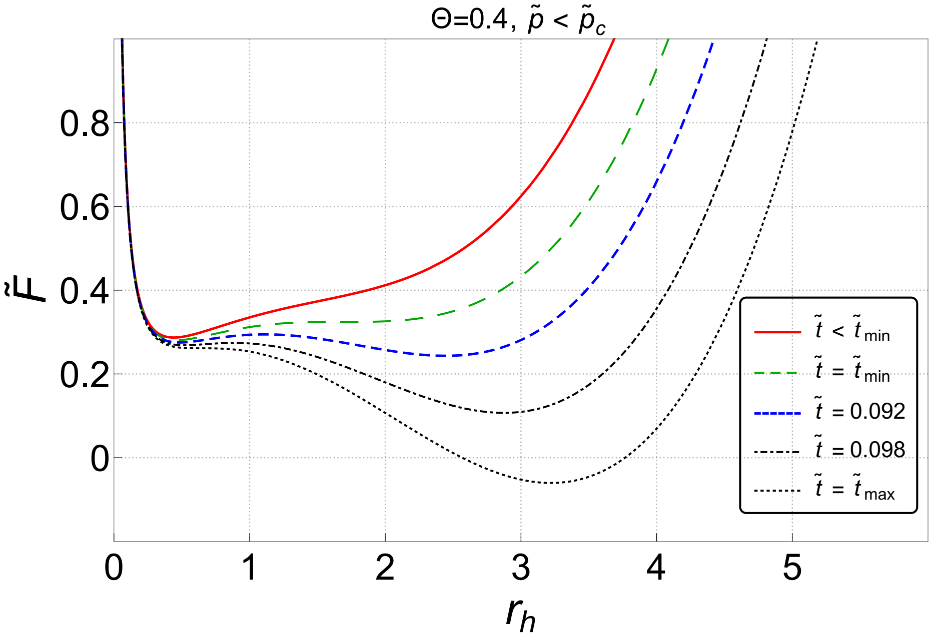

Figure 5.22: Behaviors of the new Helmholtz free energy $\tilde{F}$ as a function of r_h in NC spacetime, for different new deformed Hawking temperatures $\tilde{t}$.

The behavior of the new Helmholtz free energy as a function of the event horizon r_h and for different values of the new temperature $\tilde{t}$ is shown in Fig. 5.22. It is clear that, in the NC geometry, the new Helmholtz free energy has three extrema, where two minimum correspond to the stable BHs (LBH and SBH) and the maximum one corresponds to the unstable ones (IBH), and these three extrema are observed for $\tilde{t}_{min} \leq \tilde{t} \leqslant \tilde{t}_{max}$ and $\tilde{p} < \tilde{p}_c$, with $\Theta = 0.4$. The sizes of small, intermediate, and large BHs can be computed by solving Eq. (5.16) for r_h. Another important observation is that the behavior of the new Helmholtz free energy for NC Schwarzschild BH is similar to the one obtained for the AdS RN one in the commutative spacetime, see Ref. [245]. At this point, we confirm that the NC parameter Θ plays a similar role to the electric charge Q of RN BH. Furthermore, for a constant pressure ($\tilde{p} < \tilde{p}_c$) and varying in temperature values $0 < \tilde{t} \leqslant \tilde{t}^{max}$, the new Helmholtz free energy changes its behavior from its extremum to a minimum for $\tilde{t} \leq \tilde{t}_{min}$, where the depth of the minimum and the maximum of this free energy decreases with the increases in temperature $\tilde{t}$. As a consequence, the unstable IBH evaporates quickly to the stable ones (SBH or LBH), and that is consistent with the analysis of the profiles of $\tilde{t} - r_h$ (Fig. 5.19) and $\tilde{C} - r_h$ (Fig. 5.21).

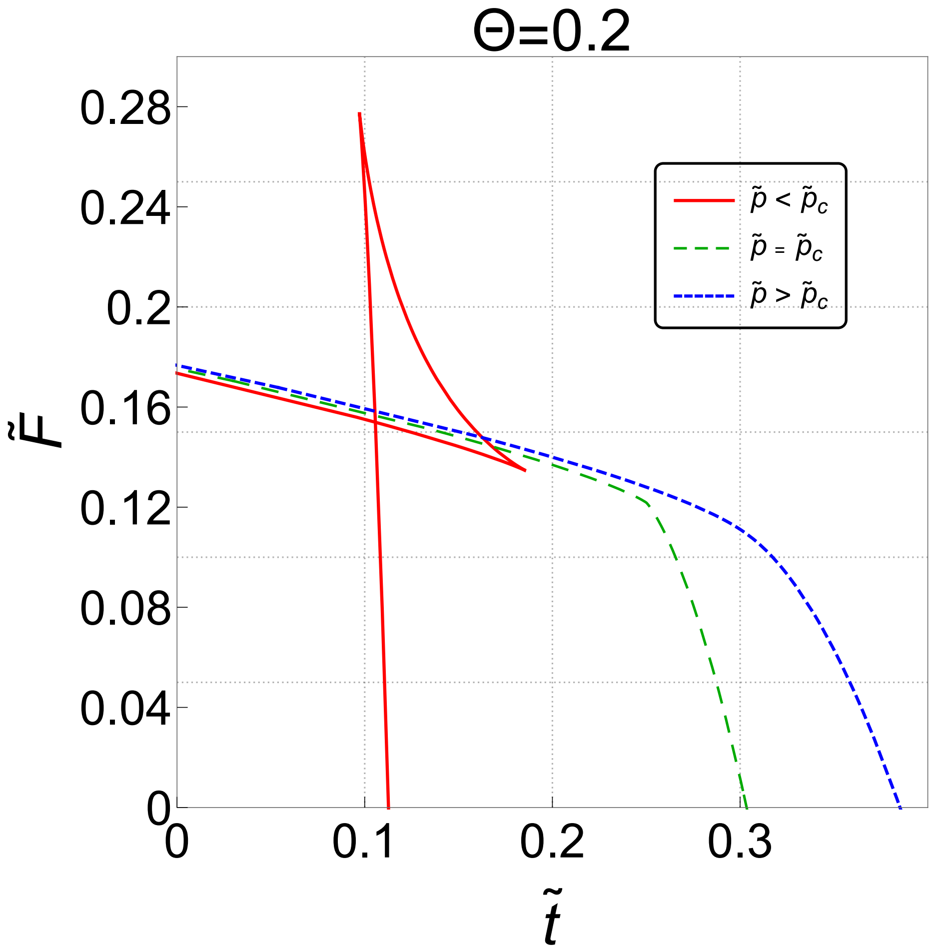

Figure 5.23: Behaviors of the new Helmholtz free energy $\tilde{F}$ as a function of the new Hawking temperature $\tilde{t}$ in NC spacetime, for different pressure $\tilde{p}$, where $\tilde{p}_c = \frac{1}{72\pi\Theta^2}$.

The behavior of the new Helmholtz free energy of the NC Schwarzschild BH as a function of the new Hawking temperature $\tilde{t}$ for different values of pressure $\tilde{p}$ is shown in Fig. 5.23. It is clear that, in this scenario, the phase structure of NC Schwarzschild BH shows an exact swallowtail structure for a pressure below the critical value $\tilde{p} < \tilde{p}_c$, which indicates a two-phase coexistence state and that describes a first-order phase transition (in this scenario, we solve the problem of the quasi-swallowtail structure that was obtained above in SubSec. 5.1.4), while for $\tilde{p} = \tilde{p}_c$, this structure disappears and an inflection point appears, where this point indicates a second-order phase transition. For $\tilde{p} > \tilde{p}_c$, this point disappears and indicates a non-phase transition, which is consistent with the profiles of $\tilde{t} - r_h$ (Fig. 5.19) and $\tilde{C} - r_h$ (Fig. 5.21).

5.2.3.2 *Phase diagram*

In order to obtain the coexistence curve, we plot the news expressions of NC pressure and the NC Hawking temperature in the $\tilde{p} - \tilde{t}$ plane. For that, we need to express the new temperature expression given in Table. 5.2 as a function of the new pressure $\tilde{p}$. In the case $\tilde{p} < \tilde{p}_c$, we can obtain the minimal and maximum temperature of BH. Using the condition given by the first derivative in Eq. (5.42), together with the equation in Table 5.2, we find

$$\tilde{t}_{min/max} = \frac{2\sqrt{\tilde{p}}}{\pi} \frac{\left(-24\tilde{p}\pi\Theta^2 + \sqrt{1-72\tilde{p}\pi\Theta^2}\right)}{\left(1 \pm \sqrt{1-72\tilde{p}\pi\Theta^2}\right)^{3/2}}. \tag{5.48}$$

The $\tilde{p} - \tilde{t}$ diagram can be obtained by drawing the above equation.

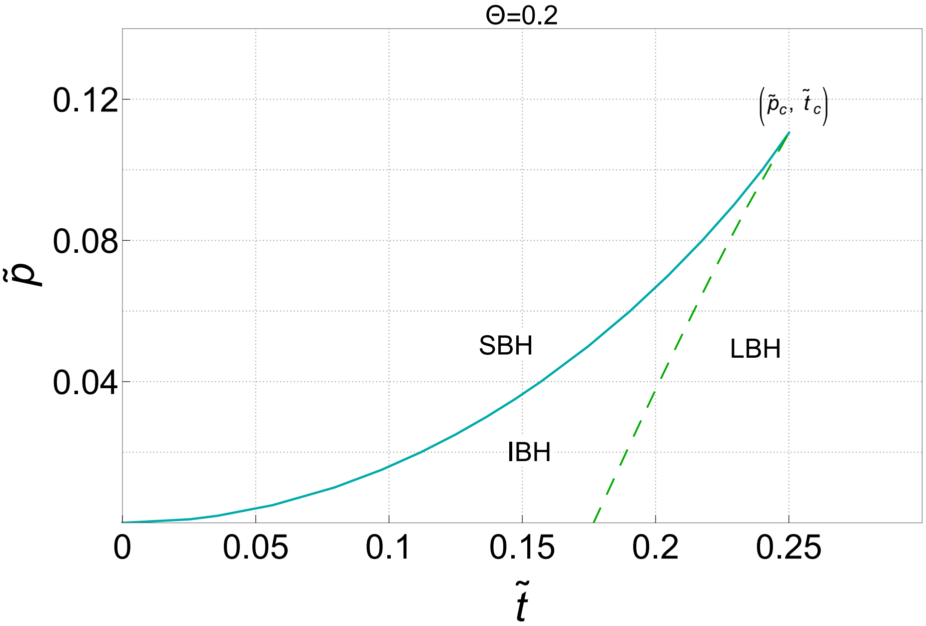

Figure 5.24: $\tilde{p} - \tilde{t}$ phase diagram of the NC Schwarzschild BH. The cyan solid line and green dashed line are the plots of $\tilde{t}_{min}$ and $\tilde{t}_{max}$, respectively, as a function of the pressure $\tilde{p}$.

The behavior of the new pressure $\tilde{p}$ as a function of the new temperature $\tilde{t}$ in the $\tilde{p} - \tilde{t}$ phase diagram is shown in Fig. 5.24. It is clear that the curves separate the $\tilde{p} - \tilde{t}$ plane into a three-phase region that is consistent with the profile $\tilde{C} - r_h$ (see Fig. 5.21), where the SBH is located above the solid curve as while the LBH one is below the dashed one, they are stable thermodynamically, and in the middle region between the solid and the dashed line, there are three solutions, which are SBH, LBH and IBH. It is worth noting that this behavior is similar to the one obtained in the commutative spacetime for the AdS RN BH, and that shows the similarity. At this point, the NC parameter Θ plays a similar role as the electric charge Q, and the non-commutativity effect can be seen in this scenario as the effect of the cosmological constant.

5.3 BLACK HOLE PHASE TRANSITION AND ISOTHERMAL CAVITY

In this section, we aim to investigate the thermodynamic properties of the NC Schwarzschild BH and their stability inside a spherical isothermal cavity, in which this cavity plays the role of the boundary condition [70–72], which fixes the temperature at its surface and that maintains the thermal stability of this BH. For that, we consider the NC Schwarzschild BH inside a spherical cavity with radius R.

As we see in the previous Sec. 5.1, the area law of BH is not respected. In order to fix this issue, we derive the NC entropy of this BH using the first law of BH thermodynamics.

$$\hat{S}_{BH} = \int \frac{d\hat{m}}{\hat{T}} = \pi r_h^2 + \frac{3\pi\Theta^2}{4} log(\pi r_h^2). \tag{5.49}$$

where we use the deformed mass (5.4) and the global temperature that is emitted by the surface horizon (5.7). It is clear that the above equation shows a logarithmic correction to the NC entropy in this geometry, and the area law recovers when we set $\Theta = 0$.

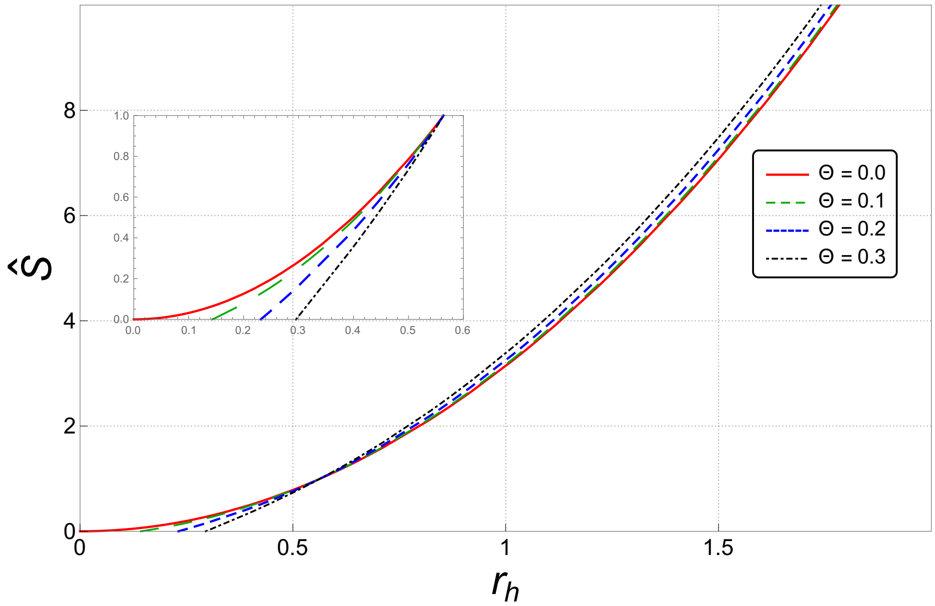

Figure 5.25: The behavior of BH entropy with logarithmic correction as a function of the event horizon r_h.

In Fig. 5.25, we show the behavior of the entropy with logarithmic correction as a function of the event horizon r_h for different values of the NC parameter Θ. It is clear that the comportment obtained from NC correction to the entropy is different from the comportment of the entropy resulting from the deformed area law in Sec. 5.1.1. Also, the non-commutativity increases the entropy of this BH for a larger one, while for a smaller one, the NC entropy is smaller than the commutative one and becomes zero for a specific radius of BH r_h, and that means, when the BH stop radiation, there is no entropy for the remnant BH.

5.3.1 *Local temperature and energy*

In which follow we use the global temperature that emitted from the surface horizon of the NC Schwarzschild BH, which is defined for open systems. However, in the case of a closed system, that means a BH inside the cavity, and the temperature emitted by this BH is limited by the surface of the cavity, so we need to define a new temperature for a closed system. For that, we use the boundary condition to obtain the NC local temperature of NC Schwarzschild BH at a finite distance R ($R > r_h^{NC}$), which is given by [70]:

$$\hat{T}_{local} = \frac{\hat{T}_H}{\sqrt{\hat{g}_{00}(R,\Theta)}}, \tag{5.50}$$

By using the deformed component (3.9a) at the leading order in m and in Θ, the local temperature is written as follows:

$$\begin{aligned} \hat{T}_{local} = \frac{1}{4r_h\pi\sqrt{1-\frac{r_h}{R}}} + \Bigg(& \frac{(-128r_h^2R^3 + 256r_hR^4) + r_h^4\left(77 - 15\sqrt{1-\frac{r_h}{R}}\right)R}{512r_h^3\pi R^3(R-r_h)^2\sqrt{1-\frac{r_h}{R}}} \\ & + \frac{16r_h^3\left(-2+\sqrt{1-\frac{r_h}{R}}\right)R^2 - 44r_h^5 - 128R^5}{512r_h^3\pi R^3(R-r_h)^2\sqrt{1-\frac{r_h}{R}}}\Bigg)\Theta^2. \end{aligned} \tag{5.51}$$

It is clear that, when $R \to \infty$, the local temperature (5.51) reduces to the NC Hawking temperature (5.7), and the commutative expression [71] recovers when we set $\Theta = 0$.

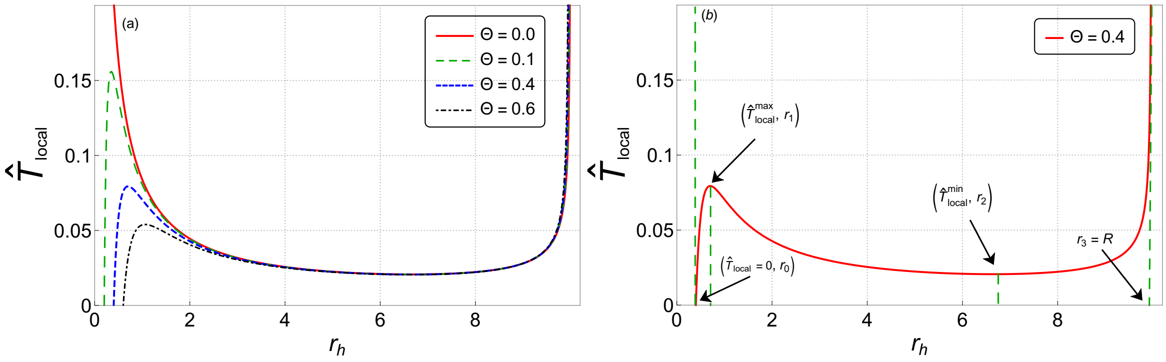

Figure 5.26: The behavior of local temperature as a function of r_h inside a cavity with radius $R = 10$.

The behavior of the NC local temperature as a function of the event horizon r_h with a fixed cavity radius $R = 10$ is shown in Fig. 5.26. It is clear that the NC local temperature has two extrema, one minimum[6] $(\hat{T}^{min}_{local}, r_2)$ and a maximum $(\hat{T}^{max}_{local} \approx \frac{0.03117}{\Theta}, r_1 \approx 1.73719\,\Theta)$ (see Fig. 5.26 (b)), where this geometry removes the divergence of the commutative case as

---

[6] The coordinates of the minimum local temperature $(\hat{T}^{min}_{local}, r_2)$ are obtained only with the numerical solution to this Eq. $\frac{\partial \hat{T}_{local}}{\partial r_h} = 0$.

in the case of open system that we studied before in previous Sec. 5.1, also in this scenario this BH stop radiation at the same point as before $r_0 = r_h^{min} = \Theta$, and for the case $R \to \infty$ the deformed Hawking temperature are analyzed in detail in SubSec. 5.1.1. As we see in Fig. 5.26 (b), at the surface of cavity $r_3 = R$ the local temperature divergent as in the commutative spacetime, and that du to the boundary condition of the isothermal cavity which prevent the radiation to emerge outside the cavity, and during the evaporation process, this temperature decreases until reach the minimum $\hat{T}_{local}^{min}$ at $r_h = r_2$, and this minimum decrease with the increasing in Θ, then this behavior starts to increase during the evaporation to reach the maximum $\hat{T}_{local}^{max}$ at r_1, then quickly fall to zero at r_0, which corresponds to a remnant BH. As we motioned above, the change in temperature from minimum to maximum indicates that the NC Schwarzschild BH inside a cavity also has two phase transitions, which hold at r_2 and r_1, in a similar way to the study of the non-commutativity effect as an external pressure that is applied by the spacetime on this deformed BH, and that shows the role of non-commutativity, which acts as a boundary condition.

Furthermore, we can obtain an estimation of the NC parameter Θ in this scenario, where we follow the same step in SubSec. 5.1.1 and find that $\Theta \approx 1.521 \times 10^{-35} m \sim l_{Planck}$, and this is consistent with the one obtained in Eq. (5.8).

Our next step is the local energy of the NC Schwarzschild BH, which can be obtained by using the first law of thermodynamics (5.1) and is written as follows [122]

$$\hat{E}_{local} = \int_{r_0}^{r_h} \hat{T}_{local} d\hat{S}_{BH}, \tag{5.52}$$

where $r_0 = m_0 = \Theta/2$ is the minimum mass of this BH (see SubSec. 5.1.1). By using the deformed local temperature (5.51) and the entropy (5.11), the above expression can be computed at the second order in Θ as fellow

$$\begin{aligned}\hat{E}_{local} = -R\sqrt{1-\frac{r_h}{R}} + \Theta^2 \Bigg(& \frac{66r_h^3 R + 96r_h(|r_h - R|)^{3/2}(R)^{3/2}\arctan(\sqrt{\frac{|r_h-R|}{R}})}{384R^{5/2}} \\ & + \frac{42r_h\sqrt{1-\frac{r_h}{R}}(r_h - R)R^2\log(1-\frac{r_h}{R}) + 45r_h^3\sqrt{1-\frac{r_h}{R}}R - 42r_h^2\sqrt{1-\frac{r_h}{R}}R^2}{768r_h\sqrt{1-\frac{r_h}{R}}R^3(R-r_h)} \\ & + \frac{88r_h^4 + 112r_h R^3 + 96R^4 - 360r_h^2R^2}{768r_h\sqrt{1-\frac{r_h}{R}}R^3(R-r_h)}\Bigg) - (r_h \to r_0).\end{aligned} \tag{5.53}$$

and the commutative expression [118] of the local energy can recover when we set $\Theta = 0$.

5.3.2 *Local heat capacity and phase transition*

In order to investigate in detail the phase transition and the thermal stability of the NC Schwarzschild BH inside a cavity, it is necessary to analyze the behavior of its heat capacity. In this scenario, we study the thermal stability of this BH inside a spherical cavity. In this context, we use the NC local quantities in the first law of thermodynamics, (5.1). The NC local heat capacity can be written as follows [70]

$$\hat{C}_{local} = \frac{\partial \hat{E}_{local}}{\partial \hat{T}_{local}} = \hat{T}_{local} \frac{\partial \hat{S}}{\partial \hat{T}_{local}}, \tag{5.54}$$

where we use the expressions of the deformed entropy (5.49) and the deformed local temperature (5.51),

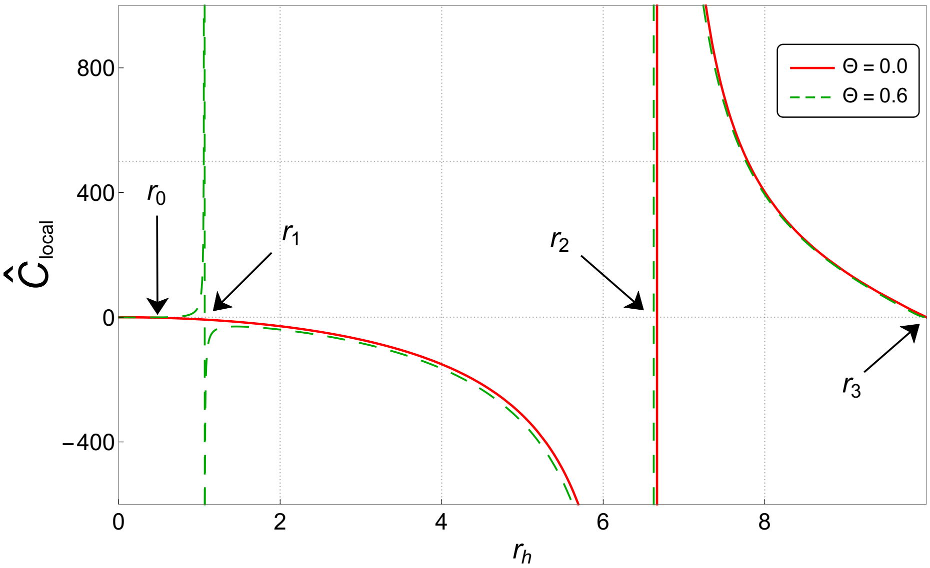

Figure 5.27: The behavior of local heat capacity as a function of r_h inside a cavity with radius $R = 10$.

The behavior of the local heat capacity as a function of the event horizon for the NC Schwarzschild BH inside an spherical isothermal cavity with constant radius R is shown in 5.27. As we see, for $\Theta = 0$, we recover the commutative local heat capacity of Schwarzschild BH inside a cavity, where this system has only two branches, and that means one phase transition. However, in the NC case $\Theta \neq 0$, the deformed local heat capacity has three branches, and that means the NC Schwarzschild BH inside a cavity has a two-phase transition as we motioned in SubSec. 5.4.1. Note that our result is consistent with some models of QG; for example, see Refs. [73, 102, 103, 121, 257].

It is clear that the NC Schwarzschild BH inside a cavity has two physical limitation points [250] at $r_h = r_0$ (related to the non-commutativity effect $r_0 = \Theta$) and $r_h = r_3$ (related to the boundary condition $r_3 = R$), in which the local heat capacity is equal to zero at these two points, which is not allowed in the previous situation. Another important observation is the divergence of the deformed local heat capacity, which holds at $r_h = r_1$ and r_2, where these two points correspond to the maximum and minimum temperature (see Fig. 5.26). This implies a two-phase transition for the NC Schwarzschild BH inside a cavity at these two points, and that is consistent with the profile $\hat{T}_{local} - r_h$ in Fig. 5.26.

In this geometry, $\hat{C}_{local}$ has three branches, which is not allowed in the commutative case, where the equilibrium (stable) system has a positive heat capacity, and that corresponds to the LBH and SBH, that are located in the regions for $r_2 < r_h < r_3$ and $r_0 < r_h <$

r_1, respectively, and these two regions are separated by a new unstable IBH region with negative heat capacity $r_1 < r_h < r_2$ (see Table. 5.5). It is worth noting that the two critical points $r_h = r_2$ and r_1, which correspond to the divergence of deformed local heat capacity getting closer to each other when we increase in Θ in a similar way to the profile $\tilde{C} = r_h$ in Fig. 5.21, also the stable stage $r_0 < r_h < r_1$ with positive $\hat{C}_{local}$ increases with increases in Θ, which means that the SBH takes longer to stop radiating and evaporating with a significant value of Θ.

Table 5.5: Region, heat capacity, state, and stability of the Schwarzschild BH surrounded by a cavity in NC/Commutative geometry for different branches.

Geometry	Branches	Region	Heat capacity	State	Stability
$\Theta = 0$	1	$r_h > r_1'$	$C > 0$	LBH	stable
	2	$r_h < r_1'$	$C < 0$	SBH	unstable
$\Theta \neq 0$	1	$r_2 < r_h < r_3$	$\hat{C} > 0$	LBH	stable
	2	$r_1 < r_h < r_2$	$\hat{C} < 0$	IBH	unstable
	3	$r_0 < r_h < r_1$	$\hat{C} > 0$	SBH	stable

The stability and the states of each region for the NC Schwarzschild BH inside a cavity are shown in Table. 5.5. It is clear that, in the commutative case $\Theta = 0$, the $\hat{C}_{local}$ has only two branches and one physical limitation point r_3 (corresponding to the boundary condition). Moreover, these two branches have different states and stability, and that means one phase transition point r_2 separates these two states, where the LBH is thermodynamically stable, which means this BH takes longer to evaporate, while the SBH is unstable and evaporates quickly. However, in this geometry $\Theta \neq 0$, the two stable states are now separated by a new unstable one that corresponds to IBH, and that means the two stable states SBH and LBH take longer to evaporate compared to the IBH, which decay quickly to LBH or SBH.

In order to investigate a detailed analysis of the stability and phase transition of the NC Schwarzschild BH inside a cavity, it is necessary to study the deformed Helmholtz free energy of this system. In this case, the on-shell free energy is given by the local temperature and local energy [122].

$$\hat{F}_{on} = \hat{E}_{local} - \hat{T}_{local}\hat{S}. \tag{5.55}$$

By using the Eqs. (5.49), together with (5.53) and (5.51), we can illustrate the free energy behavior of the NC Schwarzschild BH inside a cavity with a fixed radius R.

The behavior of the local Helmholtz free energy $\hat{F}_{on}$ as a function of the local temperature $\hat{T}_{local}$ for the NC Schwarzschild BH inside a cavity for different values of Θ is shown in Fig. 5.28. It is clear that, in this geometry, the phase structure shows an exact swallowtail structure for $\Theta < \Theta_c$, without including the pressure as in SubSec. 5.2.3, and that indicates a two-phase coexistence state, while for $\Theta \geq \Theta_c$, this structure despairs; see Fig. 5.28 (a). It is worth noting that, due to the perturbative nature of this theory, the NC parameter in natural systems is considered a small parameter $\Theta < 1$, and that suggests one and only

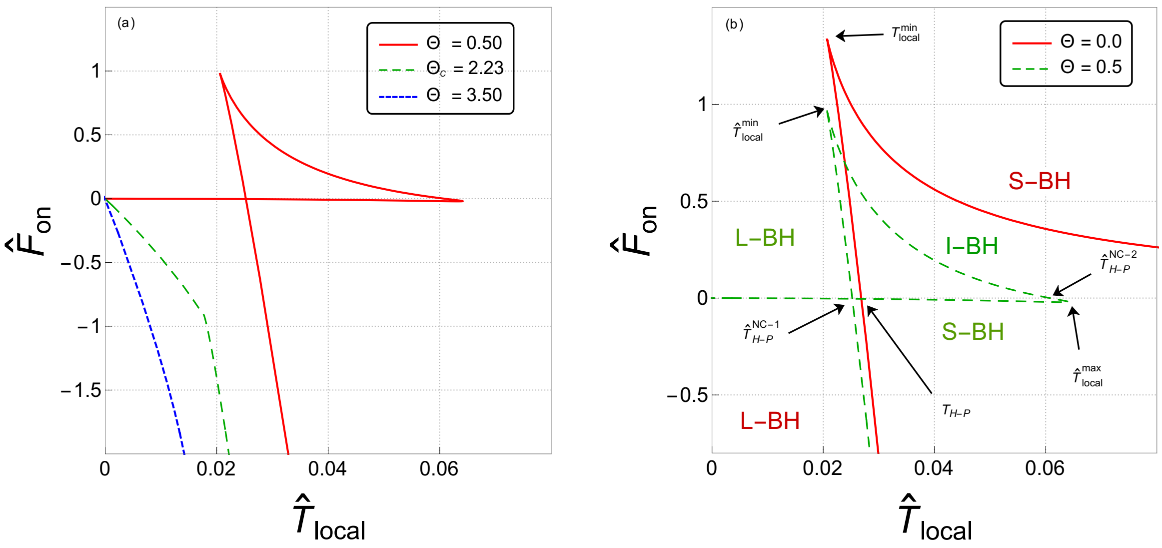

Figure 5.28: The behavior of Helmholtz free energy as a function of $\hat{T}_{local}$ inside a cavity with radius $R = 10$.

possibility, which is $\Theta < \Theta_c$, and that means in the NC spacetime this BH has only a two-phase coexistence state as a phase transition, and that is consistent with the profiles of $\hat{T}_{local} - r_h$ (Fig. 5.26) and $\hat{C}_{local} - r_h$ (Fig. 5.27). Furthermore, in commutative spacetime, the phase structure of Schwarzschild BH inside a cavity shows a Hawking-Page phase transition (see Fig. 5.28 (b) for $\Theta = 0$), which occurs at T_{H-P}. For more detail on the Hawking-Page phase transition, see Refs. [citation]. The stability of the BH can be checked by its free energy, in which this BH is stable if it has less free energy and unstable if it has high free energy. However, in the NC case $\Theta \neq 0$, this BH has a swallow-tail phase structure, with two inflection points located at $\hat{T}^{max}_{local}$ and $\hat{T}^{min}_{local}$ (see Fig. 5.28 (b)), and two Hawking-Page phase transition points located at the root of the free energy $\hat{F}_{on} = 0$, at $(\hat{T}^{NC-1}_{H-P}, \hat{T}^{NC-2}_{H-P})$, and that correspond to a two-phase coexistence state. As we observe in Fig. 5.28 (b), the location of the SBH and the LBH are respectively $(0, \hat{T}^{min}_{local})$ and $(\hat{T}_{local} > \hat{T}^{max}_{local})$, while the three states of this BH are located in $(\hat{T}^{min}_{local}, \hat{T}^{max}_{local})$, which is similar to the one obtained using GUP [257]. From the Fig. 5.28 (b), we find only one Hawking-Page critical point in commutative spacetime ($\Theta = 0$) at T_{H-P}, while for the NC geometry we find two Hawking-Page critical points at $\hat{T}^{NC-1}_{H-P}$ and $\hat{T}^{NC-2}_{H-P}$, and this result is consistent with the one obtained by RG in extended phase space [121], whereas one and three Hawking-Page critical points were observed in other models of QG such as the Refs. [75, 102, 103]. In the case of temperature located at $0 < \hat{T}^{NC-1}_{H-P}$, the free energy $\hat{F}_{on}$ of the LBH and the IBH are grater than the SBH ($\hat{F}^{I}_{on} > \hat{F}^{L}_{on} > \hat{F}^{S}_{on}$) and that mean the stable LBH and unstable IBH decay into a stable SBH, while for the case of temperature located between the two Hawking-Page critical points ($\hat{T}^{NC-1}_{H-P} < \hat{T}_{local} < \hat{T}^{NC-2}_{H-P}$), the stable SBH and the unstable IBH decay into a stable LBH, because its free energy is lower than the one of SBH and IBH ($\hat{F}^{I}_{on} > \hat{F}^{S}_{on} > \hat{F}^{L}_{on}$), and its the same case for the temperature located at $\hat{T}^{NC-2}_{H-P} < \hat{T}_{local} < \hat{T}^{max}_{local}$. As we observe from Fig. 5.27 and 5.28, the unstable IBH decay quickly to the stable ones (SBH or LBH), and that means this state of BH cannot survive for a long time in this geometry. It is worth noting that the NC gauge theory of gravity shows a good agreement with some models of QG as [73, 75, 102, 103, 118, 121, 257], and that indicates the impact of this geometry to describe the quantum effect of gravity, with a good prediction of a minimal length at Planck scale Θ.

5.4 QUANTUM TUNNELING IN NC SPACETIME

In order to investigate the tunneling process, the authors in Refs. [76, 82, 83] suggest that it is important to use stationary coordinates. These stationary coordinates exhibit no singularity at the event horizon, which is unlike the Schwarzschild coordinates, where that ensures the conservation of energy in the radiation spectrum derivative. To facilitate this, we rewrite the NC Schwarzschild BH[7] in the Painlevé-Gullstrand form [76, 82, 83, 98]. The NC line element (3.8) for a radial motion becomes

$$d\hat{s}^2 = -\hat{g}_{00}(r,\Theta)dt^2 + 2\hat{h}(r,\Theta)dtdr + dr^2 + \hat{g}_{22}(r,\Theta)d\theta^2 + \hat{g}_{33}(r,\Theta)d\phi^2, \tag{5.56}$$

where

$$\hat{h}(r,\Theta) = \sqrt{\hat{g}_{00}(r,\Theta)(\hat{g}_{11}(r,\Theta)^{-1} - 1)} \tag{5.57}$$

In the semi-classical tunneling of particles, the tunneling rat $\hat{\Gamma}$ is related to the imaginary part of the action [76, 82, 83], and is given by

$$\Gamma \sim e^{-Im\hat{S}}, \tag{5.58}$$

where $\hat{S}$ is the tunneling action of particles in the NC curved spacetime and is given by

$$\hat{S} = \int p_\mu dx^\mu, \tag{5.59}$$

where $p_\mu = \hat{g}_{\mu\nu}\frac{dx^\nu}{d\tau}$ is the conjugate momentum and τ is the affine parameter. Our interest is the tunneling of massless particles with radial motion (the angular momentum in this case is zero) and in the equatorial plan $\theta = \pi/2$. The imaginary part of this action $\hat{S}$ is reduced to

$$\begin{aligned} Im\hat{S} &= Im\int (p_t dt + p_r dr) = Im\int_{r_i}^{r_f} p_r dr, \\ &= Im\int_{r_i}^{r_f}\int_0^{p_r} dp_r' dr. \end{aligned} \tag{5.60}$$

As we see, the first term of integration does not contribute to the calculation of the imaginary part of the action because it is real. Let's turn now to the Hamiltonian equation, where the system's Hamiltonian is represented as $H = m - \omega'$. This allows us to write

$$\dot{r} = \frac{dH}{dp_r} = \frac{d(m-\omega')}{dp_r}, \tag{5.61}$$

---

[7] In this section we use the deformed metric given in Sec. 3.2, with $a = \Theta$ and $b = 0$, to insure the diagonal form.

where $\dot{r} = \frac{dr}{dt}$. Incorporating all these considerations into Eq. (5.60) and that allows us to remove the momentum from this expression, then we find

$$Im\hat{S} = Im \int_{m}^{m-\omega} \int_{r_i}^{r_f} \frac{d(m-\omega)}{\dot{r}} dr. \tag{5.62}$$

Let's assume that the particle tunneling across the event horizon follows a radial motion within the equatorial plane. Therefore, the radial null geodesic can be obtained by using the following expression $\hat{g}_{\mu\nu} U^\mu U^\nu = 0$

$$\frac{dr}{dt} = -\hat{g}_{01} + \sqrt{\hat{g}_{01}^2 + \hat{g}_{00}}. \tag{5.63}$$

By sitting the above equation into Eq. (5.62), we obtain

$$Im\hat{S} = Im \int_{m}^{m-\omega} \int_{r_i}^{r_f} \frac{d(m-\omega)}{-\hat{g}_{01} + \sqrt{\hat{g}_{01}^2 + \hat{g}_{00}}} dr. \tag{5.64}$$

where $\hat{g}_{01} = \hat{h}$ and $dH = d(m-\omega) = -d\omega$. After rearranging our expression, we obtain

$$Im\hat{S} = Im \int_{0}^{\omega} (-d\omega) \int_{r_i}^{r_f} \frac{dr}{\sqrt{\hat{g}_{00}\hat{g}_{11}} \left[1 - \sqrt{1 - \frac{1}{\hat{g}_{11}}}\right]}. \tag{5.65}$$

The above expression exhibits one singular pole at the NC event horizon $r = r_h^{NC}$. To compute this integral, we use the contour deformation technique around the pole by using the residue theorem. To ensure the conservation of the Boltzmann factor[8] $\Gamma \sim e^{-2ImS} \sim e^{-\beta\omega}$, we follow the same steps to evaluate the above integral over ω as in Refs. [96, 97]

$$Im\hat{S} = \pi \int_{0}^{\omega} \left(4m + \frac{3\Theta^2}{2m}\right) d\omega = \pi\omega \left(4m + \frac{3\Theta^2}{2m}\right). \tag{5.66}$$

The NC tunneling rate from the NC Schwarzschild BH is given by

$$\hat{\Gamma} \sim exp\left[-2\pi\omega \left(4m + \frac{3\Theta^2}{2m}\right)\right]. \tag{5.67}$$

It is clear that, when we set $\Theta = 0$, we recover the commutative expression [76, 83].

The impact of the non-commutativity on the tunneling rate of particles from the NC Schwarzschild BH is shown in Fig. 5.29. As we see, the non-commutativity has a minor influence on the tunneling rate $\hat{\Gamma}$ for emitting particles with frequency ω in the range $\omega \in [0.04, 0.15]$. In this range, the tunneling rate $\hat{\Gamma}$ decreases with the increase in the NC parameter Θ. For other values of ω or for smaller Θ, the non-commutativity effect on $\hat{\Gamma}$ became negligible.

In Fig. 5.30, we plot the behavior of the tunneling rate $\hat{\Gamma}$ of particles from NC Schwarzschild BH as a function of BH mass m for different values of the NC parameter Θ (right panel) and for different values of energy ω (left panel). As we see in the left panel, for a

---

[8] In the approximation of lower frequency $\omega \ll m$.

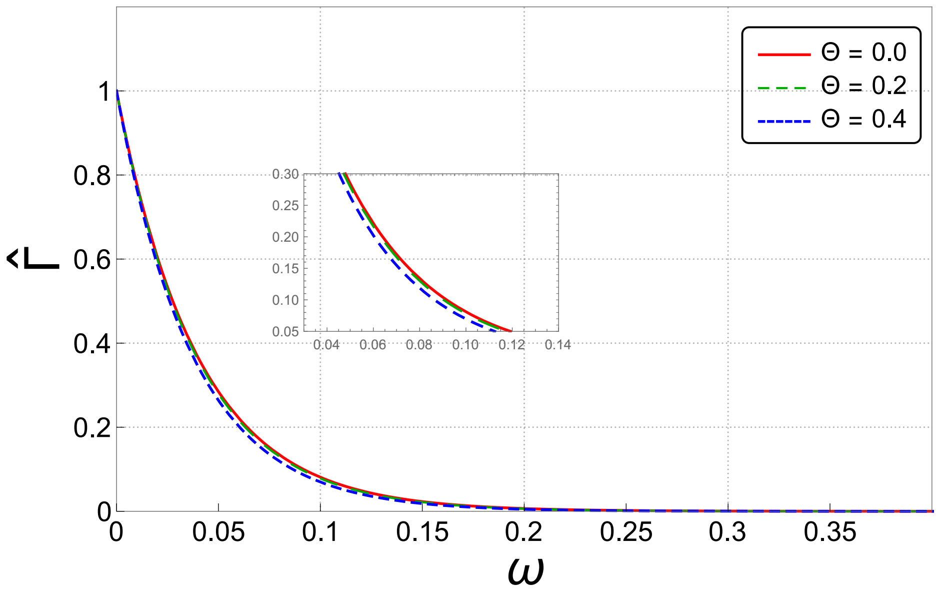

Figure 5.29: The behavior of tunneling rate BH as a function of the emitting particle energy ω, with $m = 1$.

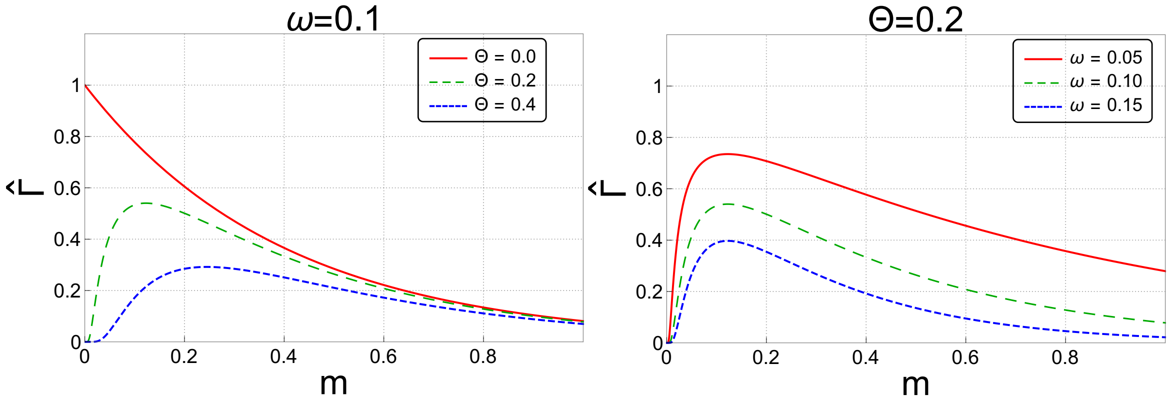

Figure 5.30: The behavior of tunneling rate as a function of BH mass m, for different values of energy ω (right panel), and for different values of the NC parameter Θ (left panel).

massive BH the tunneling rate of particles is small in both cases for commutative and NC one, and that due to the strength of gravity, this rate starts to increase during the evaporation process, which means the gravity of SBH is not as strong as before (as in the massive case). It is clear that, in the NC geometry, we observe new behavior, in which the tunneling rate of particles for the case of zero mass $m = 0$ is also zero $\hat{\Gamma} = 0$, and this behavior is not allowed in the commutative case $\Theta = 0$, and that means there are no tunneling particles with constant energy ω from an BH with zero mass, and that is more logical, and that is due to the presence of non-commutativity. Furthermore, in this geometry, the tunneling rate of particles increases during the evaporation process until it reaches a new maximum $\hat{\Gamma}^{\max}$ at the critical mass m^{crit}, then starts to decrease until it reaches zero at $m = 0$, and this maximum tunneling rate decreases with the increase of Θ, which indicates that the non-commutativity enhances the gravitational field. Also in the right panel, we see the same observation: when we increase the values of the energy frequencies ω of the particle tunneling in the NC spacetime, the tunneling rate of these particles decreases, and that means the energy of the particle is bigger, which implies a smaller tunneling rate. For more detail on the influence of these parameters m, ω, and Θ on the tunneling rate Γ, see Fig. 5.31.

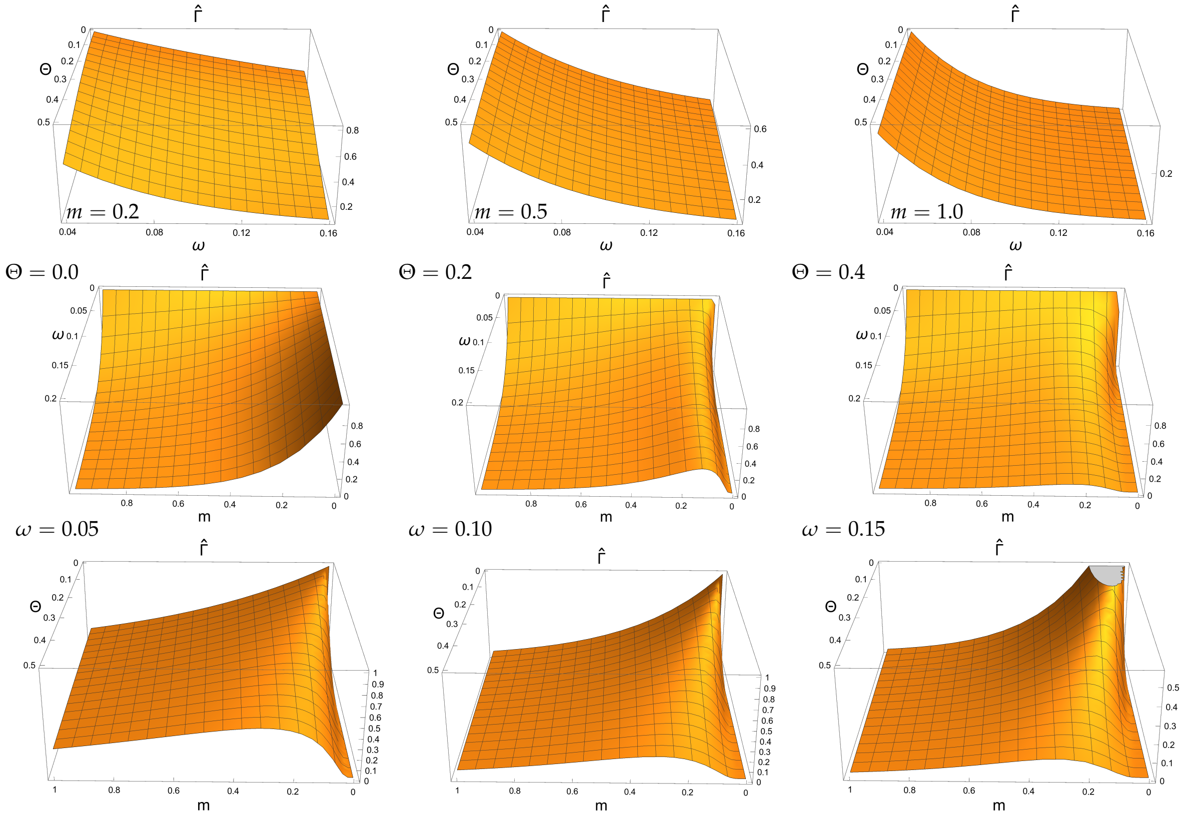

Figure 5.31: Behaviors of the tunneling rate distribution as a function of the parameters m, ω, and Θ. (raw1) as a function of ω and Θ at different masses $m = 0.2, 0.5, 1.0$. (raw2) as a function of m and ω at different NC parameters $\Theta = 0.0, 0.2, 0.04$. (raw3) as a function of m and Θ at different frequencies $\omega = 0.05, 0.10, 0.15$.

5.4.1 *NC correction to the Hawking temperature*

It is worth noting that, according to Planck's law, particles with frequency ω should be emitted at a rate described by $\Gamma \sim exp\left[-\omega/T\right]$. Consequently, the deformed temperature of this BH, as indicated by Eq. (5.67), and at leading order in Θ, can be written as follows:

$$\hat{T}_H = \frac{1}{2\pi\left(4m+\frac{3\Theta^2}{2m}\right)} \approx T_H\left(1-\frac{3\Theta^2}{2r_h^2}\right). \tag{5.68}$$

Note that, when $\Theta = 0$, the commutative Hawking temperature recovers (1.46). It is important to highlight that the above expression is obviously the same expression obtained using the surface gravity in Eq. (5.6) with a particular case $a = \Theta$ and $b = 0$, and that means the equivalence between the quantum tunneling process and the thermodynamic approach is preserved during the BH evaporation, despite the non-commutativity of spacetime.

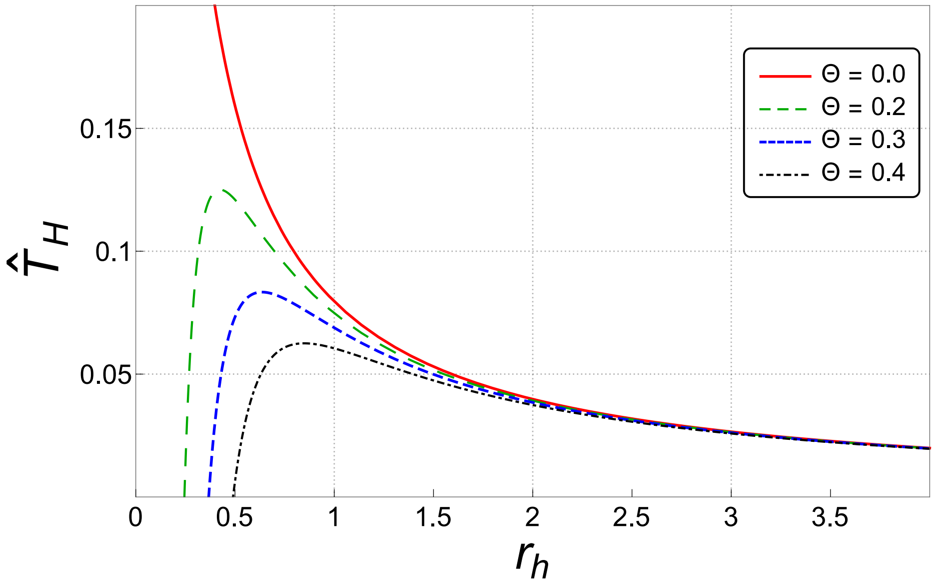

Figure 5.32: The behavior of NC Hawking temperature as a function of r_h (in the case $a = \Theta$ and $b = 0$).

The behavior of the NC Hawking temperature[9] as a function of the event horizon r_h is shown in Fig. 5.32. It is clear that we have the same behavior as in Figs. 5.2, 5.3 and 5.5, concerning the removal of the Hawking temperature divergence, leading the BH to attain a new maximum $\hat{T}_H^{\max} \approx \frac{0.025}{\Theta}$, at the critical size $r_h^{\text{crit}} \approx 2.121\,\Theta$ before turning to a zero at $r_h = 1.225\,\Theta$, at this point the BH stop radiation.

By following the same steps in SubSec. 5.1.1, we can obtain an estimation of the NC parameter Θ by using the back-reaction coordinates $(\hat{T}_H^{\max} \approx \frac{0.025}{\Theta}, r_h^{\text{crit}} \approx 2.121\,\Theta)$. In this case, the NC parameter can be estimated as follows:

$$\Theta \approx 1.854 \times 10^{-35} m \sim l_{\text{Planck}}. \tag{5.69}$$

Our results show again that the NC property of spacetime is situated at the Planck scale. This suggests that estimating the NC parameter Θ through thermal phenomena (by using the temperature behavior) provides a more accurate determination, and that is due to the direct relation of this phenomenon to the event horizon of the BH, where this last is affected by the non-commutativity. This direct relation provides a better estimation of Θ, and that means in the presence of a strong gravitational field or that the closer we are to the event horizon, the more QG effects emerge at a large scale.

5.4.2 *Logarithmic corrections to the entropy in NC spacetime*

In this subsection, we will extract the NC correction entropy arising from the tunneling process, in the case of large frequency ω, while ensuring the conservation of energy. To facilitate this, we use the definition (5.64) and integrate the relation (5.66) over the NC

---

[9] For the case $a = \Theta$ and $b = 0$.

quantity $d(\hat{m}-\omega)$, and the element of integration in the NC case can be written as follows:

$$dH = d(m-\omega) \to d\hat{H} = \left(1 - \frac{3\Theta^2}{32(m-\omega)^2}\right) d(m-\omega) \tag{5.70}$$

Inserting this relation into Eq. (5.66) and integrating this relation from the initial stat m to the final one $m-\omega$, we preserve the conservation of energy. According to Refs. [76, 83], the BH mass in (5.66) became $m-\omega$, and in our case, we use the above deformed element of integravtion, (5.70), then we obtain

$$\begin{aligned} Im\hat{S} &= -\pi \int_m^{m-\omega} \left(4(m-\omega) + \frac{3\Theta^2}{2(m-\omega)}\right) d(m-\omega) + \pi \int_m^{m-\omega} \left(\frac{3\Theta^2}{8(m-\omega)}\right) d(m-\omega), \\ &= -\pi \left(2(m-\omega)^2 + \frac{9\Theta^2}{4} log\left(m-\omega\right) - 4(m)^2 - \frac{9\Theta^2}{4} log\left(m\right)\right). \end{aligned} \tag{5.71}$$

This leads us to the usual relationship between the difference in entropy and the tunneling rate [76, 82, 83].

$$\hat{\Gamma} \sim e^{-2Im\hat{S}} = e^{\Delta \hat{S}_{BH}}. \tag{5.72}$$

where $\Delta\hat{S}_{BH} = \hat{S}_{BH}(m-\omega) - \hat{S}_{BH}(m)$ is the difference of Bekenstein-Hawking entropy for the NC Schwarzschild BH.

$$\hat{S}_{BH} = 4\pi m^2 + \frac{9\pi\Theta^2}{8} log(4\pi m^2). \tag{5.73}$$

In the NC gauge theory and also the quantum tunneling process, the relationship between the BH area and entropy is not conserved, and the NC term introduces a logarithmic correction to this entropy that is consistent with the above one obtained using the NC first law of BH thermodynamic (5.49), with a difference in the factor 3 and that due to the choice of the NC matrix.

It is worth noting that this result can be written as a similar outcome in ST and LQG (at the leading order in α) [92]:

$$\hat{S}_{BH} = \frac{A}{4} + \alpha \, log(\frac{A}{4}). \tag{5.74}$$

where A is the commutative Schwarzschild BH area (1.47), and α is a constant, depending on specific theory. In LQG, α takes a negative value, $\alpha = -\frac{1}{2}$ [263, 264], while in ST, this constant α is a 4-D central charge, which depends on the number of fields and can assume both negative and positive values [265]. Furthermore, this logarithmic correction is also observed in other theories, as examples in GUP and MDR [120, 208]. In Ref. [208], a significant result was established where the author found a connection between the prefactor of the logarithmic correction and the spacetime dimension.

It is worth noting that, when we use the NC gauge theory of gravity, this constant α consistently takes a positive value and is related to the NC parameter by $\alpha = \frac{9\pi\Theta^2}{8}$. Now, if we use our previous result for the NC parameter values (5.69), we can relate α to the

Planck length as $\alpha \sim \frac{9\pi}{4} l_{\text{Planck}}^2$. This indicates that in this theory of non-commutativity, the coefficient α of the logarithmic correction to the entropy represents a quantum area located at the Planck level, suggesting that spacetime is quantized at the Planck scale due to the NC property of spacetime.

In order to express the NC tunneling rate (5.72) as the one presented in Ref. [92], we need to write the Eq. (5.71), as follows:

$$\begin{aligned}\Delta\hat{S} &= \pi\left(4(m-\omega)^2 + \frac{9\Theta^2}{8}\ln\left(4\pi(m-\omega)^2\right) - 4(m)^2 - \frac{9\Theta^2}{8}\ln\left(4\pi m^2\right)\right), \\ &= -8\pi m\omega\left(1-\frac{\omega}{2m}\right) + \frac{9\pi\Theta^2}{8}\ln\left(1-\frac{\omega}{m}\right)^2. \end{aligned} \tag{5.75}$$

Inserting this equation inside Eq. (5.72), we get

$$\begin{aligned}\hat{\Gamma} = e^{\Delta\hat{S}_{BH}} &= e^{-\pi\left(-8m\omega\left(1-\frac{\omega}{2m}\right)+\frac{9\Theta^2}{4}\ln\left(1-\frac{\omega}{m}\right)^2\right)} \\ &= \left(1-\frac{\omega}{m}\right)^{\frac{9\pi}{4}\Theta^2} e^{-8\pi m\omega\left(1-\frac{\omega}{2m}\right)}. \end{aligned} \tag{5.76}$$

We use our results in Eq. (5.69), $\Theta \simeq l_{Planck}$. The above equation can be expressed in the following form:

$$\hat{\Gamma} = e^{\Delta\hat{S}_{BH}} = \left(1-\frac{\omega}{m}\right)^{\frac{9\pi}{4} l_{\text{Planck}}^2} e^{-8\pi m\omega\left(1-\frac{\omega}{2m}\right)}. \tag{5.77}$$

It is clear that, in our above expression, we have an exponential term with a correction factor. The exponential term corresponds to the commutative case with non-thermal radiation [92], while the correction factor in this theory depends on the Planck length. This correction factor introduces a quantum correction emergent from the non-commutativity of spacetime. In the semiclassical limit, when we set $l_{\text{Planck}} = 0$, our expression reduces to the commutative one [92].

5.4.3 *Correlations*

Now, let us examine the correlation between two successively emitted particles with different modes ω within the framework of NC gauge theory. In particular, we will focus on the context of non-thermal radiation, starting with the first massless quantum emission with frequency ω_1. In this case, the emission rate (5.77) is written in the following form:

$$\ln\hat{\Gamma}_{\omega_1} = \frac{9\pi}{4}\Theta^2\ln\left(1-\frac{\omega_1}{m}\right) - 8\pi m\omega_1\left(1-\frac{\omega_1}{2m}\right). \tag{5.78}$$

According to Refs. [266–268], the second quantum emission, characterized by energy ω_2, is independent of the first one, ω_1. This independence is valid even in the presence of QG corrections [269], and its emission rate is given by

$$\ln\hat{\Gamma}_{\omega_2} = \frac{9\pi}{4}\Theta^2\ln\left(1-\frac{\omega_2}{m}\right) - 8\pi m\omega_2\left(1-\frac{\omega_2}{2m}\right). \tag{5.79}$$

The emission rate Γ for two quantum emissions occurring simultaneously, with energies ω_1 and ω_2, is given by

$$\ln \hat{\Gamma}_{\omega_1+\omega_2} = \frac{9\pi}{4}\Theta^2 \ln\left(1-\frac{(\omega_1+\omega_2)}{m}\right) - 8\pi m(\omega_1+\omega_2)\left(1-\frac{(\omega_1+\omega_2)}{2m}\right). \tag{5.80}$$

From the above expressions, we can calculate the statistical correlation between these events [95, 266, 269] as follows:

$$\begin{aligned}\hat{\chi}(\omega_1+\omega_2;\omega_1,\omega_2) &= \ln\left(\frac{\hat{\Gamma}_{\omega_1+\omega_2}}{\hat{\Gamma}_{\omega_1}\hat{\Gamma}_{\omega_2}}\right)\\ &= 8\pi\omega_1\omega_2 + \frac{9\pi}{4}\Theta^2 \ln\left(\frac{m(m-(\omega_1+\omega_2))}{(m-\omega_1)(m-\omega_2)}\right)\end{aligned} \tag{5.81}$$

Remarkably, the correlation function $\hat{\chi}$ remains non-zero in the context of NC gauge theory, as well as in the commutative case[10] [95, 266–268]. This implies that, in the NC geometry, the different radiation modes ω during BH evaporation exhibit correlations with each other ($\hat{\chi} \neq 0$). Moreover, the presence of NC correction in this expression reduces the statistical correlations between Hawking radiations[11]. Furthermore, the non-zero correlation between successively emitted massless quantum particles suggests that information can emerge within the Hawking radiation, thus addressing the information loss paradox. In this NC framework, information is preserved within this remnant BH, and the geometry reduces these correlations, enabling information to surface from the event horizon, akin to "hidden messengers in Hawking radiation" [266].

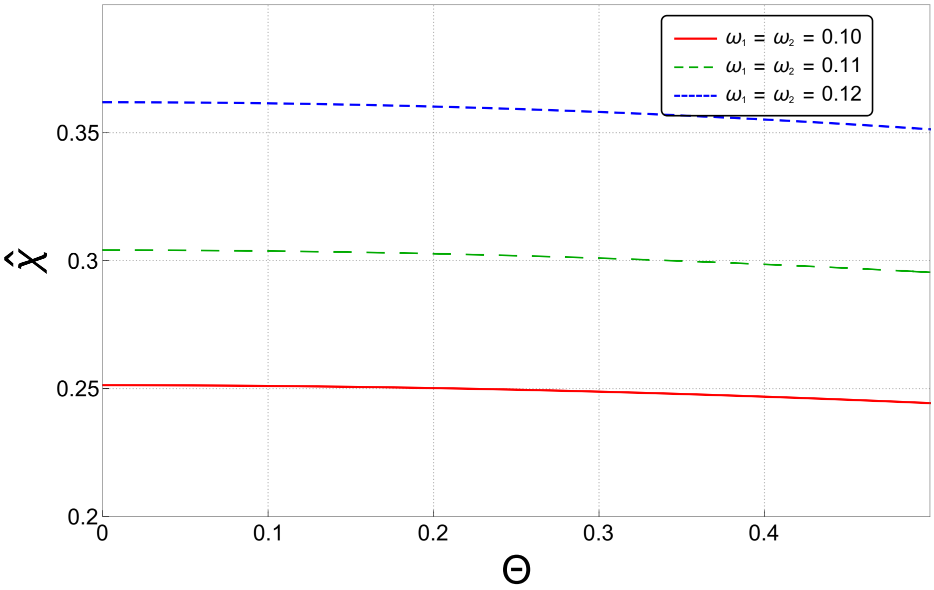

Figure 5.33: The behavior of the correlation function as a function of the NC parameter Θ for different ω.

---

[10] Note that, when we set $\Theta = 0$, we recover the commutative expression [95, 266–268].

[11] In this thesis we correct our issue in our published paper [173], where we look only to the sign of the NC correction term in Eq. (5.81), without taking into account the sign resulting from the logarithm term, which is always negative in this case.

In Fig. 5.33, we present the behavior of the statistical correlation function as a function of the NC parameter Θ for different ω. As we see in the left panel, the non-commutativity reduces the correlation function for the different values of energy, and the increases in energy lead to an increase in the correlation between Hawking radiations.

5.4.4 *NC correction to the density number of particles emitted*

In this step, we aim to investigate the NC effect on the density number of particles that are emitted by the NC Schwarzschild BH in the scenario of pure thermal radiation. According to Refs. [270–272], the density number of particles $\hat{n}$ emitted is directly related to the tunneling rate [98, 273]. In our case of thermal radiation, the density number from the tunneling rate (5.67) can be written as follows [270]

$$\hat{n} = \frac{\hat{\Gamma}}{1-\hat{\Gamma}} = \frac{1}{e^{8\pi m\omega\left(1+\frac{3\Theta^2}{8m^2}\right)}-1}, \tag{5.82}$$

Note that the obtained expression takes the same form as the Planck distribution of the black body radiation and is related to the NC parameter. Also, when we set $\Theta = 0$, we recover the commutative expression of the density number of particles emitted [53].

$$\hat{n} = \frac{1}{e^{8\pi m\omega}-1}. \tag{5.83}$$

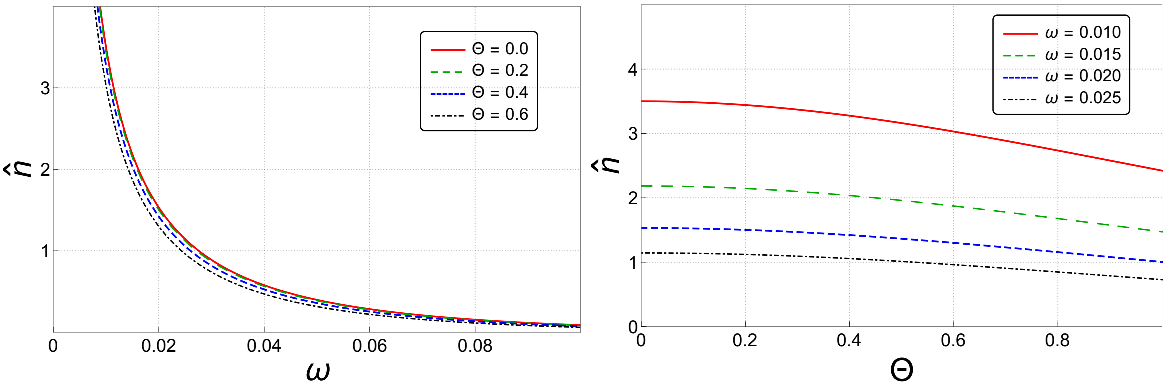

Figure 5.34: The behavior of the density number of particles emitted $\hat{n}$ from a NC Schwarzschild BH as a function of particle frequency ω (left panel) with $m = 1$ and different NC parameter Θ. (right panel) The density number of particles emitted $\hat{n}$ as a function of the NC parameter Θ with $m = 1$ and different frequency ω.

The behavior of the density number of particles emitted from the NC Schwarzschild BH as a function of particle frequency ω is shown in Fig. 5.34 (left panel). The main observation in this figure is the non-commutativity effect, which results in a decrease in the density number of particles emitted as Θ increases. and that means non-commutativity plays a similar role as potential well in quantum mechanics. In the right panel of Fig. 5.34, we show how the non-commutativity decreases the density number of particles emitted, which is the same effect observed in the commutative case, in which the increase in the BH mass m leads to a decrease in the density number of particle $\hat{n}$ (see left panel of Fig. 5.35). This indicates that the NC parameter Θ plays a similar role as the BH mass m, effectively increasing the gravitational field of the BH and explaining the decrease in the density number of particles that escape from the BH.

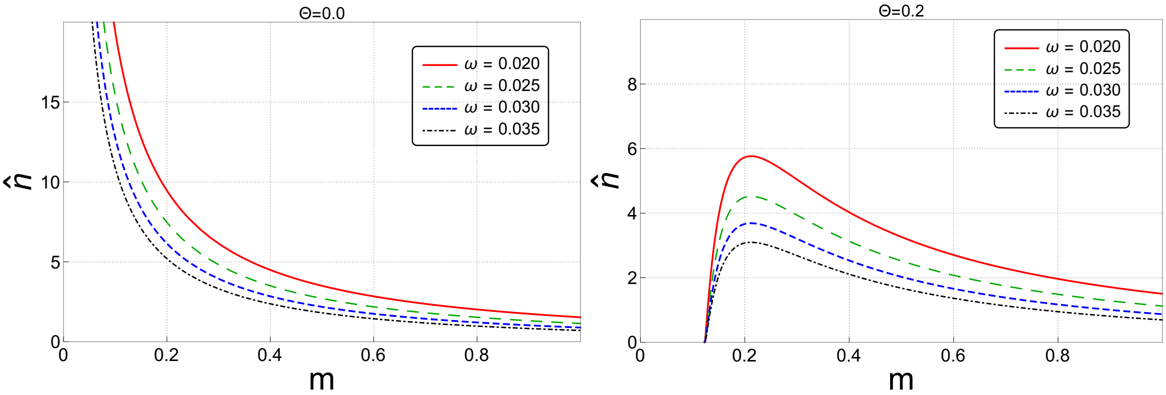

Figure 5.35: The commutative $\Theta = 0$ behavior of $\hat{n}$ as a function of the BH mass m (left panel), with different frequency ω. (right panel) The density number of particles emitted $\hat{n}$ as a function of the BH mass m in the NC spacetime $\Theta = 0.2$ and different frequency ω.

In Fig. 5.35, we present the behavior of both commutative and NC cases of the density number of particles emitted as a function of the BH mass m and for different frequencies ω. As we see, in the commutative case, the density of particles emitted increases during the evaporation of the BH and diverges when the mass of this BH reaches zero, while this issue can be fixed when we pass to the NC geometry.

For that, we use a particular case in which we use the Boltzmann factor with the NC temperature in the leading order in Θ given by Eq. (5.68), then we set that inside the density number of particles given by Eq. (5.82), to obtain the right panel of Fig. 5.35. It is clear that in the NC spacetime, this geometry removes the divergence behavior, in which the density number of particles increases during the evaporation of this BH until it reaches a maximum, then quickly falls to zero at m_{min}, and that corresponds to the remnant mass. At this point, the BH stop radiation, and that indicates that there is no more emitted particle at this point. This result is consistent with the temperature profile $\hat{T}_H - r_h$ in Fig. 5.32, and that means the non-commutativity solves the issue of the commutative case.

5.4.5 *Bekenstein entropy loss and number of particles emitted*

In this subsection, we will investigate the effect of this geometry on the Bekenstein entropy loss and the total number of particles emitted from NC Schwarzschild BH in the non-thermal case, where we follow the same steps as in other models of QG [104, 274].

The Bekenstein entropy loss of the Schwarzschild BH per emitted quanta[12], is given by [275]

$$\frac{dS}{dN} = \frac{dS/dt}{dN/dt} = 8\pi m\hbar\langle\omega\rangle, \tag{5.84}$$

---

[12] In the natural unit system $(G = \hbar = c = 1)$.

where N is the total number of particles and the average energy $\langle E\rangle$ is given by [276]

$$\langle E\rangle = \hbar\langle\omega\rangle = \frac{\pi^4}{30\zeta(3)}T_H, \tag{5.85}$$

In the presence of non-commutativity, the ordinary temperature T_H must change to the deformed one given by (5.68) in the above equation. In this case, by using Eq. (5.68), the Eq. (5.84) can be written as follows:

$$\frac{dS}{dN} = \frac{dS/dt}{dN/dt} = \frac{\pi^4}{30\zeta(3)}\left(1-\frac{3\Theta^2}{8m^2}\right), \tag{5.86}$$

According to the deformed entropy given by Eq. (5.73), the NC Bekenstein entropy loss of the NC Schwarzschild BH per emitted quanta is given by

$$\frac{d\hat{S}}{dN} = \frac{d\hat{S}/dt}{dN/dt} = \frac{dS/dt}{dN/dt}\left(1+\frac{9\pi\Theta^2}{8}\frac{1}{S}\right), \tag{5.87}$$

By substituting the Eq. (5.86) inside the above one and keeping only the leading order in Θ, we find

$$\frac{d\hat{S}}{dN} = \frac{\pi^4}{30\zeta(3)}\left(1-\frac{3\Theta^2}{32m^2}\right), \tag{5.88}$$

It is clear that, in the commutative limit $\Theta \to 0$, we recover the commutative expression [275].

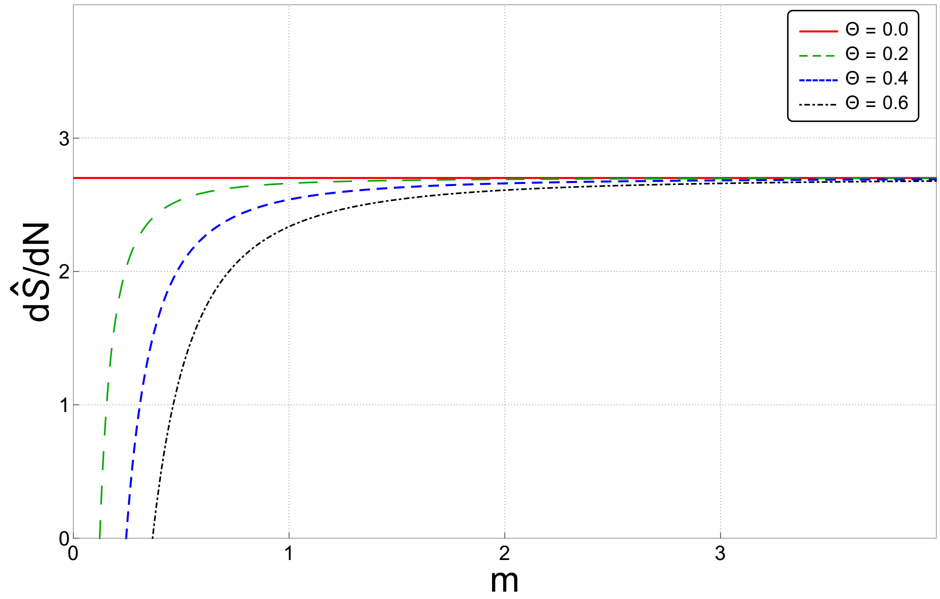

Figure 5.36: The behavior of the Bekenstein entropy loss of the NC Schwarzschild BH per emitted quanta as a function of the BH mass m and for a different NC parameter.

In Fig. 5.36, we present the variation of Bekenstein entropy loss of the NC Schwarzschild BH per emitted quanta $\frac{d\hat{S}}{dN}$ as a function of the BH mass m and for a different NC parameter Θ. As we see in the commutative case, this quantity is constant during the BH evaporation process and takes a value of about 2.7 [276]. It is clear that, in the presence of non-commutativity, we observe a new behavior, in which the effect of this geometry is negligible for a LBH (supermassive one), then $\frac{d\hat{S}}{dN}$ start decreases during the evaporation process (with the decrease of mass m) until reach a zero at m_{min}, which corresponds to a remnant mass. It is worth noting that this behavior is also observed in other models of QG, such as RG [104], and that shows a similarity between these models of QG and the non-commutativity, as we see before in the previous Sec. 5.3.

Now, we investigate the non-commutativity effect on the total number of particles emitted by this BH; for that, we use the mass element Ref. [274], and in the NC spacetime can be written as follows:

$$d\hat{m} = \langle E \rangle d\hat{N}, \tag{5.89}$$

Using the definition of average energy given in Eq. (5.85) together with Eq. (5.68), we get[13]

$$dm\left(1 - \frac{3\Theta^2}{32m^2}\right) = \frac{\pi^4 T_H}{30\zeta(3)}\left(1 - \frac{3\Theta^2}{8m^2}\right) d\hat{N}, \tag{5.90}$$

In the leading order in Θ, the element of total number of particles $d\hat{N}$ is written as

$$d\hat{N} = \frac{30\zeta(3)8\pi m}{\pi^4}\left(1 + \frac{9\Theta^2}{32m^2}\right) dm, \tag{5.91}$$

Integrating this equation, we find the NC total number of particles emitted in the non-thermal radiation.

$$\hat{N} = \frac{30\zeta(3)}{\pi^4}\left[4\pi m^2 + \frac{9\pi\Theta^2}{8}\log\left(4\pi m^2\right)\right], \tag{5.92}$$

and in terms of entropy, we have

$$\hat{N} = \frac{30\zeta(3)}{\pi^4}\left[S + \frac{9\pi\Theta^2}{8}\log\left(S\right)\right], \tag{5.93}$$

In Fig. 5.37, we show the behavior of the total number of particles emitted by the NC Schwarzschild BH as a function of mass m. As we see, this behavior is similar to the one obtained for entropy, and that is due to the use of non-thermal radiation to compute the total number of particles emitted in the presence of non-commutativity. It is clear that the effect of this geometry in this case is different from the one obtained in the above case of pure thermal radiation, in which the non-commutativity always decreases the density number of particles emitted, while in the non-thermal case we observe two scenarios where this geometry increases the total number of particles emitted for a LBH (with a mass of $m > 0.282$) and increases with Θ. In the second scenario, for a SBH (with mass $m \leq 0.82$), this effect is reversible to a reduction of the total number of particles emitted and decreases when we increase in Θ, until we reach zero at the remnant mass m_{min}. Moreover, this geometry shows again the remnant mass, which corresponds to the BH that evaporated

---

[13] The mass of this BH can be obtained using $\hat{m} = r_h^{NC}/2$, where the event horizon in this case is given by Eq. (3.11) with $a = \Theta$ and $b = 0$.

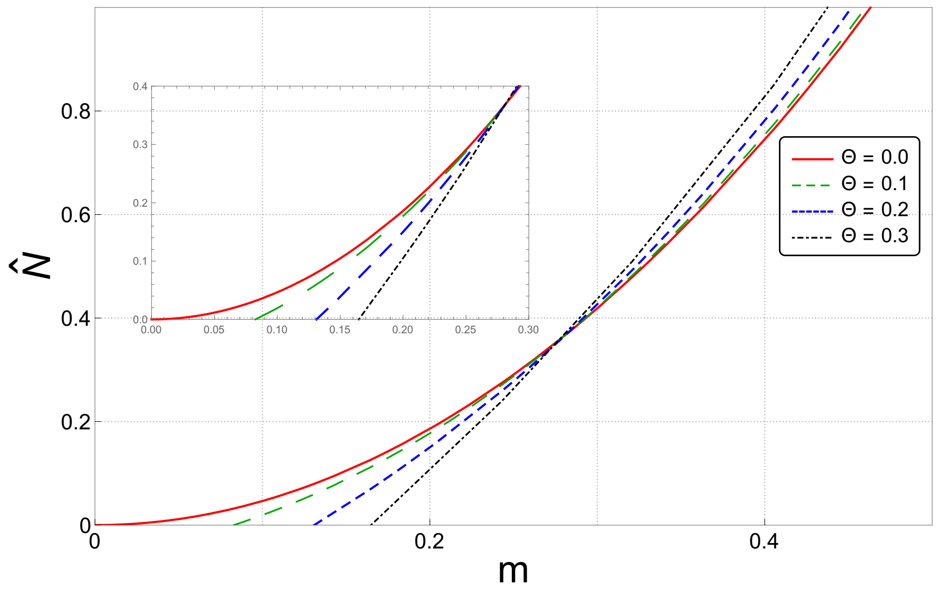

Figure 5.37: The behavior of the NC total number of particles emitted by the NC Schwarzschild BH as a function of the BH mass m and for different NC parameter.

before, and that is not allowed in the commutative case. However, this calculation can also be used for the expression of entropy resulting from the area law given by Eq. (5.11).

5.5 BLACK HOLE EVAPORATION PROCESS IN NC SPACETIME

According to our previous sections on the thermodynamics of the NC Schwarzschild BH, we find that this geometry affected the thermodynamic properties of this BH. However, in this section, we discuss the non-commutativity effect on other quantities such as luminosity, energy emission rate, and lifetime of NC Schwarzschild BH[14].

5.5.1 *Luminosity of NC SBH radiation*

In the black body case, the luminosity L related to the temperature T, and is given by the Stefan-Boltzmann black body formula:

$$L = \sigma_{SB} A\, T^4, \tag{5.94}$$

where A is the commutative BH area given by Eq. (1.47) and $\sigma_{SB} = \frac{\pi^2 k_B^4}{60\hbar^3 c^4}$ is the Stephan-Boltzmann constant. In the presence of non-commutativity, the luminosity of the NC Schwarzschild BH can be written as follows:

$$\hat{L} = \sigma_{SB} A_h^{NC} \hat{T}^4, \tag{5.95}$$

---

[14] In this section, we use thermodynamic properties that are obtained in Sec. 5.1, where we use the conditions $a = 0$ and $b = \Theta$.

where $\hat{T}$ is the NC global temperature that is emitted by the total surface horizon[15] and is given by Eq. (5.7), and the NC area of this BH is given by Eq. (5.10).

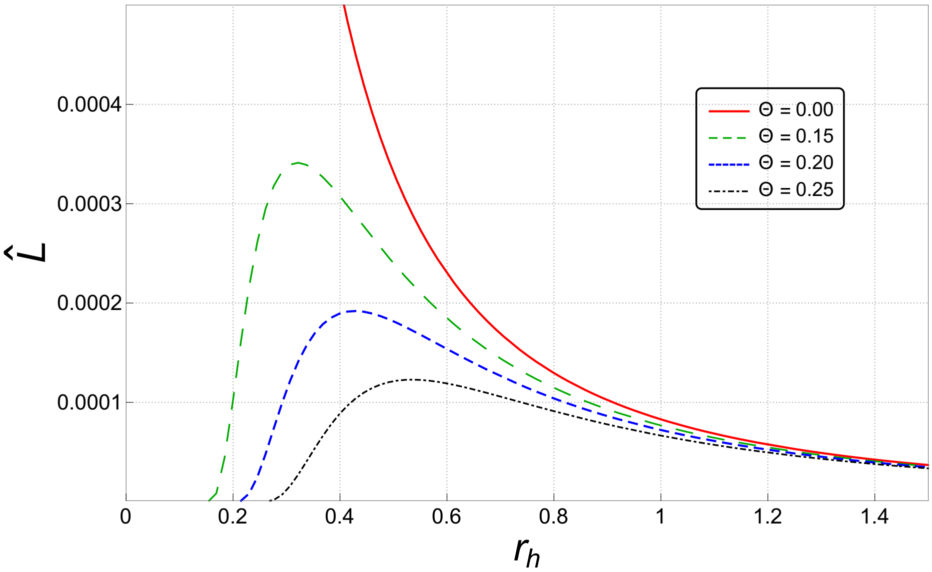

Figure 5.38: The behaviors of the NC Schwarzschild BH Luminosity $\hat{L}$ as a function of r_h.

The behavior of the NC luminosity $\hat{L}$ of the NC Schwarzschild BH as a function of the event horizon r_h for different NC parameter Θ is shown in Fig. 5.38. As we see, in the commutative case ($\Theta = 0$), the luminosity behavior represents a divergence at $r_h = 0$, while in the presence of non-commutativity this divergent is removed and a new maximum can be reached by the BH during the evaporation process, then turning to zero at $r_h^{min} = \Theta$ (at this point this BH stop evaporation process), and this maximum in the luminosity behavior is caused by the maximum activity of the BH radiation (see Fig. 5.5). It is worth noting that our result obtained in Fig. 5.38 is consistent with the one obtained by the black body radiation, where the quantization of the spacetime via the non-commutativity removes the divergence behavior just like the quantization of the spectral radiation in the black body radiation, so the quantum effect is also observed on the BH radiation in the NC geometry.

5.5.2 *Energy emission rate*

The deformed energy emission rate of the NC Schwarzschild BH in the NC spacetime is written in the same form as in the commutative one [277, 278], and is given by

$$\frac{d^2\hat{E}}{d\omega dt} = \frac{2\pi^2\hat{\sigma}_{lim}\omega^3}{e^{\omega/\hat{T}} - 1}, \tag{5.96}$$

where ω is the particle frequency, $\hat{T}$ describes the NC Hawking temperature (5.7) and σ_{lim} is the greybody factor. This factor can be expressed as the surface of the unstable photon

---

[15] It is always possible to investigate a partial luminosity in this geometry by using the partial temperature given by Eq. (5.6), analyzing the possible cases for a given a end b, and showing the difference of luminosity from one direction to the other.

sphere $\sigma_{lim} \approx \pi R^2_{shadow}$ [277]. In this case, the above energy emission rate can be written as follows:

$$\frac{d^2\hat{E}}{d\omega dt} = \frac{2\pi^3 R^2_{shadow}}{e^{\omega/\hat{T}} - 1}\omega^3, \tag{5.97}$$

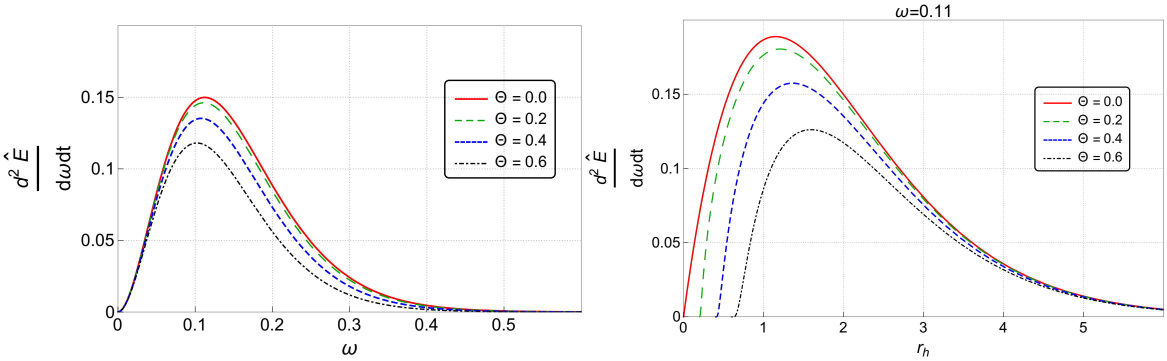

Figure 5.39: The behaviors of energy emission rate of the NC Schwarzschild BH as a function of frequency ω (left panel) and as a function of r_h (right panel).

In the right panel of Fig. 5.39, we present the NC energy emission rate as a function of the frequency ω with a different Θ. As we see, in both commutative and NC cases, we observe the same general behavior concerning the gaussian distribution pick of energy emission rate for the NC Schwarzschild BH. It is clear that this geometry decreases the peak and shifts it to the low frequency with the increase in the NC parameter Θ, which means the evaporation process of Schwarzschild BH is slow in the NC spacetime.

For the right panel of Fig. 5.39, we show the variation of the energy emission rate as a function of the event horizon r_h. It is clear that, in the NC spacetime, we observe a remnant BH, in which the energy emission rate goes to zero at a minimum size $r_h^{min} = \Theta$. We show again that this geometry predicts a remnant BH in the Planck size.

5.5.3 *NC effect on the black hole Lifetime*

In our next step, we compute the NC lifetime of this BH by using its luminosity $\hat{L} = \frac{d\hat{E}}{dt}$ given in Eq. (5.95), and that allows us to write the NC energy decay rate as follows:

$$\frac{d\hat{E}}{dt} = -\frac{d\hat{m}}{dt} = \sigma_{SB}\, A_h^{NC} \hat{T}_H^4, \tag{5.98}$$

The "$-$" sign comes from the loss of mass during the evaporation process. Using the NC expressions of area (5.10) and temperature (5.7), and we keep only the second order in Θ, then we get

$$\frac{dm}{dt} = -\frac{\sigma_{SB}}{256\, m^2\, \pi^3} + \frac{25\, \sigma_{SB}\Theta^2}{8192\, m^4\, \pi^3} + \mathcal{O}(\Theta^4). \tag{5.99}$$

The variation of the NC evaporation rate as a function of the BH mass m with different NC parameters Θ is shown in Fig. 5.40. As we see, a new minimum appears in this geom-

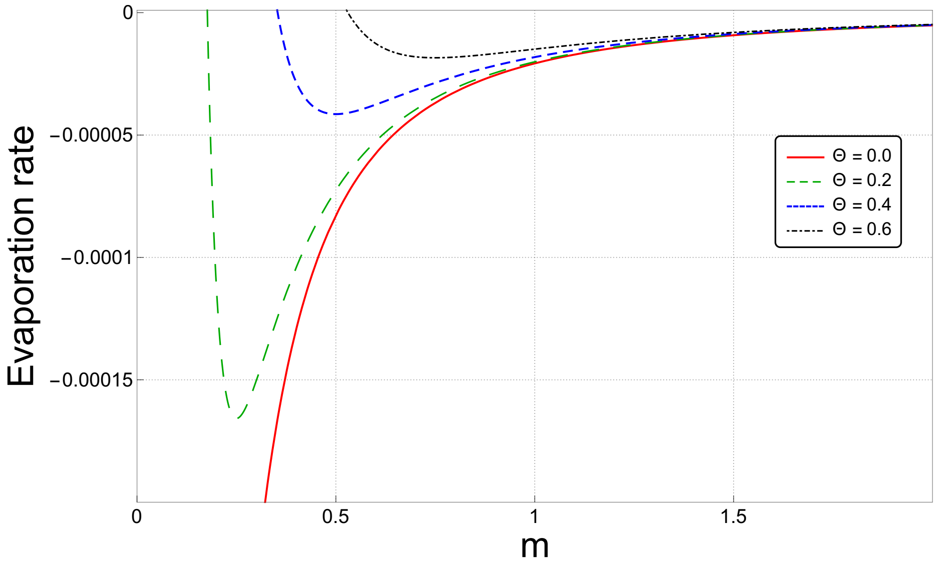

Figure 5.40: The behaviors of NC evaporation rate as a function of mass m with different values of Θ.

etry, in which the non-commutativity removes the commutative divergence behavior at $m \to 0$, and this geometry allows the evaporation rate to reach zero at a minimum mass of m_{min}, which indicates the end of the evaporation process of this BH. In particular, a similar result can be found in the novel GUP framework introduced in Ref. [116], where the BH is completely evaporated ($\frac{dm}{dt} = 0$ at $m = 0$), contrary to our case, in which the evaporation rate goes to zero at m_{min} and that means the deformed BH stop evaporation before $m = 0$ and that leads to a remnant BH.

In order to express the NC lifetime of the Schwarzschild BH, we separated the variables of Eq. (5.99), and we found

$$\sigma_{SB} \int_0^t dt = \int_m^{m_i} dm \left(256\, m^2 \pi^3 + 200\, \pi^3 \Theta^2\right). \tag{5.100}$$

Integrate the above expression with the boundary condition $(t = 0, m = m_i) \to (t, m)$ (where m_i is the initial mass and m is the current one.), and after some calculation, the lifetime of the NC Schwarzschild BH is written as follows:

$$\hat{t} = \left(\frac{256\, \pi^3}{3\sigma_{SB}} (m_i^3 - m^3) + \frac{200\, \pi^3 \Theta^2}{\sigma_{SB}} (m_i - m) \right). \tag{5.101}$$

Note that when we set $\Theta = 0$, we recover the commutative expression. It is worth noting that the non-commutativity increases the lifetime of the NC Schwarzschild BH, and that means the evaporation process passes slowly in this geometry. A similar observation can be seen in Ref. [165]. Moreover, in the final stage of BH evaporation, we aim to examine two possible scenarios. The first is concerning the complete evaporation ($m_f = 0$). For that, the BH lifetime in this case is given as follows:

$$\hat{t}_f^{(1)} = \left(\frac{256\,\pi^3}{3\sigma_{SB}} m_i^3 + \frac{200\,\pi^3\Theta^2}{\sigma_{SB}} m_i \right), \tag{5.102}$$

It is clear that the non-commutativity increases the lifetime of a complete evaporation process, and according to our previous findings about the remnant BH, this scenario is not acceptable. However, in the second scenario, concerning the presence of a remnant mass $\hat{m}_0 = \Theta/2$ (see SubSec. 5.1.1) in the final stage of evaporation, this geometry prevents Schwarzschild BH from the complete evaporation (see the profile $\hat{T} - r_h$ in Figs. 5.2, 5.3, 5.4, and 5.5). The BH lifetime in this case is written as follows:

$$\hat{t}_f^{(2)} = \left(\frac{256\,\pi^3}{3\sigma_{SB}} m_i^3 + \left(200\,m_i \pi^3 - \frac{332\,\pi^3}{3} \right) \frac{\Theta^2}{\sigma_{SB}} \right), \tag{5.103}$$

Remarkably, the above expression shows that, in this scenario, the BH lifetime is smaller than the first one (5.102), which means this BH stopped radiation before the above case, and that led to a remnant BH, and that is consistent with our findings in the previous sections.

Table 5.6: Evaporation time for two possible scenarios of the NC Schwarzschild BH, with different Θ, and remnant mass $\hat{m}_0 = \Theta/2$.

Scenarios	$\Theta = 0$	$\Theta = 0.2$	$\Theta = 0.4$	$\Theta = 0.6$
$\hat{m} = 0$, $\hat{t}_f^{(1)} (\times 10^7)$	1.6085	1.6100	1.61453	1.62207
$\hat{m} = \hat{m}_0$, $\hat{t}_f^{(2)} (\times 10^7)$	/	1.60999	1.61439	1.62162

The two possible scenarios of the NC Schwarzschild BH evaporation expressed by Eqs. (5.102) and (5.103) are presented in Table. 5.6, for a different value of the NC parameter Θ. It is clear that, in the second scenario, in the presence of a remnant mass (5.103), the BH stop radiation before the first scenario given by Eq. (5.102). Another remark is that this geometry increases the lifetime of the NC Schwarzschild BH with the increase in Θ.

Let's check the behavior of mass decay as a function of the BH lifetime in the NC spacetime. For that, we solve Eq. (5.101) for m. The general solution in the NC geometry is supposed to be in the following form:

$$m(t) = A(t) + B(t)\,\Theta^2. \tag{5.104}$$

where $A(t) = \frac{\left(256 m_i^3 \pi^3 - 3\sigma_{SB} t\right)^{1/3}}{2^{2/3} 4\pi}$ is the commutative solution to Eq. (5.101) with $\Theta = 0$, and $B(t)$ is the NC correction term and is a function of the BH lifetime t. For that, substituting the Eq. (5.104) inside (5.101) and solving it for $B(t)$, we find

$$m(t) = \frac{\left(256 m_i^3 \pi^3 - 3\sigma_{SB} t\right)^{1/3}}{2^{2/3} 4\pi}$$

$$-\frac{24\pi\left(-8m_i\pi+2^{1/3}\left(256m_i^3\pi^3-3\sigma_{SB}t\right)^{1/3}\right)}{2^{2/3}4\left(256m_i^3\pi^3-3\sigma_{SB}t\right)^{2/3}}\Theta^2+\mathcal{O}(\Theta^2). \tag{5.105}$$

It is clear that, for the commutative Schwarzschild BH with initial mass $m_i = 10$, the BH mass vanishes $m \to 0$ as $t \to \frac{256mi^3\pi^3}{3\sigma_{SB}} \simeq 1.608 \times 10^7$, and that is a necessary finite time for a complete evaporation, while for the NC Schwarzschild BH stop evaporation before the time $\hat{t} < t = 1.608 \times 10^7$, with a minimum $\hat{m}_{min}$.

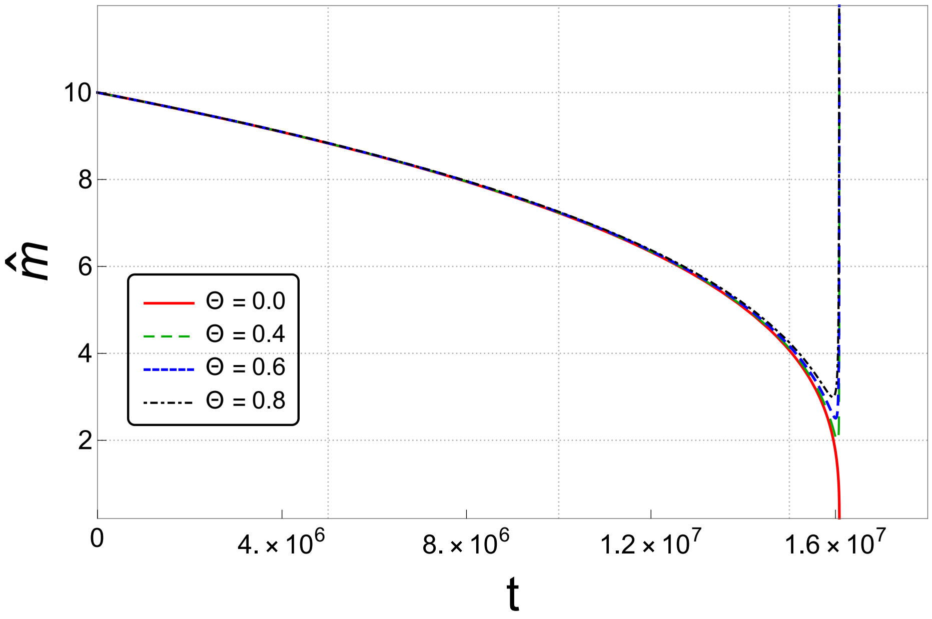

Figure 5.41: The behaviors of the NC Schwarzschild BH mass during the evaporation process $\hat{m}$ as a function of BH lifetime t, with initial mass $m_i = 10$.

The evolution of NC Schwarzschild BH mass $\hat{m}$ during the evaporation process as a function of the BH lifetime t for various values of Θ is shown in Fig. 5.41.

It is clear that the commutative Schwarzschild BH ($\Theta = 0$) is completely evaporated at $t_{evap} = 1.6085 \times 10^7$, while for the NC case ($\Theta \neq 0$), this geometry prevents this BH from a complete evaporation and leads to a new minimum mass m_{min} (remnant mass) at a finite time $\hat{t}^{NC}_{evap} < t_{evap}$ for a given Θ, in which at this time the NC Schwarzschild BH stop radiation and that leads to a remnant BH with a minimum mass $\hat{m}_0$, where these results are consistent with our previous sections.

Table 5.7: Evaporation time $\hat{t}$ of NC Schwarzschild BH in the scenario of remnant BH with its minimum mass, for different values of Θ

Θ	Minimum mass	Evaporation time $\hat{t}_f(\times 10^7)$
0.0	–	1.60849
0.2	1.24623	1.60747
0.4	1.94265	1.60474
0.6	2.50714	1.60023

The influence of the NC parameter Θ on the lifetime $\hat{t}_f$ and the minimum mass $\hat{m}_0$ of the remnant BH in the NC spacetime are present in Table. 5.7. As we see, this remnant mass increases with the increase in Θ, and that allows BH to stop radiation before the previous case with a small remnant mass and a small Θ, and that leads to a decrease in the evaporation time with increases in Θ.

5.5.3.1 *Evaporation process of NC Schwarzschild BH*

The evaporation process of BH is an important direct consequence of Hawking radiation. Unfortunately, in the semi-classical approach, the end of the evaporation process is unknown, and the final stage of commutative Schwarzschild BH is still a question in the absence of a QG theory. One of the explanations for the divergence behavior of radiation in the final stage of evaporation is that when the BH lost all its mass $m \to 0$, the Schwarzschild BH finished with a quantum explosion [279, 280], which is a catastrophe scenario for any BHs. In order to know exactly what happened in the final stage of Schwarzschild BH at the quantum level, we need QG theory, to solve this mystery.

In this work, where we use the NC geometry as a candidate of QG theory to study the BH physics as the thermodynamic phenomena of Schwarzschild BH (see previous sections.), we show important results that emerged from this theory. Non-commutativity reveals the mystery of This geometry reveals the mystery of the final stage in the evaporation process, which ends in a peaceful manner. According to our findings in the previous sections, the non-commutativity presents a new scenario of evaporation in which this geometry prevents the BH from a complete evaporation and predicts a remnant BH in the finale stage of Schwarzschild BH evaporation (see Fig. 5.42).

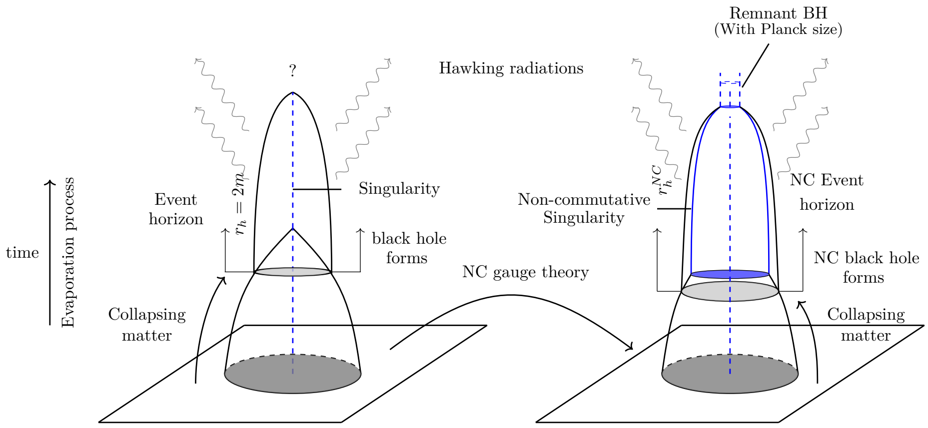

Figure 5.42: A schematic picture of the formation and evaporation process of BH in the NC spacetime.

Moreover, this remnant has a minimum mass $\hat{m}_0$ and area A^0_Θ with zero entropy and temperature (for more detail see Sec. 5.1), as we show it in the schematic picture in Fig. 5.42. The prediction of this remnant is expected to be in the Planck scale, and that is due to our estimation of the NC parameter Θ in different situations and scenarios, which show again that the non-commutativity of spacetime appears at the Planck scale.

CONCLUSIONS

In this thesis, we study various implications of non-commutativity on the BH physics in order to investigate the effects of QG theory. In this context, we use a NC gauge theory of gravity to describe a quantum correction to the BH metric by using a general form of the tetrad fields. Then we u use this deformed metric to investigate the geometrical properties, the motion, and the thermal radiation in the presence of non-commutativity. This work is divided into three principal parts, of which the first is devoted to some geometrical properties of the deformed BH. The second part is devoted to study the motion of test particles around the deformed BH. The third part is devoted to the thermal properties and evaporation process of the deformed BH.

In Chap. 3, we study some geometrical properties of the deformed BH that was obtained in the NC gauge theory of gravity, in different cases of NC matrix. Then we show that this geometry breaks the spherical symmetry of the metric in the specific case of NC matrix. As an application to our general form of deformed metric, we choose the Schwarzschild BH and the RN one, where this geometry predicts a singularity at a finite radius $r^{NC}_{\text{singularity}}$ for both cases also this geometry increases the even horizon $r_h^{NC} > r_h$. Then we present briefly, the formation of the NC Schwarzschild BH from a collapsing matter.

In Chap. 4, we study the motion of three types of particles in two types of NC spacetime (presented in Chap. 3). In the first case, we choose the NC Schwarzschild spacetime as a background to investigate the motion of massive and massless particles and the effect of this geometry. As a first step, we investigate the non-commutative effect on the radial motion of both massive and massless test particles. We observe that the massive and massless test particles take an infinite time to reach the NC singularity in the affine parameter framework, and that's not allowed in the commutative case. For the coordinate time, these particles take an infinite time to reach the NC event horizon. Secondly, we study the circular motion and its stability in this geometry for both massive and massless test particles, where the motion of these particles in this geometry presents new types of motion near the NC event horizon and it's SCO, which is not allowed in the commutative Schwarzschild spacetime. For the massive particles, we obtain multiple SCO separated by an unstable region. Then, for the massless one, these orbits represent a two-photon sphere; the inner one (the new SCO) is stable, while the outer one is unstable, as in the commutative case. Therefore, we support our findings by investigating in detail the Lyapunov exponent to establish the instability of orbits for both massive and massless test particles. Then, we show the effect of the non-commutativity on the shadow of the NC Schwarzschild BH, where this geometry increases the shadow radius in a similar case to the mass, and that indicates that the non-commutativity of spacetime increases the gravitational field of BH.

In the second case of this chapter, we use NC RN BH as a background to investigate the motion of an uncharged/charged massive test particle. In this pursuit, the analysis of the effective potential for uncharged/charged massive test particles shows a new SCO near the event horizon, in which the non-commutativity shifts the inner minimum of the effective potential to the outside of the NC event horizon, and again, in this geometry, we have a multiple SCO as in the NC Schwarzschild spacetime. Then we solve the geodesic equation for both uncharged and charged test particles and also for the Schwarzschild limit.

Finally, we investigate in detail the NC effect on the four classical tests of GR, concerning the periastron advance, red-shift, deflection of light, and time delay. We find that the lower bound of the NC parameter Θ^{phy} falls within the range of $(10^{-31}m - 10^{-36}m)$, which is close to the Planck scale.

In Chap. 5, we investigate in detail the non-commutativity effect on the thermodynamic properties and thermal stability of NC Schwarzschild BH in a different scenario. As a first step, we study the classical BH thermodynamic of NC Schwarzschild one, in which we obtain the thermal quantities in the presence of non-commutativity. Moreover, the estimation of Θ through thermal phenomena is found in the order of Planck scale $\Theta^{\text{phy}} \approx 1.523 \times 10^{-35}\,\text{m} \sim l_{\text{Planck}}$. Then, we check the thermal stability of this BH, where the results show a phase transition of the unstable Schwarzschild LBH to a stable SBH one. Also, we show a new scenario of evaporation in this geometry, which is summarized below.

- The evaporation of a Schwarzschild BH starts from the equator and goes up to the poles.
- The non-commutativity prevents the Schwarzschild BH from complete evaporation, and then we obtain a quantum object with an area of A_0^{Θ} with a minimum mass of $\hat{m}_0 = 0.5\,l_p$ and a radius of $r_h^{\min} = l_p$, interpreted as a microscopic remnant BH and it's thermodynamically stable.
- Also, this remnant can preserve the information, which solves the problem of lost information.

However, the phase transition of the NC Schwarzschild BH in the presence of pressure shows a Hawking-Page-like phase transition at the critical value $\hat{P}_c$, and that means a second-order phase transition in this geometry. Then, we establish a similarity between NC Schwarzschild BH and the AdS RN, representing in a direct mathematical relation between the Θ and the electric charge Q, $\Theta^2 = \frac{4}{3}Q^2$. Also, we present a new treatment of non-commutativity, which is treated as an external pressure applied to this BH. We observe a new scenario of evaporation in which a new unstable intermediate region (IBH) appears between two stable ones (SBH and LBH), and we get two-coexistence phase transition similarly to the AdS RN BH. Moreover, in this scenario, we find that Θ plays the same role as the electric charge Q, and the non-commutativity effect applies to the Schwarzschild BH is similar to the cosmological constant effect.

Secondly, we check the stability and the phase transition of the NC Schwarzschild BH inside a thermal spherical cavity. The analysis thermal phenomena inside this cavity shows that, in the presence of non-commutativity, this BH has a two-phase transition of second order, in a similar way to the previous scenario. Then we obtain again a two-coexistence phase transition, similar to the other models of QG theories, and that indicates the impact of this geometry to describe the quantum effect of gravity at large scale.

Then,we examine the NC effect on the Hawking radiation by extending the semi-classical approach of the quantum tunneling process to the NC geometry, where we are exploring two distinct scenarios. In the first scenario, we examin the case of pure thermal radiation from the NC Schwarzschild BH, where in this geometry we have established an equivalence between the quantum tunneling process and the thermodynamic one. Our analysis of the non-commutativity impact on the tunneling rate of these massless particles shows a similar role for a potential well in quantum mechanics. In the second scenario, we take into account the conservation of energy and the context of large-frequency emissions. The results are consistent with an underlying unitary quantum theory in which the tunneling rate is related to changes in Bekenstein entropy. Our findings of the NC correction to the entropy of NC Schwarzschild BH have unveiled a logarithmic correction. This correction is consistent with other QG theories. Also,we investigate the correlation between successively emitted particles with different frequencies ω in this geometry for a non-thermal emission. The results have highlighted the presence of correlations between successive emissions, with non-commutativity playing a role in reducing these correlations within Hawking radiation. The non-commutativity not only preserves information within the remnant BH but also enables information to emerge from the event horizon, coding in Hawking radiation. Then, we check the effect of non-commutativity on the number of particles emitted from the NC Schwarzschild BH in two cases from both thermal and non-thermal radiation. Firstly, we obtain the NC correction to the density number of particles using pure thermal radiation at a lower frequency approximation, and our results confirm the effect of non-commutativity, leading to a decrease in the density number of particles. Secondly, we use the non-thermal radiation to express the NC to the total number of particles emitted by this BH, where we use the Bekenstein entropy loss in the presence of this geometry, which is found related to the NC entropy.

In the final step, we analyze some phenomenological aspects of the NC SBH and its evaporation process. As an application, we choose the luminosity, and our results show a similar behavior to the black body radiation, in which the non-commutativity removes the divergence behavior of the Schwarzschild BH luminosity in a similar way as the quantization of the black body radiation, and that confirms the role of the non-commutativity concerning the quantization of spacetime in GR. Then we show the effect of non-commutativity on the energy emission rate and lifetime, where we find that, in this geometry, the Schwarzschild BH evaporates slowly and the non-commutativity prevents this BH from the complete evaporation, and that leads to a remnant BH as we motioned above.

The use of the NC gauge theory of gravity allows us to obtain good results on the bound of the NC parameter. This theory needs more attention, and it may be beneficial to describe QG in the future.

Although the good results and predictions of NC gauge theory of gravity, it is still not a final theory of QG, more work and development for other application is needed. One of our aims is to reduce the complexity of calculations and preserve all the physical results,find another method to solve the deformed Einstein's equations in the presence of non-commutativity in the leading order of corrections, and compare them to this work. Also, we believe that, the application of this approach on rotating BH can lead to bright results and predict a new scenario about the evolution of this BH. All of that is still just a theory without any validation by experiments, and that is the dream of every theoretical physicist.

A

SPHERICAL SYMMETRIC METRIC IN NC GAUGE THEORY

The general spherical symmetric of the the Schwarzschild-type metric is given by the following line element

$$ds^2 = -A^2(r)\, dt^2 + B^2(r)\, dr^2 + r^2\, d\theta^2 + r^2\, sin\theta^2\, d\phi^2 \tag{A.1}$$

and the non-zero Christoffel symbols:

$$\begin{aligned}\Gamma^t_{t\,r} =&\Gamma^t_{r\,t} = \frac{A'(r)}{A(r)},\, \Gamma^r_{t\,t} = \frac{A(r)A'(r)}{B(r)^2},\, \Gamma^r_{r\,r} = \frac{B'(r)}{B(r)},\, \Gamma^r_{\theta\,\theta} = \frac{r}{B(r)^2},\, \Gamma^r_{\phi\,\phi} = -\frac{rsin\theta^2}{B(r)^2},\\ \Gamma^\theta_{r\,\theta} &= \Gamma^\theta_{\theta\,r} = \frac{1}{r},\, \Gamma^\theta_{\phi\,\phi} = -sin\theta\, cos\theta,\, \Gamma^\phi_{r\,\phi} = \Gamma^\phi_{\phi\,r} = \frac{1}{r},\, \Gamma^\phi_{\phi\,\theta} = \Gamma^\phi_{\theta\,\phi} = cot\theta.\end{aligned} \tag{A.2}$$

and the general tetrad fields of the metric (A.1) is written as:

$$e^a_\mu = \begin{pmatrix} A(r) & 0 & 0 & 0 \\ 0 & B(r)\, sin\theta\, cos\phi & r\, cos\theta\, cos\phi & -r\, sin\theta\, sin\phi \\ 0 & B(r)\, sin\theta\, sin\phi & r\, cos\theta\, sin\phi & r\, sin\theta\, cos\phi \\ 0 & B(r)\, cos\theta & -r\, sin\theta & 0 \end{pmatrix} \tag{A.3}$$

and the inverse tetrad fields:

$$e^{a\,\mu} = \begin{pmatrix} -\frac{1}{A(r)} & 0 & 0 & 0 \\ 0 & \frac{sin\theta\, cos\phi}{B(r)} & \frac{cos\theta\, cos\phi}{r} & -\frac{sin\theta\, sin\phi}{r} \\ 0 & \frac{sin\theta\, sin\phi}{B(r)} & \frac{cos\theta\, sin\phi}{r} & \sin\theta\, cos\phi \\ 0 & \frac{cos\theta}{B(r)} & -\frac{sin\theta}{r} & 0 \end{pmatrix} \tag{A.4}$$

A.1 SPIN CONNECTION

The commutative spin-connections components can be computed using the definition:

$$\omega^{a\,b}_\mu = -e^{b\nu}\partial_\mu e^a_\nu + e^{b\nu}\Gamma^\lambda_{\mu\,\nu} e^a_\lambda, \tag{A.5}$$

using this definition and the Eqs. (A.2), (A.3) and (A.4), we can computed the non-zero spin-connections components.

$$\begin{aligned}
\omega_t^{0\,1} &= -\underbrace{e^{1\nu}\partial_t e_\nu^0}_{=0} + e^{1\nu}\Gamma^\lambda_{t\,\nu}e^0_\lambda,\\
&= \underbrace{e^{1\,t}}_{=0}\Gamma^r_{t\,t}e^0_r + e^{1\,r}\Gamma^t_{t\,r}e^0_t,\\
&= \frac{A'(r)}{B(r)} sin\theta\, cos\phi.
\end{aligned}\tag{A.6}$$

$$\begin{aligned}
\omega_t^{0\,3} &= -\underbrace{e^{3\nu}\partial_t e_\nu^0}_{=0} + e^{3\nu}\Gamma^\lambda_{t\,\nu}e^0_\lambda,\\
&= e^{3\,r}\Gamma^t_{t\,r}e^0_t,\\
&= \frac{A'(r)}{B(r)} cos\theta.
\end{aligned}\tag{A.7}$$

$$\begin{aligned}
\omega_\phi^{1\,3} &= -e^{3\nu}\partial_\phi e^1_\nu + e^{3\nu}\Gamma^\lambda_{\phi\,\nu}e^1_\lambda,\\
&= -e^{3r}\partial_\phi e^1_r - e^{3\theta}\partial_\phi e^1_\theta - \underbrace{e^{3\phi}}_{=0}\partial_\phi e^1_\phi\\
&+ e^{3\theta}\Gamma^\phi_{\phi\,\theta}e^1_\phi + e^{3r}\Gamma^\phi_{\phi\,r}e^1_\phi + e^{3\phi}\Gamma^\theta_{\phi\,\phi}e^1_\theta\\
&+ e^{3\phi}\Gamma^r_{\phi\,\phi}e^1_r,\\
&= \left(1 - \frac{1}{B(r)}\right) sin\theta\, cos\theta\, sin\phi.
\end{aligned}\tag{A.8}$$

$$\begin{aligned}
\omega_\theta^{1\,3} &= -e^{3\nu}\partial_\theta e^1_\nu + e^{1\nu}\Gamma^\lambda_{\theta\,\nu}e^1_\lambda,\\
&= -e^{3r}\partial_\theta e^1_r - e^{3\theta}\partial_\theta e^1_\theta - \underbrace{e^{3\phi}}_{=0}\partial_\theta e^1_\phi\\
&+ e^{3r}\Gamma^\theta_{\theta\,r}e^1_\theta + e^{3\theta}\Gamma^r_{\theta\,\theta}e^1_r + \underbrace{e^{3\phi}}_{=0}\Gamma^\phi_{\theta\,\phi}e^1_\phi,\\
&= -\left(1 - \frac{1}{B(r)}\right) cos\phi.
\end{aligned}\tag{A.9}$$

$$\begin{aligned}
\omega_t^{0\,2} &= -\underbrace{e^{2\nu}\partial_t e_\nu^0}_{=0} + e^{2\nu}\Gamma^\lambda_{t\,\nu}e^0_\lambda,\\
&= e^{2\,r}\Gamma^t_{t\,r}e^0_t,\\
&= \frac{A'(r)}{B(r)} sin\theta\, sin\phi.
\end{aligned}\tag{A.10}$$

$$\begin{aligned}
\omega_\phi^{1\,2} &= -e^{2\nu}\partial_\phi e^1_\nu + e^{2\nu}\Gamma^\lambda_{\phi\,\nu}e^1_\lambda,\\
&= -e^{2r}\partial_\phi e^1_r - e^{2\theta}\partial_\phi e^1_\theta - e^{2\phi}\partial_\phi e^1_\phi\\
&+ e^{2\phi}\Gamma^\theta_{\phi\,\phi}e^1_\theta + e^{2\theta}\Gamma^\phi_{\phi\,\theta}e^1_\phi + e^{2r}\Gamma^\phi_{\phi\,r}e^1_\phi\\
&+ e^{2\phi}\Gamma^r_{\phi\,\phi}e^1_r,\\
&= \left(1 - \frac{1}{B(r)}\right) sin\theta^2.
\end{aligned}\tag{A.11}$$

$$\begin{aligned}
\omega_\phi^{2\,3} &= -e^{3\nu}\partial_\phi e^2_\nu + e^{3\nu}\Gamma^\lambda_{\phi\,\nu}e^2_\lambda,\\
&- e^{3r}\partial_\phi e^2_r - e^{3\theta}\partial_\phi e^2_\theta - \underbrace{e^{3\phi}}_{=0}\partial_\phi e^2_\phi\\
&+ e^{3\theta}\Gamma^\phi_{\phi\,\theta}e^2_\phi + e^{3r}\Gamma^\phi_{\phi\,r}e^2_\phi + e^{3\phi}\Gamma^\theta_{\phi\,\phi}e^2_\theta\\
&+ e^{3\phi}\Gamma^r_{\phi\,\phi}e^2_r,\\
&= -\left(1 - \frac{1}{B(r)}\right) sin\theta\, cos\theta\, cos\phi.
\end{aligned}\tag{A.12}$$

$$\begin{aligned}
\omega_\theta^{2\,3} &= -e^{3\nu}\partial_\theta e^2_\nu + e^{3\nu}\Gamma^\lambda_{\theta\,\nu}e^2_\lambda,\\
&= -e^{3r}\partial_\theta e^2_r - e^{3\theta}\partial_\theta e^2_\theta - \underbrace{e^{3\phi}}_{=0}\partial_\theta e^2_\phi\\
&+ e^{3r}\Gamma^\theta_{\theta\,r}e^2_\theta + e^{3\theta}\Gamma^r_{\theta\,\theta}e^2_r + \underbrace{e^{3\phi}}_{=0}\Gamma^\phi_{\theta\,\phi}e^2_\phi,\\
&= -\left(1 - \frac{1}{B(r)}\right) sin\phi.
\end{aligned}\tag{A.13}$$

A.2 CURVATURE TENSOR

In the gauge theory of gravity the curvature tensor $F^{a\,b}_{\mu\,\nu}$ is given by (1.55) in the limit of $\lambda \to 0$:

$$F^{ab}_{\mu\nu} = \partial_\mu\omega^{ab}_\nu - \partial_\nu\omega^{ab}_\mu + \left(\omega^{ac}_\mu\omega^{db}_\nu - \omega^{ac}_\nu\omega^{db}_\mu\right)\eta_{cd} \tag{A.14}$$

using the above components of the spin-connections, we compute the non-zero components of curvature tensor

For $[ab] = [01]$:

$$\begin{align}
F^{01}_{t\,r} &= \underbrace{\partial_t\omega^{01}_r}_{=0} - \partial_r\omega^{01}_t + \left(\omega^{0c}_t \underbrace{\omega^{d1}_r}_{=0} - \underbrace{\omega^{0c}_r}_{=0} \omega^{d1}_t\right)\eta_{cd}, \notag\\
&= -\partial_r\omega^{01}_t = -\left(\frac{A''(r)}{B(r)} - \frac{A'(r)B'(r)}{B(r)^2}\right) sin\theta\, cos\phi. \tag{A.15}\\
F^{01}_{t\,\theta} &= \underbrace{\partial_t\omega^{01}_\theta}_{=0} - \partial_\theta\omega^{01}_t + \left(\omega^{02}_t \underbrace{\omega^{21}_\theta}_{=0} + \omega^{03}_t\omega^{31}_\theta - \underbrace{\omega^{02}_\theta}_{=0} \omega^{21}_t - \omega^{03}_\theta \underbrace{\omega^{31}_t}_{=0}\right), \notag\\
&= -\partial_\theta\omega^{01}_t + \omega^{03}_t\omega^{31}_\theta, \tag{A.16}\\
&= -\frac{A'(r)}{B(r)^2} cos\theta\, cos\phi. \tag{A.17}\\
F^{01}_{t\,\phi} &= \underbrace{\partial_t\omega^{01}_\phi}_{=0} - \partial_\phi\omega^{01}_t + \left(\omega^{02}_t\omega^{21}_\phi + \omega^{03}_t\omega^{31}_\phi - \underbrace{\omega^{02}_\phi}_{=0} \omega^{21}_t - \omega^{03}_\phi \underbrace{\omega^{31}_t}_{=0}\right), \notag\\
&= -\partial_\phi\omega^{01}_t + \omega^{02}_t\omega^{21}_\phi + \omega^{03}_t\omega^{31}_\phi, \notag\\
&= \frac{A'(r)}{B(r)^2} sin\theta\, sin\phi. \tag{A.18}
\end{align}$$

$[ab] = [02]$:

$$\begin{align}
F^{02}_{t\,r} &= \underbrace{\partial_t\omega^{02}_r}_{=0} - \partial_r\omega^{02}_t + \left(\omega^{0c}_t \underbrace{\omega^{d2}_r}_{=0} - \underbrace{\omega^{0c}_r}_{=0} \omega^{d2}_t\right)\eta_{cd}, \notag\\
&= -\partial_r\omega^{02}_t = -\left(\frac{A''(r)}{B(r)} - \frac{A'(r)B'(r)}{B(r)^2}\right) sin\theta\, sin\phi. \tag{A.19}\\
F^{02}_{t\,\theta} &= \underbrace{\partial_t\omega^{02}_\theta}_{=0} - \partial_\theta\omega^{02}_t + \left(\omega^{01}_t \underbrace{\omega^{12}_\theta}_{=0} + \omega^{03}_t\omega^{32}_\theta - \underbrace{\omega^{01}_\theta}_{=0} \omega^{12}_t - \omega^{03}_\theta \underbrace{\omega^{32}_t}_{=0}\right), \notag\\
&= -\partial_\theta\omega^{01}_t + \omega^{03}_t\omega^{32}_\theta, \tag{A.20}\\
&= -\frac{A'(r)}{B(r)^2} cos\theta\, sin\phi. \tag{A.21}\\
F^{02}_{t\,\phi} &= \underbrace{\partial_t\omega^{02}_\phi}_{=0} - \partial_\phi\omega^{02}_t + \left(\omega^{01}_t\omega^{12}_\phi + \omega^{03}_t\omega^{32}_\phi - \underbrace{\omega^{01}_\phi}_{=0} \omega^{12}_t - \omega^{03}_\phi \underbrace{\omega^{32}_t}_{=0}\right), \notag\\
&= -\partial_\phi\omega^{02}_t + \omega^{01}_t\omega^{12}_\phi + \omega^{03}_t\omega^{32}_\phi, \notag\\
&= \frac{A'(r)}{B(r)^2} sin\theta\, cos\phi. \tag{A.22}
\end{align}$$

$[ab] = [03]$:

$$F^{03}_{t\,r} = \underbrace{\partial_t\omega^{03}_r}_{=0} - \partial_r\omega^{03}_t + \left(\omega^{0c}_t \underbrace{\omega^{d3}_r}_{=0} - \underbrace{\omega^{0c}_r}_{=0} \omega^{d2}_t\right)\eta_{cd},$$

$$= -\partial_r \omega_t^{03} = -\left(\frac{A''(r)}{B(r)} - \frac{A'(r)B'(r)}{B(r)^2}\right) cos\theta. \tag{A.23}$$

$$\begin{aligned} F_{t\theta}^{03} &= \underbrace{\partial_t \omega_\theta^{03}}_{=0} - \partial_\theta \omega_t^{03} + \left(\omega_t^{01}\omega_\theta^{13} + \omega_t^{02}\omega_\theta^{23} - \underbrace{\omega_\theta^{01}\omega_t^{13}}_{=0} - \underbrace{\omega_\theta^{02}\omega_t^{23}}_{=0}\right), \\ &= -\partial_\theta \omega_t^{03} + \omega_t^{02}\omega_\theta^{23} + \omega_t^{02}\omega_\theta^{23}, \\ &= \frac{A'(r)}{B(r)^2} sin\theta. \end{aligned} \tag{A.24}$$

$[ab] = [12]$:

$$\begin{aligned} F_{r\phi}^{12} &= \partial_r \omega_\phi^{12} - \underbrace{\partial_\phi \omega_r^{12}}_{=0} + \left(\underbrace{\omega_r^{1c}}_{=0}\omega_\phi^{d2} - \underbrace{\omega_r^{1c}}_{=0}\omega_\phi^{d2}\right)\eta_{cd}, \\ &= \partial_r \omega_\phi^{12} = \frac{B'(r)}{B(r)^2} sin\theta^2. \end{aligned} \tag{A.25}$$

$$\begin{aligned} F_{\theta\phi}^{12} &= \partial_\theta \omega_\phi^{12} - \underbrace{\partial_\phi \omega_\theta^{12}}_{=0} + \left(\underbrace{\omega_\theta^{10}\omega_\phi^{02}}_{=0} + \omega_\theta^{13}\omega_\phi^{32} - \underbrace{\omega_\theta^{10}\omega_\phi^{02}}_{=0} - \omega_\theta^{13}\omega_\phi^{32}\right), \\ &= \partial_\theta \omega_\phi^{12} + \omega_\theta^{13}\omega_\phi^{32} - \omega_\theta^{13}\omega_\phi^{32}, \\ &= \left(1 - \frac{1}{B(r)^2}\right) sin\theta\, cos\theta. \end{aligned} \tag{A.26}$$

$[ab] = [13]$:

$$\begin{aligned} F_{r\theta}^{13} &= \partial_r \omega_\theta^{13} - \underbrace{\partial_\theta \omega_r^{13}}_{=0} + \left(\underbrace{\omega_r^{1c}}_{=0}\omega_\theta^{d3} - \underbrace{\omega_r^{1c}}_{=0}\omega_\theta^{d3}\right)\eta_{cd}, \\ &= \partial_r \omega_\phi^{13} = -\frac{B'(r)}{B(r)^2} cos\phi. \end{aligned} \tag{A.27}$$

$$\begin{aligned} F_{r\phi}^{13} &= \partial_r \omega_\phi^{13} - \underbrace{\partial_\phi \omega_r^{13}}_{=0} + \left(\underbrace{\omega_r^{1c}}_{=0}\omega_\phi^{d3} - \underbrace{\omega_r^{1c}}_{=0}\omega_\phi^{d3}\right)\eta_{cd}, \\ &= \partial_r \omega_\phi^{13} = \frac{B'(r)}{B(r)^2} sin\theta\, cos\theta\, sin\phi. \end{aligned} \tag{A.28}$$

$$\begin{aligned} F_{\theta\phi}^{13} &= \partial_\theta \omega_\phi^{13} - \partial_\phi \omega_\theta^{13} + \left(\underbrace{\omega_\theta^{10}\omega_\phi^{03}}_{=0} + \underbrace{\omega_\theta^{12}\omega_\phi^{23}}_{=0} - \underbrace{\omega_\theta^{10}\omega_\phi^{03}}_{=0} - \omega_\theta^{12}\omega_\phi^{23}\right), \\ &= \partial_\theta \omega_\phi^{13} - \partial_\phi \omega_\theta^{13} - \omega_\theta^{12}\omega_\phi^{23}, \\ &= -\left(1 - \frac{1}{B(r)^2}\right) sin\theta^2\, sin\phi. \end{aligned} \tag{A.29}$$

$[ab] = [23]$:

$$\begin{aligned} F^{23}_{r\,\theta} &= \partial_r \omega^{23}_{\theta} - \underbrace{\partial_{\theta}\omega^{23}_{r}}_{=0} + \left(\underbrace{\omega^{2c}_{r}}_{=0}\, \omega^{d3}_{\theta} - \underbrace{\omega^{2c}_{r}}_{=0}\, \omega^{d3}_{\theta} \right) \eta_{cd}, \\ &= \partial_r \omega^{23}_{\phi} = -\frac{B'(r)}{B(r)^2}\, sin\phi. \end{aligned} \tag{A.30}$$

$$\begin{aligned} F^{23}_{r\,\phi} &= \partial_r \omega^{23}_{\phi} - \underbrace{\partial_{\phi}\omega^{23}_{r}}_{=0} + \left(\underbrace{\omega^{2c}_{r}}_{=0}\, \omega^{d3}_{\phi} - \underbrace{\omega^{2c}_{r}}_{=0}\, \omega^{d3}_{\phi} \right) \eta_{cd}, \\ &= \partial_r \omega^{23}_{\phi} = -\frac{B'(r)}{B(r)^2}\, sin\theta\, cos\theta\, cos\phi. \end{aligned} \tag{A.31}$$

$$\begin{aligned} F^{23}_{\theta\,\phi} &= \partial_{\theta} \omega^{23}_{\phi} - \partial_{\phi}\omega^{23}_{\theta} + \left(\underbrace{\omega^{20}_{\theta}\omega^{03}_{\phi}}_{=0} + \underbrace{\omega^{21}_{\theta}\omega^{13}_{\phi}}_{=0} - \underbrace{\omega^{20}_{\theta}\omega^{03}_{\phi}}_{=0} - \omega^{21}_{\theta}\omega^{13}_{\phi} \right), \\ &= \partial_{\theta} \omega^{23}_{\phi} - \partial_{\phi}\omega^{23}_{\theta} - \omega^{21}_{\theta}\omega^{13}_{\phi}, \\ &= \left(1 - \frac{1}{B(r)^2} \right) sin\theta^2\, cos\phi. \end{aligned} \tag{A.32}$$

A.3 NON-COMMUTATIVE TETRAD FIELDS

The Non-commutative corrections to the tetrad fields (A.3) can be calculated using the SW maps, which is described in the power of Θ up to the second-order by (2.32)

$$\hat{e}^a_{\mu}(x, \Theta) = e^a_{\mu}(x) - i\Theta^{\nu\rho} e^a_{\mu\nu\rho}(x) + \Theta^{\nu\rho}\Theta^{\lambda\tau} e^a_{\mu\nu\rho\lambda\tau}(x) + \mathcal{O}(\Theta^3). \tag{A.33}$$

the first and the second order correction is written as Eq. (2.34) and (2.33)

$$e^a_{\mu\nu\rho} = \frac{1}{4}[\omega^{ac}_{\nu}\partial_{\rho}e^d_{\mu} + (\partial_{\rho}\omega^{ac}_{\mu} + F^{ac}_{\rho\mu})e^d_{\nu}]\eta_{cd} \tag{A.34}$$

$$\begin{aligned} e^a_{\mu\nu\rho\lambda\tau} = \frac{1}{32} \Big[& 2\{F_{\tau\nu}, F_{\mu\rho}\}^{ab} e^c_{\lambda} - \omega^{ab}_{\lambda}(D_{\rho}F^{cd}_{\tau\mu} + \partial_{\rho}F^{cd}_{\tau\mu})e^m_{\nu}\eta_{dm} \\ & - \{\omega_{\nu}, (D_{\rho}F_{\tau\nu} + \partial_{\rho}F_{\tau\nu})\}^{ab} e^c_{\lambda} - \partial_{\tau}\{\omega_{\nu}, (\partial_{\rho}\omega_{\mu} + F_{\rho\mu})\}^{ab} e^c_{\lambda} \\ & - \omega^{ab}_{\lambda} \left(\omega^{cd}_{\nu}\partial_{\rho}e^m_{\mu} + \left(\partial_{\rho}\omega^{cd}_{\mu} + F^{cd}_{\rho\mu} \right) e^m_{\nu} \right) \eta_{dm} + 2\partial_{\nu}\omega^{ab}_{\lambda}\partial_{\rho}\partial_{\tau}e^c_{\lambda} \\ & - 2\partial_{\rho} \left(\partial_{\tau}\omega^{ab}_{\mu} + F^{ab}_{\tau\mu} \right) \partial_{\nu}e^c_{\lambda} - \{\omega_{\nu}, (\partial_{\rho}\omega_{\lambda} + F_{\rho\lambda})\}^{ab} \partial_{\tau}e^c_{\mu} \\ & - \left(\partial_{\tau}\omega_{\mu} + F_{\tau\mu} \right) \left(\omega^{cd}_{\nu}\partial_{\rho}e^m_{\lambda} + \left((\partial_{\rho}\omega_{\lambda} + F_{\rho\lambda}) \right) e^m_{\nu} \right) \eta_{dm} \Big] \eta_{cb} \end{aligned} \tag{A.35}$$

where

$$\{\alpha, \beta\}^{ab} = \left(\alpha^{ac}\beta^{db} + \beta^{ac}\alpha^{db} \right) \eta_{cd}, \quad [\alpha, \beta]^{ab} = \left(\alpha^{ac}\beta^{db} - \beta^{ac}\alpha^{db} \right) \eta_{cd} \tag{A.36}$$

$$D_{\mu}F^{ab}_{\rho\sigma} = \partial_{\mu}F^{ab}_{\rho\sigma} + \left(\omega^{ac}_{\mu}F^{db}_{\rho\sigma} + \omega^{bc}_{\mu}F^{da}_{\rho\sigma} \right) \eta_{cd} \tag{A.37}$$

In our calculation we take only space-space noncommutativity, so that the parameters $\Theta^{\mu\nu}$:

$$\Theta^{\mu\nu} = \begin{pmatrix} 0 & 0 & 0 & 0 \\ 0 & 0 & 0 & \Theta \\ 0 & 0 & 0 & 0 \\ 0 & -\Theta & 0 & 0 \end{pmatrix}, \quad \mu,\nu = 0,1,2,3. \tag{A.38}$$

The non-zero components of the deformed tetrad field are computed as follows:

For $\hat{e}^0_t$:

$$\begin{aligned} \hat{e}^0_t &= e^0_t - i\Theta^{\nu\rho}e^0_{t\nu\rho} + \Theta^{\nu\rho}\Theta^{\lambda\tau}e^0_{t\nu\rho\lambda\tau} + \mathcal{O}(\Theta^3), \\ &= e^0_t - i\left[\Theta^{r\phi}e^0_{tr\phi} + \Theta^{\phi r}e^0_{t\phi r}\right] + \left[\Theta^{r\phi}\Theta^{r\phi}e^0_{tr\phi r\phi} + \Theta^{r\phi}\Theta^{\phi r}e^0_{tr\phi\phi r}\right. \\ &\quad \left. + \Theta^{\phi r}\Theta^{r\phi}e^0_{t\phi rr\phi} + \Theta^{\phi r}\Theta^{\phi r}e^0_{t\phi r\phi r}\right] + \mathcal{O}(\Theta^3), \\ &= e^0_t - i\Theta\left[\underbrace{e^0_{tr\phi}}_{=0} - \underbrace{e^0_{t\phi r}}_{=0}\right] + \Theta^2\left[e^0_{tr\phi r\phi} - e^0_{tr\phi\phi r} - e^0_{t\phi rr\phi} + e^0_{t\phi r\phi r}\right] + \mathcal{O}(\Theta^3). \end{aligned} \tag{A.39}$$

the non-zero components of the second order are:

$$\begin{aligned} e^0_{tr\phi r\phi} &= \frac{1}{32}\left(2\left\{F_{\phi r}, F_{t\phi}\right\}^{ab} e^c_r - 2\partial_\phi\left(\partial_\phi\omega^{0b}_t + F^{0b}_{\phi t}\right)\partial_r e^c_r - \left(\partial_\phi\omega^{0b}_t + F^{0b}_{\phi t}\right)F^{cd}_{\phi r}e^m_\nu\eta_{dm}\right)\eta_{bc}, \\ &= \frac{1}{32}\left(\frac{A'(r)B'(r)(-3+2B(r)^2+B(r))}{B(r)^3}\right) sin^2\theta, \end{aligned} \tag{A.40a}$$

the same steps to computing the other components, then we find:

$$\begin{aligned} e^0_{t\phi r\phi r} &= \frac{1}{16}\left(\frac{8rA'(r)B'(r)^2 - B(r)(8rB'(r)A''(r) + A''(r)(B'(r) + 2rB''(r)))}{B(r)^4}\right. \\ &\quad \left. + \frac{B(r)^2(A'(r)B'(r) + A''(r) + 2rA'''(r)) - B(r)^3A''(r)}{B(r)^4}\right) sin^2\theta, \end{aligned} \tag{A.40b}$$

$$e^0_{t\phi rr\phi} = \frac{1}{32}\left(\frac{A'(r)B'(r)(-3+2B(r)^2+B(r)) - 2B(r)A''(r)(1+B(r))}{B(r)^3}\right) sin^2\theta, \tag{A.40c}$$

$$e^0_{tr\phi\phi r} = \frac{1}{8}\left(\frac{A'(r)B'(r) - B(r)A''(r)}{B(r)^2}\right) sin^2\theta. \tag{A.40d}$$

Substituting now the above component into the Eq. (A.39), we obtain the first deformed tetrad field

$$\begin{aligned} \hat{e}^0_t = A(r) + \frac{\Theta^2 sin^2\theta}{32B^4(r)} &\{-4B(r)(4rB'(r)A''(r) + A'(r)(2B'(r) + rB''(r))) + 16rA'(r)B'^2(r) \\ &+ B^3(r)(A'(r)B'(r) + 4A''(r)) + B^2(r)(-3A'(r)B'(r) + 4(A''(r) + rA'''(r)))\}, \end{aligned} \tag{A.41a}$$

In the similar way, we find the other non-zero deformed components

$$
\begin{aligned}
\hat{e}^1_1 = {} & B(r)sin\theta cos\phi + \frac{i\Theta}{4}B'(r)sin\theta sin\phi + \frac{\Theta^2}{64B^3(r)}\{8(2B'(r) - B(r)B''(r))sin^2\theta \\
& + B^3(r)B''(r)(3 + cos2\theta) + B(r)(B'^2(r) - B(r)B''(r))(1 + 3cos2\theta)\}\, sin\theta cos\phi,
\end{aligned} \tag{A.41b}
$$

$$
\begin{aligned}
\hat{e}^2_1 = {} & B(r)sin\theta sin\phi - \frac{i\Theta}{4}B'(r)sin\theta cos\phi + \frac{\Theta^2}{64B^3(r)}\{8(2B'(r) - B(r)B''(r))sin^2\theta \\
& + B^3(r)B''(r)(3 + cos2\theta) + B(r)(B'^2(r) - B(r)B''(r))(1 + 3cos2\theta)\}\, sin\theta sin\phi,
\end{aligned} \tag{A.41c}
$$

$$
\begin{aligned}
\hat{e}^3_1 = {} & \frac{\Theta^2 sin^2\theta}{32B^3(r)}\{(8 - 3B(r))B'^2(r) - B(r)B''(r)(4 + (-3 + B(r))B(r))\}\, cos\theta \\
& + B(r)cos\theta,
\end{aligned} \tag{A.41d}
$$

$$
\begin{aligned}
\hat{e}^1_2 = {} & rcos\theta cos\phi - \frac{i\Theta}{4}[B(r) - 1]\, cos\theta sin\phi + \frac{\Theta^2}{32B^4(r)}\Big\{B^4(r)B'(r)(-3 + cos2\theta) \\
& + sin^2\theta\left[16rB'^2(r) - B^2(r)(B'(r) - 4rB''(r)) - 4B(r)(2B'(r) + 2rB'^2(r) + rB''(r))\right] \\
& - \frac{1}{2}B^3(r)B'(r)(-9 + 5cos2\theta)\Big\}\, cos\theta cos\phi,
\end{aligned} \tag{A.41e}
$$

$$
\begin{aligned}
\hat{e}^2_2 = {} & rcos\theta sin\phi + \frac{i\Theta}{4}[B(r) - 1]\, cos\theta cos\phi + \frac{\Theta^2}{32B^4(r)}\Big\{B^4(r)B'(r)(-3 + cos(2\theta)) \\
& + sin^2\theta\left[16rB'^2(r) - B^2(r)(B'(r) - 4rB''(r)) - 4B(r)(2B'(r) + 2rB'^2(r) + rB''(r))\right] \\
& - \frac{1}{2}B^3(r)B'(r)(-9 + 5cos(2\theta))\Big\}\, cos\theta sin\phi,
\end{aligned} \tag{A.41f}
$$

$$
\begin{aligned}
\hat{e}^3_2 = {} & -rsin\theta + \frac{\Theta^2 sin\theta}{64B^4(r)}\{sin^2\theta\left[4B(r)B'(r)(4 + B^3(r)) - 32rB'^2(r) + 8rB(r)B''(r)\right] \\
& + B^2(r)B'(r)(5 - B(r) + (-1 + 5B(r))cos(2\theta)) + 8rB(r)(B(r)B''(r) - 2B'^2(r))cos^2\theta\},
\end{aligned} \tag{A.41g}
$$

$$
\begin{aligned}
\hat{e}^1_3 = {} & -rsin\theta sin\phi - \frac{i\Theta}{4}\left[(B(r) - 1)\, cos^2\theta - ((1 - \frac{1}{B(r)}) + 2\frac{B'(r)}{B^2(r)}r)sin^2\theta\right] sin\theta cos\phi \\
& + \frac{\Theta^2}{32B^4(r)}\{[+3B^2(r)B'(r) + 36rB'^2(r) + 8rB^2(r)B''(r) - B(r)(7B'(r) + 16rB'^2(r) \\
& + 12rB''(r))]sin^2\theta + 2B^3(r)B'(r) - 2B^4(r)B'(r)cos^2\theta\Big\}\, (-sin\theta sin\phi),
\end{aligned} \tag{A.41h}
$$

$$
\begin{aligned}
\hat{e}^2_3 = {} & rsin\theta cos\phi + \frac{i\Theta}{4}\left[(B(r) - 1)\, cos^2\theta - ((1 - \frac{1}{B(r)}) + 2\frac{B'(r)}{B^2(r)}r)sin^2\theta\right] (-sin\theta sin\phi) \\
& + \frac{\Theta^2}{32B^4(r)}\{[+3B^2(r)B'(r) + 36rB'^2(r) + 8rB^2(r)B''(r) - B(r)(7B'(r) + 16rB'^2(r) \\
& + 12rB''(r))]sin^2\theta + 2B^3(r)B'(r) - 2B^4(r)B'(r)cos^2\theta\Big\}\, (sin\theta cos\phi),
\end{aligned} \tag{A.41i}
$$

$$
\hat{e}^3_3 = \frac{i\Theta}{4B(r)^2}\left[(-B(r) + B(r)^3 + 2rB'(r))\right] sin^2\theta cos\theta. \tag{A.41j}
$$

B

ENERGY AND ANGULAR MOMENTUM OF THE CIRCULAR ORBIT AROUND NC RN BH

B.1 UNCHARGED MASSIVE TEST PARTICLE

We provide here the full expressions for the energy and the angular momentum of circular orbits for a uncharged massive test particle, in the second-order in Θ:

$$E_c^2 \simeq \frac{(Q^2 - 2mr_c + r_c^2)^2}{r_c^2(2Q^2 - 3mr_c + r_c^2)} + \left(\frac{\mathcal{X}(r_c) + \mathcal{G}(r_c)\sqrt{1 - \frac{2m}{r_c} + \frac{Q^2}{r_c}}}{32 r_c^6 (2Q^2 - 3mr_c + r_c^2)^2 \sqrt{1 - \frac{2m}{r_c} + \frac{Q^2}{r_c}}} \right) \Theta^2 + \mathcal{O}(\Theta^4), \tag{B.1a}$$

$$L_c^2 \simeq \frac{(mr_c^3 - Q^2 r_c^2)}{2Q^2 - 3mr_c + r_c^2} - \left(\frac{\mathcal{W}(r_c) + \mathcal{V}(r_c)\sqrt{1 - \frac{2m}{r_c} + \frac{Q^2}{r_c^2}}}{32 r_c^2 \mathcal{V}_0^2 (Q^2 + r_c(-2m + r_c)) \sqrt{1 - \frac{2m}{r_c} + \frac{Q^2}{r_c^2}}} \right) \Theta^2 + \mathcal{O}(\Theta^4). \tag{B.1b}$$

with

$$\begin{aligned} \mathcal{X}(r_c) &= 44Q^8 - 259mQ^6 r_c + 537m^2Q^4r_c^2 + 102Q^6r_c^2 - 426m^3Q^2r_c^3 - 424mQ^4r_c^3 + 120m^4r_c^4 \\ &\quad + 436m^2Q^2r_c^4 + 94Q^4r_c^4 - 162m^3r_c^5 - 117mQ^2r_c^5 + 71m^2r_c^6 - 12Q^2r_c^6 - 4mr^7, \qquad \text{(B.2a)} \\ \mathcal{G}(r_c) &= -120Q^8 + 541mQ^6r_c - 833m^2Q^4r_c^2 - 106Q^6r_c^2 + 568m^3Q^2r_c^3 + 180mQ^4r_c^3 + 4mr_c^7 \\ &\quad - 204m^4r_c^4 - 96m^2Q^2r_c^4 + 76Q^4r_c^4 + 174m^3r_c^5 - 195mQ^2r_c^5 - 41m^2r_c^6 + 52Q^2r_c^6, \qquad \text{(B.2b)} \\ \mathcal{W}(r_c) &= -44Q^8 + 251mQ^6r_c - 453m^2Q^4r_c^2 - 142Q^6r_c^2 + 270m^3Q^2r_c^3 + 480mQ^4r_c^3 \\ &\quad - 48m^4r_c^4 - 392m^2Q^2r_c^4 - 90Q^4r_c^4 + 126m^3r_c^5 + 73mQ^2r_c^5 - 55m^2r_c^6 + 24Q^2r_c^6, \qquad \text{(B.2c)} \\ \mathcal{V}(r_c) &= 16Q^8 + 123mQ^6r_c - 629m^2Q^4r_c^2 - 166Q^6r_c^2 + 698m^3Q^2r_c^3 + 944mQ^4r_c^3 \\ &\quad - 120m^4r_c^4 - 1224m^2Q^2r_c^4 - 290Q^4r_c^4 + 174m^3r_c^5 + 645mQ^2r_c^5 - 75m^2r_c^6 \\ &\quad - 104Q^2r_c^6 + 8mr_c^7. \qquad \text{(B.2d)} \\ \mathcal{V}_0(r_c) &= 2Q^2 - 3mr_c + r_c^2. \qquad \text{(B.2e)} \end{aligned}$$

B.2 CHARGED MASSIVE TEST PARTICLE

For convenience, we provide here the full expressions for the energy and the angular momentum of circular orbits for a charged massive test particle, in the second-order in Θ

$$
\begin{aligned}
E_c^2 \simeq{}& \frac{1}{r_c^2}\left(-qQ + r\sqrt{\frac{\left(1-\frac{2m}{r_c}+\frac{Q^2}{r_c^2}\right)\mathcal{V}_1(r_c)}{\mathcal{V}_2(r_c)}}\right)^2 + \left(qQ - r\sqrt{\frac{\left(1-\frac{2m}{r_c}+\frac{Q^2}{r_c^2}\right)\mathcal{V}_1(r_c)}{\mathcal{V}_2(r_c)}}\right) \\
&\times \sqrt{\frac{\left(1-\frac{2m}{r_c}+\frac{Q^2}{r_c^2}\right)\mathcal{V}_1(r_c)}{\mathcal{V}_2(r_c)}}\left(\frac{\mathcal{X}_1(r_c)+\mathcal{G}_1(r_c)\sqrt{1-\frac{2m}{r_c}+\frac{Q^2}{r_c}}}{16r_c^6(Q^2-2mr_c+r_c^2)\mathcal{V}_1(r_c)\mathcal{V}_2(r_c)}\right)\Theta^2 + \mathcal{O}(\Theta^4), \qquad \text{(B.3a)}\\
L_c^2 \simeq{}& -\frac{2r_c^2\left(2Q^2-mr_c+qQr\sqrt{1-\frac{2m}{r_c}+\frac{Q^2}{r_c^2}}\right)}{\mathcal{V}_2(r_c)} \\
&+\left(\frac{\mathcal{X}_2(r_c)+\mathcal{G}_2(r_c)\sqrt{1-\frac{2m}{r_c}+\frac{Q^2}{r_c^2}}}{16r_c^3(Q^2-2mr_c+r_c^2)\mathcal{V}_(r_c)^2\sqrt{1-\frac{2m}{r_c}+\frac{Q^2}{r_c^2}}}\right)\Theta^2+\mathcal{O}(\Theta^4). \qquad \text{(B.3b)}
\end{aligned}
$$

where:

$$
\mathcal{V}_1(r_c) = 2Q^2 - 4mr_c + 2r_c^2 - qQr\sqrt{1-\frac{2m}{r_c}+\frac{Q^2}{r_c^2}}, \qquad \text{(B.4a)}
$$

$$
\mathcal{V}_2(r_c) = 4Q^2 - 6mr_c + 2r_c^2 + qQr\sqrt{1-\frac{2m}{r_c}+\frac{Q^2}{r_c^2}}, \qquad \text{(B.4b)}
$$

$$
\begin{aligned}
\mathcal{X}_1(r_c) ={}& -88Q^8r_c + 518mQ^6r_c^2 - 1074m^2Q^4r_c^3 - 204Q^6r_c^3 + 852m^3Q^2r_c^4 + 848mQ^4r_c^4 \\
&- 240m^4r_c^5 - 872m^2Q^2r_c^5 - 188Q^4r_c^5 + 324m^3r_c^6 + 234mQ^2r_c^6 - 142m^2r_c^7 + 24Q^2r_c \\
&+ 8mr_c^8 + q\,(520Q^9 - 3298mQ^7r_c + 7304m^2Q^5r_c^2 + 1591Q^7r_c^2 - 6380m^3Q^3r^3 \\
&-6885mQ^5r^3 + 1608m^4Qr_c^4 + 8703m^2Q^3r_c^4 + 1596Q^5r_c^4 - 2699m^3Qr_c^5 + 40Qr_c^8 \\
&-3872mQ^3r_c^5 + 1634m^2Qr_c^6 + 560Q^3r_c^6 - 422mQr^7) \\
&+ q^2\left(11Q^8r_c - 52mQ^6r_c^2 + 75m^2Q^4r_c^3 + 23Q^6r_c^3 - 30m^3Q^2r_c^4 - 62mQ^4r_c^4\right. \\
&\left.+31m^2Q^2r_c^5 + 12Q^4r_c^5 - 8mQ^2r_c^6\right), \qquad \text{(B.4c)}
\end{aligned}
$$

$$
\begin{aligned}
\mathcal{G}_1(r_c) ={}& 240Q^8r_c - 1082mQ^6r_c^2 + 1666m^2Q^4r_c^3 + 212Q^6r_c^3 - 1136m^3Q^2r_c^4 - 360mQ^4r_c^4 \\
&+ 408m^4r_c^5 + 192m^2Q^2r_c^5 - 152Q^4r_c^5 - 348m^3r_c^6 + 390mQ^2r_c^6 + 82m^2r_c^7 - 104Q^2r_c^7 \\
&- 8mr_c^8 + q\left(-110Q^7r_c^2 + 576mQ^5r_c^3 - 912m^2Q^3r_c^4 + 300m^3Qr_c^5 + 1034mQ^3r_c^5\right. \\
&\left.-310Q^5r_c^4 - 456m^2Qr_c^6 - 324Q^3r_c^6 + 226mQr_c^7 - 24Qr_c^8\right) + q^2\,(-56Q^8r_c \\
&+232mQ^6r_c^2 - 93Q^6r_c^3 + 88m^3Q^2r_c^4 + 210mQ^4r_c^4 - 77m^2Q^2r_c^5 - 36Q^4r_c^5 \\
&+16mQ^2r_c^6)\,. \qquad \text{(B.4d)}
\end{aligned}
$$

$$
\mathcal{X}_2(r_c) = 88Q^8r_c - 502mQ^6r_c^2 + 906m^2Q^4r_c^3 + 284Q^6r_c^3 - 540m^3Q^2r_c^4 - 960mQ^4r_c^4
$$

$$
\begin{aligned}
&+ 96m^4r_c^5 + 784m^2Q^2r_c^5 + 180Q^4r_c^5 - 252m^3r_c^6 - 146m^3r_c^6 + 110m^2r_c^7 + 48Q^2r_c^7 \\
&+ q\,(-932Q^9 + 5644mQ^7r_c - 12066m^2Q^5r_c^2 - 2577Q^7r_c^2 + 10380m^3Q^3r_c^3 - 80Qr_c^8 \\
&+5970mQ^3r_c^5 - 2736m^4Qr_c^4 - 13725m^2Q^3r_c^4 - 2420Q^5r_c^4 + 4637m^3Qr_c^5 - 852Q^3r_c^6 \\
&+10863mQ^5r_c^3 - 2896m^2Qr_c^6 + 790mQr_c^7) \\
&+ q^2\left(22Q^2r_c - 122mQ^6r_c^2 + 192m^2Q^4r_c^3 + 88Q^6r_c^3 - 72m^3Q^2r_c^4 - 268mQ^4r_c^4\right. \\
&\left.+152m^2Q^2r_c^5 + 78Q^4r_c^5 - 82mQ^2r_c^6 + 12Q^2r_c^7\right). \qquad \text{(B.4e)}
\end{aligned}
$$

$$
\begin{aligned}
\mathcal{G}_2(r_c) = &-32Q^8r_c - 246mQ^6r_c^2 + 1258m^2Q^4r_c^3 + 332Q^6r_c^3 - 1396m^3Q^2r_c^4 + 240m^4r_c^5 \\
&- 1888mQ^4r_c^4 + 2448m^2Q^2r_c^5 + 580Q^4r_c^5 - 348m^3r_c^6 - 1290mQ^2r_c^6 + 150m^2r_c^7 \\
&+ 208Q^2r_c^7 - 16mr_c^8 + q\left(242Q^7r_c^2 - 1202mQ^5r_c^3 + 1728m^2Q^3r_c^4 + 708Q^5r_c^4\right. \\
&\left.-582m^3Qr_c^5 - 1982mQ^3r_c^5 + 950m^2Qr_c^6 + 516Q^3r_c^6 - 426mQr_c^7 + 48Qr_c^8\right) \\
&+ q^2\left(-60Q^8r_c + 270mQ^6r_c^2 - 368m^2Q^4r_c^3 - 136Q^6r_c^3 + 136m^3Q^2r_c^4 - 96Q^4r_c^5\right. \\
&\left.+376mQ^4r_c^4 - 216m^2Q^2r_c^5 + 114mQ^2r_c^6 - 20Q^2r_c^7\right). \qquad \text{(B.4f)}
\end{aligned}
$$

BIBLIOGRAPHY

[1] S. Weinberg, *Gravitation and Cosmology: Principles and Applications of the General Theory of Relativity*. New York: Wiley, 1972.

[2] B. P. Abbott, R. Abbott, T. Abbott, M. Abernathy, F. Acernese, K. Ackley, C. Adams, T. Adams, P. Addesso, R. Adhikari, *et al.*, "Observation of gravitational waves from a binary black hole merger", *Physical review letters*, vol. 116, no. 6, p. 061 102, 2016.

[3] E. H. T. Collaboration *et al.*, "First m87 event horizon telescope results. i. the shadow of the supermassive black hole", *arXiv preprint arXiv:1906.11238*, 2019.

[4] A. Eckart, R. Genzel, T. Ott, and R. Schödel, "Stellar orbits near sagittarius a*", *Monthly Notices of the Royal Astronomical Society*, vol. 331, no. 4, pp. 917–934, Apr. 2002, ISSN: 0035-8711. DOI: `10.1046/j.1365-8711.2002.05237.x`. eprint: `https://academic.oup.com/mnras/article-pdf/331/4/917/3792378/331-4-917.pdf`. [Online]. Available: `https://doi.org/10.1046/j.1365-8711.2002.05237.x`.

[5] S Gillessen, F. Eisenhauer, T. Fritz, H Bartko, K Dodds-Eden, O Pfuhl, T Ott, and R Genzel, "The orbit of the star s2 around sgr a* from very large telescope and keck data", *The Astrophysical Journal*, vol. 707, no. 2, p. L114, 2009.

[6] R. Gainutdinov, "Ppn motion of s-stars around sgr a*", *Astrophysics*, vol. 63, no. 4, pp. 470–481, 2020.

[7] F. Peißker, A. Eckart, M. Zajaček, B. Ali, and M. Parsa, "S62 and s4711: Indications of a population of faint fast-moving stars inside the s2 orbit—s4711 on a 7.6 yr orbit around sgr a*", *The Astrophysical Journal*, vol. 899, no. 1, p. 50, 2020.

[8] C. Subrahmanyan, *Mathematical Theory of Black Holes*. Oxford University Press, 1999.

[9] G. Gibbons, C. Warnick, and M. Werner, "Light bending in schwarzschild–de sitter: Projective geometry of the optical metric", *Classical and Quantum Gravity*, vol. 25, no. 24, p. 245 009, 2008.

[10] J. Islam, "The cosmological constant and classical tests of general relativity", *Physics Letters A*, vol. 97, no. 6, pp. 239–241, 1983.

[11] M. Jaklitsch, C. Hellaby, and D. Matravers, "Particle motion in the spherically symmetric vacuum solution with positive cosmological constant", *General relativity and gravitation*, vol. 21, no. 9, pp. 941–951, 1989.

[12] Z. Stuchlik and M. Calvani, "Null geodesics in black hole metrics with non-zero cosmological constant", *General Relativity and Gravitation*, vol. 23, no. 5, pp. 507–519, 1991.

[13] G. Kraniotis and S. Whitehouse, "Compact calculation of the perihelion precession of mercury in general relativity, the cosmological constant and jacobi's inversion problem", *Classical and Quantum Gravity*, vol. 20, no. 22, p. 4817, 2003.

[14] G. Kraniotis, "Precise relativistic orbits in kerr and kerr–(anti) de sitter spacetimes", *Classical and Quantum Gravity*, vol. 21, no. 19, p. 4743, 2004.

[15] N. Cruz, M. Olivares, and J. R. Villanueva, "The geodesic structure of the schwarzschild anti-de sitter black hole", *Classical and Quantum Gravity*, vol. 22, no. 6, p. 1167, 2005.

[16] E. Hackmann, V. Kagramanova, J. Kunz, and C. Lämmerzahl, "Analytic solutions of the geodesic equation in higher dimensional static spherically symmetric spacetimes", *Physical Review D*, vol. 78, no. 12, p. 124 018, 2008.

[17] V. Kagramanova, J. Kunz, E. Hackmann, and C. Lämmerzahl, "Analytic treatment of complete and incomplete geodesics in taub-nut space-times", *Physical Review D*, vol. 81, no. 12, p. 124 044, 2010.

[18] E. Hackmann, C. Lämmerzahl, V. Kagramanova, and J. Kunz, "Analytical solution of the geodesic equation in kerr-(anti-) de sitter space-times", *Physical Review D*, vol. 81, no. 4, p. 044 020, 2010.

[19] E. Hackmann, V Kagramanova, J Kunz, and C Lämmerzahl, "Analytic solutions of the geodesic equation in axially symmetric space-times", *EPL (Europhysics Letters)*, vol. 88, no. 3, p. 30 008, 2009.

[20] J. Levin and G. Perez-Giz, "A periodic table for black hole orbits", *Physical Review D*, vol. 77, no. 10, p. 103 005, 2008.

[21] S. Grunau and V. Kagramanova, "Geodesics of electrically and magnetically charged test particles in the reissner-nordström space-time: Analytical solutions", *Physical Review D*, vol. 83, no. 4, p. 044 009, 2011.

[22] E. Belbruno and F. Pretorius, "A dynamical system's approach to schwarzschild null geodesics", *Classical and Quantum Gravity*, vol. 28, no. 19, p. 195 007, 2011.

[23] L. Barack and N. Sago, "Beyond the geodesic approximation: Conservative effects of the gravitational self-force in eccentric orbits around a schwarzschild black hole", *Physical Review D*, vol. 83, no. 8, p. 084 023, 2011.

[24] D. Pugliese, H. Quevedo, and R. Ruffini, "Circular motion of neutral test particles in reissner-nordström spacetime", *Physical Review D*, vol. 83, no. 2, p. 024 021, 2011.

[25] ——, "Circular motion in reissner–nordstrÖm spacetime", in *The Twelfth Marcel Grossmann Meeting: On Recent Developments in Theoretical and Experimental General Relativity, Astrophysics and Relativistic Field Theories (In 3 Volumes)*, World Scientific, 2012, pp. 1017–1021.

[26] K. S. Virbhadra and G. F. Ellis, "Gravitational lensing by naked singularities", *Physical Review D*, vol. 65, no. 10, p. 103 004, 2002.

[27] K. Virbhadra and C. Keeton, "Time delay and magnification centroid due to gravitational lensing by black holes and naked singularities", *Physical Review D*, vol. 77, no. 12, p. 124 014, 2008.

[28] P. Pradhan and P. Majumdar, "Circular orbits in extremal reissner–nordstrom spacetime", *Physics Letters A*, vol. 375, no. 3, pp. 474–479, 2011.

[29] M. Olivares, J. Saavedra, C. Leiva, and J. R. Villanueva, "Motion of charged particles on the reissner–nordström (anti)-de sitter black hole spacetime", *Modern Physics Letters A*, vol. 26, no. 39, pp. 2923–2950, 2011.

[30] J. Villanueva, J. Saavedra, M. Olivares, and N. Cruz, "Photons motion in charged anti-de sitter black holes", *Astrophysics and Space Science*, vol. 344, no. 2, pp. 437–446, 2013.

[31] D. Pugliese, H. Quevedo, and R. Ruffini, "Motion of charged test particles in reissner-nordström spacetime", *Physical Review D*, vol. 83, no. 10, p. 104 052, 2011.

[32] ——, "General classification of charged test particle circular orbits in reissner–nordström spacetime", *The European Physical Journal C*, vol. 77, no. 4, pp. 1–18, 2017.

[33] A. M. Lyapunov, "The general problem of the stability of motion", *International journal of control*, vol. 55, no. 3, pp. 531–534, 1992.

[34] N. J. Cornish and J. Levin, "Lyapunov timescales and black hole binaries", *Classical and Quantum Gravity*, vol. 20, no. 9, p. 1649, 2003.

[35] F. Pretorius and D. Khurana, "Black hole mergers and unstable circular orbits", *Classical and Quantum Gravity*, vol. 24, no. 12, S83, 2007.

[36] V. Cardoso, A. S. Miranda, E. Berti, H. Witek, and V. T. Zanchin, "Geodesic stability, lyapunov exponents, and quasinormal modes", *Physical Review D*, vol. 79, no. 6, p. 064 016, 2009.

[37] M. Setare and D Momeni, "Geodesic stability for kehagias-sfetsos black hole in hořava-lifshitz gravity via lyapunov exponents", *International Journal of Theoretical Physics*, vol. 50, pp. 106–113, 2011.

[38] S. Fernando, "Schwarzschild black hole surrounded by quintessence: Null geodesics", *General Relativity and Gravitation*, vol. 44, pp. 1857–1879, 2012.

[39] B Malakolkalami and K Ghaderi, "Schwarzschild-anti de sitter black hole with quintessence", *Astrophysics and Space Science*, vol. 357, no. 2, p. 112, 2015.

[40] P. Pradhan, "Stability analysis and quasinormal modes of reissner–nordstrøm space-time via lyapunov exponent", *Pramana*, vol. 87, pp. 1–9, 2016.

[41] K Ghaderi, "Geodesics of black holes with dark energy", *Astrophysics and Space Science*, vol. 362, no. 12, p. 218, 2017.

[42] M. Mondal, P. Pradhan, F. Rahaman, and I. Karar, "Geodesic stability and quasi normal modes via lyapunov exponent for hayward black hole", *Modern Physics Letters A*, vol. 35, no. 30, p. 2 050 249, 2020.

[43] S. Giri and H. Nandan, "Stability analysis of geodesics and quasinormal modes of a dual stringy black hole via lyapunov exponents", *General Relativity and Gravitation*, vol. 53, no. 8, p. 76, 2021.

[44] M. Mondal, F. Rahaman, and K. N. Singh, "Lyapunov exponent, isco and kolmogorov–senai entropy for kerr–kiselev black hole", *The European Physical Journal C*, vol. 81, pp. 1–16, 2021.

[45] D. Lüst and S. Theisen, *Lectures on string theory*. Springer, 1989, vol. 346.

[46] R. Blumenhagen, D. Lüst, and S. Theisen, *Basic concepts of string theory*. Springer, 2013, vol. 17.

[47] C. Rovelli, *Quantum gravity*. Cambridge university press, 2004.

[48] ——, "Loop quantum gravity", *Living reviews in relativity*, vol. 11, no. 1, pp. 1–69, 2008.

[49] D. Z. Freedman and P Van Nieuwenhuizen, “Properties of supergravity theory”, *Physical Review D*, vol. 14, no. 4, p. 912, 1976.

[50] S. D. Deser and B. Zumino, “Consistent supergravity”, *Phys. Lett. B*, vol. 62, no. CERN-TH-2164, pp. 335–337, 1976.

[51] D. Z. Freedman, P. v. Nieuwenhuizen, and S. Ferrara, “Progress toward a theory of supergravity”, in *Supergravities in Diverse Dimensions: Commentary and Reprints (In 2 Volumes)*, World Scientific, 1989, pp. 512–516.

[52] P. van Nieuwenhuizen, “Supergravity”, *Physics Reports*, vol. 68, no. 4, pp. 189–398, 1981, ISSN: 0370-1573. DOI: `https://doi.org/10.1016/0370-1573(81)90157-5`. [Online]. Available: `https://www.sciencedirect.com/science/article/pii/0370157381901575`.

[53] S. W. Hawking, “Particle creation by black holes”, in *Euclidean quantum gravity*, World Scientific, 1975, pp. 167–188.

[54] R. Utiyama, “Invariant theoretical interpretation of interaction”, *Physical Review*, vol. 101, no. 5, p. 1597, 1956.

[55] T. W. Kibble, “Lorentz invariance and the gravitational field”, *Journal of mathematical physics*, vol. 2, no. 2, pp. 212–221, 1961.

[56] T. Eguchi, P. B. Gilkey, and A. J. Hanson, “Gravitation, gauge theories and differential geometry”, *Physics reports*, vol. 66, no. 6, pp. 213–393, 1980.

[57] F. W. Hehl, J. D. McCrea, E. W. Mielke, and Y. Ne’eman, “Metric-affine gauge theory of gravity: Field equations, noether identities, world spinors, and breaking of dilation invariance”, *Physics Reports*, vol. 258, no. 1-2, pp. 1–171, 1995.

[58] M. Blagojevic, *Gravitation and gauge symmetries*. CRC Press, 2001.

[59] G Zet and V Manta, “Self-dual poincaré gauge theory of gravitation”, *International Journal of Modern Physics C*, vol. 13, no. 04, pp. 509–516, 2002.

[60] G Zet, V Manta, and S Babeti, “Desitter gauge theory of gravitation”, *International Journal of Modern Physics C*, vol. 14, no. 01, pp. 41–48, 2003.

[61] G Zet, C. Oprisan, and S Babeti, “Solutions without singularities in gauge theory of gravitation”, *International Journal of Modern Physics C*, vol. 15, no. 07, pp. 1031–1038, 2004.

[62] G. W. Gibbons and S. W. Hawking, “Cosmological event horizons, thermodynamics, and particle creation”, *Phys. Rev. D*, vol. 15, pp. 2738–2751, 10 May 1977. DOI: `10.1103/PhysRevD.15.2738`. [Online]. Available: `https://link.aps.org/doi/10.1103/PhysRevD.15.2738`.

[63] J. M. Bardeen, B. Carter, and S. W. Hawking, “The four laws of black hole mechanics”, *Communications in mathematical physics*, vol. 31, pp. 161–170, 1973.

[64] B Harms and Y Leblanc, “Statistical mechanics of black holes”, *Physical Review D*, vol. 46, no. 6, p. 2334, 1992.

[65] C. Vaz, “Canonical quantization and the statistical entropy of the schwarzschild black hole”, *Physical Review D*, vol. 61, no. 6, p. 064 017, 2000.

[66] I. Haranas and I. Gkigkitzis, “Entropic gravity resulting from a yukawa type of correction to the metric for a solar mass black hole”, *Astrophysics and Space Science*, vol. 347, no. 1, pp. 77–82, 2013.

[67] D. Hansen, D. Kubizňák, and R. B. Mann, “Criticality and surface tension in rotating horizon thermodynamics”, *Classical and Quantum Gravity*, vol. 33, no. 16, p. 165 005, 2016.

[68] A. Jawad and A. Khawer, “Thermodynamic consequences of well-known regular black holes under modified first law”, *The European Physical Journal C*, vol. 78, no. 10, pp. 1–10, 2018.

[69] D. Chen, J. Tao, *et al.*, “The modified first laws of thermodynamics of anti-de sitter and de sitter space–times”, *Nuclear Physics B*, vol. 918, pp. 115–128, 2017.

[70] J. W. York Jr, “Black-hole thermodynamics and the euclidean einstein action”, *Physical Review D*, vol. 33, no. 8, p. 2092, 1986.

[71] M. Akbar and S. Das, “Entropy corrections for schwarzschild and reissner–nordström black holes”, *Classical and Quantum Gravity*, vol. 21, no. 6, p. 1383, 2004.

[72] A. P. Lundgren, “Charged black hole in a canonical ensemble”, *Physical Review D*, vol. 77, no. 4, p. 044 014, 2008.

[73] S. Md, “Phase transition of quantum-corrected schwarzschild black hole in rainbow gravity”, *Physics Letters B*, vol. 784, pp. 6–11, 2018.

[74] P. Wang, H. Wu, and H. Yang, “Thermodynamics and phase transition of a nonlinear electrodynamics black hole in a cavity”, *Journal of High Energy Physics*, vol. 2019, no. 7, pp. 1–19, 2019.

[75] P. Wang, H. Wu, H. Yang, and F. Yao, “Extended phase space thermodynamics for black holes in a cavity”, *Journal of High Energy Physics*, vol. 2020, no. 9, pp. 1–19, 2020.

[76] M. K. Parikh and F. Wilczek, “Hawking radiation as tunneling”, *Physical review letters*, vol. 85, no. 24, p. 5042, 2000. [Online]. Available: `https://doi.org/10.1103/PhysRevLett.85.5042`.

[77] K Srinivasan and T Padmanabhan, “Particle production and complex path analysis”, *Physical Review D*, vol. 60, no. 2, p. 024 007, 1999.

[78] S. M. Christensen and S. A. Fulling, “Trace anomalies and the hawking effect”, *Physical Review D*, vol. 15, no. 8, p. 2088, 1977.

[79] S. P. Robinson and F. Wilczek, “Relationship between hawking radiation and gravitational anomalies”, *Physical review letters*, vol. 95, no. 1, p. 011 303, 2005.

[80] R. Banerjee and S. Kulkarni, “Hawking radiation and covariant anomalies”, *Physical Review D*, vol. 77, no. 2, p. 024 018, 2008.

[81] P. Kraus and F. Wilczek, “Self-interaction correction to black hole radiance”, *Nuclear Physics B*, vol. 433, no. 2, pp. 403–420, 1995.

[82] M. Parikh, “A secret tunnel through the horizon”, *General Relativity and Gravitation*, vol. 36, pp. 2419–2422, 2004. [Online]. Available: `https://doi.org/10.1023/B:GERG.0000046850.67053.49`.

[83] M. K. Parikh, “Energy conservation and hawking radiation”, *arXiv preprint hep-th/0402166*, 2004. [Online]. Available: `https://doi.org/10.1142/9789812704030_0155`.

[84] S. Hemming and E. Keski-Vakkuri, “Hawking radiation from ads black holes”, *Physical Review D*, vol. 64, no. 4, p. 044 006, 2001.

[85] E. C. Vagenas, “Are extremal 2d black holes really frozen?”, *Physics Letters B*, vol. 503, no. 3-4, pp. 399–403, 2001.

[86] A. Medved, “Radiation via tunneling from a de sitter cosmological horizon”, *Physical Review D*, vol. 66, no. 12, p. 124 009, 2002.

[87] E. C. Vagenas, “Semiclassical corrections to the bekenstein–hawking entropy of the btz black hole via self-gravitation”, *Physics Letters B*, vol. 533, no. 3-4, pp. 302–306, 2002.

[88] ——, “Two-dimensional dilatonic black holes and hawking radiation”, *Modern Physics Letters A*, vol. 17, no. 10, pp. 609–618, 2002.

[89] ——, “Generalization of the kkw analysis for black hole radiation”, *Physics Letters B*, vol. 559, no. 1-2, pp. 65–73, 2003.

[90] J. Zhang and Z. Zhao, “Hawking radiation via tunneling from kerr black holes”, *Modern Physics Letters A*, vol. 20, no. 22, pp. 1673–1681, 2005.

[91] ——, “New coordinates for kerr–newman black hole radiation”, *Physics Letters B*, vol. 618, no. 1-4, pp. 14–22, 2005.

[92] M. Arzano, A. J. M. Medved, and E. C. Vagenas, “Hawking radiation as tunneling through the quantum horizon”, *Journal of High Energy Physics*, vol. 2005, no. 09, p. 037, 2005.

[93] W. Liu, “New coordinates for btz black hole and hawking radiation via tunnelling”, *Physics Letters B*, vol. 634, no. 5-6, pp. 541–544, 2006.

[94] P Mitra, “Hawking temperature from tunnelling formalism”, *Physics Letters B*, vol. 648, no. 2-3, pp. 240–242, 2007.

[95] L Vanzo, G Acquaviva, and R Di Criscienzo, “Tunnelling methods and hawking’s radiation: Achievements and prospects”, *Classical and Quantum Gravity*, vol. 28, no. 18, p. 183 001, 2011.

[96] G. Johnson and J. March-Russell, “Hawking radiation of extended objects”, *Journal of High Energy Physics*, vol. 2020, no. 4, pp. 1–16, 2020.

[97] Y. Liu, “The effect of quantum correction on hawking radiation for schwarzschild black holes”, *arXiv preprint arXiv:2201.00599*, 2022.

[98] X. Calmet, S. D. Hsu, and M. Sebastianutti, “Quantum gravitational corrections to particle creation by black holes”, *Physics Letters B*, p. 137 820, 2023.

[99] B Hamil and B. Lütfüoğlu, “Effect of snyder–de sitter model on the black hole thermodynamics in the context of rainbow gravity”, *International Journal of Geometric Methods in Modern Physics*, vol. 19, no. 03, p. 2 250 047, 2022.

[100] B. C. Lütfüoğ lu, B. Hamil, and L. Dahbi, "Quantum corrections to the thermodynamics of rotating charged BTZ black hole in gravity's rainbow", *International Journal of Modern Physics A*, vol. 37, no. 18, Jun. 2022. DOI: `10.1142/s0217751x22501263`. [Online]. Available: `https://doi.org/10.1142%2Fs0217751x22501263`.

[101] B Hamil and B. Lütfüoğlu, "Thermodynamics of schwarzschild black hole surrounded by quintessence in gravity's rainbow", *Nuclear Physics B*, vol. 990, p. 116 191, 2023.

[102] Z.-W. Feng and S.-Z. Yang, "Thermodynamic phase transition of a black hole in rainbow gravity", *Physics Letters B*, vol. 772, pp. 737–742, 2017.

[103] Z.-W. Feng, D.-L. Tang, D.-D. Feng, and S.-Z. Yang, "The thermodynamics and phase transition of a rainbow black hole", *Modern Physics Letters A*, vol. 35, no. 05, p. 2 050 010, 2020.

[104] Z.-W. Feng, X. Zhou, S.-Q. Zhou, and D.-D. Feng, "Rainbow gravity corrections to the information flux of a black hole and the sparsity of hawking radiation", *Annals of Physics*, vol. 416, p. 168 144, 2020.

[105] Z. Feng, H. Li, X. Zu, and S. Yang, "Quantum corrections to the thermodynamics of schwarzschild–tangherlini black hole and the generalized uncertainty principle", *The European Physical Journal C*, vol. 76, pp. 1–9, 2016.

[106] Z.-Y. Fu and H.-L. Li, "The effect of gup on thermodynamic phase transition of rutz-schwarzschild black hole", *Nuclear Physics B*, vol. 969, p. 115 475, 2021.

[107] B. Hamil and B. Lütfüoğlu, "Effect of the modified heisenberg algebra on the black hole thermodynamics", *Europhysics Letters*, vol. 133, no. 3, p. 30 003, 2021.

[108] B Hamil and B. Lütfüoğlu, "The effect of higher-order extended uncertainty principle on the black hole thermodynamics", *Europhysics Letters*, vol. 134, no. 5, p. 50 007, 2021.

[109] B. Hamil and B. C. Lütfüoğlu, "Black hole thermodynamics in the presence of a maximal length and minimum measurable in momentum", *Europhysics Letters*, vol. 135, no. 5, p. 59 001, 2021.

[110] B Hamil, B. Lütfüoğlu, and L Dahbi, "Eup-corrected thermodynamics of btz black hole", *International Journal of Modern Physics A*, vol. 37, no. 22, p. 2 250 130, 2022.

[111] H. Chen, H. Hassanabadi, B. C. Lütfüoğlu, and Z.-W. Long, "Quantum corrections to the quasinormal modes of the schwarzschild black hole", *General Relativity and Gravitation*, vol. 54, no. 11, p. 143, Nov. 2022. DOI: `10.1007/s10714-022-03037-9`. [Online]. Available: `https://doi.org/10.1007/s10714-022-03037-9`.

[112] H. Chen, B. C. Lütfüoğlu, H. Hassanabadi, and Z.-W. Long, "Thermodynamics of the reissner-nordström black hole with quintessence matter on the egup framework", *Physics Letters B*, vol. 827, p. 136 994, 2022.

[113] B. Lütfüoğlu, B Hamil, and L Dahbi, "Thermodynamics of schwarzschild black hole surrounded by quintessence with generalized uncertainty principle", *The European Physical Journal Plus*, vol. 136, no. 9, p. 976, 2021.

[114] B Hamil and B. Lütfüoğlu, "The effect of modified dispersion relations on the thermodynamics of schwarzschild black hole surrounded by quintessence", *The European Physical Journal Plus*, vol. 137, no. 10, p. 1124, 2022.

[115] Y. C. Ong, "An effective black hole remnant via infinite evaporation time due to generalized uncertainty principle", *Journal of High Energy Physics*, vol. 2018, no. 10, pp. 1–11, 2018.

[116] L. Petruzziello, "Generalized uncertainty principle with maximal observable momentum and no minimal length indeterminacy", *Classical and Quantum Gravity*, vol. 38, no. 13, p. 135 005, 2021.

[117] K. Nouicer, "Quantum-corrected black hole thermodynamics to all orders in the planck length", *Physics Letters B*, vol. 646, no. 2-3, pp. 63–71, 2007.

[118] X. Zhou, Z.-W. Feng, and S.-Q. Zhou, "Impacts of generalized uncertainty principle on the black hole thermodynamics and phase transition in a cavity", *Frontiers in Physics*, vol. 10, p. 887 410, 2022.

[119] K. Nozari and A. Sefidgar, "On the existence of the logarithmic correction term in black hole entropy-area relation", *General Relativity and Gravitation*, vol. 39, pp. 501–509, 2007.

[120] ——, "Comparison of approaches to quantum correction of black hole thermodynamics", *Physics Letters B*, vol. 635, no. 2-3, pp. 156–160, 2006.

[121] Z.-W. Feng, X. Zhou, S. Zhou, and S. Yang, "Quantum corrections to the thermodynamics and phase transition of a black hole surrounded by a cavity in the extended phase space", *Communications in Theoretical Physics*, vol. 74, no. 8, p. 085 403, 2022.

[122] Y. Gim and W. Kim, "Thermodynamic phase transition in the rainbow schwarzschild black hole", *Journal of Cosmology and Astroparticle Physics*, vol. 2014, no. 10, p. 003, 2014.

[123] A. Connes, *Noncommutative geometry*. Springer, 1994.

[124] M. Wohlgenannt, “Introduction to a non-commutative version of the standard model”, *arXiv preprint hep-th/0302070*, 2003.

[125] G. Barnich, F. Brandt, and M. Grigoriev, “Seiberg-witten maps and noncommutative yang-mills theories for arbitrary gauge groups”, *Journal of High Energy Physics*, vol. 2002, no. 08, p. 023, 2002.

[126] P. Aschieri, B Jurčo, P. Schupp, and J. Wess, “Noncommutative guts, standard model and c, p, t”, *Nuclear Physics B*, vol. 651, no. 1-2, pp. 45–70, 2003.

[127] R. H. Brandenberger, “String theory, space-time non-commutativity and structure formation”, *Progress of Theoretical Physics Supplement*, vol. 171, pp. 121–132, 2007.

[128] J. Bellissard, “Noncommutative geometry and quantum hall effect”, in *Proceedings of the International Congress of Mathematicians: August 3–11, 1994 Zürich, Switzerland*, Springer, 1995, pp. 1238–1246.

[129] S. Dulat and K. Li, “Quantum hall effect in noncommutative quantum mechanics”, *The European Physical Journal C*, vol. 60, pp. 163–168, 2009.

[130] R. J. Szabo, “Quantum field theory on noncommutative spaces”, *Physics Reports*, vol. 378, no. 4, pp. 207–299, 2003.

[131] P. Aschieri, *Noncommutative spacetimes: symmetries in noncommutative geometry and field theory*. Springer Science & Business Media, 2009, vol. 774.

[132] K. NOZARI and B. FAZLPOUR, “Thermodynamics of noncommutative schwarzschild black hole”, *Modern Physics Letters A*, vol. 22, no. 38, pp. 2917–2930, 2007. DOI: `10.1142/S0217732307023602`. eprint: `https://doi.org/10.1142/S0217732307023602`. [Online]. Available: `https://doi.org/10.1142/S0217732307023602`.

[133] K. Nozari and S. Akhshabi, “Orbits of particles in noncommutative schwarzschild spacetime”, *EPL (Europhysics Letters)*, vol. 80, no. 2, p. 20 002, 2007.

[134] ——, “On the stability of planetary circular orbits in noncommutative spaces”, *arXiv preprint gr-qc/0608076*, 2006.

[135] R. S. Kuniyal, R. Uniyal, A. Biswas, H. Nandan, and K. Purohit, “Null geodesics and red–blue shifts of photons emitted from geodesic particles around a noncommutative black hole space–time”, *International Journal of Modern Physics A*, vol. 33, no. 16, p. 1 850 098, 2018.

[136] B Mirza and M Dehghani, “Noncommutative geometry and classical orbits of particles in a central force potential”, *Communications in Theoretical Physics*, vol. 42, no. 2, p. 183, 2004.

[137] S. Ulhoa, R. Amorim, and A. Santos, “On non-commutative geodesic motion”, *General Relativity and Gravitation*, vol. 46, no. 7, p. 1760, 2014.

[138] A. Larranaga, “Geodesic structure of the noncommutative schwarzschild anti-de sitter black hole i: Timelike geodesics”, *arXiv preprint arXiv:1110.0778*, 2011.

[139] K. Nozari, S. Akhshabi, and N. Sadeghnezhad, “Stability of circular orbits in noncommutative schwarzschild spacetime.”, *Acta Physica Polonica B*, vol. 39, no. 11, 2008.

[140] S. Giri, H. Nandan, L. K. Joshi, and S. D. Maharaj, “Geodesic stability and quasinormal modes of non-commutative schwarzschild black hole employing lyapunov exponent”, *The European Physical Journal Plus*, vol. 137, no. 2, pp. 1–11, 2022.

[141] P. Bhar, F. Rahaman, R. Biswas, and U. Mondal, “Particles and scalar waves in noncommutative charged black hole spacetime”, *Communications in Theoretical Physics*, vol. 64, no. 1, p. 1, 2015.

[142] E Harikumar, S. K. Panja, and V. Rajagopal, “Maximal acceleration in a lorentz invariant non-commutative space-time”, *arXiv preprint arXiv:2202.06591*, 2022.

[143] E Harikumar and V. Rajagopal, “Maximal acceleration in non-commutative space–time and its implications”, *Annals of Physics*, vol. 423, p. 168 332, 2020.

[144] M Sharif and S. Iftikhar, “Shadow of a charged rotating non-commutative black hole”, *The European Physical Journal C*, vol. 76, no. 11, pp. 1–9, 2016.

[145] P. Nicolini, “A model of radiating black hole in noncommutative geometry”, *Journal of Physics A: Mathematical and General*, vol. 38, no. 39, pp. L631–L638, Sep. 2005. DOI: `10.1088/0305-4470/38/39/l02`. [Online]. Available: `https://doi.org/10.1088/0305-4470/38/39/l02`.

[146] J. C. Lopez-Dominguez, O. Obregón, M. Sabido, and C. Ramirez, “Towards noncommutative quantum black holes”, *Phys. Rev. D*, vol. 74, p. 084 024, 8 Oct. 2006. DOI: `10.1103/PhysRevD.74.084024`. [Online]. Available: `https://link.aps.org/doi/10.1103/PhysRevD.74.084024`.

[147] K. Nozari and B. Fazlpour, *Reissner-nordström black hole thermodynamics in noncommutative spaces*, 2006. arXiv: `gr-qc/0608077 [gr-qc]`.

[148] Y. S. Myung, Y.-W. Kim, and Y.-J. Park, "Thermodynamics and evaporation of the noncommutative black hole", *Journal of High Energy Physics*, vol. 2007, no. 02, pp. 012–012, Feb. 2007. DOI: `10.1088/1126-6708/2007/02/012`. [Online]. Available: `https://doi.org/10.1088/1126-6708/2007/02/012`.

[149] M. Chaichian, A. Tureanu, M. Setare, and G Zet, "On black holes and cosmological constant in noncommutative gauge theory of gravity", *Journal of High Energy Physics*, vol. 2008, no. 04, p. 064, 2008.

[150] P. Mukherjee and A. Saha, "Deformed reissner–nordstrom solutions in noncommutative gravity", *Physical Review D*, vol. 77, no. 6, p. 064 014, 2008.

[151] R. Linares, M. Maceda, and O. Sánchez-Santos, "Thermodynamical properties of a noncommutative anti–de sitter–einstein-born-infeld spacetime from gauge theory of gravity", *Phys. Rev. D*, vol. 101, p. 044 008, 4 Feb. 2020. DOI: `10.1103/PhysRevD.101.044008`. [Online]. Available: `https://link.aps.org/doi/10.1103/PhysRevD.101.044008`.

[152] R. Casadio and P. Nicolini, "The decay-time of non-commutative micro-black holes", *Journal of High Energy Physics*, vol. 2008, no. 11, p. 072, 2008.

[153] K. Nozari and S. H. Mehdipour, "Hawking radiation as quantum tunneling from a noncommutative schwarzschild black hole", *Classical and Quantum Gravity*, vol. 25, no. 17, p. 175 015, 2008.

[154] R. Banerjee, B. R. Majhi, and S. Samanta, "Noncommutative black hole thermodynamics", *Physical Review D*, vol. 77, no. 12, p. 124 035, 2008.

[155] K. Nozari and S. H. Mehdipour, "Parikh-wilczek tunneling from noncommutative higher dimensional black holes", *Journal of High Energy Physics*, vol. 2009, no. 03, p. 061, 2009.

[156] Y.-G. Miao, Z. Xue, and S.-J. Zhang, "Quantum tunneling and spectroscopy of noncommutative inspired kerr black hole", *International Journal of Modern Physics D*, vol. 21, no. 02, p. 1 250 018, 2012.

[157] ——, "Tunneling of massive particles from noncommutative inspired schwarzschild black hole", *General Relativity and Gravitation*, vol. 44, pp. 555–566, 2012.

[158] K. Nozari and S. Islamzadeh, "Tunneling of massive and charged particles from noncommutative reissner-nordström black hole", *Astrophysics and Space Science*, vol. 347, pp. 299–304, 2013.

[159] A. Övgün and K. Jusufi, "Massive vector particles tunneling from noncommutative charged black holes and their gup-corrected thermodynamics", *The European Physical Journal Plus*, vol. 131, no. 5, p. 177, 2016.

[160] N. Seiberg and E. Witten, "String theory and noncommutative geometry", *Journal of High Energy Physics*, vol. 1999, no. 09, p. 032, 1999.

[161] A. H. Chamseddine, "Deforming einstein's gravity", *Physics Letters B*, vol. 504, no. 1-2, pp. 33–37, 2001.

[162] M. Chaichian, A. Tureanu, and G Zet, "Corrections to schwarzschild solution in noncommutative gauge theory of gravity", *Physics Letters B*, vol. 660, no. 5, pp. 573–578, 2008.

[163] W. Kim, E. J. Son, and M. Yoon, "Thermodynamic similarity between the noncommutative schwarzschild black hole and the reissner-nordström black hole", *Journal of High Energy Physics*, vol. 2008, no. 04, p. 042, 2008.

[164] S. Zaim and H. Rezki, "Thermodynamic properties of a yukawa–schwarzschild black hole in noncommutative gauge gravity", *Gravitation and Cosmology*, vol. 26, no. 3, pp. 200–207, 2020.

[165] A. Araújo Filho, S. Zare, P. Porfírio, J. Kříž, and H. Hassanabadi, "Thermodynamics and evaporation of a modified schwarzschild black hole in a non–commutative gauge theory", *Physics Letters B*, vol. 838, p. 137 744, 2023, ISSN: 0370-2693. DOI: `https://doi.org/10.1016/j.physletb.2023.137744`. [Online]. Available: `https://www.sciencedirect.com/science/article/pii/S0370269323000783`.

[166] N Heidari, H Hassanabadi, J Kuríuz, S Zare, P. Porfírio, *et al.*, "Gravitational signatures of a non–commutative stable black hole", *arXiv preprint arXiv:2305.06838*, 2023.

[167] A. Touati and S. Zaim, "Geodesic equation in non-commutative gauge theory of gravity", *Chinese Physics C*, vol. 46, no. 10, p. 105 101, Jun. 2022. DOI: `10.1088/1674-1137/ac75ca`. [Online]. Available: `https://doi.org/10.1088/1674-1137/ac75ca`.

[168] ——, "Lyapunov exponents and geodesic stability of schwarzschild black hole in the non-commutative gauge theory of gravity", *arXiv preprint arXiv:2405.01743*, 2024.

[169] ——, "The bound of the non-commutative parameter based on gravitational measurements", in *Physical Sciences Forum*, MDPI, vol. 7, 2023, p. 54. DOI: `https://doi.org/10.3390/ECU2023-14061`. [Online]. Available: `https://www.mdpi.com/2673-9984/7/1/54`.

[170] ——, "Thermodynamic properties of schwarzschild black hole in non-commutative gauge theory of gravity", *Annals of Physics*, vol. 455, p. 169 394, 2023, ISSN: 0003-4916. DOI: https://doi.org/10.1016/j.aop.2023.169394. [Online]. Available: https://www.sciencedirect.com/science/article/pii/S000349162300180X.

[171] ——, "Schwarzschild black hole surrounded by a cavity and phase transition in the non-commutative gauge theory of gravity", *Astroparticle Physics*, vol. 161, p. 102 988, 2024, ISSN: 0927-6505. DOI: https://doi.org/10.1016/j.astropartphys.2024.102988. [Online]. Available: https://www.sciencedirect.com/science/article/pii/S0927650524000653.

[172] ——, "On modified first law of black hole thermodynamics in the non-commutative gauge theory", *arXiv preprint arXiv:2205.13052*, 2022.

[173] A. Touati and Z. Slimane, "Quantum tunneling from schwarzschild black hole in non-commutative gauge theory of gravity", *Physics Letters B*, vol. 848, p. 138 335, 2024, ISSN: 0370-2693. DOI: https://doi.org/10.1016/j.physletb.2023.138335. [Online]. Available: https://www.sciencedirect.com/science/article/pii/S037026932300669X.

[174] L. D. Landau, *The classical theory of fields*. Butterworth Heinemann, 1980, vol. 2.

[175] R. M. Wald, *General relativity*. University of Chicago press, 1984.

[176] M. P. Hobson, G. P. Efstathiou, and A. N. Lasenby, *General relativity: an introduction for physicists*. Cambridge University Press, 2006.

[177] A. Das, *Lectures on gravitation*. World scientific, 2011.

[178] B. Ydri, *Lectures on General Relativity, Cosmology and Quantum Black Holes*, ser. 2053-2563. IOP Publishing, 2017, ISBN: 978-0-7503-1478-7. DOI: 10.1088/978-0-7503-1478-7. [Online]. Available: https://dx.doi.org/10.1088/978-0-7503-1478-7.

[179] S. M. Carroll, *Spacetime and geometry*. Cambridge University Press, 2019.

[180] H.Andrillat, *La théorie de la relativité générale*, https://national.udppc.asso.fr/attachments/article/559/relativite_generale_andrillat2.pdf, 1994.

[181] S. Weinberg, "Gravitation and cosmology: Principles and applications of gr", 1972.

[182] L. Ryder, *Introduction to general relativity*. Cambridge University Press, 2009.

[183] I. I. Shapiro, "Fourth test of general relativity", *Physical Review Letters*, vol. 13, no. 26, p. 789, 1964.

[184] S. Benczik, L. N. Chang, D. Minic, N. Okamura, S. Rayyan, and T. Takeuchi, "Short distance versus long distance physics: The classical limit of the minimal length uncertainty relation", *Physical Review D*, vol. 66, no. 2, p. 026 003, 2002.

[185] G. Nyambuya, "Azimuthally symmetric theory of gravitation–i. on the perihelion precession of planetary orbits", *Monthly Notices of the Royal Astronomical Society*, vol. 403, no. 3, pp. 1381–1391, 2010.

[186] ——, "Azimuthally symmetric theory of gravitation–ii. on the perihelion precession of solar planetary orbits", *Monthly Notices of the Royal Astronomical Society*, vol. 451, no. 3, pp. 3034–3043, 2015.

[187] S. Weinberg, *Gravitation and cosmology: principles and applications of the general theory of relativity*. John Wiley & Sons, 2004.

[188] B. Schutz, *A first course in general relativity*. Cambridge university press, 2022.

[189] J. D. Bekenstein, "Black holes and entropy", *Physical Review D*, vol. 7, no. 8, p. 2333, 1973.

[190] S. W. Hawking, "Gravitational radiation from colliding black holes", *Physical Review Letters*, vol. 26, no. 21, p. 1344, 1971.

[191] N. A. Batakis, "General relativity reformed to a genuine yang-mills gauge theory for gravity", *arXiv preprint gr-qc/9711054*, 1997.

[192] G. Zet, V. Manta, S Oancea, I. Radinschi, and B. Ciobanu, "A computer aided study of de-sitter gauge theory of gravitation", *Mathematical and computer modelling*, vol. 43, no. 5-6, pp. 458–465, 2006.

[193] R. ALDROVANDI, J. Beltrán Almeida, and J. Pereira, "Cosmological term and fundamental physics", *International Journal of Modern Physics D*, vol. 13, no. 10, pp. 2241–2248, 2004.

[194] L. Möller, "Second order expansion of action functionals of noncommutative gauge theories", *Journal of High Energy Physics*, vol. 2004, no. 10, p. 063, 2004.

[195] K. Uelker and B. Yapışkan, "Seiberg-witten maps to all orders", *Physical Review D*, vol. 77, no. 6, p. 065 006, 2008.

[196] B. Ydri, *Lectures on matrix field theory*. Springer, 2017.

[197] R Jackiw, "Physical instances of noncommuting coordinates", 2001.

[198] L. J. Garay, “Quantum gravity and minimum length”, *International Journal of Modern Physics A*, vol. 10, no. 02, pp. 145–165, 1995.

[199] M. A. Rieffel, *Deformation Quantization for Actions of R^d*. American Mathematical Soc., 1993.

[200] H. J. Groenewold and H. J. Groenewold, *On the principles of elementary quantum mechanics*. Springer, 1946.

[201] J. E. Moyal, “Quantum mechanics as a statistical theory”, in *Mathematical Proceedings of the Cambridge Philosophical Society*, Cambridge University Press, vol. 45, 1949, pp. 99–124.

[202] M. M. Sheikh-Jabbari and A. Tureanu, “Realization of Cohen-Glashow Very Special Relativity on Noncommutative Space-Time”, *Phys. Rev. Lett.*, vol. 101, p. 261 601, 2008. DOI: `10.1103/PhysRevLett.101.261601`. arXiv: `0806.3699 [hep-th]`.

[203] P. Nicolini, “Noncommutative black holes, the final appeal to quantum gravity: A review”, *International Journal of Modern Physics A*, vol. 24, no. 07, pp. 1229–1308, 2009.

[204] P. Bhar, F. Rahaman, R. Biswas, and U. Mondal, “Particles and scalar waves in noncommutative charged black hole spacetime”, *Communications in Theoretical Physics*, vol. 64, no. 1, p. 1, 2015.

[205] F Rahaman, I Radinschi, U. Mondal, and P Bhar, “Particle’s motion around a non-commutative black hole”, *International Journal of Theoretical Physics*, vol. 54, no. 3, pp. 1038–1051, 2015.

[206] D. Kazakov and S. Solodukhin, “On quantum deformation of the schwarzschild solution”, *Nuclear Physics B*, vol. 429, no. 1, pp. 153–176, 1994.

[207] X.-M. Deng, “Geodesics and periodic orbits around quantum-corrected black holes”, *Physics of the Dark Universe*, vol. 30, p. 100 629, 2020.

[208] K. Nozari and M. Hajebrahimi, “Geodesic structure of the quantum-corrected schwarzschild black hole surrounded by quintessence”, *arXiv preprint arXiv:2004.14775*, 2020.

[209] A. F. Zakharov, “Constraints on tidal charge of the supermassive black hole at the galactic center with trajectories of bright stars”, *The European Physical Journal C*, vol. 78, no. 8, pp. 1–7, 2018.

[210] R Abuter, A Amorim, M Bauböck, J. Berger, H Bonnet, W Brandner, V Cardoso, Y Clénet, P. De Zeeuw, J Dexter, *et al.*, “Detection of the schwarzschild precession in the orbit of the star s2 near the galactic centre massive black hole”, *Astronomy & Astrophysics*, vol. 636, p. L5, 2020.

[211] M Sharif and S. Iftikhar, “Effects of electromagnetic field on the motion of particles in dyonic reissner–nordström black hole”, *International Journal of Modern Physics D*, vol. 26, no. 09, p. 1 750 091, 2017.

[212] S. Grunau and V. Kagramanova, “Geodesics of electrically and magnetically charged test particles in the reissner-nordström space-time: Analytical solutions”, *Physical Review D*, vol. 83, no. 4, p. 044 009, 2011.

[213] M. A. Abramowicz and P. C. Fragile, “Foundations of black hole accretion disk theory”, *Living Reviews in Relativity*, vol. 16, no. 1, pp. 1–88, 2013.

[214] D. Pérez, G. E. Romero, and S. P. Bergliaffa, “Accretion disks around black holes in modified strong gravity”, *Astronomy & Astrophysics*, vol. 551, A4, 2013.

[215] M Jaroszynski, M. Abramowicz, and B Paczynski, “Supercritical accretion disks around black holes”, *Acta Astronomica*, vol. 30, pp. 1–34, 1980.

[216] S. K. Chakrabarti and L. G. Titarchuk, “Spectral properties of accretion disks around galactic and extragalactic black holes”, *arXiv preprint astro-ph/9510005*, 1995.

[217] D. W. Weedman, *Quasar astronomy*, 10. Cambridge University Press, 1988.

[218] B. Peterson, *Quasar*, `https://www.britannica.com/science/quasar`, Online; Accessed 18 September 2021, Jun. 2019. [Online]. Available: `https://www.britannica.com/science/quasar`.

[219] V. Misra and J. Levin, “Rational orbits around charged black holes”, *Physical Review D*, vol. 82, no. 8, p. 083 001, 2010.

[220] M. Hong, “Motion of a test particle in the reissner-nordstrom spacetime”, *arXiv preprint arXiv:1709.08978*, 2017.

[221] J.-P. Hu, L.-L. Shi, Y. Zhang, and P.-F. Duan, “Analytical time-like geodesics in modified hayward black hole space-time”, *Astrophysics and Space Science*, vol. 363, no. 10, pp. 1–8, 2018.

[222] O. Pedraza, L. López, R Arceo, and I Cabrera-Munguia, “Geodesics of hayward black hole surrounded by quintessence”, *General Relativity and Gravitation*, vol. 53, no. 3, pp. 1–17, 2021.

[223] S. Giri, H. Nandan, L. K. Joshi, and S. D. Maharaj, “Geodesic stability and quasinormal modes of non-commutative schwarzschild black hole employing lyapunov exponent”, *The European Physical Journal Plus*, vol. 137, no. 2, pp. 1–11, 2022.

[224] M. Wanas and M. Bakry, “Notes on applications of general relativity in free space: Implication from the motion of a test particle”, *Astrophysics and Space Science*, vol. 228, no. 1, pp. 203–220, 1995.

[225] M. Heydari-Fard, M. Heydari-Fard, and H. R. Sepangi, “Null geodesics and shadow of hairy black holes in einstein-maxwell-dilaton gravity”, *Physical Review D*, vol. 105, no. 12, p. 124 009, 2022.

[226] S. Iftikhar, “Particle dynamics around a charged black hole”, in *EPJ Web of Conferences*, EDP Sciences, vol. 168, 2018, p. 04 006.

[227] A. Al Zahrani, “Circular orbits of charged particles around a weakly charged and magnetized schwarzschild black hole”, *Physical Review D*, vol. 103, no. 8, p. 084 008, 2021.

[228] T. Berry, A. Simpson, and M. Visser, “Photon spheres, iscos, and oscos: Astrophysical observables for regular black holes with asymptotically minkowski cores”, *Universe*, vol. 7, no. 1, p. 2, 2020.

[229] P. Das, R. Sk, and S. Ghosh, “Motion of charged particle in reissner–nordström spacetime: A jacobi-metric approach”, *The European Physical Journal C*, vol. 77, no. 11, pp. 1–14, 2017.

[230] G. S. Adkins and J. McDonnell, “Orbital precession due to central-force perturbations”, *Physical Review D*, vol. 75, no. 8, p. 082 001, 2007.

[231] A Avalos-Vargas and G Ares de Parga, “The precession of the orbit of a test neutral body interacting with a massive charged body”, *The European Physical Journal Plus*, vol. 126, no. 11, pp. 1–7, 2011.

[232] J. M. Romero and J. D. Vergara, “The kepler problem and noncommutativity”, *Modern Physics Letters A*, vol. 18, no. 24, pp. 1673–1680, 2003.

[233] S. Bahamonde and J. G. Valcarcel, “Observational constraints in metric-affine gravity”, *The European Physical Journal C*, vol. 81, no. 6, pp. 1–14, 2021.

[234] L. Iorio, “Constraining the electric charges of some astronomical bodies in reissner–nordström spacetimes and generic r- 2-type power-law potentials from orbital motions”, *General Relativity and Gravitation*, vol. 44, no. 7, pp. 1753–1767, 2012.

[235] A Avalos-Vargas and G Ares de Parga, “The precession of the orbit of a charged body interacting with a massive charged body in general relativity”, *The European Physical Journal Plus*, vol. 127, no. 12, pp. 1–11, 2012.

[236] H. Müller, A. Peters, and S. Chu, “A precision measurement of the gravitational redshift by the interference of matter waves”, *Nature*, vol. 463, no. 7283, pp. 926–929, 2010.

[237] M. Karimabadi, S. A. Alavi, and D. M. Yekta, “Non-commutative effects on gravitational measurements”, *Classical and Quantum Gravity*, vol. 37, no. 8, p. 085 009, 2020.

[238] P. Chingangbam, S. Das, *et al.*, “Constraint on noncommutative spacetime from planck data”, *Physical Review D*, vol. 91, no. 8, p. 083 503, 2015.

[239] R. F. Vessot, M. W. Levine, E. M. Mattison, E. Blomberg, T. Hoffman, G. Nystrom, B. Farrel, R. Decher, P. B. Eby, C. Baugher, *et al.*, “Test of relativistic gravitation with a space-borne hydrogen maser”, *Physical Review Letters*, vol. 45, no. 26, p. 2081, 1980.

[240] E. Goldoni and L. Stefanini, “A century of light-bending measurements: Bringing solar eclipses into the classroom”, *Physics Education*, vol. 55, no. 4, p. 045 009, 2020.

[241] A. K. Das and K. Abhyankar, “Difference of temperature between pole and equator of the sun”, *Nature*, vol. 172, no. 4376, pp. 496–497, 1953.

[242] A. Das and K. Abhyankar, “Temperature at the poles and at the equator of the sun”, *Vistas in Astronomy*, vol. 1, pp. 658–666, 1955.

[243] R. C. Altrock and R. C. Canfield, “Observations of photospheric pole-equator temperature differences”, *Solar Physics*, vol. 23, no. 2, pp. 257–264, 1972.

[244] A Peraiah, “Temperature difference between pole and equator of the sun”, *Solar Physics*, vol. 30, pp. 29–30, 1973.

[245] R. Li, K. Zhang, and J. Wang, “Thermal dynamic phase transition of reissner-nordström anti-de sitter black holes on free energy landscape”, *Journal of High Energy Physics*, vol. 2020, no. 10, pp. 1–25, 2020.

[246] A. Kobakhidze, C. Lagger, and A. Manning, “Constraining noncommutative spacetime from gw150914”, *Physical Review D*, vol. 94, no. 6, p. 064 033, 2016.

[247] P. Nicolini, A. Smailagic, and E. Spallucci, “Noncommutative geometry inspired schwarzschild black hole”, *Physics Letters B*, vol. 632, no. 4, pp. 547–551, 2006.

[248] S. A. Alavi, “Reissner-nordstrom black hole in noncommutative spaces”, *arXiv preprint arXiv:0909.1688*, 2009.

[249] W. Kim and D. Lee, “Bound of noncommutativity parameter based on black hole entropy”, *Modern Physics Letters A*, vol. 25, no. 38, pp. 3213–3218, 2010.

[250] S. Soroushfar, R. Saffari, and S. Upadhyay, “Thermodynamic geometry of a black hole surrounded by perfect fluid in rastall theory”, *General Relativity and Gravitation*, vol. 51, no. 10, pp. 1–16, 2019.

[251] X. Calmet and F. Kuipers, “Quantum gravitational corrections to the entropy of a schwarzschild black hole”, *Physical Review D*, vol. 104, no. 6, p. 066 012, 2021.

[252] ——, “Black holes in quantum gravity”, *arXiv preprint arXiv:2202.02584*, 2022.

[253] R. C. Delgado, “Quantum gravitational corrections to the entropy of a reissner-nordström black hole”, *arXiv preprint arXiv:2201.08293*, 2022.

[254] D. Hansen, D. Kubizňák, and R. B. Mann, “Universality of p- v criticality in horizon thermodynamics”, *Journal of High Energy Physics*, vol. 2017, no. 1, pp. 1–24, 2017.

[255] Z.-M. Xu, B. Wu, and W.-L. Yang, “Van der waals fluid and charged ads black hole in the landau theory”, *Classical and Quantum Gravity*, vol. 38, no. 20, p. 205 008, 2021.

[256] D. Kubizňák and R. B. Mann, “P- v criticality of charged ads black holes”, *Journal of High Energy Physics*, vol. 2012, no. 7, pp. 1–25, 2012.

[257] Y. Chen and H.-L. Li, *Thermodynamic phase transition of a schwarzschild black hole with global monopole under gup*, 2020. arXiv: `2001.11193 [hep-th]`.

[258] S. Md, “Phase transition of quantum-corrected schwarzschild black hole in rainbow gravity”, *Physics Letters B*, vol. 784, pp. 6–11, 2018.

[259] A. Jawad, I. Siddique, I. P. Lobo, and W. Us Salam, “Effects of gauss–bonnet entropy on thermodynamics of kiselev black hole”, *International Journal of Modern Physics D*, vol. 29, no. 15, p. 2 050 101, 2020.

[260] P. Paul, S. Upadhyay, Y. Myrzakulov, D. V. Singh, and K. Myrzakulov, “More exact thermodynamics of nonlinear charged ads black holes in 4d critical gravity”, *Nuclear Physics B*, p. 116 259, 2023.

[261] Y.-G. Miao and Z.-M. Xu, “Thermodynamics of noncommutative high-dimensional ads black holes with non-gaussian smeared matter distributions”, *The European Physical Journal C*, vol. 76, pp. 1–13, 2016.

[262] D. Kastor, S. Ray, and J. Traschen, “Enthalpy and the mechanics of ads black holes”, *Classical and Quantum Gravity*, vol. 26, no. 19, p. 195 011, 2009.

[263] K. A. Meissner, “Black-hole entropy in loop quantum gravity”, *Classical and Quantum Gravity*, vol. 21, no. 22, p. 5245, 2004.

[264] A. Ghosh and P. Mitra, “Log correction to the black hole area law”, *Physical Review D*, vol. 71, no. 2, p. 027 502, 2005.

[265] S. N. Solodukhin, “Entropy of the schwarzschild black hole and the string–black-hole correspondence”, *Physical Review D*, vol. 57, no. 4, p. 2410, 1998.

[266] B. Zhang, Q.-y. Cai, L. You, and M.-s. Zhan, “Hidden messenger revealed in hawking radiation: A resolution to the paradox of black hole information loss”, *Physics Letters B*, vol. 675, no. 1, pp. 98–101, 2009.

[267] B. Zhang, Q.-y. Cai, M.-s. Zhan, and L. You, “Entropy is conserved in hawking radiation as tunneling: A revisit of the black hole information loss paradox”, *Annals of Physics*, vol. 326, no. 2, pp. 350–363, 2011.

[268] ——, “Information conservation is fundamental: Recovering the lost information in hawking radiation”, *International Journal of Modern Physics D*, vol. 22, no. 12, p. 1 341 014, 2013.

[269] X.-K. Guo and Q.-y. Cai, “Information recovery with hawking radiation from dynamical horizons”, *International Journal of Theoretical Physics*, vol. 53, pp. 2980–2987, 2014.

[270] S. Sannan, “Heuristic derivation of the probability distributions of particles emitted by a black hole”, *General Relativity and Gravitation*, vol. 20, pp. 239–246, 1988.

[271] H. Vieira, V. Bezerra, and G. Silva, “Analytic solutions in the dyon black hole with a cosmic string: Scalar fields, hawking radiation and energy flux”, *Annals of Physics*, vol. 362, pp. 576–592, 2015.

[272] H. Vieira and V. Bezerra, “Confluent heun functions and the physics of black holes: Resonant frequencies, hawking radiation and scattering of scalar waves”, *Annals of Physics*, vol. 373, pp. 28–42, 2016.

[273] G. Johnson, “Tunnelling of charged particles from black holes”, *Journal of High Energy Physics*, vol. 2020, no. 3, Mar. 2020. DOI: `10.1007/jhep03(2020)038`. [Online]. Available: `https://doi.org/10.1007%2Fjhep03%282020%29038`.

[274] A. Alonso-Serrano, M. P. Dąbrowski, and H. Gohar, “Generalized uncertainty principle impact onto the black holes information flux and the sparsity of hawking radiation”, *Physical Review D*, vol. 97, no. 4, p. 044 029, 2018.

[275] A. Alonso-Serrano and M. Visser, “Entropy/information flux in hawking radiation”, *Physics Letters B*, vol. 776, pp. 10–16, 2018.

[276] ——, “On burning a lump of coal”, *Physics Letters B*, vol. 757, pp. 383–386, 2016.

[277] S.-W. Wei and Y.-X. Liu, “Observing the shadow of einstein-maxwell-dilaton-axion black hole”, *Journal of Cosmology and Astroparticle Physics*, vol. 2013, no. 11, p. 063, 2013.

[278] A Belhaj, M Benali, A El Balali, H El Moumni, and S. Ennadifi, “Deflection angle and shadow behaviors of quintessential black holes in arbitrary dimensions”, *Classical and Quantum Gravity*, vol. 37, no. 21, p. 215 004, 2020.

[279] S. W. Hawking, “Black hole explosions?”, *Nature*, vol. 248, no. 5443, pp. 30–31, 1974.

[280] X. Calmet, B. Carr, and E. Winstanley, *Quantum black holes*. Springer, 2014, vol. 2072.

COLOPHON

This document was authored using `TeXstudio`[1] and typeset based on the `La Trobe PhD Thesis Template`[2] (customization of the `classicthesis`[3] LaTeX template) using `TeX Live`[4] on a machine running `Ubuntu`[5]. Other notable software tools used during the production of this document: `Wolfram Mathematica`[6] management.

---

[1] https://www.texstudio.org
[2] https://github.com/bashimao/ltu-thesis
[3] https://bitbucket.org/amiede/classicthesis
[4] https://tug.org/texlive
[5] https://ubuntu.com/download
[6] https://www.wolfram.com/mathematica/